Vers une mesure de l'angle γ du Triangle d'Unitarité avec le détecteur LHCb auprès du LHC (CERN) : étalonnage des calorimètres avec une technique de flux d'énergie et première observation de la désintégration Bs0 -> D0K*0

Aurélien Martens

LAL 11-172
9 Septembre 2011

Université Paris-sud 11

Ecole Doctorale Particules, Noyaux et Cosmos - ED 517
Laboratoire de l'Accélérateur Linéaire - UMR 8607

Discipline : Physique des particules

THÈSE DE DOCTORAT

présentée par

Aurélien MARTENS

Towards a measurement of the angle γ of the Unitarity Triangle with the LHCb detector at the LHC (CERN): calibration of the calorimeters using an energy flow technique and first observation of the $B_s^0 \to \overline{D}^0 \overline{K}^{*0}$ decay.

Vers une mesure de l'angle γ du Triangle d'Unitarité
avec le détecteur LHCb auprès du LHC (CERN) :
étalonnage des calorimètres avec une technique de flux d'énergie
et première observation de la désintégration $B_s^0 \to \overline{D}^0 \overline{K}^{*0}$.

Soutenue le 9 septembre 2011 devant le Jury composé de :

M.	A. Bevan	Rapporteur
M.	S. Descotes-Genon	Examinateur
M.	T. Gershon	Examinateur
M.	R. Forty	Examinateur
M.	F. Machefert	Directeur de thèse
Mme.	M.-H. Schune	Co-encadrante de thèse
M.	A. Stocchi	Président du Jury
Mme.	I. Wingerter-Seez	Rapporteuse

À mes parents,
À Véro.

Contents

Résumé

A ce jour la détermination de l'angle γ du Triangle d'Unitarité de la matrice de Cabibbo-Kabayashi-Maskawa est statistiquement limitée par la rareté des transitions $b \to u$. La précision obtenue en combinant les résultats des expériences BABAR et BELLE est proche de 10°. L'expérience LHCb auprès du LHC présente un fort potentiel d'amélioration pour ce paramètre de violation de CP, notamment via la désintégration $B^0 \to D^0 K^{*0}$, un des canaux clés de cette mesure. Les désintégrations $D^0 \to K^{\pm}\pi^{\mp}$, $D^0 \to K^{\pm}\pi^{\mp}\pi^0$ et $D^0 \to K^{\pm}\pi^{\mp}\pi^{+}\pi^{-}$ sont étudiées dans cette thèse. L'utilisation de désintégrations faisant intervenir des π^0 nécessite un bon étalonnage en énergie des calorimètres électromagnétiques. Une méthode d'étalonnage inter-cellules du ECAL basée sur le flux d'énergie, permet d'obtenir une inter-calibration de l'ordre de 1,5 %, l'échelle d'énergie absolue étant obtenue par des méthodes indépendantes non étudiées ici. La détermination du rapport d'embranchement de la désintégration $B_s^0 \to \overline{D}^0 \overline{K}^{*0}$, première étape du programme aboutissant à la mesure de la violation de CP dans le canal $B^0 \to D^0 K^{*0}$, est réalisée relativement au rapport d'embranchement de $B^0 \to \overline{D}^0 \rho^0$. Le résultat final obtenu avec 36 pb^{-1} de données collectées par LHCb en 2010 reste dominé par l'erreur statistique :

$$\frac{\mathcal{B}\left(\overline{B}_s^0 \to D^0 K^{*0}\right)}{\mathcal{B}\left(B^0 \to \overline{D}^0 \rho^0\right)} = 1,48 \pm 0,34\ (\text{stat}) \pm 0,15\ (\text{syst}) \pm 0,12\,(f_d/f_s)\,.$$

Mots clés : Physique des particules, Hadrons - Désintégration, Mésons, Violation CP, CKM, Triangle d'unitarité, UT, Grand Collisionneur de Hadrons, LHC, LHCb, Calorimètres électromagnétiques, Etalonnage.

Abstract

The present status on the determination of the angle γ of the Cabibbo-Kabayashi-Maskawa Unitary Triangle is statistically limited by the rarity of $b \to u$ transitions. The obtained precision combining results from the BABAR and BELLE experiments is close to $10°$. The LHCb experiment at the LHC has a strong potential to reduce the uncertainty on this CP violation parameter, especially through the $B^0 \to D^0 K^{*0}$ decay, one of the key channels for this measurement. The $D^0 \to K^{\pm}\pi^{\mp}$, $D^0 \to K^{\pm}\pi^{\mp}\pi^0$ and $D^0 \to K^{\pm}\pi^{\mp}\pi^{+}\pi^{-}$ decays are studied in this thesis. Decays involving π^0 require an accurate energy calibration of electromagnetic calorimeters. An inter-calibration technique based on the energy flow allows to obtain the 1.5 % level, the absolute scale being obtained from independent methods studied elsewhere. The determination of the $B_s^0 \to \overline{D}^0 \overline{K}^{*0}$ decay branching ratio, first step towards a measurement of CP violation in the $B^0 \to D^0 K^{*0}$ channel, is performed relatively to the $B^0 \to \overline{D}^0 \rho^0$ decay. The final result, obtained with 36 pb^{-1} of data collected by LHCb in 2010 is dominated by the statistical uncertainty:

$$\frac{\mathcal{B}\left(\overline{B}_s^0 \to D^0 K^{*0}\right)}{\mathcal{B}\left(B^0 \to \overline{D}^0 \rho^0\right)} = 1.48 \pm 0.34 \text{ (stat)} \pm 0.15 \text{ (syst)} \pm 0.12 \left(f_d/f_s\right)$$

Key words: Particles, Hadrons - Decay, Mesons, CP Violation, CKM, Unitarity Triangle, UT, Large Hadron Collider, LHC, LHCb, Electromagnetic calorimeters, Calibration.

Synthèse

- La culture burgonde ? Je ne savais même pas qu'il y en avait une... Non, moi je voulais faire grec moderne, mais il n'y avait plus de place. Il ne restait que burgonde ou anglais. AAAnglais ! Mais c'est encore moins répandu.

Lauràn Deutsh alias *L'interprète burgonde*
in *L'interprète*, **Kaamelott, Livre I**, Tome 1, Épisode 24,
écrit par Alexandre Astier.

Introduction

A ce jour aucun signe non-ambigu de nouvelle physique n'a été observé, ni de manière directe ni de manière indirecte via des mesures de violation de *CP*. En particulier les contraintes sur le triangle d'unitarité de la matrice CKM atteignent la précision du pourcent pour la plupart d'entre elles, grâce aux efforts considérables réalisés auprès des usines à mésons B, BABAR et BELLE. Néanmoins, l'angle $\gamma = \phi_3$ reste mal connu étant donné que la sensibilité à ce paramètre intervient dans l'interférence entre les transitions rares $b \to u$ et les transitions $b \to c$. Une précision de l'ordre de 10° est effectivement obtenue par BABAR et BELLE sur la mesure directe de l'angle γ dans les désintégrations charmées de mésons B. Cette mesure est encore limitée statistiquement et LHCb présente un fort potentiel d'amélioration grâce à la grande section efficace de production de paires $b\overline{b}$ et au taux de collisions élevé du LHC, $\sigma_{b\overline{b}} = 280\ \text{pb}^{-1}$ avec $\mathcal{L}_{\text{int.}} = 1\ \text{fb}^{-1}$ en 2011 au point de collision de LHCb.

Les canaux d'études de γ accessibles à LHCb sont nombreux et variés. Il sera en particulier possible de réaliser des mesures de γ à la fois influencées par de la nouvelle physique (γ *dans les boucles*, où les contributions de diagrammes pingouins dominent et cachent potentiellement de nouvelles particules) et des mesures dites *aux arbres*, où aucun diagramme pingouin ne contribue dans le Modèle Standard de la physique des particules. Les désintégrations sans charme du type $B^0 \to h^{\pm}h'^{\mp}$ permettent la detemination de γ, sous l'influence d'une potentielle nouvelle physique tandis que les désintégrations charmées $B \to DX$ permettent une détermination de γ sans influence attendue de nouvelle physique.

Parmi ces dernières, deux types importants de mesures subsistent : premièrement les mesures qui nécessitent des analyses dépendantes du temps avec un état final qui n'est pas spécifique à la saveur du B et deuxièmement celles qui ont un état final spécifique à la saveur du B (désintégrations dites auto-étiquettées) qui permettent une mesure intégrée sur le temps, et se limitent à une expérience de comptage. Les premières permettent une détermination de $\gamma + \phi_{\text{mélange}}$ où $\phi_{\text{mélange}}$ est l'angle de mélange qui intervient dans l'oscillation du méson B, mesuré par ailleurs précisement. Les secondes permettent une mesure directe de l'angle γ. Le paradigme de la matrice CKM sous-tend que l'ensemble de ces mesures de violation de CP sont régies par le même angle γ, ces dernières formant un test important de la matrice CKM.

Les désintégrations intégrées en temps ont permis aux usines à B d'obtenir une précision statistique combinée de 10° grâce aux désintégrations $B^{\pm} \to DK^{\pm}$ avec $D^0 \to K^0_S h^+ h^-$, un mode étudié dans le plan de Dalitz. Les autres canaux de désintégrations du D^0 dans un état propre de *CP* (méthode de Gronau-London-Wyler, GLW) ou dans un état final commun au D^0 et au $\overline{D}^0$ (méthode dite de Atwood-Dunietz-Soni, ADS) ne sont pas pour le moment compétitifs. L'extraction de la violation de *CP* se fait dans l'interférence des transitions $b \to c$ et $b \to u$ qui interviennent soit dans la succession d'une désintégration par émission d'un W externe suivie d'une désintégration du D^0 défavorisée de Cabibbo ($b \to c$), soit dans une désintégration supprimée de couleur (où le boson médiateur W est émis de manière *interne*) suivie d'une désintégration du D^0 favorisée de Cabibbo ($b \to u$). L'amplitude du terme d'interférence qui résulte de ces deux chemins vers le même état final est diluée par un facteur noté r_B qui est de l'ordre de 0,1 dans le cas de $B^{\pm} \to DK^{\pm}$ et l'erreur sur γ varie comme l'inverse de r_B.

Pour remédier à ce défaut, le canal $B^0 \to DK^{*0}$ a commencé à être étudié expérimentalement à BABAR. Dans ce canal, la saveur du méson B qui se désintègre est étiquetée par la saveur du méson vecteur K^{*0} et donc la charge du K de l'état final reconstruit comme provenant du K^{*0}. La désintégration du B se fait désormais par deux voies qui sont toutes deux supprimées de couleurs et l'interférence n'est plus diluée que par un facteur r_B de l'ordre de 0,3. Malgré toute la statistique accumulée à BABAR, ce canal étant plus rare que le précédent, une mesure précise de r_B n'a pu être réalisée et consiste en une première étape vers une mesure de violation de *CP*. Ainsi $B^0 \to DK^{*0}$, au même titre que $B^{\pm} \to DK^{\pm}$, est une voie *en or* pour la détermination de γ dans le cadre du Modèle Standard à LHCb.

Selon les projections faites à partir de l'étude menée sur simulation et avec les données 2010 pour $B^0 \to DK^{*0}$ avec l'expérience LHCb, 200 pb^{-1} de données LHCb (soit un cinquième des données qui seront collectées d'ici la fin de l'année 2011) a approximativement la même force statistique que la totalité des données de BABAR.

Etude de sensibilité

Dans cette thèse, seul le canal $B^0 \to DK^{*0}$ est étudié. Une première étude sur simulation permet de mettre en place un jeu de critères de sélection (pour la reconstruction du D^0 dans le canal $D^0 \to K^{\pm}\pi^{\mp}$) permettant de faire ressortir le signal du bruit de fond important présent dans les collisions pp au LHC. Cette étude montre qu'il est possible d'obtenir approximativement 450 événements $B^0 \to \overline{D}^0 K^{*0}$ et une trentaine d'événements $B^0 \to D^0 K^{*0}$ dans 1 fb^{-1} c'est à dire d'ici la fin de l'année 2011. Un tel lot d'événements est sans précedent pour ce canal et permettra une première mesure du rapport d'embranchement de $B^0 \to D^0 K^{*0}$, une étape importante vers la mesure de violation de CP.

L'étude Monte Carlo a également permis de démontrer l'existence d'un potentiel bruit de fond dangereux pour le mode défavorisé $B^0 \to D^0 K^{*0}$. Effectivement, le B_s^0 peut se désintégrer dans un état final identique. Si $B_s^0 \to \overline{D}^0 \overline{K}^{*0}$ n'est pas un mode, à proprement dit dangereux, grâce à l'excellente résolution en masse invariante du détecteur, $B_s^0 \to \overline{D}^{*0} \overline{K}^{*0}$ en est un. Effectivement, la désintégration du D^{*0} peut intervenir dans deux canaux $D^{*0} \to D^0\gamma$ et $D^{*0} \to D^0\pi^0$ faisant intervenir une particule neutre difficile à détecter. La désintégration $D^{*0} \to D^0\pi^0$ étant quasi monochromatique, elle ne pollue pas la zone de signal du B^0 contrairement à la désintégration faisant intervenir un photon. Il en découle que le bon contrôle du bruit provenant des désintégrations partiellement reconstruites $B_s^0 \to \overline{D}^{*0} \overline{K}^{*0}$ sera un des points importants de l'analyse finale. Des paramétrisations ad-hoc de ces bruits de fond partiellement reconstruits sont proposées et utilisées sur le Monte Carlo.

Les critères de sélection sont ensuite adaptés aux canaux secondaires $D^0 \to K^{\pm}\pi^{\mp}\pi^0$ et $D^0 \to K^{\pm}\pi^{\mp}\pi^+\pi^-$, qui sont des bras de levier supplémentaires dans l'extraction de γ. Ces canaux permettent effectivement de rajouter des contraintes légèrement différentes sur γ et donc de lever partiellement certaines ambiguïtés inhérentes à la détermination d'une phase. Il est important de préciser que l'extension à de tels canaux n'est pas triviale pour diverses raisons. Si les désintégrations $D^0 \to K^{\pm}\pi^{\mp}\pi^0$ et $D^0 \to K^{\pm}\pi^{\mp}\pi^+\pi^-$ présentent l'avantage d'avoir des rapports d'embranchements plus élevés que $D^0 \to K^{\pm}\pi^{\mp}$, ils ont le net désavantage d'avoir un grand nombre de particules dans l'état final.

D'un côté $B^0 \to DK^{*0}$ avec $D^0 \to K^{\pm}\pi^{\mp}\pi^+\pi^-$ présente six hadrons dans l'état final, et il est fréquent qu'une des traces ne soit pas reconstruite, car elle ne passe pas les seuils en impulsion transverse. Un gain substantiel d'efficacité est obtenu en rabaissant les seuils d'impulsion transverse par rapport à l'analyse présentée pour $D^0 \to K^{\pm}\pi^{\mp}$. Ceci se traduit bien entendu par une augmentation du bruit de fond. Il est également important de noter que la probabilité de déclencher l'expérience sur de tels événements est plus faible que pour $D^0 \to K^{\pm}\pi^{\mp}$, et résulte en une perte additionnelle d'efficacité.

D'un autre côté $B^0 \to DK^{*0}$ avec $D^0 \to K^{\pm}\pi^{\mp}\pi^0$ présente une particule neutre dans l'état final. Le π^0 se désintégrant en deux photons, l'état final de cette désintégration com-

porte également six particules dont deux photons. L'essentiel de la perte d'efficacité est due à la présence des photons dans l'état final. Premièrement, les efficacités de déclenchement de l'expérience sont plus faibles car il n'est pas possible de déclencher sur de tels photons avec relativement peu d'énergie transverse. Deuxièmement, la reconstruction des photons présente des difficultés intrinsèques. Les seuils de détection des photons sont situés à 250 MeV d'énergie transverse et ils peuvent se convertir avant l'aimant ; ces deux effets résultent en une perte d'efficacité importante. Enfin, le bruit de fond combinatoire pour former un π^0 est très important et donc le bruit de fond dans l'état final est en partie dominé par des combinaisons aléatoires de vrais photons, difficile à rejeter avec une bonne efficacité pour le signal.

L'ensemble de ces études permettent d'obtenir les nombres d'événements attendus pour le signal et le bruit de fond dans ces différents canaux et permet de mener à bien une étude de sensibilité. Cette thèse démontre qu'il sera possible de réaliser une mesure de violation de *CP*, dans le canal $B^0 \to DK^{*0}$ avec $D^0 \to K^\pm\pi^\mp$ en utilisant 5 fb^{-1} de données à $\sqrt{s} = 7$ TeV, à approximativement 3 déviations standards (d'incertitude statistique). Ce sera la première fois qu'une mesure aussi précise sera réalisée dans ce canal particulier et permettra de donner des contraintes significatives sur l'extraction de l'angle γ. En ajoutant à cela des canaux supplémentaires tels que $D^0 \to K^\pm\pi^\mp\pi^0$ et $D^0 \to K^\pm\pi^\mp\pi^+\pi^-$, cela devrait permettre une mesure de γ avec une précision statistique de 20° à 25°.

Cette valeur semble encore loin de la précision déjà obtenue par les expériences passées sur ce paramètre. Néanmoins, compte tenu que l'ensemble de ces modes font partie des modes ADS, une contrainte précise sur γ n'est possible qu'en les associant à un où plusieurs modes de type GLW. De tels canaux ($D^0 \to K^\pm K^\mp$ ou $D^0 \to \pi^\pm\pi^\mp$ typiquement) ne sont pas étudiés dans cette thèse, et permetteront d'obtenir une contrainte bien plus précise sur l'angle γ (voir Figs. 1-2). Ce phénomène est expliqué en utilisant des coordonnées cartésiennes, introduites dans cet objectif.

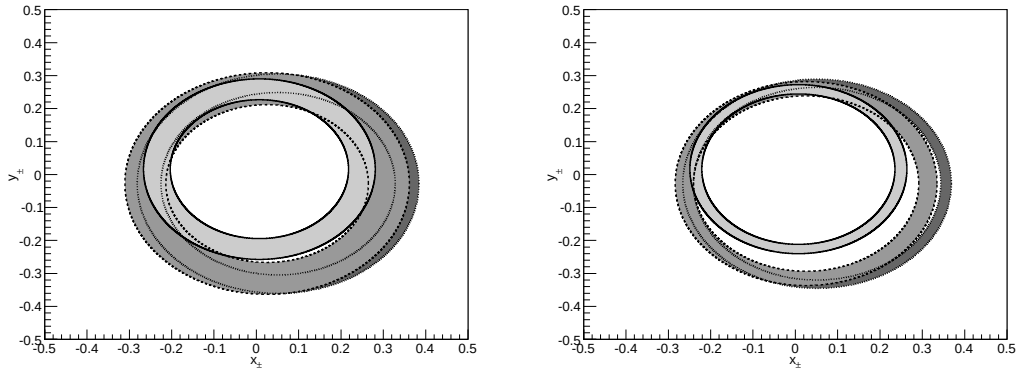

FIGURE 1 – Les contraintes provenant des analyses ADS avec $D^0 \to K^{\pm}\pi^{\mp}$ (gris sombre), $D^0 \to K^{\pm}\pi^{\mp}\pi^0$ (gris intermédiaire) et $D^0 \to K^{\pm}\pi^{\mp}\pi^{+}\pi^{-}$ (gris léger) en supposant 1 fb^{-1} (à gauche) ou 5 fb^{-1} (à droite) de données de l'expérience LHCb à $\sqrt{s} = 7$ TeV dans le plan $x_+ = r_B \cos(\gamma + \delta_B)\,, y_+ = r_B \sin(\gamma + \delta_B)$ (des courbes similaires pourraient être tracées dans le plan x_-, y_-). Les paramètres cartésiens sont mal déterminés par la méthode ADS prise seule.

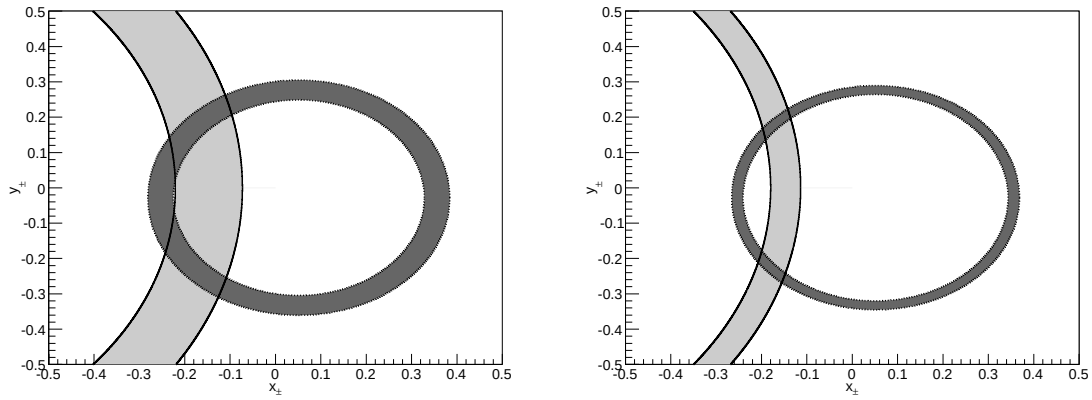

FIGURE 2 – Les contraintes provenant des analyses GLW et ADS pour 1 fb^{-1} (à gauche) ou 5 fb^{-1} (à droite) de données de l'expérience LHCb à $\sqrt{s} = 7$ TeV dans le plan $x_+ = r_B \cos(\gamma + \delta_B)\,, y_+ = r_B \sin(\gamma + \delta_B)$ (des courbes similaires pourraient être tracées dans le plan x_-, y_-). Le rayon (qui dépend de r_B, δ_B, γ, r_D, δ_D et du facteur de cohérence le cas échéant) est bien déterminé par la méthode ADS, alors que x est mieux déterminé par la méthode GLW. La combinaison des deux méthodes permet une bonne détermination des deux paramètres x et y.

Etalonnage des calorimètres

La mesure de γ faisant intervenir des désintégrations avec des pions neutres dans l'état final, un étalonnage précis des calorimètres est nécessaire de sorte à ne pas perdre la bonne résolution intrinsèque du détecteur, le terme constant étant de l'ordre de 1 % pour un terme stochastique de 9-10 % à 1 GeV. Cette résolution est également un élément clé pour les désintégrations radiatives rares de mésons B telles que $B_s^0 \to \phi^0\gamma$ et $B^0 \to K^{*0}\gamma$, dans lesquelles la résolution et le bon étalonnage interviennent de manière directe dans la résolution en masse invariante du B et donc dans le rapport signal à bruit obtenu en fin de compte.

L'étalonnage du calorimètre électromagnétique (ECAL) consiste en plusieurs étapes distinctes. Dans un premier temps, l'étalonnage est réalisé à l'aide de la photostatistique fournie par le système de diodes électro-luminescentes de LHCb, permettant d'obtenir une précision sur l'étalonnage de 8 à 10 %. Ce système permettant en principe un suivi des gains au niveau du pourcent. Après cette première étape une technique utilisant le flux d'énergie dans les calorimètres est utilisée pour atteindre de 4 à 5 % de mauvais étalonnage résiduel. Enfin une technique basée sur la reconstruction de π^0 permet d'atteindre en principe la précision souhaitée de l'ordre de 1 %.

La technique basée sur le flux d'énergie a été développée et étudiée en détails sur simulation puis mise en œuvre sur les données collectées en 2010 puis en 2011, après de premières études préliminaires en 2009. Il est démontré dans cette thèse que la technique de flux d'énergie permet effectivement d'améliorer l'étalonnage relatif des cellules du calorimètre électromagnétique avant l'étalonnage *fin* réalisé en reconstruisant des π^0 (avec les données réelles). Ceci constitue une première étape importante puisque cela permet de faciliter la convergence et de réduire le nombre d'itérations de l'étalonnage avec les π^0, ce dernier étant très consommateur en temps de calcul.

La méthode a aussi été étendue pour pouvoir permettre de contrôler l'étalonnage *fin*. Effectivement, celui-ci peut être limité par une reconstruction non parfaite des candidats photons et en particulier de leur position dans le calorimètre, limitation qui n'intervient pas dans le cas du flux d'énergie puisque ne faisant pas intervenir d'algorithme de reconstruction. Cette seconde utilisation du flux d'énergie nécessite une normalisation du flux, non plus globale par le nombre d'événements détectés, mais cellule par cellule par le nombre d'événements qui ont effectivement touché chaque cellule. Cela permet, au détriment d'une perte de sensibilité, de réduire la systématique dominante sur la forme du flux d'énergie à moins de 1 %. Au-delà d'une simple vérification du niveau d'étalonnage relatif entre les cellules, cette technique a été utilisée pour étalonner à nouveau le calorimètre, après l'étalonnage par π^0.

Il est à noter que les systématiques liées à la forme du dépôt moyen d'énergie dans le calorimètre, les effets liés au déclenchement ou à l'empilement d'événements dans le détecteur ont été étudiés et il a été démontré que ces effets pouvent être négligés pour étalonner de manière satisfaisante les gains des PMTs. En outre, les biais potentiels liés à l'asymétrie de détection du

détecteur ont été étudiés sur la simulation. Le résultat final permet d'atteindre un étalonnage inter-cellules de l'ordre de 1.5 % dans le ECAL. La méthode a également été utilisée comme outil de compréhension des calibration des autres sous détecteurs, avec une précision meilleure que 2 % dans le HCAL et de 3-4 % dans le PS.

Cet étalonnage final a été utilisé à la fois pour les analyses basées sur les données 2010 mais aussi comme point de départ pour l'étalonnage de 2011. Le flux d'énergie est par conséquent un outil standard et important pour l'analyse des données collectées par le calorimètre. Les résultats publics de l'expérience qui exploitent des particules électromagnétiques neutres dans l'état final font donc usage de cet étalonnage effectué avec la technique du flux d'énergie.

Première mesure de physique avec les données 2010

La mesure du rapport d'embranchement de la désintégration $B_s^0 \to \overline{D}^0 \overline{K}^{*0}$ est réalisée avec l'ensemble des données collectées en 2010 par le détecteur LHCb. Elle est réalisée relativement au rapport d'embranchement de la désintégration $B^0 \to \overline{D}^0 \rho^0$, puisque 36 pb^{-1} ne permettent pas de réaliser l'observation du canal $B^0 \to \overline{D}^0 K^{*0}$. En effet, les rapports d'embranchement de désintégration du méson vecteur ainsi que du méson B sont tels que le nombre d'événements attendus dans le canal $B^0 \to \overline{D}^0 \rho^0$ est dix fois plus important que dans le canal $B^0 \to \overline{D}^0 K^{*0}$. Ceci permet de réduire significativement les incertitudes statistiques au détriment d'un accroissement des incertitudes systématiques expérimentales.

Le nombre d'événements de signal ajusté est de $34,5 \pm 6,9$ et l'hypothèse de bruit de fond seule est rejetée à plus de neuf déviations standard statistiques (voir Figs. 3-4).

Une première systématique dominante est due aux différences dans l'identification des particules et des cinématiques associées. Elle est estimée à partir d'une procédure d'étalonnage utilisant des données réelles. Les efficacités sont obtenues à partir d'un lot pur de candidats $D^0 \to K^-\pi^+$ reconstruits dans les données réelles et dont les propriétés cinématiques sont pondérées par celles de $B_s^0 \to \overline{D}^0 \overline{K}^{*0}$ et $B^0 \to \overline{D}^0 \rho^0$ obtenues à partir de la simulation. En effet le nombre d'événements observés dans l'analyse finale n'est pas suffisant pour extraire avec précision les propriétés cinématiques du signal à partir des données réelles. La différence entre les propriétés cinématiques de la simulation et des données est estimée et prise en compte dans l'erreur sur les nombres obtenus. Cette erreur comporte également deux composantes, statistique (dominée par le nombre d'événements dans la simulation) et systématiques sur la procédure de pondération en elle-même (obtenue en réalisant la procédure sur simulation uniquement et en comparant le résultat obtenu avec celui attendu). La contribution dans le résultat final de la systématique sur l'identification des particules est de 5,8 %. Des contributions de diaphonie du $B^0 \to \overline{D}^0 \rho^0$ dans la selection du $B^0 \to \overline{D}^0 K^{*0}$ sont prises en compte lors de l'ajustement final des données.

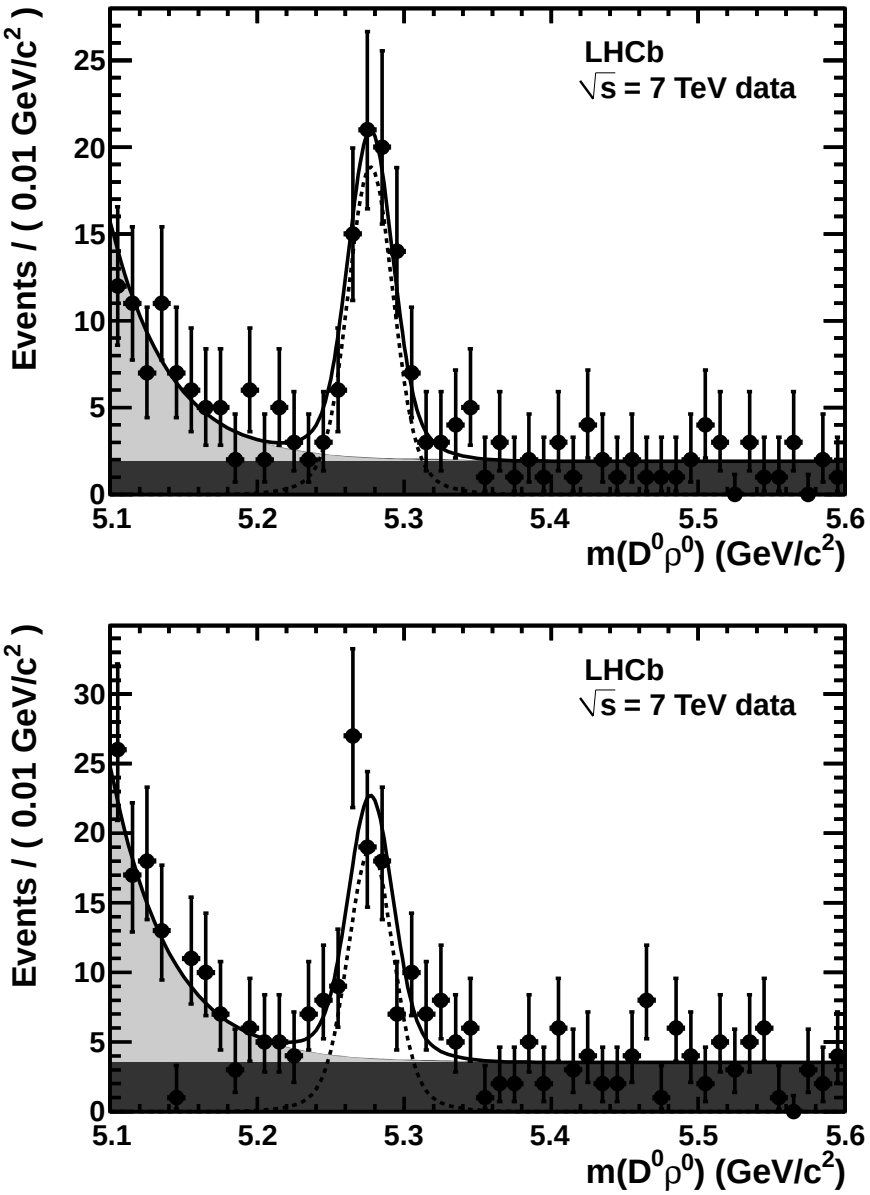

FIGURE 3 – Distribution de la masse invariante pour le mode de désintégration $B^0 \to \overline{D}^0\rho^0$ pour les événements déclenchés sur le signal (en haut) et sur le reste de l'événement (en bas) avec la fonction d'ajustement superposée, pour 36 pb^{-1}. Les points noirs correspondent aux données et le résultat du fit est représenté par une ligne pleine. Le signal est ajusté par une somme de deux gaussiennes (ligne pointillée), le bruit de fond partiellement reconstruit par une fonction exponentielle (zone pleine en gris léger) et le bruit de fond combinatoire avec une fonction constante (zone gris sombre). Les contributions de diaphonie due au $B^0 \to DK^{*0}$ et $B_s^0 \to D\overline{K}^{*0}$ sont négligeables et ne sont pas visibles.

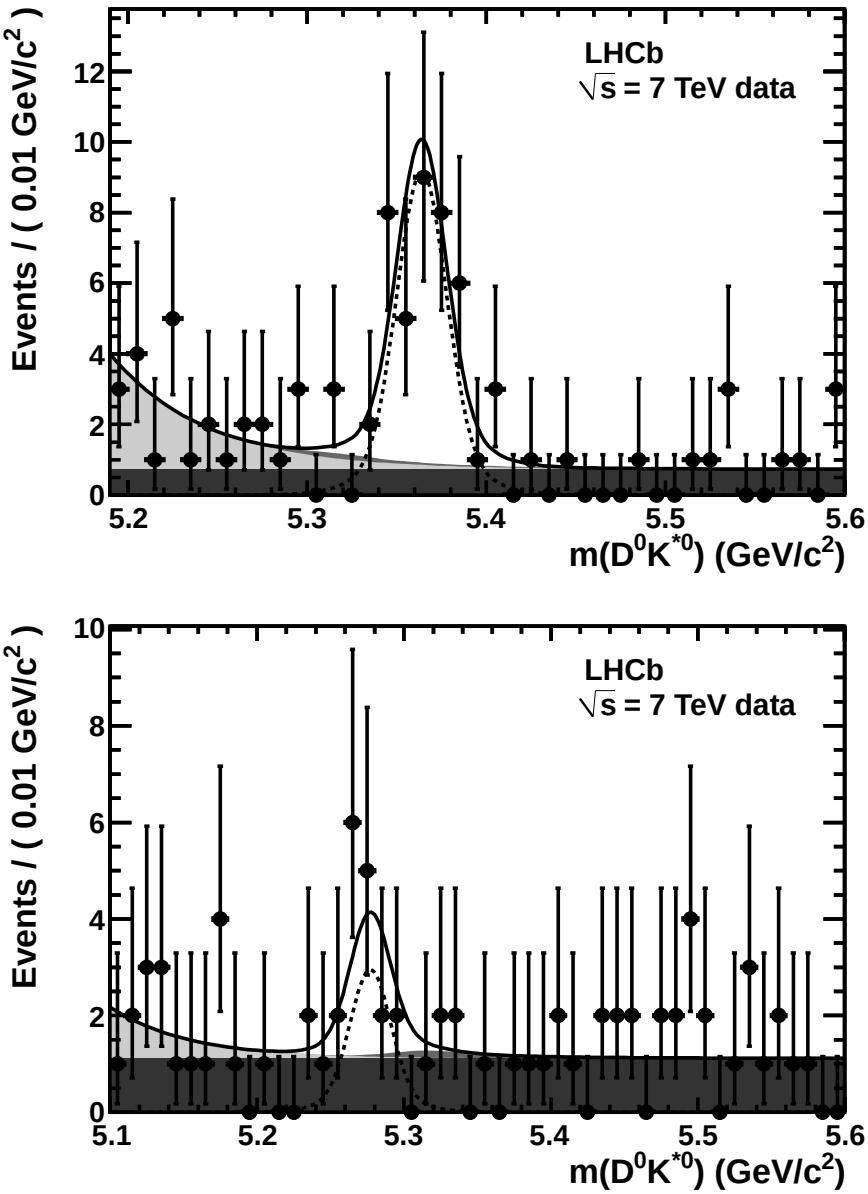

FIGURE 4 – Distribution de la masse invariante pour le mode de désintégration $\overline{B}{}^0_s \to D^0 K^{*0}$ (kaons de même charge, en haut) et $B^0 \to D^0 K^{*0}$ (kaons de charge opposée, en bas) avec la fonction d'ajustement superposée, pour 36 pb^{-1}. Les points noirs correspondent aux données et le résultat du fit est représenté par une ligne pleine. Le signal est ajusté par une somme de deux gaussiennes (ligne pointillée), le bruit de fond partiellement reconstruit par une fonction exponentielle (zone pleine en gris léger), le bruit de fond combinatoire avec une fonction constante (zone gris sombre) et la diaphonie due aux $B^0 \to \overline{D}{}^0 \rho^0$ mal identifiés est représentée en gris intermédiaire.

Une autre systématique importante est liée à la largeur intrinsèque du ρ^0. Dans la zone en masse invariante du ρ^0, une fraction non-négligeable d'événements provient de contributions (résonnantes ou non) de vrais pions provenant d'une désintégration du type $B^0 \to D\pi^+\pi^-$. Différentes paramétrisations ont été testées, à la fois pour la composante non-ρ^0 et pour la forme de la distribution de masse du ρ^0, toutes avec des résultats en accord : 20 % des événements dans le pic du B^0 proviennent de contributions $B^0 \to D\pi^+\pi^-$ qui ne sont pas $B^0 \to \overline{D}^0\rho^0$ (voir Fig. 5). La systématique associée à ce nombre est estimée en prenant l'erreur statistique sur le nombre d'événements non-ρ^0. L'incertitude obtenue est de 6,8 % sur le résultat final.

Les autres systématiques expérimentales, non dominantes, sont liées à l'estimation des efficacités de déclenchement de l'expérience sur les modes recherchés (3,0 %), les différences d'efficacités de sélection entre les deux modes entre simulation et données réelles (2,5 % sur les impulsions transverses des particules de l'état final) et la paramétrisation de la masse invariante D^0K^{*0} et $\overline{D}^0\rho^0$ (1,0 %).

Une dernière systématique dominante, mais non liée à l'analyse en tant que telle, est celle liée à la connaissance du rapport des taux d'hadronisation des quarks b en B_s^0 et B^0. Celui-ci présente une systématique de 7,8 % un peu plus faible que l'incertitude issue de l'analyse.

Enfin, l'incertitude statistique sur le résultat final atteint 23 % et domine largement la détermination obtenue du rapport des rapports d'embranchements :

$$\frac{\mathcal{B}\left(\overline{B}_s^0 \to D^0K^{*0}\right)}{\mathcal{B}\left(B^0 \to \overline{D}^0\rho^0\right)} = 1,48 \pm 0,34\ (\text{stat}) \pm 0,15\ (\text{syst}) \pm 0,12\,(f_d/f_s)\,.$$

Cette valeur peut être convertie en une mesure du rapport d'embranchement de la désintégration $\overline{B}_s^0 \to D^0K^{*0}$ sachant que celle de $B^0 \to \overline{D}^0\rho^0$ est connue par ailleurs :

$$\mathcal{B}\left(\overline{B}_s^0 \to D^0K^{*0}\right) = (4,72 \pm 1,07\ (\text{stat.}) \pm 0,48\ (\text{syst.}) \pm 0,37\,(f_d/f_s) \pm 0,74\ (\text{BR.})) \times 10^{-4}.$$

Ce résultat final est compatible avec les prédictions théoriques.

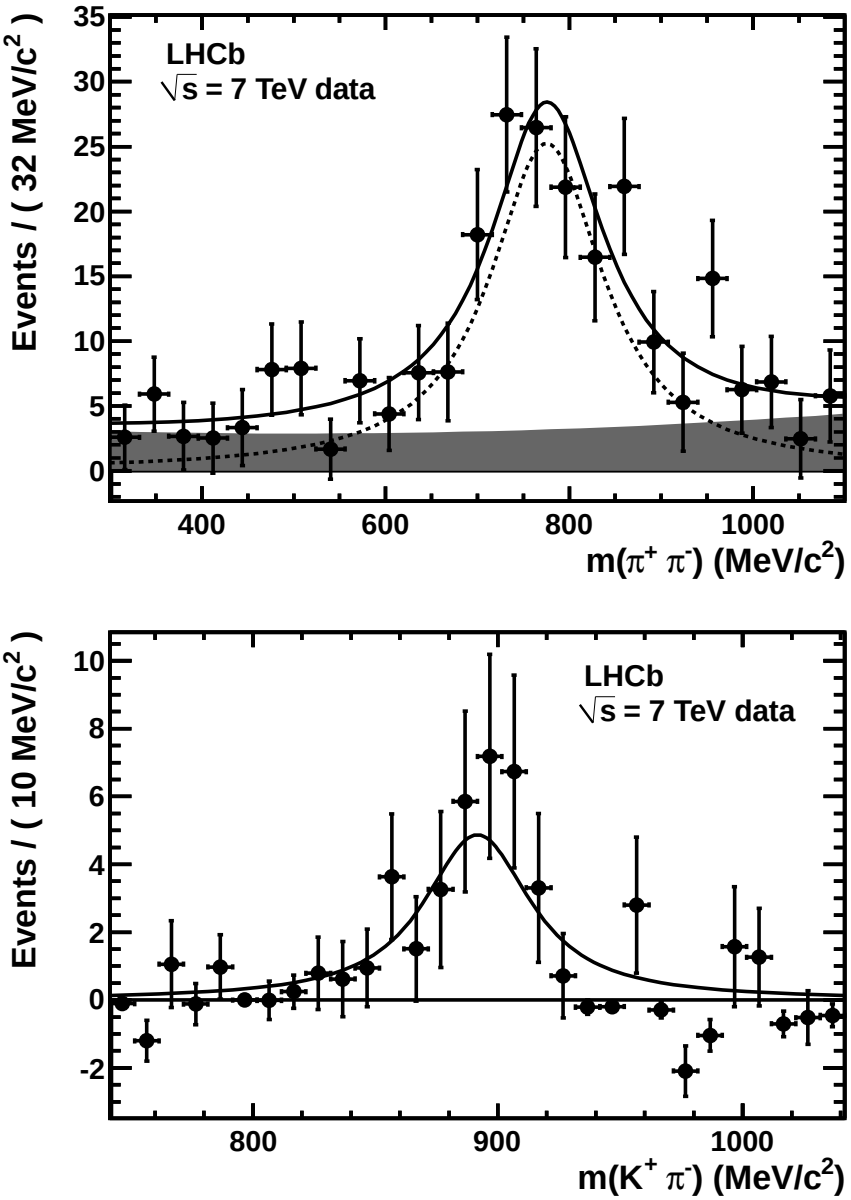

FIGURE 5 – Distributions de masse invariante du ρ^0 (en haut) et K^{*0} (en bas) obtenues à partir des données en exploitant une technique de soustraction du bruit de fond dédiée (sPlot). Le niveau des combinaisons autres que K^{*0} dans le pic de $\overline{B}{}^0_s \to D^0 K^{*0}$ est négligeable. A l'inverse, le pic de $B^0 \to \overline{D}{}^0 \rho^0$, bien que dominé par les combinaisons D^0 ρ^0 contient une contribution non négligeable d'événements "non-ρ^0" pour lesquels on applique un facteur correctif dans l'analyse. Les points noirs correspondent aux données et les résultats de l'ajustement sont représentés par une ligne pleine. La composante résonnante est ajustée avec une fonction de Breit-Wigner convoluée avec une fonction gaussienne (ligne pointillée) et la partie non résonnante est ajustée, le cas échéant, avec un polynôme d'ordre deux (zone grisée).

Introduction

- Ben si vous ne vous sentez pas de taille, vous n'avez qu'à décliner la mission !
- On peut faire ça ?
- Non !

Christian Bujeau alias *Le maître d'armes* et Alexandre Astier alias *Arthur* in *L'assemblée des rois (1ère partie)*, **Kaamelott, Livre III**, Tome 1, Épisode 26, écrit par Alexandre Astier.

The elementary particles of matter and their interactions are described by the *Standard Model* (SM) of particle physics. Its validity has been widely tested in the past decades mainly thanks to precision measurements in the electroweak sector, with the observation of the weak interaction mediators and their properties. Another key sector that was subject to a deep investigation in the last decade is the flavour sector of the SM. The CKM paradigm has been tested against experimental data especially at the B-factories (BABAR at SLAC, Stanford, USA and BELLE at KEK, Tsukuba, Japan).

Despite the highly predictive power of the SM (for example CP-violation is described by a single phase in this model), questions remain open. Among those questions two are striking.

- Why the magnitude of the gravitational interaction (resp. the Planck mass scale) is much smaller (resp. greater) than the weak interaction (resp. W boson mass scale) ? Assuming that SM is true up to the Planck scale would imply that loop corrections to the W boson mass are of the order of the Planck mass, and that the contributions to the W mass compensate in an *un-natural* way. The *hierarchy* and *naturalness* problems are related to each other and call for new particles, hence for New Physics (NP) beyond the SM to compensate *naturally* for the divergence of the W mass.

- Why the size of the measured CP-violation in the SM does not allow to quantitatively describe the matter-antimatter asymmetry in the Universe ?

Among the CP-violation measurements of the CKM Unitarity Triangle, the γ angle remains poorly constrained (see chapter I), since accessible through $b \to u$ transitions that are suppressed in the SM. Pioneering measurements have nevertheless been performed at B-factories through

$B \to DX$ decays. A new generation of experiments is thus required to perform more precise measurements. Among these experiments, LHCb (see chapter II) is the first one to be ready to produce fresh results.

LHCb is able to provide measurements of γ through decays influenced or not by contribution of new particles and thus able to provide a standalone constraint on NP. Moreover many channels are accessible at LHCb, some uniquely (in particular B_s^0 decays). Golden channels for γ measurements at LHCb at tree-level (free from new physics contributions) are $B^\pm \to DK^\pm$ and $B^0 \to DK^{*0}$, with various D decays that can involve neutral pions in the final state.

Calorimetry is thus an important tool to provide additional constraints on γ using decays involving neutral mesons. Additional key LHCb channels, as radiative B decays, need an accurate calibration of the calorimeters, in order not to spoil the resolution of the detector. An energy flow technique has been developed to precisely inter-calibrate the 6016 channels of the ECAL of LHCb (see chapter III) and is an important step in the calibration procedure.

On the road to measurements of *CP*-violation in $B^0 \to DK^{*0}$ decays, steps are identified (see chapter IV). The first of these steps, the observation of a new B_s^0 decay mode, $B_s^0 \to \overline{D}^0 \overline{K}^{*0}$, is performed with the LHC data collected in 2010 (see chapter V). Consistency with Monte Carlo predictions is discussed briefly given the limited available statistics.

Chapter I

Theoretical overview

- Plus qu'un véritable problème, ce serait plutôt une remarque. [...] Eh bien d'après mes derniers renseignements, il serait tout à fait possible que le Graal ne soit ni un vase, ni une coupe, mais... un récipient.
- ...
- Ça fait plaisir de voir que ça avance...

Nicolas Gabion alias *Bohort* et Alexandre Astier alias *Arthur*
in *En forme de Graal*, **Kaamelott, Livre I**, Tome 1, Épisode 18,
écrit par Alexandre Astier.

Contents

I.1 The Standard Model

I.1.1 A short historical introduction

Just after the pion discovery [1] a new puzzling observation of *strange* particles in cosmic rays happened in 1947 [2]. Particles of a rather long lifetime of 10^{-10} s (typical of weak interactions), called V^0 due to their signature in the cloud chamber, which was the observation of two tracks originating from a common vertex (thus creating a V in the detector) were found to be produced in pairs [3] and with rates typical of strong interactions, as learned soon after from accelerator based experiments at Brookhaven and Berkeley. In fact a particle of similar mass but charged was discovered three years earlier, before the pions discovery, also in cosmic rays [4]. These discoveries lead to the notion of "strangeness" [5] and the idea of "quarks" [6, 7, 8].

Soon after, the idea of parity violation of weak interactions came up to solve the so-called $\theta - \tau$ puzzle [9] and was indeed discovered to be effective [10], rapidly followed by an independent confirmation [11]. Breaking the idea that the discrete symmetries are conserved by all fundamental interactions pushed to look at the conservation of the other elementary discrete symmetries. The discovery of the violation of the charge conjugation symmetry was obtained one year later through the observation of only left-handed neutrinos [12]. The *CP* symmetry was then thought to be conserved but proved to be violated in kaon decays in 1964 [13].

In the meantime the discovery of quarks and the trials to understand the lifetimes of the kaon compared to the pion lead to the introduction of the Cabibbo angle [14] that broke the idea that weak couplings were universal. Indeed the strange quark couples less easily with the up-quark than the down-quark through weak interactions. A new quark, the charm, was then predicted [15] to explain the fact that the neutral currents were not observed to violate the flavour, as the charged current does. This prediction of a new quark was experimentally confirmed in 1974 simultaneously by two experiments [16, 17]. The weak neutral currents were discovered in 1973 [18, 19], and confirmed ten years later by the direct observation of the W [20, 21] and Z^0 bosons [22, 23].

These two fields, the discovery of new quarks and the violation of symmetries meet again in the Kobayashi-Maskawa paper [24] that demonstrates that the minimal amount of quark families to have *CP*-violation in the quark sector is three, thus predicting a new family of quarks. This was confirmed a few years later with the discovery of the b quark [25] and lead six years later to the first measurement of the b lifetime [26, 27]. This later measurement was surprisingly small leading to a suppressed coupling of the b to the quark, of the order of $|V_{cb}| \simeq 0.04$. This triggered the introduction of the Wolfenstein parametrization [28] that re-parametrizes the CKM matrix as powers of λ, see section I.1.3.

Finally the top quark was discovered in 1995 at the TEVATRON [29, 30] almost completing the picture of the SM, the only experimentally missing piece being the Higgs boson [31, 32].

I.1.2 Symmetries

As shown by the history section I.1.1, the symmetries are of primary importance in building phenomelogical models, since the symmetry properties of a system are connected to the conservation laws that characterize this system and its observables, as stated by Noether's theorem for continuous symmetries [33]. One distinguish three different elementary discrete symmetries.

- The symmetry under parity transformation $\mathcal{P}$, or left-right symmetry, transforms covariant to contravariant space coordinates, i.e. flips the sign of the spatial coordinates.
- The symmetry under time reversal $\mathcal{T}$ reverses the time variables of the equations. Under its conservation, this symmetry is responsible for having the same amplitudes for the $AB \to CD$ and $CD \to AB$ decays.
- The symmetry under charge conjugation $\mathcal{C}$ changes the charge of the particles i.e. replaces particles by antiparticles.

These symmetries can also be combined two by two to give new symmetries, like for example CP. The combination of all these three symmetries is the $\mathcal{CPT}$ symmetry and is conserved, by theorem, in the quantum field theory since related to the Lorentz invariance (see for example [34] and references therein for an article related to the subject). Since each elementary symmetry ($\mathcal{P}$, $\mathcal{T}$, $\mathcal{C}$) is violated by the weak interactions of the SM, any combination of two of the elementary symmetries is violated by the weak interactions of the SM, by conservation of $\mathcal{CPT}$.

It should be noticed that in principle CP-violation is allowed by QCD. This however would allow for an electric dipole moment of the neutron, which has never been observed yet leading to a non natural CP-conservation of strong interactions unexplained by SM. This problem, known under the strong CP problem, is a potential clue to discover new physics processes.

I.1.3 Quark mixing and CKM matrix

The SM is based on the gauge symmetry $SU(3)_c \times SU(2)_L \times U(1)_Y$, where the three terms respectively correspond to the symmetry under which the colour is conserved in strong interactions, the isospin symmetry under which left-handed fermion doublets transform, and the hypercharge symmetry responsible for the charge conservation.

A spontaneous symmetry breaking is required in addition to the gauge symmetry to allow non-vanishing masses to the gauge bosons and the elementary fermions, this feature being solved in the SM by the so-called Higgs mechanism. The Lagrangian, respecting these symmetries, is thus composed of three terms: a kinetic term, a Yukawa term that give masses to the elementary fermions, and the Higgs field Lagrangian that is necessary to spontaneously break the electroweak symmetry.

The Yukawa terms can be transformed to let appear the mass-eigenstates of the quark fields, that are in general different than the flavour eigenstates. The charged current interactions for quarks can be written, in the mass eigenstates basis, as follows:

$$\mathcal{L}_W = -\frac{g}{\sqrt{2}}(\overline{u}\ \overline{c}\ \overline{t})_L \gamma^\mu V_{CKM} \begin{pmatrix} d \\ s \\ b \end{pmatrix}_L W_\mu^+ + \text{ h.c.}, \tag{I.1}$$

$$V_{CKM} = \begin{pmatrix} V_{\rm ud} & V_{\rm us} & V_{\rm ub} \\ V_{\rm cd} & V_{\rm cs} & V_{\rm cb} \\ V_{\rm td} & V_{\rm ts} & V_{\rm tb} \end{pmatrix} \tag{I.2}$$

The CKM matrix V_{CKM} in Eq. I.2 is by construction unitary since $V_{CKM} = V_L^{(u)} V_L^{(d)\dagger}$ and is of dimension $N = 3$ in the SM. Among the $2N^2 = 18$ parameters of this matrix, $N^2 = 9$ vanish by unitarity and $2N-1 = 5$ vanish by rephasing freedom of the quark fields (one common phase of all the quark fields remains). This amounts to a total of four independent parameters, three are real parameters (mixing phases of Euler transformations) and one is a complex phase (the only *CP*-violation parameter). This latter parameter is the only source of *CP* violation in the Standard Model. Any new *CP* violation contribution would require a more complex Higgs sector to allow for *CP* violation in the Higgs sector, new generation of fermions or *CP* violation in the leptonic sector.

A first parametrisation of the CKM matrix, see Eq. I.3, can be performed by expressing it as the product of three independent 2×2 transformations (Euler rotations).

$$V_{\rm CKM} = \begin{pmatrix} c_{12}c_{13} & s_{12}c_{13} & s_{13}e^{-i\delta} \\ -s_{12}c_{23} - c_{12}s_{23}s_{13}e^{i\delta} & c_{12}c_{23} - s_{12}s_{23}s_{13}e^{i\delta} & s_{23}c_{13} \\ s_{12}s_{23} - c_{12}c_{23}s_{13}e^{i\delta} & -s_{23}c_{12} - s_{12}c_{23}s_{13}e^{i\delta} & c_{23}c_{13} \end{pmatrix}, \tag{I.3a}$$

$$\text{where } c_{ij} = \cos\theta_{ij} \text{ and } s_{ij} = \sin\theta_{ij},\ (i,j = 1,2,3,\ j > i). \tag{I.3b}$$

But as pointed out in section I.1.1, the Wolfenstein parametrization [28, 35], Eq. I.4, is more natural since it makes the hierarchy of the CKM coupling more obvious.

$$\begin{pmatrix} 1 - \frac{1}{2}\lambda^2 & \lambda & A\lambda^3(\bar{\rho} - i\bar{\eta}) \\ -\lambda & 1 - \frac{1}{2}\lambda^2 & A\lambda^2 \\ A\lambda^3(1 - \bar{\rho} - i\bar{\eta}) & -A\lambda^2 & 1 \end{pmatrix} + \mathcal{O}(\lambda^4) \tag{I.4}$$

where $\bar{\rho}$ and $\bar{\eta}$ are related to ρ and η by:

$$s_{12} = \lambda, \tag{I.5a}$$

$$s_{23} = A\lambda^2, \tag{I.5b}$$

$$\frac{s_{13}e^{i\delta}}{s_{12}s_{23}} = \rho + i\eta, \tag{I.5c}$$

$$\bar{\rho} = \rho\,(1 - \frac{\lambda^2}{2}), \tag{I.5d}$$

$$\bar{\eta} = \eta\,(1 - \frac{\lambda^2}{2}) \tag{I.5e}$$

$$\tag{I.5f}$$

I.1.4 The Unitarity Triangle and *CP*-violation

The unitarity of the CKM matrix allows for a graphical representation of the CKM matrix with triangles. Indeed there are six vanishing equations that come out from the unitarity relations of Eq. I.6, corresponding to six triangles with areas all equal to the Jarlskog [36] invariant given in Eq. I.7. A recent estimate of the Jarlskog invariant provides $J = (3.09 \pm 0.11) \times 10^{-5}$ [37]. Among these triangles, only one, given in Eq. I.8, contains three terms of similar amplitudes and thus is not squashed. This triangle is known under the name of Unitarity Triangle, and is represented in Fig. I.1.

$$\sum_{i=1}^{3} V_{ij} V_{ik}^* = \delta_{jk} \text{ and } \sum_{i=1}^{3} V_{ij} V_{kj}^* = \delta_{ik}. \tag{I.6}$$

$$J \equiv c_{12} c_{23} c_{13}^2 s_{12} s_{23} s_{13} \sin\delta. \tag{I.7}$$

$$V_{\rm ud} V_{\rm ub}^* + V_{\rm cd} V_{\rm cb}^* + V_{\rm td} V_{\rm tb}^* = 0 \tag{I.8a}$$

$$\frac{V_{\rm ud} V_{\rm ub}^*}{V_{\rm cd} V_{\rm cb}^*} + 1 + \frac{V_{\rm td} V_{\rm tb}^*}{V_{\rm cd} V_{\rm cb}^*} = 0. \tag{I.8b}$$

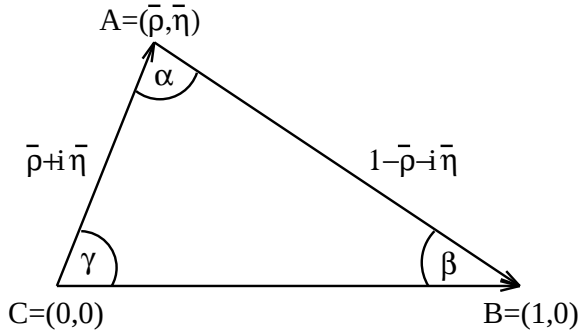

Figure I.1: The Unitarity Triangle in the $\bar{\rho} - \bar{\eta}$ plane.

I.1.5 Current knowledge of the CKM matrix

I.1.5.1 Sides of the Unitarity Triangle

The sides of the UT are determined by the magnitudes of the CKM matrix elements. Most of these nine parameters are already accurately determined, as emphasized in the following.

- $|V_{ud}|$ is precisely determined in (super-allowed) nuclear β transitions. The current average is $|V_{ud}| = 0.97425 \pm 0.00022$ [38, 39], the dominant uncertainty being from theory.
- $|V_{us}|$ is extracted from semileptonic kaon decays and the average of the different measurements yields to $|V_{us}| = 0.2252 \pm 0.0009$ [38]. The uncertainty is dominated by lattice QCD imprecisions.

- $|V_{cd}|$ determination is based on neutrino and antineutrino interactions. The current average is $|V_{cd}| = 0.230 \pm 0.011$ [38].
- $|V_{cs}|$ is extracted from semileptonic D decays and leptonic D_s^+ decays. The uncertainty on the best average $|V_{cs}| = 1.023 \pm 0.036$ is dominated by QCD calculations [38].
- $|V_{cb}|$ is measured in the semileptonic B decays to charm both in inclusive and exclusive decays. These two determinations are inconsistent, the combination with scaled uncertainty to take into account this inconsistency, is $|V_{cb}| = (40.6 \pm 1.3) \times 10^{-3}$ [38].
- $|V_{ub}|$ is also inclusively and exclusively determined, the measurement giving $|V_{ub}| = (3.89 \pm 0.44) \times 10^{-3}$[38].
- $|V_{td}|$ and $|V_{ts}|$ are both determined from B–$\overline{B}$ oscillations using lattice QCD calculations. Their values, assuming $|V_{tb}| = 1$, are $|V_{td}| = (8.4 \pm 0.6) \times 10^{-3}$ and $|V_{ts}| = (38.7 \pm 2.1) \times 10^{-3}$ [38], where the dominant uncertainty comes from lattice QCD calculations.
- $|V_{tb}|$ was used to be determined from the W transitions of top quarks to lighter quarks, but assumed the unitary relation $\sum |V_{tq}| = 1$. Recent top quark production measurements provide a determination free of this assumption and the combination of the current determinations is $|V_{tb}| = 0.88 \pm 0.07$ [38]. More improvements are expected on this measurement with the LHC data.

I.1.5.2 Determination of the angles of the CKM matrix

As the sides of the CKM matrix, the angles of the Unitarity Triangle provides a framework for check of consistency of the CKM paradigm.

- $\phi_1 = \beta = \arg\left(-\frac{V_{cd}V_{cb}^*}{V_{td}V_{tb}^*}\right)$ is determined by time dependent CP asymmetries measurements in neutral B decays. The golden mode (theoretically the cleanest mode) for this determination is $B^0 \to J/\psi K_S^0$, leading to $\sin 2\beta = 0.673 \pm 0.023$. Part of the inherent four-fold ambiguity is resolved thanks to a time-dependent $B^0 \to J/\psi K^{*0}$ angular analysis and $B^0 \to \overline{D}^0 h^0$ decays (where h^0 is either a π, η or a ω). It should be also emphasized that $B^0 \to \overline{D}^0 \rho^0$ can be used to extract $\cos\beta$, thanks to a Dalitz plane analysis [40].
- $\phi_2 = \alpha = \arg\left(-\frac{V_{td}V_{tb}^*}{V_{ud}V_{ub}^*}\right)$ is extracted from isospin analyses of charmless B decays to two pions or two ρ (for which the penguin contributions are measured to be negligible contrary to $\pi^+\pi^-$ decays). $B \to \rho\pi$ decays can also be used to extract α, the average of the measurements is $\alpha = \left(89.0^{+4.4}_{-4.2}\right)^\circ$ [41].
- $\phi_3 = \gamma = \arg\left(-\frac{V_{ud}V_{ub}^*}{V_{cd}V_{cb}^*}\right)$ current most precise determination comes from Dalitz analysis of $B^\pm \to DK^\pm$ with $D \to K_S^0\pi^+\pi^-$, the combination with other current measurements (through ADS and GLW methods) is $\gamma = \left(71^{+21}_{-25}\right)^\circ$ [41] or $\gamma = (74 \pm 11)^\circ$ [37] depending

on the statistical treatment of the combination of various measurements. Details on these methods are given in section I.2.

I.1.5.3 Global fits of the CKM matrix

Two collaborations [37, 41] provide fits of all the CKM measurements to check the global consistency of the CKM paradigm. So far, no unambiguous sign of inconsistency has been seen, as observed on Fig. I.2, though discrepancies still have to be worked out.

Comparing the Standard Model fit result (combining direct and indirect constraints, assuming the validity of the Standard Model) on the angle γ ($(67.2 \pm 3.9)^\circ$ [41] or $(69.8 \pm 3.0)^\circ$ [37]) with the direct measurements ($\left(71^{+21}_{-25}\right)^\circ$ [41] or $(74 \pm 11)^\circ$ [37]) shows a good agreement but also that the direct measurements are not precise enough to allow an accurate consistency check. This is due to the fact that sensitivity to γ arises in $b \to u$ transitions that are suppressed and thus statistical uncertainties still dominate the result. More copious productions of such suppressed channels are expected at LHCb compared to the B-factories, and LHCb has thus a great potential in improving the precision on this parameter.

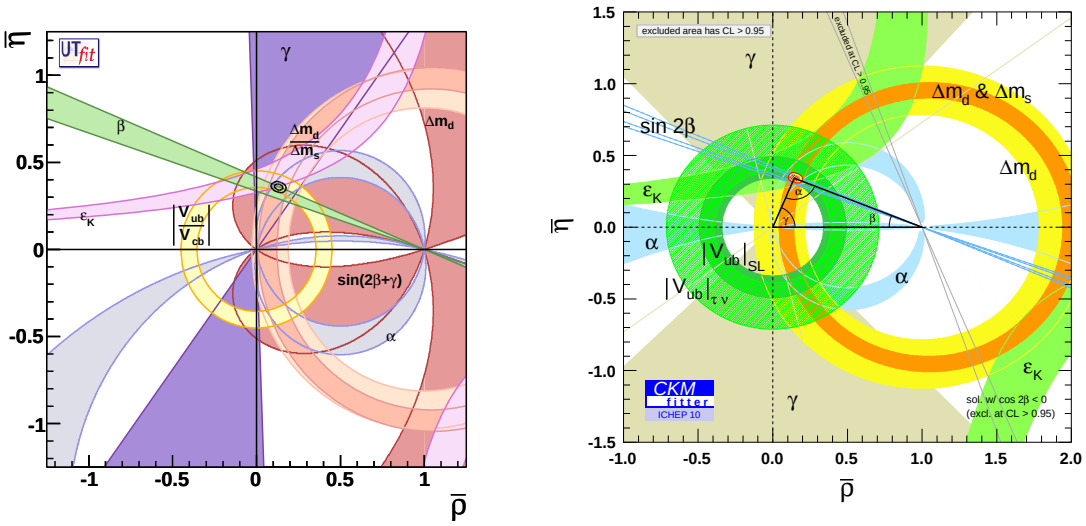

Figure I.2: The Standard Model fit provided by global fitters. In both cases there is a good consistency of all the constraints. [37, 41]

I.2 γ measurements and γ measurements at LHCb

Precise measurements of γ would thus allow for precise consistency check of the CKM matrix paradigm. Another important feature of the angle γ is that it can be measured by three independent classes of methods, allowing for direct and mixing induced CP-violation measurements

which are differently sensitive to New Physics effects. Indeed *tree* determinations of γ are insensitive to New Physics effects while *loop* determinations of γ are potentially sensitive to New Physics mediated by new heavy particles. A comparison of these determinations will provide valuable constraints on New Physics parameters.

I.2.1 γ from loops

An extraction of γ, potentially sensitive to New Physics can be performed by measuring the *CP* violation in $B^0 \to h^{\pm}h'^{\mp}$ decays, where B represents either a B^0 or a B_s^0 and $h^{(\prime)}$ either a K or a π [42]. These six decays have different contributions from Tree (T), Penguin (P), Penguin Annihilation (PA), Colour-suppressed Electroweak Penguin (P_{EW}^C) and Exchange (E) topologies, summarized in Fig. I.3 taken from [43]. γ is extracted from the direct and mixing-induced *CP*-asymmetries (given in Eq. I.9) in $B^0 \to \pi^+\pi^-$ and $B_s^0 \to K^+K^-$. The mixing phases are constrained from external measurements, and the system of four equations of five unknowns is solved by making use of using U-spin symmetry to reduce the number of unknowns. The validity of this assumption is checked using $B_s^0 \to K\pi$ and $B^0 \to K\pi$ (the *CP*-asymmetry in $B_s^0 \to K\pi$ and $B^0 \to \pi^+\pi^-$ are equal under this assumption) the size of Penguin Annihilation (PA) and Exchange (E) contributions, is probed by the $B^0 \to K^+K^-$ and $B_s^0 \to \pi^+\pi^-$ channels that are only sensitive to these topologies. The resulting γ measurement, compared with the two tree level measurements of γ, can then provide a useful probe of New Physics.

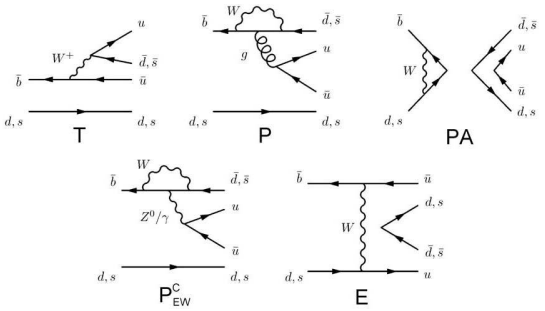

Decay mode	Contributing diagrams
$B^0 \to \pi^+\pi^-$	T, P, PA, P_{EW}^C, E
$B^0 \to K^+\pi^-$	T, P, P_{EW}^C
$B_s^0 \to \pi^+K^-$	T, P, P_{EW}^C
$B_s^0 \to K^+K^-$	T, P, PA, P_{EW}^C, E
$B^0 \to K^+K^-$	PA, E
$B_s^0 \to \pi^+\pi^-$	PA, E

Figure I.3: The different topologies (left) contributing to the different decays in $B^0 \to h^{\pm}h'^{\mp}$ and the correspondence between each decay and the contributing topologies to this decay (right) from [43].

Mode	A_{CP}	$A^{dir.}$	$A^{mix.}$
$B^0 \to \pi^+\pi^-$	n/a	0.38 ± 0.06	-0.65 ± 0.07
$B^0 \to K\pi$	$-0.098^{+0.012}_{-0.011}$	n/a	n/a
$B^0_s \to K\pi$	0.39 ± 0.17	n/a	n/a

Table I.1: Summary of the current averages [44] of the *CP* violation measurements in $B^0 \to h^\pm h'^\mp$ modes.

$$A^{dir.}_{\pi^+\pi^-} = \frac{2d_{\pi^+\pi^-}\sin(\theta_{\pi^+\pi^-})\sin(\gamma)}{1 - 2d_{\pi^+\pi^-}\cos(\theta_{\pi^+\pi^-})\cos(\gamma) + d^2_{\pi^+\pi^-}} \tag{I.9a}$$

$$A^{mix.}_{\pi^+\pi^-} = -\frac{\sin(\phi_d + 2\gamma) - 2d_{\pi^+\pi^-}\cos(\theta_{\pi^+\pi^-})\sin(\phi_d + \gamma) + d^2\sin(\phi_d)}{1 - 2d_{\pi^+\pi^-}\cos(\theta_{\pi^+\pi^-})\cos(\gamma) + d^2_{\pi^+\pi^-}} \tag{I.9b}$$

$$A^{dir.}_{K^+K^-} = \frac{2d_{K^+K^-}\sin(\theta_{K^+K^-})\sin(\gamma)}{1 - 2d_{K^+K^-}\cos(\theta_{K^+K^-})\cos(\gamma) + d^2_{K^+K^-}} \tag{I.9c}$$

$$A^{mix.}_{K^+K^-} = -\frac{\sin(\phi_d + 2\gamma) - 2d_{K^+K^-}\cos(\theta_{K^+K^-})\sin(\phi_d + \gamma) + d^2\sin(\phi_d)}{1 - 2d_{K^+K^-}\cos(\theta_{K^+K^-})\cos(\gamma) + d^2_{K^+K^-}} \tag{I.9d}$$

The current constraints on the *CP*-asymmetries are summarized in Tab. I.1. If the direct and mixing-induced *CP* asymmetries are measured in $B^0 \to \pi^+\pi^-$, they are not in $B^0_s \to K^+K^-$.

I.2.2 Time-dependent γ from trees

γ can be extracted up to a mixing phase that is known by precise and model-independent mixing measurements (already well measured in the B^0 sector and will be precisely known thanks to $B^0_s \to J/\psi\,\phi$ decays), from time-dependent charmed B decays [45, 46, 47, 48]. This additional benchmark measurement could eventually be combined with time-integrated measurements to provide a precise reference for New Physics tests.

The eight inherent ambiguities in the extraction of the *CP*-angle are resolved in the $B^0_s \to D^+_s K$ channel (except an irreducible 180 degrees ambiguity) thanks to the non-vanishing lifetime difference $\Delta\Gamma_s$ and exploiting the $B^0_s \to D^\pm_s\pi^\mp$ mode. This channel is expected to be unique to LHCb. Despite a branching fraction of $\mathcal{B}\left(B^0_s \to D^+_s K\right) = (3.0 \pm 0.7)\cdot 10^{-4}$ the ratio of $b \to u$ to $b \to c$ amplitudes (which drives the amplitude of the interference term) is of $x_{B^0_s \to D^+_s K} \simeq 0.4$ which allows for an easier extraction from data than for $B^0 \to D^\pm\pi^\mp$, for which $\mathcal{B}\left(B^0 \to D^\pm\pi^\mp\right) = (2.7 \pm 0.1)\cdot 10^{-3}$ and $x_{B^0 \to D^\pm\pi^\mp} \simeq 0.02$ (which is too small to be extracted directly from data). This latter can still be used to extract γ, but the ambiguities are not well resolved in this case. These two problems (remaining ambiguities and small interference term) can be worked out by use of an U-spin analysis combining the two sensitive channels $B^0_s \to D^+_s K$ and $B^0 \to D^\pm\pi^\mp$.

Already existing measurements, from B-factories have been averaged by HFAG [44]. The result is shown on Fig. I.4. Here LHCb has also a strong potential to improve the world average, since γ is still poorly constrained in these decays.

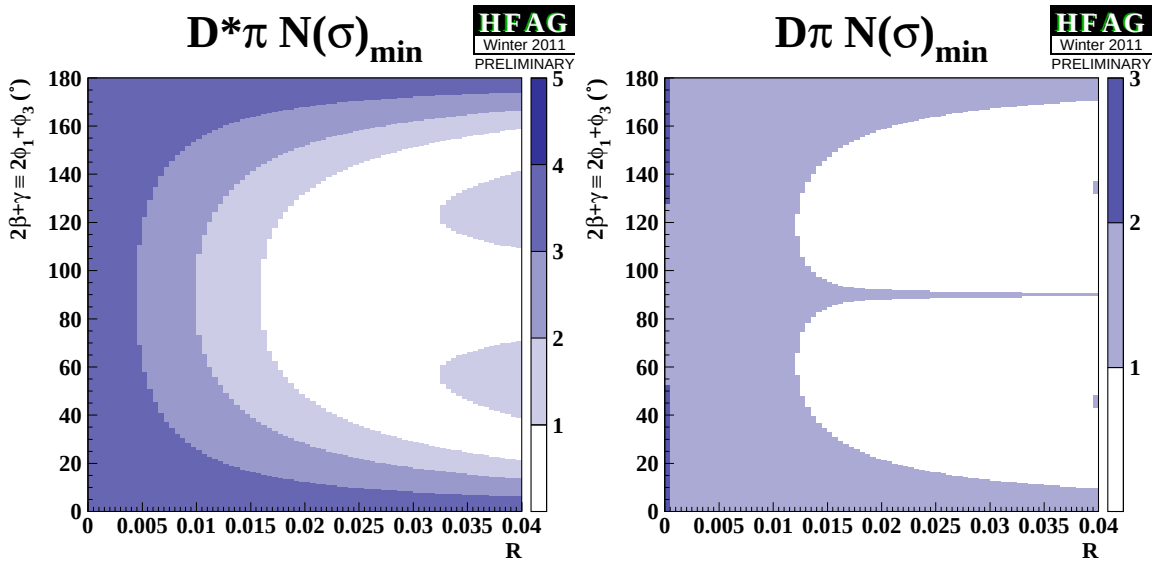

Figure I.4: The current status on time-dependent γ measurements performed at BABAR and BELLE. The figure shows the number of standard deviations as a function of the value of the weak angle and the amplitude of the interference term, $R = x_d$. Only a small interval of values of the angle $2\beta+\gamma$ is excluded independently of the value of $R = x_d$ in both of the two channels, $B^0 \to D^{*\pm}\pi^{\mp}$ (left) and $B^0 \to D^{\pm}\pi^{\mp}$ (right). [44]

I.2.3 Time integrated γ from trees

I.2.3.1 General idea

Both charmed $B^{\pm}$ decays and self-tagging charmed B^0 decays are pure tree decays and allow for a benchmark measurement of γ in the Standard Model, since they are expected to be free from New Physics contributions. These decays are extremely clean theoretically with an irreducible uncertainty on the higher electroweak corrections of $\delta\gamma/\gamma \simeq 10^{-6}$ [49], this precision being reached with $\mathcal{O}\left(10^{18}\right)$ pairs of B mesons produced, which is far beyond the scope of LHCb or a super B-factory. CP-violation and D-$\overline{D}$ mixing can be accounted for by using precise measurements.

The measurement is performed taking advantage of the interference of $b \to c$ and $b \to u$ transitions, the latter being sensitive to the CP-angle γ. Thus there is a compromise to find between the absolute rate of the decay and the relative size of its interference term that drives the sensitivity to γ. Usually considered as the most powerful are the decays $B^{\pm} \to DK^{\pm}$ and $B^0 \to DK^{*0}$ for which the branching fractions are $\mathcal{B}\left(B^+ \to \overline{D}^0 K^+\right) = (3.7 \pm 0.3) \cdot 10^{-4}$ and $\mathcal{B}\left(B^0 \to \overline{D}^0 K^{*0}\right) = (4.2 \pm 0.6) \cdot 10^{-5}$ and the ratios of $b \to u$ to $b \to c$ amplitudes (that gives the

size of the interference term and hence drives the sensitivity to γ) are $r_{B^\pm\to DK^\pm} = 0.11 \pm 0.02$ [37] and $r_{B^0\to DK^{*0}} = 0.26 \pm 0.08$ [50], leading to similar sensitivity to γ.

I.2.3.2 GLW strategy

Different approaches exist for the reconstruction of a D meson[1]. The Gronau-London-Wyler [51, 52] strategy exploits D decays in CP-eigenstates. Thus the decays of D^0 and $\overline{D}^0$ in the same final state have the same branching fractions in absence of CP-violation and no additional unknown is added in the extraction. The observed yields are parametrized in Eq. I.10, where $r_B e^{\imath\delta_B}$ denotes the ratio of suppressed to favoured $B^\pm \to D_{CP}K^\pm$ amplitudes, where D_{CP} denotes either a D^0 or a $\overline{D}^0$ decaying into a CP eigenstate. CP-violation only appears if γ is different from zero, and is measurable in these decays if in addition $\delta_B \neq 0$.

$$\Gamma_{B^+\to D_{CP\pm}K^+} = \Gamma_0\left(1 + r^2_{B^\pm\to DK^\pm} \pm 2r_{B^\pm\to DK^\pm}\cos\left(\delta_B + \gamma\right)\right) \quad \text{(I.10a)}$$

$$\Gamma_{B^-\to D_{CP\pm}K^-} = \Gamma_0\left(1 + r^2_{B^\pm\to DK^\pm} \pm 2r_{B^\pm\to DK^\pm}\cos\left(\delta_B - \gamma\right)\right) \quad \text{(I.10b)}$$

These four observables are rewritten in a different way in Eq. I.11, to let appear the CP violation asymmetries $A_{CP\pm}$ (that are vanishing in the case of absence of CP-violation). In the case of vanishing CP violation and strong phase in the B decay, the $R_{CP\pm}$ ratios are simply $(1 \pm r_B)^2$. It is also important to note that these four parameters are related by $R_{CP+}A_{CP+} + R_{CP-}A_{CP-} = 0$.

$$A_{CP\pm} = \frac{\Gamma_{B^-\to D_{CP\pm}K^-} - \Gamma_{B^+\to D_{CP\pm}K^+}}{\Gamma_{B^-\to D_{CP\pm}K^-} + \Gamma_{B^+\to D_{CP\pm}K^+}} \quad \text{(I.11a)}$$

$$= \frac{\pm 2r_{B^\pm\to DK^\pm}\sin\left(\delta_B\right)\sin\left(\gamma\right)}{1 + r^2_{B^\pm\to DK^\pm} \pm 2r_{B^\pm\to DK^\pm}\cos\left(\delta_B\right)\cos\left(\gamma\right)} \quad \text{(I.11b)}$$

$$R_{CP\pm} = \frac{\Gamma_{B^-\to D_{CP\pm}K^-} + \Gamma_{B^+\to D_{CP\pm}K^+}}{\Gamma_{B^-\to DK^-} + \Gamma_{B^+\to DK^+}} \quad \text{(I.11c)}$$

$$= 1 + r^2_{B^\pm\to DK^\pm} \pm 2r_{B^\pm\to DK^\pm}\cos\left(\delta_B\right)\cos\left(\gamma\right) \quad \text{(I.11d)}$$

The current constraints averaged by HFAG [44] (but dominated by BABAR measurements and by statistical uncertainties), are summarized in Tab. I.2. Since the strong phases of the three modes summarized in the table are not the same, it is not possible to combine these measurements easily. It is however interesting to note that the central value for A_{CP+} is 4σ away from zero in the $B^\pm \to D_{CP}K^\pm$ mode.

[1] D represents either a D^0 or a $\overline{D}^0$ meson.

Mode	A_{CP+}	A_{CP-}	R_{CP+}	R_{CP-}
$B^{\pm} \to D_{CP} K^{\pm}$	0.24 ± 0.06	-0.10 ± 0.07	1.18 ± 0.08	1.09 ± 0.08
$B^{\pm} \to D^{*}_{CP} K^{\pm}$	-0.12 ± 0.08	0.07 ± 0.10	1.33 ± 0.12	1.10 ± 0.12
$B^{\pm} \to D_{CP} K^{*\pm}$	0.09 ± 0.14	-0.23 ± 0.22	2.17 ± 0.36	1.03 ± 0.30

Table I.2: Summary of the current average [44] of the *CP* violation measurements in $B^{\pm} \to D_{CP} K^{\pm}$ modes, where the D is reconstructed in a *CP* eigenstate mode (GLW method).

I.2.3.3 ADS strategy

The GLW method has been extended to non *CP*-eigenstates decay channels common to D^0 and $\overline{D}^0$ in the so-called Atwood-Dunietz-Soni method [53, 54]. In this case, two unknowns are added: the ratio of branching fractions of the D^0 decay to a given final state f with respect to the $\overline{D}^0$ decay to the same final state (r_D^2) and a difference of strong phases (δ_D). These additional parameters r_D and δ_D (defined in a similar way than for the B decay) can be constrained by $\psi(3770) \to D\overline{D}$ data from CLEO or BES, resulting in a constant number of unknowns for an increase of observables. The observed yields are parametrized in Eq. I.12 (more details on the derivation of these equations are given in chapter IV).

$$\Gamma_{B^+ \to \overline{f} K^+} = \Gamma_0 \left(1 + r^2_{B^{\pm} \to DK^{\pm}} r^2_{D \to f} + 2 r_{B^{\pm} \to DK^{\pm}} r_{D \to f} \cos\left(\delta_B + \delta_D + \gamma\right)\right) \quad \text{(I.12a)}$$

$$\Gamma_{B^- \to f K^-} = \Gamma_0 \left(1 + r^2_{B^{\pm} \to DK^{\pm}} r^2_{D \to f} + 2 r_{B^{\pm} \to DK^{\pm}} r_{D \to f} \cos\left(\delta_B + \delta_D - \gamma\right)\right) \quad \text{(I.12b)}$$

$$\Gamma_{B^+ \to f K^+} = \Gamma_0 \left(r^2_{B^{\pm} \to DK^{\pm}} + r^2_{D \to f} + 2 r_{B^{\pm} \to DK^{\pm}} r_{D \to f} \cos\left(\delta_B - \delta_D + \gamma\right)\right) \quad \text{(I.12c)}$$

$$\Gamma_{B^- \to \overline{f} K^-} = \Gamma_0 \left(r^2_{B^{\pm} \to DK^{\pm}} + r^2_{D \to f} + 2 r_{B^{\pm} \to DK^{\pm}} r_{D \to f} \cos\left(\delta_B - \delta_D - \gamma\right)\right) \quad \text{(I.12d)}$$

These four observables are rewritten in Eq. I.13[2], in a similar way to the GLW case. The $A^{'}_{\mathrm{ADS}}$ is expected to be suppressed (and is thus not measured by experiments) since it corresponds to the $\mathcal{C}^{'}_{asymmetry}$ in the favoured mode, where the *CP*-violating term is small compared to the total branching fraction (this is emphasized in more details in chapter IV). On the contrary the A_{ADS} is expected to be sizeable, thanks to the large interference term in the total branching fraction of the suppressed modes. The R_{ADS} approximately drives the sensitivity to A_{ADS}: the larger R_{ADS}, the smaller A_{ADS} and the larger the statistics is needed to observe *CP*-violation in this decay.

[2]The convention chosen here for the strong phase in the D decay, δ_D, may differ in some texts.

Mode	$A_{\rm ADS}$	$R_{\rm ADS}$
$B^\pm \to DK^\pm$	-0.53 ± 0.21	0.0153 ± 0.0034
$B^\pm \to D\pi^\pm$	0.03 ± 0.08	0.00339 ± 0.00033
$B^0 \to DK^{*0}$ $(D^0 \to K^\pm\pi^\mp)$	n/a	$0.067^{+0.07}_{-0.054} \pm 0.018$
$B^0 \to DK^{*0}$ $(D^0 \to K^\pm\pi^\mp\pi^0)$	n/a	$0.060^{+0.055}_{-0.037} \pm 0.009$
$B^0 \to DK^{*0}$ $(D^0 \to K^\pm\pi^\mp\pi^+\pi^-)$	n/a	$0.137^{+0.113}_{-0.095} \pm 0.022$

Table I.3: Summary of the current average [44] of the *CP* violation measurements in $B^\pm \to Dh$ modes, where the D is reconstructed in a common final state for both D^0 and $\overline{D}^0$ (ADS method).

$$A_{\rm ADS} = \frac{\Gamma_{B^-\to\overline{f}K^-} - \Gamma_{B^+\to fK^+}}{\Gamma_{B^-\to\overline{f}K^-} + \Gamma_{B^+\to fK^+}} \tag{I.13a}$$

$$= \frac{\pm 2 r_{B^\pm\to DK^\pm} r_{D\to f} \sin(\delta_B - \delta_D)\sin(\gamma)}{r^2_{B^\pm\to DK^\pm} + r^2_{D\to f} \pm 2 r_{B^\pm\to DK^\pm} r_{D\to f}\cos(\delta_B - \delta_D)\cos(\gamma)} \tag{I.13b}$$

$$A'_{\rm ADS} = \frac{\Gamma_{B^-\to fK^-} - \Gamma_{B^+\to\overline{f}K^+}}{\Gamma_{B^-\to fK^-} + \Gamma_{B^+\to\overline{f}K^+}} \tag{I.13c}$$

$$= \frac{\pm 2 r_{B^\pm\to DK^\pm} r_{D\to f} \sin(\delta_B + \delta_D)\sin(\gamma)}{1 + r^2_{B^\pm\to DK^\pm} r^2_{D\to f} \pm 2 r_{B^\pm\to DK^\pm} r_{D\to f}\cos(\delta_B + \delta_D)\cos(\gamma)} \tag{I.13d}$$

$$R_{\rm ADS} = \frac{\Gamma_{B^-\to\overline{f}K^-} + \Gamma_{B^+\to fK^+}}{\Gamma_{B^-\to fK^-} + \Gamma_{B^+\to\overline{f}K^+}} \tag{I.13e}$$

$$= \frac{r^2_{B^\pm\to DK^\pm} + r^2_{D\to f} \pm 2 r_{B^\pm\to DK^\pm} r_{D\to f}\cos(\delta_B - \delta_D)\cos(\gamma)}{1 + r^2_{B^\pm\to DK^\pm} r^2_{D\to f} \pm 2 r_{B^\pm\to DK^\pm} r_{D\to f}\cos(\delta_B + \delta_D)\cos(\gamma)} \tag{I.13f}$$

The current constraints averaged by HFAG [44] (dominated by BABAR and BELLE measurements and by statistical uncertainties), are summarized in table Tab. I.3. The decay modes with a D^{*0} or a $K^{*\pm}$ are not mentioned in this summary table since they are less precise. In the table the D is reconstructed in the $D^0 \to K^\pm\pi^\mp$ mode. Additional multi (> 2) body decays can be used but need small adaptation to the original method. Also it is possible to use broad resonances instead of the bachelor K of the B decay, which needs to introduce a coherence factor. These technicalities are introduced in a dedicated section of the chapter IV.

I.2.3.4 GGSZ strategy

Finally the use of multibody D decays is advantageous to recover some statistical power by using Dalitz plot studies of the D decays in the Giri-Grossman-Soffer-Zupan [55] approach. In this approach the most popular decays (and also of interest for LHCb) are $D^0 \to f = D^0 \to K^0_S h^+ h^-$ where h denotes either a K or a π. For these decays, the strong phase in the D decay now depends on the phase space, and the branching fractions can be expressed as in Eq. I.14, where the ratio of suppressed to favoured D decays is $e^{-\delta_D(+-)} f_{-+}/f_{+-}$, and $f_{-+} = |f(m^2_-, m^2_+)|$ is

the absolute value of the amplitude for the $D^0 \to K^0_S h^+ h^-$ process when $m_{K^0_S h^-} = m_-$ and $m_{K^0_S h^+} = m_+$. It is noticeable that these equations are very similar to the ADS equations[3], but with an explicit Dalitz point dependence, while in the ADS method with multibody D decays, the D decay parameters are averaged over the Dalitz plane.

$$\Gamma_{B^+ \to \overline{f} K^+} = \Gamma_0 \left(f^2_{+-} + r^2_B f^2_{-+} + 2 r_{B^\pm \to DK^\pm} f_{+-} f_{-+} \cos\left(\delta_B + \delta_D\left(+-\right) + \gamma\right)\right) \quad \text{(I.14a)}$$

$$\Gamma_{B^- \to \overline{f} K^-} = \Gamma_0 \left(f^2_{-+} + r^2_B f^2_{+-} + 2 r_{B^\pm \to DK^\pm} f_{+-} f_{-+} \cos\left(\delta_B - \delta_D\left(+-\right) - \gamma\right)\right) \quad \text{(I.14b)}$$

Instead of fitting r_B, δ_B and γ (with the available statistics, a maximum extended maximum likelihood fit overestimates r_B and thus underestimates the error on γ, see for instance [56]), it has been demonstrated that it is more interesting to fit the Cartesian coordinates given in Eq. I.15.

$$x_\pm + i y_\pm = r_B e^{i(\delta_B \pm \gamma)} \quad \text{(I.15)}$$

The present status of these measurements is summarized in Tab. I.4, from HFAG averages [44]. As mentioned in the HFAG website, the averages here do not take into account model uncertainties (the D decays used by BABAR and BELLE are not the same, for example BELLE do not include $D^0 \to K^0_S K^+ K^-$, and thus model uncertainties are difficult to average). It is also worth to mention that measurements of bins of the Dalitz plane for these D decays at CLEO, allow a model independent extraction of gamma (the last error comes from the knowledge of the measured Dalitz plane). This latest measurement is a preliminary measurement from BELLE, which is competitive with the model dependent determinations (it cannot be combined with these measurements due to the strong correlation of statistical uncertainties and systematic errors).

I.2.3.5 Summary of the present measurements

The different methods do not have the same sensitivity to the weak phase γ. As shown on the Fig. I.5, taken from the UTFit collaboration [37], the Dalitz techniques are dominating the γ measurements, compared to the combination of GLW and ADS methods.

This can be understood, thanks to the remarks made in [57], on the use of Cartesian coordinates for the three time-independent methods. Indeed the constraint of the GGSZ method in the (x, y) plane is a disk, a corona for ADS and the area of an ellipse for GLW. It turns out that GGSZ gives a good estimation of the x and y variables at the same time, while the GLW method performs an accurate estimation of x but a poor estimate of y and the ADS method accurately estimates $r_B \simeq \sqrt{x^2 + y^2}$. The equations can indeed be parametrized as in Eq. I.16

[3] This is easily seen by factorizing f^2_{+-} in the GGSZ equations.

Mode	$x_\pm$	$y_\pm$
$B^+ \to DK^+$	-0.104 ± 0.029	-0.038 ± 0.038
$B^- \to DK^-$	0.085 ± 0.030	0.105 ± 0.036
$B^+ \to D^*K^+$	0.130 ± 0.048	0.031 ± 0.063
$B^- \to D^*K^-$	-0.090 ± 0.050	-0.099 ± 0.056
$B^+ \to D^*K^{*+}$	-0.152 ± 0.077	0.024 ± 0.091
$B^- \to D^*K^{*-}$	-0.043 ± 0.094	0.091 ± 0.096
$B^+ \to DK^+$ (m.i.)	$-0.110 \pm 0.043 \pm 0.014 \pm 0.016$	$-0.050^{+0.052}_{-0.055} \pm 0.011 \pm 0.021$
$B^- \to DK^-$ (m.i.)	$0.095 \pm 0.045 \pm 0.014 \pm 0.017$	$0.137 + 0.053 - 0.057 \pm 0.019 \pm 0.029$

Table I.4: Summary of the current averages [44] of the *CP* violation measurements in $B^\pm \to DK^\pm$ modes, where the D is reconstructed in a $D^0 \to K^0_S h^+ h^-$ mode (GGSZ method). The last two measurements (m.i.) are model independent measurements recently performed by BELLE.

for the GLW method and as in Eq. I.17 for ADS (where the factor $K = \kappa_B \kappa_D$ takes into account the coherence factor in the B and D decays, when needed, see chapter IV). These equations are only quoted here for the decay of interest in this thesis, $B^0 \to DK^{*0}$.

In the ADS equations the term $(1 - K^2) r_D^2$ is important to avoid bias at small r_B values and the neglected term always introduce less than 5 % uncertainty on the measurement, as shown in Fig. I.6. On this figure the relative difference between the approximate expression and the true parametrisation of the ratio of yields is given in the color code, while the circles for r_B values of 0.1, 0.25 and 0.4 are given in black. The introduced bias is negligible compared to the statistical precision of the measurement for an integrated luminosity smaller than 5 fb^{-1} (see chapter IV for the estimate of the yields with 5 fb^{-1} and the value of r_B in the case of $B^0 \to DK^{*0}$).

It is noticeable that the equations for GLW and ADS are the same assuming $r_D = 1$, $K = 1$ and $\delta_D = 0$ or $\delta_D = \pi$, thanks to the D decay in *CP* eigenstate. It results that there are two circles (with a strong phase difference of π) in each (x, y) plane while there is only one from the ADS (the other constraint would be useless since with an extremely large error on the radius of the circle). Thus the determination of x is excellent while the determination of y is poor with the GLW method.

The GLW and ADS constraints are represented on Fig. I.7 in the x_+, y_+ plane assuming a negligible uncertainty on the D decay parameters, and an integrated luminosity of 1 fb^{-1} (see chapter IV for the expected yields). The ADS method is complementary to the GLW in the sense that it allows to split the degenerate levels y. Vice versa, the GLW method allows to choose between two particular solutions to the problem on the circular constraint provided by the ADS method.

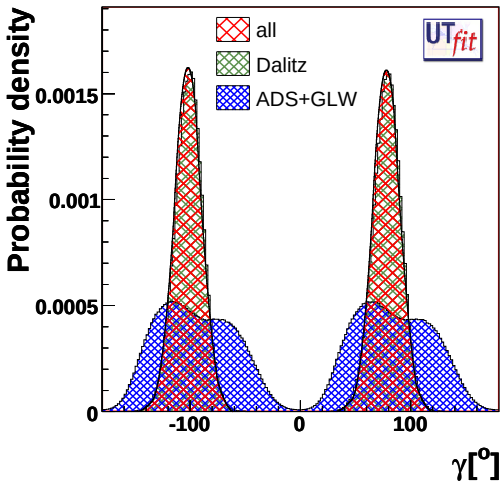

Figure I.5: The current status [37] on time-independent γ measurements performed at BABAR and BELLE. The figure shows the constraint on γ independently from GGSZ method and a combination of ADS and GLW methods. The combination of all the methods is also given and shows that the average of time-independent measurements is dominated by the GGSZ method.

$$\frac{\Gamma_{\overline{B}^0\to D_{CP\pm}\overline{K}^{*0}}}{\Gamma_{\overline{B}^0\to D\overline{K}^{*0}}} = (x_- \pm 1)^2 + y_-^2 \tag{I.16a}$$

$$\frac{\Gamma_{B^0\to D_{CP\pm}K^{*0}}}{\Gamma_{B^0\to DK^{*0}}} = (x_+ \pm 1)^2 + y_+^2 \tag{I.16b}$$

$$\frac{\Gamma_{\overline{B}^0\to \overline{D}^0\overline{K}^{*0}}}{\Gamma_{\overline{B}^0\to D^0\overline{K}^{*0}}} = \frac{(x_- + Kx_D)^2 + (y_- + Ky_D)^2 + (1-K^2)r_D^2}{(r_D x_- + Kx_D/r_D)^2 + (r_D y_- - Ky_D/r_D)^2 + (1-K^2)} \tag{I.17a}$$

$$\simeq (x_- + Kx_D)^2 + (y_- + Ky_D)^2 + (1-K^2)r_D^2 \tag{I.17b}$$

$$\frac{\Gamma_{B^0\to D^0K^{*0}}}{\Gamma_{B^0\to \overline{D}^0K^{*0}}} \simeq (x_+ + Kx_D)^2 + (y_+ + Ky_D)^2 + (1-K^2)r_D^2 \tag{I.17c}$$

where $x_D + iy_D = r_D e^{\imath(\delta_D)}$. (I.17d)

I.2.3.6 Expectations at LHCb

From previous studies that combine $B^\pm \to DK^\pm$ with $D^0 \to h^+h^-$ (GLW method where h is a K or a π), $D^0 \to K^\pm\pi^\mp\pi^+\pi^-$ and $D^0 \to K^0_S\pi^+\pi^-$ (ADS) but also $B^0 \to DK^{*0}$ with $D^0 \to K^\pm\pi^\mp$ (ADS) and $D^0 \to K^\pm K^\mp$ (GLW), a sensitivity of the order of $9° - 12°$ is expected with 0.5 fb^{-1} at $\sqrt{s} = 14$ TeV [43, 58]. This estimation of the sensitivity takes advantage of the CLEO constraints on the parameters of the D decays, in particular for the $D^0 \to K^0_S\pi^+\pi^-$ channel for which a model independent extraction is performed. This number can be roughly

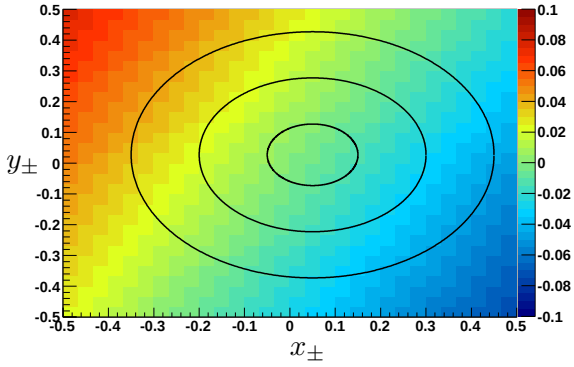

Figure I.6: The bias introduced by the approximation in Eq. I.17 is of 2 % in the case of $r_B = 0.25$, which is smaller than the statistical uncertainty expected on the ratio of number of events with 5 fb^{-1}.

extrapolated to the 2011 data sample sensitivity, arguing that a factor ~ 2 of statistics is lost due to the lower centre-of-mass energy, and an additional factor ~ 2 is lost due to lower hardware trigger efficiencies (mainly because thresholds are higher than initially planned, due to the higher interaction rate). Thus a $13^\circ - 17^\circ$ precision on γ can be expected with 2011 data.

However, the sensitivity to γ can be improved by studying additional modes, especially in $B^0 \to DK^{*0}$, where the sensitivity is expected to be similar to the one of $B^\pm \to DK^\pm$. In addition to the already studied modes in $B^0 \to DK^{*0}$ (K^+K^-, $\pi^+\pi^-$ (GLW), $K^\mp\pi^\pm$), it is possible to expect some improvements from $K^\mp\pi^\pm\pi^0$, $K^\mp\pi^\pm\pi^+\pi^-$ (ADS) or $K^0_S\pi^\pm\pi^\mp$, $K^0_S K^\pm K^\mp$ (GGSZ). Also interesting extensions to $B^0 \to D^0 K\pi$ [59, 60] or untagged $B^0_s \to D^0\phi$ [61, 62] can also be developed at LHCb.

I.2.3.7 Content of the thesis

In this thesis the $K^\mp\pi^\pm$ mode is studied in detail with a recent Monte Carlo simulation and the first real data. Additional work on the $K^\mp\pi^\pm\pi^0$ and $K^\mp\pi^\pm\pi^+\pi^-$ modes, with an older version of the simulation, is also shown. Since a first analysis with two body D decays was already existing at the beginning of my work on the analysis [63], a new selection was developed, with a more recent Monte Carlo. The chapter IV concentrates on the sensitivity study on Monte Carlo, using yields in agreement with what has been observed in 2010, as presented in chapter V. The chapter V shows the results with 2010 data for the $B^0 \to DK^{*0}$ modes with $D^0 \to K^\pm\pi^\mp$, and shows the first observation of the $B^0_s \to \overline{D}^0\overline{K}^{*0}$ mode.

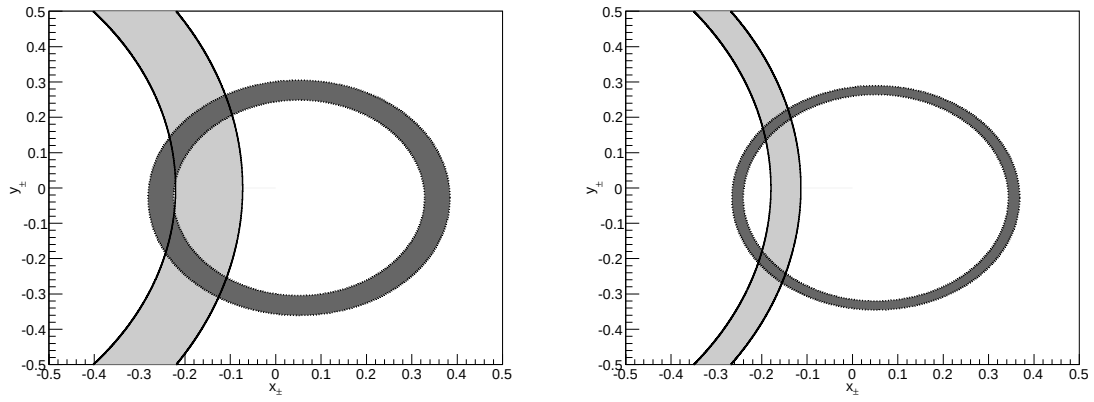

Figure I.7: The constraints from GLW and ADS analyses assuming 1 fb^{-1} (left) or 5 fb^{-1} (right) of LHCb data without background at $\sqrt{s} = 7$ TeV in the x_+, y_+ plane (similar curves are also valid for the x_-, y_- plane). The radius (that depends on r_B, δ_B, γ, r_D, δ_D and the coherence factor, if needed) is well determined by ADS, while x is better determined by GLW. The combination of the two methods provides a good determination of both parameters x and y.

Chapter II

The LHCb experiment

- Ou alors le mec qu'on dirait qu'il marche normalement mais en fait il marche alternativement à cloche pied sur chaque pied.
- Ouais.
- Voilà.

Jean-Christophe Hembert alias *Karadoc* et Franck Pitiot alias *Perceval*
in *La Roche et le Fer*, **Kaamelott, Livre V**, Tome 1, Épisode 2,
écrit par Alexandre Astier.

Contents

The LHCb detector (see section section II.2) is located at the intersection point 8 (IP8, the same intersection point as for the DELPHI experiment of the LEP era) of the LHC ring at CERN (Geneva, Switzerland). LHCb is dedicated to flavour physics studies and probes new physics through the contributions of new amplitudes to *CP*-violation parameters and branching fractions of suppressed modes in the Standard Model (SM). LHCb mainly concentrates its efforts to study B and D meson decays, although some other topics (W and Z^0 production asymmetries in forward direction, spectroscopy and quarkonia production processes, etc.) are of interest for the collaboration and the physics community.

II.1 The Large Hadron Collider

The Large Hadron Collider (LHC) [64] is a proton-proton collider located at CERN, near Geneva, Switzerland. The full chain of accelerators together with the position of the different interaction points of the proton beams, where are located the main four experiments (ALICE, ATLAS, CMS, LHCb) are given on Fig. II.1. ALICE [65] physics program is to study strongly interacting matter at extreme energy densities, where signs of a new phase of the matter, the quark gluon plasma is expected. ATLAS [66] and CMS [67] are general purpose experiments mainly dedicated to direct observations of new particles and the expected Higgs boson, on mass shell. An important part of their physics program concentrates also on top-quark and W boson precision studies. LHCb [68] aims at finding signs of new physics beyond the Standard Model through indirect observations. Three additional experimental facilities, smaller in size, are installed on the LHC ring. TOTEM [69] is an experiment dedicated to the measurement of total cross section, elastic scattering and diffractive processes at LHC energies. LHCf [70] is dedicated to measure the production cross-section of neutral particles in the forward direction in pp and heavy ions collisions at the LHC energies, to better constrain models of energetic showers. MoEDAL [71], dedicated to search for magnetic monopole and other highly ionizing stable massive particles, is located in the LHCb pit.

In 2009 few collision events at $\sqrt{s} = 900$ GeV have been recorded, mainly for commissioning of the detectors. In 2010, the center-of-mass energy was increased to $\sqrt{s} = 7$ TeV and an integrated luminosity of 42 pb^{-1} has been delivered to LHC experiments[1], with 90 % efficiency for LHCb.

II.2 Overview of the LHCb detector

LHCb [68] is a single arm forward spectrometer with angular coverage in the $[10\text{ mrad}, 300\text{ mrad}\,(250\text{ mrad})]$ range in the bending (non-bending) plane, since the $b\overline{b}$ pairs are predominantly produced in the same forward (or backward) direction at the LHC, as shown

[1] Only a fraction of it was delivered to ALICE, on request by the experiment.

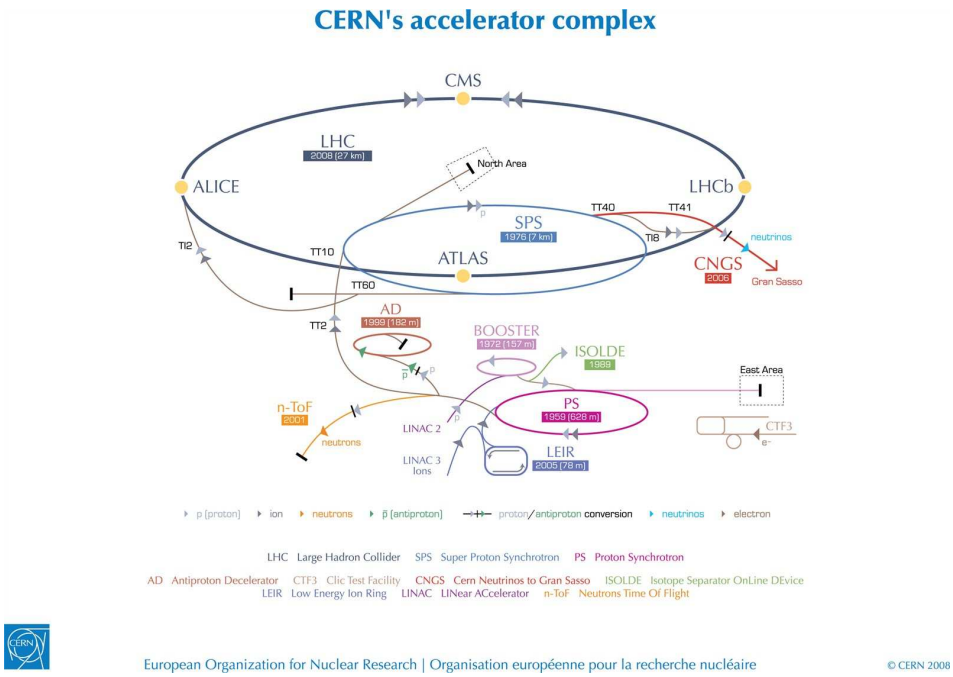

Figure II.1: The complex of accelerator from the LINAC to the LHC at the location of the four main LHC interaction point. The LHC acceleration chain complex comprises the LINAC2, the BOOSTER, the PS, the SPS and finally the LHC.

on Fig. II.2, from a PYTHIA [72] simulation. The main components of the detector, the vertex reconstruction system (VELO), the tracking system (tracking stations and magnet) and the particle identification system (cherenkov detectors, calorimeters and muon chambers) as well as the trigger and offline processing, are briefly described in the rest of the chapter. Finally more details are given on the calorimeter system, which is the subject of the calibration procedure developed in chapter III.

II.2.1 Tracking system and vertex reconstruction

The momentum resolution and the impact parameter resolution are of first interest for the background suppression when optimizing signal efficiency and background rejection for any decay mode. Thus a very well performing tracking system is required at LHCb, coping with the high occupancy in the forward direction, the high radiation level close to the interaction point and the smallest bunch crossing separation of 25 ns.

The tracking system of LHCb is composed of a silicon strips vertex locator (VELO), a warm magnet, silicon strips tracking stations (trigger tracker - TT- upstream of the magnet and inner tracker - IT- downstream of the magnet) and a drift time detector, the outer tracker (OT), in the low occupancy region downstream of the magnet.

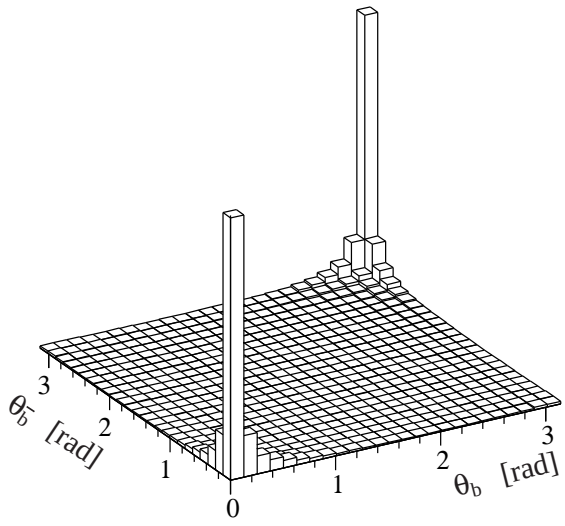

Figure II.2: Correlation between the production angles of the b and the $\overline{b}$ at the LHC (from [73]). This result is obtained from a PYTHIA simulation et $\sqrt{s} = 14$ TeV. The LHCb acceptance corresponds to the four bins at $\theta_b < 300$ mrad and $\theta_{\overline{b}} < 300$ mrad.

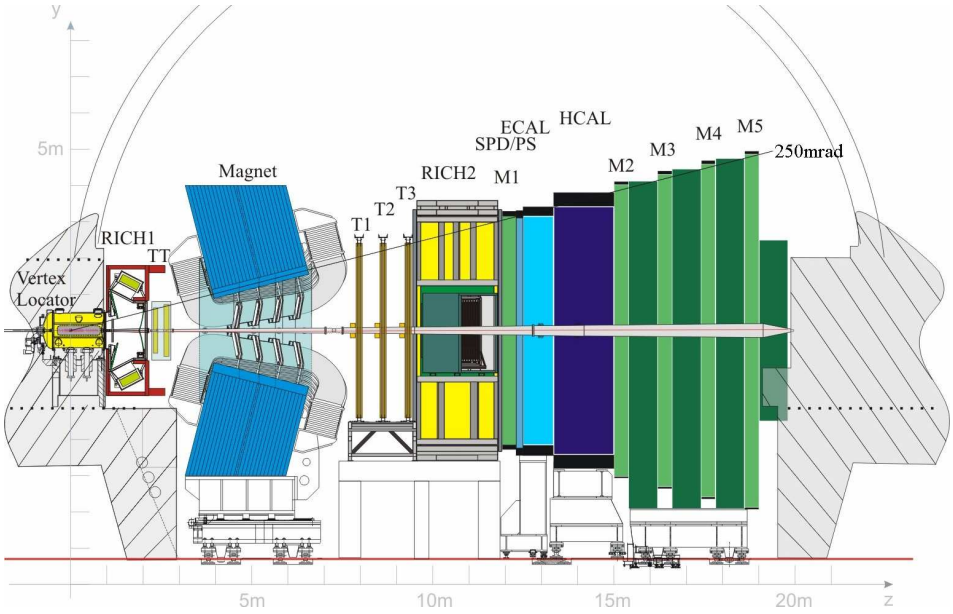

Figure II.3: The layout of the LHCb single arm spectrometer [68]. The LHCb calorimeters are located at approximately 12 m far from the interaction point. The ECAL is in light blue, the HCAL in dark blue and the SPD and PS are in intermediate blue.

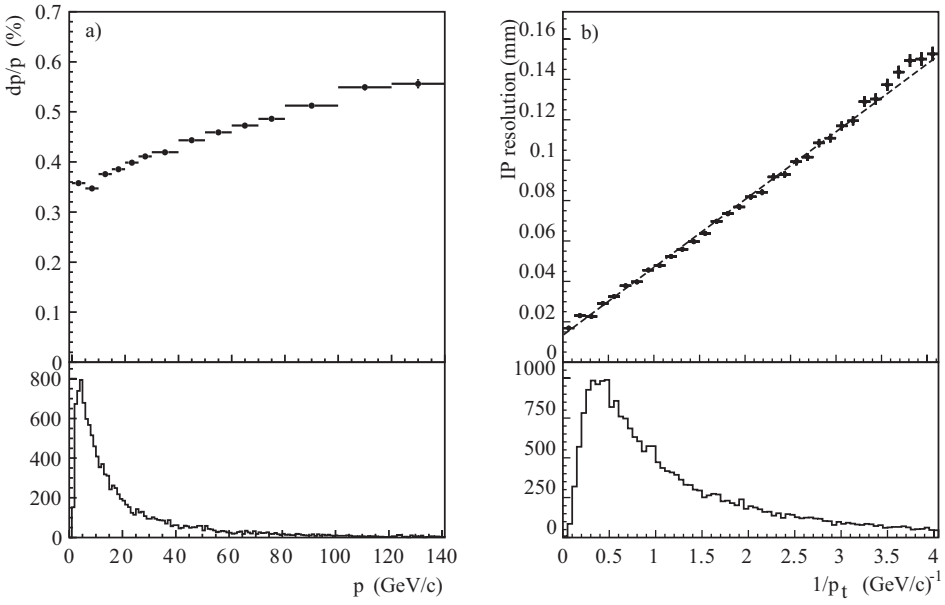

Figure II.4: The momentum resolution (left) and the impact parameter resolution (right) as a function of p and $1/p_T$ respectively are dominated by multiple scattering [68]. Note that the momentum resolution saturates at very low momentum.

The momentum resolution, dominated by multiple scattering, together with the impact parameter resolution is shown on Fig. II.4 for simulated events.

II.2.1.1 The vertex locator: VELO

The VELO, the closest sub-detector to the beam axis and the interaction point, aims at precise primary vertex determination and thus precise determination of the separation between primary and secondary vertices. In particular, the impact parameter resolution (the distance of closest approach of the track to a vertex) is determined by the VELO. Downstream of the interaction point, there are 21 VELO stations on each side (see Fig. II.5), each constituted by one ϕ-measuring and one R-measuring module, alternatively on upstream and downstream. Two additional *pile-up* stations, constituted by two R-measuring sensors, are placed upstream of the interaction point to allow a fast determination of the number of primary vertices in the event at the hardware L0 trigger, see section II.2.3.1. The design of the VELO is aimed at having:

- an impact parameter resolution of 50 µm at $p_T = 1$ GeV/c, which constrains the cluster resolution of the detector;
- a polar angle coverage down to 15 mrad for tracks emerging $2\sigma_{z,\,\mathrm{beam}} = 10.6$ cm away from the nominal interaction point;

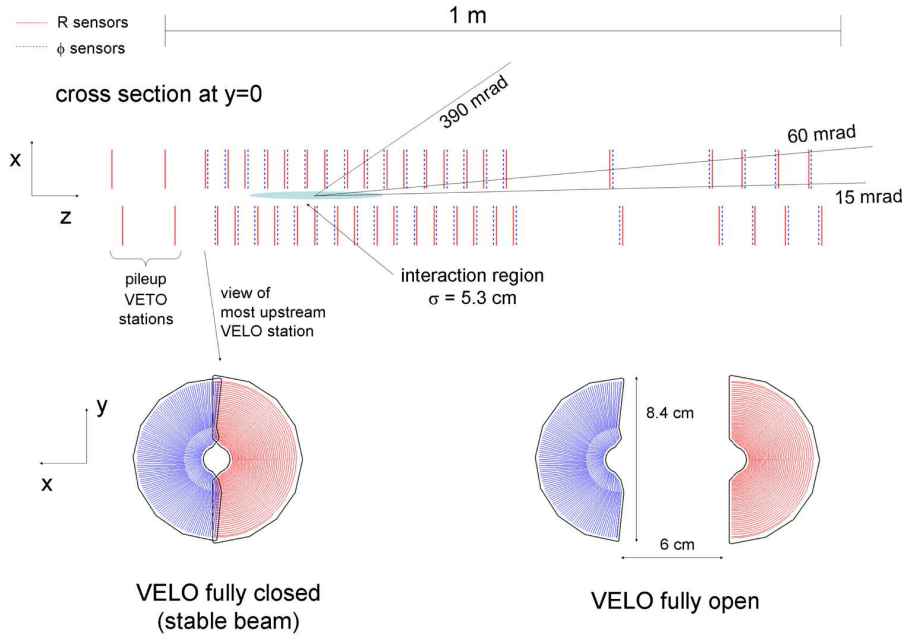

Figure II.5: Cross section in the (x, z) plane of the VELO silicon sensors, at $y = 0$, with the detector in the fully closed position (top). The front face of the first modules is also illustrated in both the closed and open positions (bottom left and right respectivley). The two pile-up veto stations are located upstream of the VELO sensors. ϕ-measuring and R-measuring are respectively in blue and red. Figures taken from [68].

- a sensitive area as close as 8 mm to the beam axis, to minimise the impact parameter resolution while keeping a safe distance with respect to the beam position;
- to be retractable, due to the larger aperture of the beams during injection;
- to have any track crossing at least three VELO stations, which constrains the inter-module pitch;
- an overlapping of the two sides of the VELO for alignment purposes;
- a radiation hardness to be able to operate with the same sensors during three years of nominal running, without significant loss of efficiency.

The impact parameter resolution obtained with the 2010 real data is already in rather good agreement with the Monte Carlo description. The resolution at high p_T is well described by the Monte Carlo, while the slope of the resolution as function of $1/p_T$ is larger in data than on Monte Carlo, which could be explained by missing material in the simulation (since the dominant contribution to the impact parameter resolution is from multiple scattering).

II.2.1.2 The magnet

The magnetic field of LHCb, required for a high momentum resolution, is a non superconducting (warm) dipole of which the main component is on the vertical y axis[2]. The amplitude of the magnetic field is of 1 T while the integrated field magnitude over the full tracking system is on average 3.7 Tm.

II.2.1.3 The silicon tracker

The silicon tracker is the generic name for two tracking systems. The first one, the TT, is located upstream of the magnet and the second one, the IT, is located downstream of the magnet in the inner regions of the tracking stations, where the radiation and the multiplicity are too high to have a drift time detector. They both use microstrip sensors.

The main constraints on the design are the following:

- The momentum resolution is dominated by the multiple scattering over (almost) the full range of particle momenta for a single hit resolution of 50 µm. This constrains the ST to have a strip pitch of 200 µm.
- A full single hit efficiency with a low noise hit rate is required by asking to have at least a signal amplitude over RMS of the single strip noise ratio of at least 12, after 10 years of operations. This is obtained by requiring a hit occupancy of a few percents at most in each strip and a cooling temperature of 5°C.

The Turicensis tracker or trigger tracker The four tracking layers of the TT (Turicensis tracker or trigger tracker) are located upstream of the magnet and downstream of the RICH1, allowing for a fast determination of the momentum (with 20 %–40 % precision) and cover the full acceptance of the LHCb detector. TT segments are mainly used in the HLT, but are also the only information available upstream of the magnet for long lived V^0 particles, since K^0_S and Λ can decay outside the VELO.

Each layer is made of silicon strip sensors disposed along the x, u, v and x axis, where the u and v axis are titled around the z axis by $-5°$ and $+5°$ respectively. These four layers are grouped two by two, and separated by 27 cm along the beam axis z to ease the reconstruction.

The inner tracker The three inner tracker (IT) stations are located downstream of the magnet, in the most inner part of the outer tracker stations. Each station also follows the $x-u-v-x$ geometry employed for the TT. Each one consists in four overlapping detector boxes (for alignment, and to avoid gaps in the detector) positioned around the beam pipe. The

[2]This displaces also the beams and thus with magnetic field up and down, the crossing angle of the beams is not the same at the interaction point of LHCb.

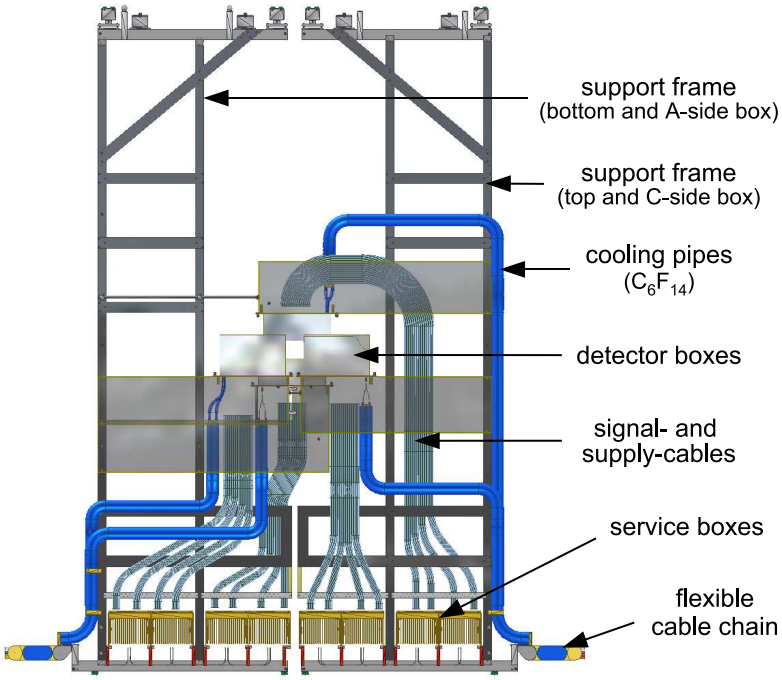

Figure II.6: Front view of an IT detector station [68]. The cooling system induce strong material non uniformities, which have a sensible effect on the energy flow, see chapter III.

non operating region, close to the beam pipe is approximately a square of 22×22 cm^2. It should be noticed that the cooling system of the IT cannot be placed outside the LHCb acceptance and results in a non-uniform material budget, peaking at 30 % of X_0 in the region of cooling rods, see Fig. II.6. As shown in chapter III, this material non-uniformity is found to have a sensible effect on the energy flow of the ECAL.

II.2.1.4 The outer tracker

The main requirement of the outer tracker OT, is to provide an excellent momentum resolution of $\delta p/p \simeq 0.4$ % to allow a 10 MeV/c^2 mass resolution for the $B_s^0 \to D_s^{\pm}\pi^{\mp}$ decay mode, for instance. The OT (see Fig. II.7) is located in the outer region of the tracking stations downstream of the magnet, in the same planes than the IT. Each station made of an array of individual gas-tight straw-tubes also follows the same $x-u-v-x$ geometry used for the other tracking stations. The gas is an admixture of 70 % of Argon and 30 % of CO_2, to guarantee a drift time below 50 ns.

II.2.2 Particle Identification

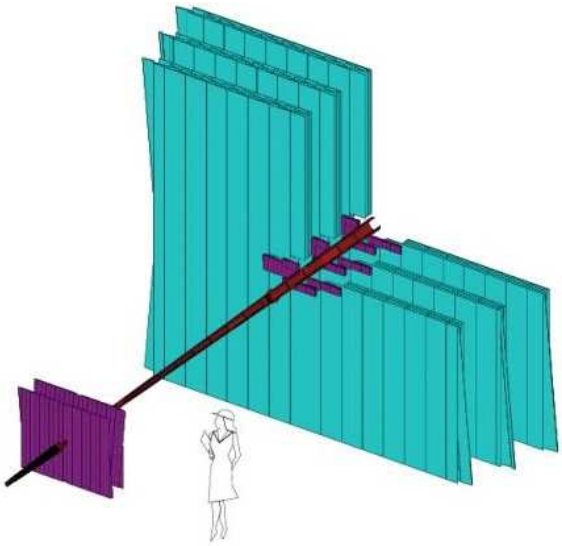

Figure II.7: Arrangement of OT straw-tube modules in layers and stations (light blue) and the ST stations (purple) [68].

II.2.2.1 The RICH

The precise particle identification, mainly needed to discriminate between different hadronic channels, is performed by two dedicated Ring Imaging Cherenkov (RICH) systems. Low momentum range of 1–60 GeV/c is covered by a first RICH detector (RICH1) located upstream of the magnet while particles with momenta from 15 GeV/c to beyond 100 GeV/c are discriminated by a second detector RICH2 located downstream of the magnet. The RICH1 covers the LHCb acceptance from 25 mrad to 300 mrad (250 mrad) in the bending (non-bending) plane and is made of aerogel and fluorobutane C_4F_{10}. The RICH2 has a limited acceptance from 15 mrad to 120 mrad (100 mrad) in the bending (non-bending) plane, but covers a region where very high momentum particles are located.

In both cases the Cherenkov light is reflected by a combination of mirrors and is read by Hybrid Photon Detectors (HPDs) outside the LHCb acceptance. The Cherenkov angle, defined only for particles with a velocity $c\beta$ greater than the speed of light c/n in the material, is expressed as $\cos\theta_{\text{Cherenkov}} = \frac{1}{n\beta}$ and its value as a function of the momentum, the particle type and the Cherenkov radiator is given on Fig. II.8.

The particle identification efficiency which depends on the Cherenkov angle resolution, is not found to be in perfect agreement between data and Monte Carlo, resulting in a less performing particle identification, especially for the aerogel.

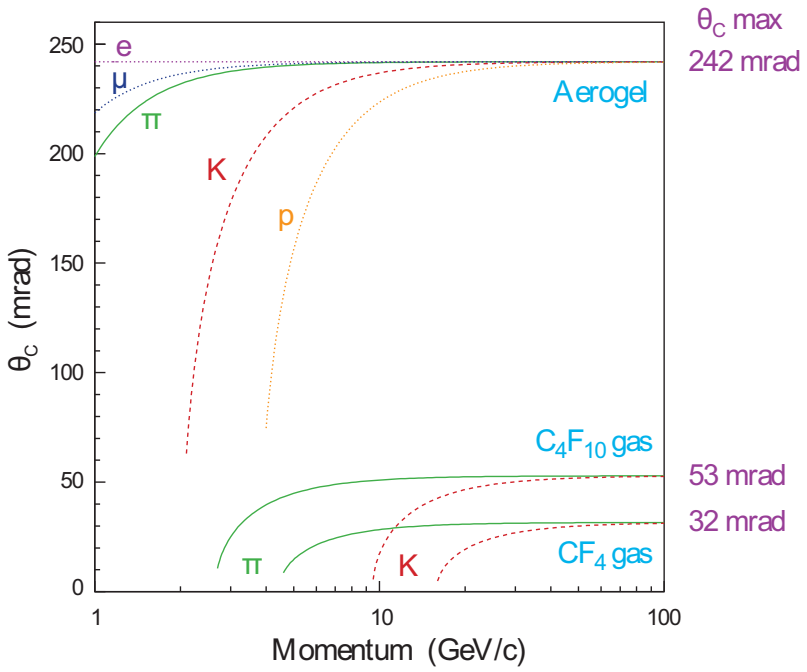

Figure II.8: Cherenkov angle versus particle momentum for different RICH radiators and different particle masses [68]. The discrimination power to separate $e^{\pm}$, $\mu^{\pm}$ and $\pi^{\pm}$ is limited to the very low momenta ($p < 3$ GeV/c) region and is thus dominated by the calorimeter and the muon particle identifications.

II.2.2.2 The calorimeter system

The calorimeter, divided in four subsystems, is mainly used for electromagnetic particle identification in the offline reconstruction and the hardware trigger level. Since it is the subject of a part of the work presented in this document, it is detailed in a dedicated section II.3.

II.2.2.3 The muon system

Five rectangular-shaped muon stations provide an essential triggering information as well as offline particle identification. Stations M2 to M5, separated by 80 cm thick iron plates, are placed at the downstream of end of the detector while the M1 station is placed upstream of the calorimeter, to improve the muon p_T measurement at the trigger level. Each detector uses multiwire proportional chambers (MWPC), except in the most radiation sensitive region in the inner part of the M1 chamber where triple-GEM foil is used. To have a rather constant particle flux and channel occupancy over the muon detector surface, each station is divided in four regions, with segmentation scale ratios of 1:2:4:8 from the innermost to the outermost parts.

M1-M3 are used to perform a standalone p_T measurement with 20 % resolution on the momentum, while M4 and M5 stations, with limited spatial resolution, are mainly used to identify

muons with momentum typically above 6 GeV/c against hadrons by identifying penetrating particles.

II.2.3 Trigger system

The trigger system, needed to reduce the rate of events written on tape from 40 MHz down to a few kHz, is based on two main levels. The first trigger level, the L0 trigger system, is a hardware trigger able to cope with the 25 ns bunch crossing and reduce the trigger rate down to slightly more than 1 MHz. The second level, the HLT, is a software trigger that reduces the rate down to a few kHz, refining the selection requirements thanks to a more evolved reconstruction. The output rate, limited by the offline processing capabilities (disk storage, time of processing) constrains the HLT input rate under given computing farm conditions, since an increased L0 rate would induce an increased CPU time consumption and retention of events.

II.2.3.1 The L0 trigger system

The L0 aims at being efficient on $b\bar{b}$ events while rejecting most of the minimum bias events. It is composed of three components: a pile-up unit, the calorimeters and the muon system. The idea is to exploit the main characteristics of a typical $b\bar{b}$ signal compared to a minimum bias event.

- The large b-hadrons invariant masses imply the presence of several GeV/c transverse momentum particles in $b\bar{b}$ events[3].
- The long b-hadrons lifetime induces large impact parameters for the final state particles compared to minimum bias events, for which all the final state particles are originating from the primary vertices.

The calorimeter system allows a fast estimate of transverse energies of hadronic and electromagnetic particles. Discrimination power to separate between hadrons and electromagnetic particles is provided by the PS, that identifies the beginning of the electromagnetic showers, hadrons hardly interacting before the ECAL. Photons and electrons are separated by the SPD that allows to distinguish charged and neutral particles. Thus electron, photon, π^0 and hadron candidates are built by summing the energy in 2×2 clusters of the ECAL, and the HCAL only for the hadron candidates. The electronics looks for the most energetic particle in the detector and compare it with a threshold. The typical transverse energy cut in the most limiting conditions of 2010 was $E_T > 3.5$ GeV for hadrons, which already corresponds to a tight selection on the transverse momentum for B decays in more than 4 particles in the final state.

[3]The b-hadrons have also a significant p_T, that is also reflected in the daughters p_T.

Additional important discrimination is given by the muon system that provides both a single muon ($p_T > 1.28$ GeV/c) and a di-muon candidate (the sum of the p_T has to be greater than 1.48 GeV/c).

Global Event Cuts (GEC), mainly based on the SPD multiplicity are applied. This GEC was subject to changes during the 2010 data taking due to the varying pile-up conditions and the completion of the trigger computer farm used for the HLT.

II.2.3.2 The High Level Trigger

To optimize the use of the computation power of the computer farm, the software trigger is splitted in two levels.

The HLT1 The first level [74] of the high level trigger (HLT1) is very inclusive and looks for tracks originating typically from b-hadrons. It is made with a fast reconstruction of the data, aiming at reducing the rate down to 50 kHz. Busy events that would saturate the reconstruction algorithm, or would generate large number of fake tracks, are removed by applying GECs:

- the number of OT clusters is required to be $N_{\text{clusters}} < 10000$;
- the number of IT clusters is required to be $N_{\text{clusters}} < 3000$;
- the number of VELO clusters is required to be $N_{\text{clusters}} < 3000$.

The main selection requirements are based on the following facts:

- tracks originating from a b-hadron have a large impact parameter with respect to the primary vertex;
- tracks originating from a b-hadron have a large transverse momentum;
- tracks originating from a b-hadron have a large momentum and thus a rather good track quality.

After finding the PV thanks to a full 3D pattern recognition of the VELO, VELO tracks are selected according to their impact parameter (IP) and their track quality. Then, these tracks are extrapolated to the tracking stations and a momentum cut $p > 12.5$ GeV/c is applied. Finally the last selection requirements are based on $p_T > 1.5$ GeV/c, $\chi^2_{\text{track}} < 3$ (the track is required to have a good quality, the χ^2 of the track fitting is good) and $\chi^2_{\text{IP}} > 36$ (which is similar to ask that the impact parameter is separated from the PV by more than 6 standard deviations of the error on the measurement of the IP). This strategy, that differs from the original baseline that was confirming the L0 candidates, allows to use any L0 line as input for the HLT1 and results in an increased HLT efficiency (especially for hadrons), and, more important, rather stable retention rate and time consumption as a function of the pile-up.

The HLT2 The second HLT level (HLT2) is more specific to the channel of interest, and aims at reducing the rate down to approximately 2 kHz. For B meson decays to hadrons, an inclusive topological trigger is used to allow high efficiency for B meson decays in two charged tracks at least. Tracks from events passing the HLT1, are selected to form a B candidate if $p_T > 500\,\text{MeV}/c$ and $p > 5\,\text{GeV}/c$ due to time constraints for the reconstruction algorithm, $\chi^2_{\text{track}} < 5$ to reduce fake tracks and $\chi^2_{\text{IP}} > 16$ to reduce prompt background. Since the mass of the final state particles is small compared to the B mass, a kaon hypothesis is assigned to any track. Then, a n-body candidate is recursively selected as follows:

- an elementary particle and the $n-1$-body candidate are combined to form a n-body candidate;
- the n-body object is selected if its distance of closest approach (DOCA) is less than 0.15 mm;
- the mass corrected for missing transverse $p_{T,\,\text{miss.}}$ (of missing final state particles in the n-body combination of a $> n$-body B decay), $m_{\text{corr.}} = \sqrt{m^2 + p^2_{T,\,\text{miss.}}} + |p_{T,\,\text{miss.}}|$, is required to be in the range $\left[4\,\text{GeV}/c^2, 7\,\text{GeV}/c^2\right]$;
- additional requirements to further reduce the background are $\max_{\text{tracks}} p_T > 15\,\text{GeV}/c$, $\sum_{\text{daughters}} p_T > 4\,\text{GeV}/c$, $4.25\,\text{GeV}/c$ or $4.5\,\text{GeV}/c$ respectively for 2-, 3- and 4-body topological triggers, $\min_{\text{tracks}} \chi^2_{\text{track}} < 3$ (in line wit HLT1 cut), $\chi^2_{\text{Flight distance}} > 64$ (the flight distance deviates by at least 8 standard deviations of the measured error on this variable), $\sum_{\text{daughters}} \chi^2_{\text{IP}} > 100$, 150, 200 respectively for 2-, 3- and 4-body topological triggers, a positive flight distance;
- prompt D background is then removed by requiring that $n-1$-body object used to build the n-body candidate either has a mass larger than $2.5\,\text{MeV}/c^2$ or have $\chi^2_{\text{IP}} > 16$.

The efficiency for B decays with more than two tracks is thus greater than 80 % for all channels. Complications arise when dealing with neutral particles, including K^0_S, and can be taken into account to recover some efficiency.

Trigger efficiencies from data If trigger efficiencies are rather easy to compute on simulations they are much more complicated to compute on real data, since the amount of not triggered events is unknown. However, assuming that one is able to find a trigger line independent of the trigger line of interest it is possible to compute the efficiency of the trigger line of interest by counting the probability to have an event triggered on the trigger line of interest in a data sample of events triggered by the other independent line. This solution is limited by:

- the statistics since you ask to have triggered two independent lines,

- the assumption of independence of the lines, which is not necessarily true (assuming muon or hadron triggers ask for rather hard events, the probability to fire the hadron line, once the muon line is fired can be enhanced for example).

To overcome this difficulty, another solution consist in finding an Trigger Independent of the Signal (TIS) in the same data sample (possibly with the same trigger line). This is done by removing the particles forming the candidate of interest and looking if the rest of the event fires the trigger (the event is called TIS if it is the case). TOS events are events triggered on the signal only: the final state particles of the selected candidate fire the trigger. Finally, it can happen that the event is neither a TIS nor a TOS, and that tracks from the underlying event and the signal candidates are needed to fire the trigger (this is easy to visualize when considering a di-muon trigger for example: the trigger is fired with one track from the signal candidate and another random track allow to pass the trigger), such a candidate is called TOB (Trigger On Both). This assumes that the underlying event and the signal candidate are independent, which is wrong due to the correlation through the momenta of the b's. Indeed, a b flavoured event tends to be harder than a non-b event and a high momentum B hadron candidate tends to have a high momentum B companion. Since the correlation only appears through kinematic variables, a binning in these variables allow to reduce the correlation in practice and to perform this procedure on real data which high statistics data samples.

The TOS (TIS) efficiency is thus the fraction of TOS (TIS) candidates in the TIS (TOS) events, assuming absence of TOB events, and the decorrelation of TIS and TOS. If interested in the total trigger efficiency, it can be calculated by dividing the TIS efficiency by the fraction of TIS events in the total data sample of triggered events.

In the data analysis performed in chapter V we do not calculate the trigger efficiencies on data, due to statistical limitations, but we make use of the TIS and TOS definitions.

II.2.4 The LHCb software

The LHCb framework for event processing application, GAUDI, is the general interface, giving common functionalities, for the different LHCb projects, each one being dedicated to a specific task. Among these projects there are five main applications. The first two, GAUSS and BOOLE, only used for simulations, are respectively dedicated to the event generation (from the generation of pp collisions based on PYTHIA to the propagation of the particles in the detector with GEANT 4, through the decay of particles using EVTGEN) and the digitization (converting the hits of the GEANT 4 particles in the detector into its response, emulating part of the electronics).

The MOORE project is dedicated to the HLT applications, running in the computing farm and being able to emulate the HLT response for simulated events, exactly in the same way as the software that runs at the pit.

The reconstruction is performed by BRUNEL, translating the detector response in a set of reconstructed elementary particles. The reconstruction software was used for the study on the calorimeter performed on chapter III. Finally DAVINCI, which was used for the physics analysis presented in chapter IV and chapter V allows to reconstruct high level particles and compute high level informations.

II.3 The LHCb calorimeters

II.3.1 General design

The basic requirements on the LHCb calorimeters are manifolds. The LHCb calorimeters are firstly a key ingredient in the hardware trigger of the experiment, and therefore has to be sufficiently selective to be efficient to select b-events while reducing the minimum-bias events. This should be done in the time constraints of the LHC collision frequency of at most one collision in 25 ns. This requirement of having a calorimeter capable of particle identification at the hardware trigger level, within 25 ns is rather demanding and is performed by sampling in z (the beam axis direction) the calorimeter. The most demanding operation consists in identifying the electrons in a high background of charged pions, which requires a longitudinal segmentation of the electromagnetic shower, the preshower (PS). The identification of electrons is then limited by the background from the large number of neutral pions produced in the collisions. This separation is performed by the detection of the beginning of the shower, thanks to a scintillator pad detector (SPD). With this design the background of the electron trigger is dominated by photon conversions, which cannot be disentangled at this level.

Moreover physics requirements are the study of radiative B mesons decays, for which an excellent energy resolution for photons is required to study these decays, with an unprecedented precision. For these decays the B invariant mass resolution is directly proportional to the energy resolution of the calorimeters and especially the constant term [43], see chapter III. Additional CP-violating B or D decays involving π^0 are also of interest and studied at LHCb (as for example the $B \to DX$ decays with $D^0 \to K^{\pm}\pi^{\mp}\pi^0$). These channels also require an excellent resolution on the π^0 mass to have a sufficiently clean extraction of the signal and a good resolution (for some of these channels it is possible to get rid of the calorimeter resolution by applying mass constraints, which improves the resolution, but not necessarily the selection purity).

The radiation levels in forward direction (together with the requirement of a sampling period of 25 ns) is discarding gaseous and liquid Argon detectors while an argument of cost discards the use of crystals (that would allow an appreciable improvement of the resolution). The design technology is thus based on scintillator and Pb skewered by optical fibres.

Since the occupancy varies by two orders of magnitude on the calorimeter surface, it has been found that having three granularity zones (two in HCAL) is a good compromise between

Sub-detector	SPD and PS	ECAL	HCAL
Number of channels	6016 each	6016	1488
Lateral size	6.2×7.6 m^2	6.3×7.8 m^2	6.8×8.4 m^2
Longitudinal depth	2.5 X_0– 0.1 λ_{int}	25 X_0– 1.1 λ_{int}	5.6 λ_{int}
Basic requirement	~ 25 phe per MIP	$10\ \%/\sqrt{E\,[GeV]} \oplus 1\ \%$	$80\ \%/\sqrt{E\,[GeV]} \oplus 10\ \%$

Table II.1: The basic requirements of the LHCb calorimeter system. Note that SPD, PS and ECAL geometry is projective to the interaction point.

the cost of material and the resolution, see Fig. II.9. Details on the number of cells in each sub-detector is given in the corresponding sub-section. To ease the reconstruction, the SPD and PS granularity and cell sizes are chosen to be projective with respect to the ECAL.

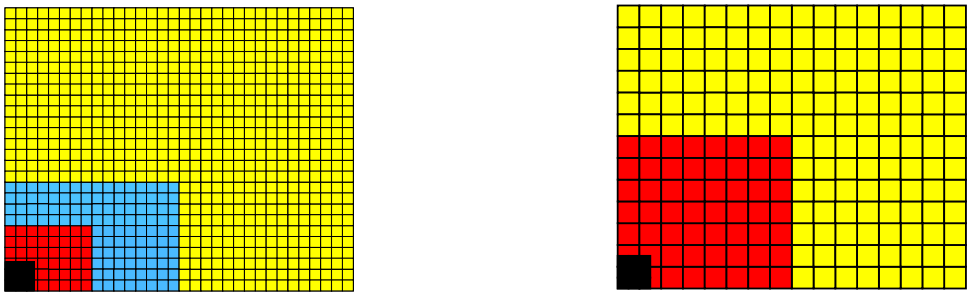

Figure II.9: Lateral segmentation of the SPD/PS and ECAL (left) and the HCAL (right). One quarter of the detector front face is shown. The black area corresponds to the not instrumented region where the beam pipe is located. The red, blue and yellow filled areas correspond to the inner, middle and outer parts of each sub-detector respectively. The cell sizes are 121.2 mm, 60.6 mm and 40.4 mm in the ECAL and are projective in the PS. Cell sizes are 262.6 mm and 131.3 mm in the HCAL. Figures taken from [68].

The basic properties are summarized in Tab. II.1.

II.3.1.1 The PS and SPD

The SPD and PS are made of single scintillating pads (Fig. II.10 left) in between which a Pb layer equivalent to $2.5X_0$ is sandwiched. The optimization of its thickness is a compromise between trigger performances (better with a thicker PS thanks to a larger number of secondaries) and ultimate energy resolution (better with a thinner PS since this would induce a smaller invisible energy)[4]. Each polystyrene scintillating pad is traversed by a wavelength shifting fibre (WLS) optically connected to clear fibre that is readout by multi-anode photomultiplier (MAPMT) located on top and bottom of the calorimeter wall, outside the acceptance of the detector. This allows reducing at the maximum the amount of material in front of the ECAL.

[4]The energy loss in the absorber of the PS is compensated offline, and a $2.5X_0$ PS do not significantly degrades the energy resolution.

The light collection efficiency was optimized by carefully looking at different aspects.

- Two different coupling techniques of the fibres to the scintillator pad were studied [75]. The most simple solution, consisting in machining a groove into the large side of the scintillator pad is easy and cheaper to produce and found to have a more uniform response to a MIP. The light yields varies by 2-3 % in the largest 12 cm $\times$ 12 cm cells.
- Two different scintillator materials (plastic and polystyrene) were studied [75]. Even if the light yield is 1.6 times larger with plastic scintillator, the polysterene is chosen for robustness of machining procedure and cost reduction. The light yield being found to be proportional to the thickness of the pad, a 50 % larger pad is used for polystyrene compared to plastic scintillator.
- The type of the chosen fibre has been optimized taking into account mechanical durability (bending in the small pads in the inner part of the detector), the radiation hardness and the timing requirements.
- The optimal length of the fibre results from a compromise between signal dispersion (the width of the signal increases by 5 ns/m and light collection efficiency that increases with the length of fibre in contact with the scintillator but decreases for a certain number of turns due the attenuation length (of 50 to100 m in a bent fibre). The final design of 3.5 turns is chosen for all cell sizes.
- The light collection efficiency is further improved by wrapping the entire pad with TYVEK paper. Aluminizing of the sides or chemical treatments have smaller collection efficiency for large cell sizes.

II.3.1.2 The ECAL

The requirement of having an ECAL resistant to an irradiation of an expected 0.25 MRad per year (integrated luminosity of 2×10^{32} cm^{-2} s^{-1} and collisions duration of 10^7 s) at the shower maximum [75] in the innermost part of the detector, together with a good resolution and a sampling every 25 ns, lead to the choice of a 'shashlik' technology. Thus the ECAL is made of 66 successive layers of lead and scintillating polystyrene skewed by WLS fibres and readout by photomultipliers (PMTs). The fibre density has been optimized in regard to the uniformity of the fibre response (the local uniformity is linked to the typical distance between to neighbouring fibres) and the constraint on the photocathode uniformity of the PMT. 144 fibres per module are chosen for inner (9 cells per modules) and middle modules (4 cells per modules), while 64 fibres are chosen for the outer, where the PMT uniformity is more demanding. The picture of an outer ECAL module is given for illustration in Fig. II.11.

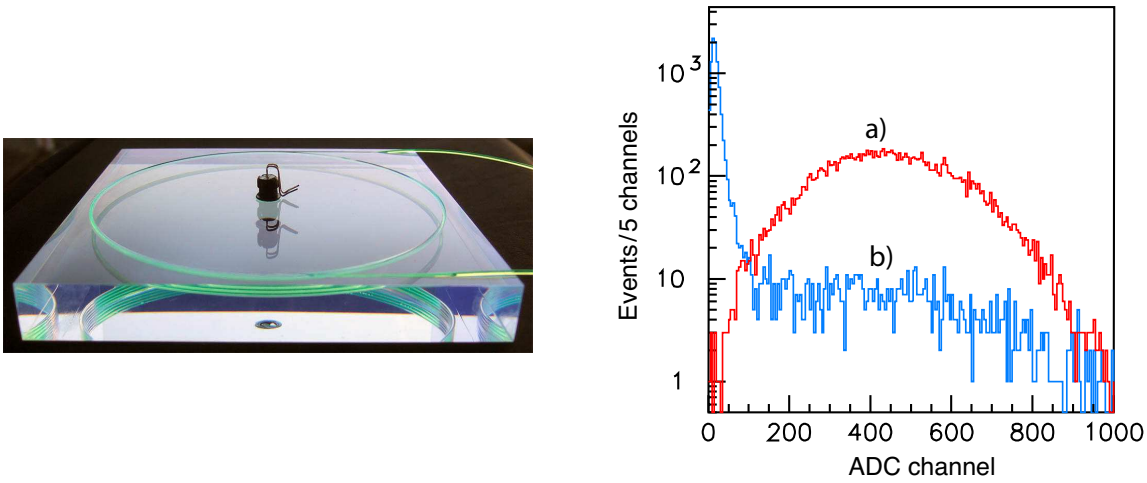

Figure II.10: A cell of the SPD or the PS with the WLS fibre inside and the LED in the middle of the scintillator pad (left). The performance of the electron (population a in red) versus pion (population b in blue) separation from test beam data, using the discrimination performed by the PS (right). Figures taken from [68].

The size of the cells where the occupancy is the largest is close to the Moliere radius of 3.5 cm, guaranteeing that most of the energy is contained in a unique cell. There is in total 6016 cells of 4.04, 6.06 and 12.12 cm respectively in the inner, middle and outer area. This also influences the spatial resolution. An optimal energy resolution is obtained with a full containment of the electromagnetic shower in the longitudinal direction by requiring a 25 X_0 thick ECAL. It has been measured to be of 9.4 %$\pm$0.2 % for the stochastic term and 0.83 %$\pm$0.02 % for the constant term thanks to electron beam tests at different energies.

The transverse energy spectra being the same on the whole calorimeter surface (the rapidity varies from $\eta = 1.9$ to 4.9 in the LHCb acceptance) in absence of magnetic field, it has been chosen to calibrate the PMT gain in transverse energy rather than in energy. Thus the maximal energy $7 + 10$ GeV/$\sin(\theta)$ measured in one given cell of the ECAL depends on its position with respect to the beam axis, defining by θ its angle in cylindrical coordinates. The typical dynamic range of a PMT in the ECAL is of 3000 photoelectrons per GeV. The uniformity of the PMT as well as for the fibre density has been looked at with special care in order not to lose in energy resolution. It has been found useful to equip each cell by a prism mixer to connect the fibres to the PMT window.

II.3.1.3 The HCAL

The HCAL granularity is bigger (with respect to the other calorimeter sub-detectors), since the shower transverse development is larger. It has been separated in two areas with two different cell sizes of 13.1 cm and 26.2 cm respectively in the inner and outer parts. The HCAL active

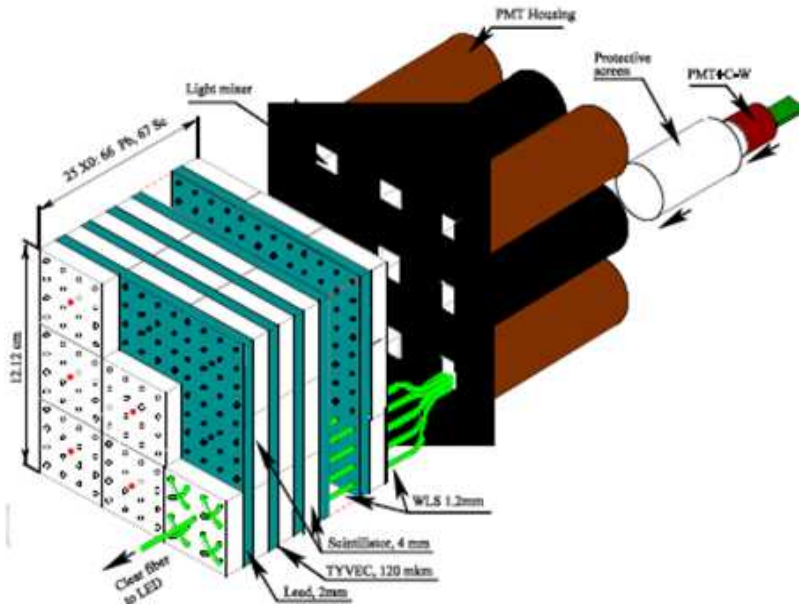

Figure II.11: A module of the ECAL. It is important to notice that the signal from the LED is not transmitted by the same fibres (clear fibre in the middle of each cell) than those used for the usual readout (skewed and bent WLS fibres).

material is iron[5], the produced light being collected by scintillating tiles and WLS fibres readout by PMTs, see Fig. II.12. The radiation in the HCAL has been estimated to be of 50 kRad per year in the most inner part and then still influences the choice of WLS fibres. The HCAL being mainly used for the trigger system, the energy resolution is only of $69\,\% \pm 5\,\%$ for the stochastic term and $9\,\% \pm 2\,\%$ for the constant term. For the same reason, adding some spatial constraints and keeping in mind that the ECAL is $1.1\lambda_{int}$ the HCAL length is only of $5.6\lambda_{int}$. The leakage of the most energetic particles introduces an angular dependence of the reconstructed energy of incoming particles. It has been measured on the HCAL alone that the measured energy is wrong by less than 3 % for 80 GeV/c pions. This leakage is even reduced by the presence of the $1.1\lambda_{int}$ ECAL upstream. The typical dynamic range of the HCAL PMT is of the order of 100 photoelectrons per GeV.

II.3.2 Electronics readout

The electronics of the calorimeter required a careful design to cope with the 25 ns separation between colliding bunches.

[5]The iron is the *active* material since it produces the shower. It is a *passive* material on the side of the measure: only the energy is the scintillator is detected and measured.

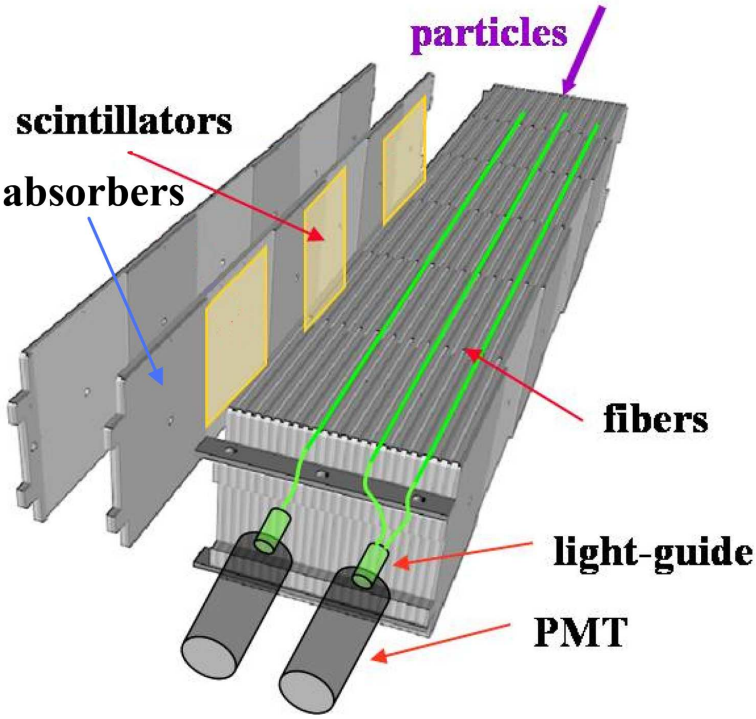

Figure II.12: A module of the HCAL, figure from [68].

II.3.2.1 The ECAL and HCAL

The readout being the same for the ECAL and HCAL, the electronics are the same. To ensure a full containment of the electronic signal shape, a clipping line is added just after the PMT with a resistor to adjust the return to 0 V. A 10 m to 15 m coaxial cable transports the signal to the front end electronics located in racks on top of the calorimeter wall, outside the detector acceptance. After integration performed in 25 ns the plateau is found to be of 4 ns within 1 % and the tail in the next sampling is found to be of $2\ \% \pm 1\ \%$, which are important constraints not to degrade the energy resolution, see Fig. II.13. The discharge of the integrator is ensured by a subtraction of the signal 25 ns later. The signal is then sent to the 12 bits ADC converter with an adjustable clock to ensure precise sampling and time alignment of each cell of the calorimeter. The full electronics is introducing 1.2 ADC counts of noise. Pedestal subtraction is then performed in dedicated FPGA (field-programmable gate array) in which the smallest of the two preceding samples is subtracted. This ensures to limit the probability of subtracting significant signal to less than 0.25 % in nominal conditions and where the occupancy is the largest. In return, there is a small average pedestal shift of less than 1 ADC count.

II.3.2.2 The PS and SPD

Concerning the PS and SPD, one has to cope with the important fluctuations of the signal. In particular a MIP produces typically 25 photoelectrons and thus requires exploiting the full integration window of 25 ns. The design is then based on two integrators running at 20 MHz for each channel. While the signal is sent to one integrator the other one is reset thanks to switches. The integrator is followed by a tracker-holder and a multiplexer. In the case of the SPD 15 % of the signal in the preceding sampling is subtracted to take into account that a substantial part of the signal falls in the next sample. The SPD also uses a simple discriminator to determine if the signal corresponds to a charged particle. The PS signal is sent to the front end boards by Ethernet twisted cables as well as the digital SPD information of the corresponding cell. The PS ADC range is of 10 bits to which is added the SPD information of 1 bit. The pedestal, the gain variations and the correction for the 15 % to 20 % of energy in the next sampling are corrected in a FPGA in the case of the PS.

II.3.3 Monitoring of the calorimeters

During the functioning of the experiment, the stability of the channels will be monitored online by a LED system in each of the subdetectors. For the PS and SPD there is one LED per channel, while there is 512 LEDs for the whole ECAL. This also allows for detecting dead channels rapidly. The LEDs as glued on the scintillating pad for both the SPD and the PS. The ECAL LED monitoring system controls only the readout part since the LED light is sent directly to PMT using splitters and specific fibres. The LED are flashed with an adjustable pulse rate in empty bunches of the LHC beam structure, so when no collision occurs. The LED pulse is measured in parallel by PIN diode to cope with the instability of the LED light, one PIN diode being used for 8 LED.

II.3.4 Time alignment of the calorimeters

The time alignment and the energy calibration of the calorimeters is of first importance to be sure not to degrade the performance of the detector for the two typical physics case presented in introduction. The first task achieved by the calorimeter group was the time alignment of the calorimeters [76]. In nominal conditions, the collisions taking place every 25 ns it is of primary importance to control the time alignment at the 1 ns level, in order to keep the spill over at a very low level. The time alignment was first studied in 2008 and 2009 using cosmic events and events from machine injection tests and pursued with the first collision data collected until now. The overall time alignment of the detector is now within 1 ns. The time alignment requires measuring the energy in one cell for successive samplings, the perfect alignment corresponding to the situation where the energy measurement is maximal. In practice, using the ability of the

electronics to measure 5 successive events specific time alignment event (TAE) mode are used to align in time the subdectectors. In such configuration the energy deposition in the current, the two previous and two next bunch crossings is stored. The sensitivity to the time alignment is better if the detector is shifted by half a period of 25 ns (because close the optimal, a plateau is reached). The time used for this procedure has to be minimized to keep the largest sample for physics studies. A similar technique is used for PS and SPD.

The 1 MHz L0 rate constrains the amount of data transmitted by the calorimeters. To apply a *zero suppression*[6], in addition to the data compression (done in the *Tell1*[7] for ECAL and HCAL), allows to reduce the amount of data. If the ECAL and HCAL do not need such a suppression at the hardware level (but only in the *Farm*), the PS has such a suppression in the *Tell1*. This aspect of the LHCb calorimeters is shown in section III.2.1.3 to be an important feature when looking at energy flow deposits.

II.3.5 Calibration

The calibration strategy for the calorimeters is detailed in the chapter III.

[6] *Zero Suppression* means that only significant deposits are transmitted to the next step of the reconstruction.
[7] The *Tell1* is a LHCb standardized that reads out the front end electronics data of the subdetectors and shape the digits that are sent to the Data Acquisition System (DAQ).

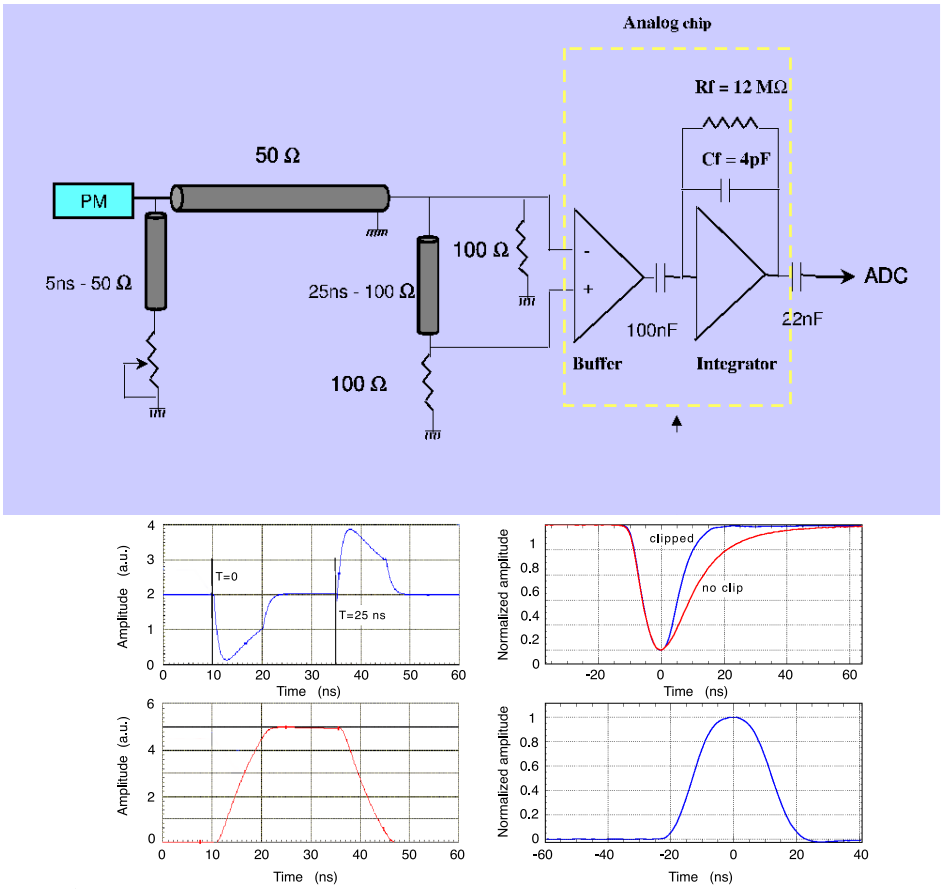

Figure II.13: A schematic of the front end electronics of the ECAL and HCAL (top) and the signals response to a pulse (bottom), figures taken from [68]. The signal in output of the PMT is transmitted to the amplifier through a delay line. The signal is also clipped thanks to a 5 ns delay line to accelerate the return of the signal to the reference. After 25 ns the signal is substracted by the buffer and a delay line to discharge the integrator. Response before (resp. after) to a 10 ns rectangular pulse is shown on the top (resp. bottom) plot of the bottom left part of the figure. The response to 80 GeV HCAL signals is given on the right part of the bottom figure, before the integrator (top) with (blue) and without (red) clipping and after the integrator (bottom). The shaping of the signal is performed by the transmission line itself.

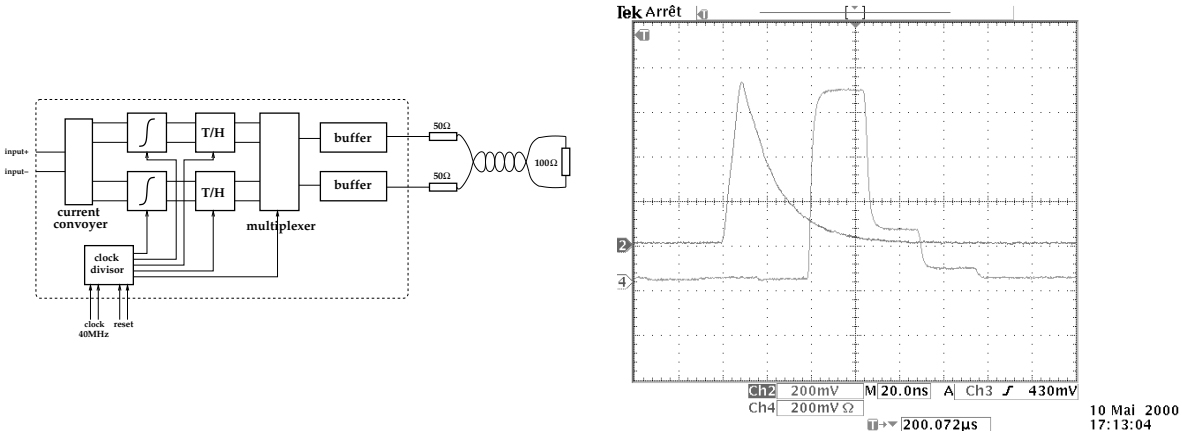

Figure II.14: A schematic of the very front end electronics of the PS (left) and the response to a pulse (right), figures taken from [68]. The integration over 25 ns is performed alternatively by two different integrators, the other one being reset while one is active. The signal is tracked and held before being sent to the multiplexer that select the relevant input. The multiplexer picks up alternatively the proper input corresponding to the active integrator. The input pulse (peaky distribution) and the output (step distribution) of the multiplexer is given on the right plot. It is noticeable that approximately 20 % of the signal falls in the next bunch crossing of 25 ns.

Chapter III

Energy calibration of the LHCb calorimeters

- Je suis désolé mais je travaille.
- Réjouissez-vous, on va vous donner l'occasion d'arrêter de bricoler dans le vide, vous allez travailler utile, pas vrai ?

Jacques Chambon alias *Merlin* et Joëlle Sevilla alias *Séli*
in *La Potion de Fécondité II*, **Kaamelott, Livre II**, Tome 2, Épisode 20,
écrit par Alexandre Astier.

Contents

The properties of the LHCb calorimeters are detailed in the chapter II, however some basic properties are first recalled here for the self consistency of the discussion. After a short introduction to the different methods used for the in situ calibration, the energy flow technique is described as well as the results obtained on Monte Carlo and real data. This method aims at providing an accurate inter-calibration of the calorimeter cells, the absolute calibration being provided by other methods.

III.1 Overview of the energy calibration methods

III.1.1 Energy resolution

The optimal energy resolution of the ECAL modules and associated electronics [75, 68], is parametrized as

$$\frac{\sigma_E}{E} = \frac{a}{\sqrt{E}} \oplus b \oplus \frac{c}{E \sin\theta_{i,j}} \tag{III.1}$$

where E is the energy deposit (in GeV) in a cell (i,j) and $\theta_{i,j}$ is the inclination of a photon produced at the primary vertex[1]. The stochastic term is found to be $8.5\ \% < a < 9.5\ \%$ and the constant term is $b \sim 0.8\ \%$ from test beam data [68]. The noise term c is measured on the full electronic chain and is inversely proportional to $E_T\,(i,j) = E \sin\theta_{i,j}$ since the PMT gains of the ECAL and HCAL are set accordingly to their rapidity[2]. The noise is limited to $\sigma_{\text{noise}} = 1.2$ ADC counts in the ECAL and HCAL (see Fig. III.1) electronics. Since for each channel, the smallest value measured in the two previous time slots of 25 ns is subtracted from the current value, there is a systematic underestimate of the pedestal of $\simeq 0.4$ ADC, subtracted in the reconstruction. As the signal is digitized on 12 bits on a transverse energy range of approximately 10 GeV, this corresponds to $c = 0.003$ GeV. The parameters for the HCAL resolution were found to be equal to $a = 69 \pm 5\ \%$ and $b = 9 \pm 2\ \%$ [68], the c term being identical for ECAL and HCAL since they have the same electronics.

III.1.2 Calibration methods for LHCb calorimeters

The calibration methods are rather different for each subsystem of the LHCb calorimeters.

- The HCAL is build with an in situ calibration system, using two ^{137}Cs sources travelling in the detector through pipes [75, 68]. A test beam calibration with 50 GeV pions showed that the accuracy of the method is within 2–3 %.

[1] The primary vertex position is assumed to be at the geometrical origin of the detector. This is a reasonable assumption since the interaction region is characterized by $\sigma_z = \pm 5.3$ cm, to be compared to the 12.5 m that separate the ECAL to the VELO. We also assume that the photon hits the geometrical barycentre (x,y) of the cells and that it interacts at the typical position of the shower maximum which is at 7.4 $X_0 = 12.4$ cm for 10 GeV photons.

[2] The constant digitization scale in E_T allows to have a smoother dependence of the multiplicity with the cell position.

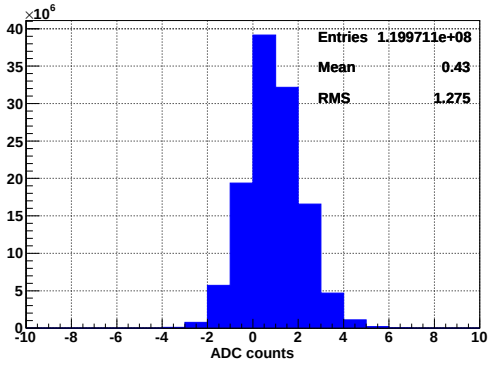

Figure III.1: Front end electronics noise in the ECAL estimated at 1 MHz with random triggers. The result is cumulated over the 6016 cells of the ECAL. The width equals to $\sigma_{\text{noise}} = 1.3$ ADC counts while the shift of 0.4 ADC is due to the pedestal subtraction procedure as described in section III.1.1.

- The ECAL uses different dedicated calibration methods described below.
- The PS calibration is based on the MIP measurement matching tracks with hits in the PS. A typical precision of 10 % was obtained on cosmic data.
- The SPD calibration is obtained by scanning the decision threshold for a charged particle and measuring the corresponding efficiency and by matching charged tracks with the trackers.

The ECAL, that provides a measurement of the energy of photons for key channels as $b \to s$ radiative transitions, needs an accurate calibration typically at the level of 1 % in order not to degrade the constant term of the resolution. Monte Carlo studies [43] show that with 3 % residual miscalibration the resolution is increased by 20 % on $B_s^0 \to \phi^0\gamma$, reducing the signal over background ratio. Decreasing the residual miscalibration from 10 % to 1 % allows to reduce the B_s^0 width from 270 MeV/c^2 to 80 MeV/c^2 approximately.

It is required for the ECAL calibration procedure to :

- be precise down to the 1 % level,
- be robust against a change of external conditions (pile-up and trigger for instance),
- and possibly use a small amount of data without using a lot of CPU.

The different methods [77] used to calibrate the ECAL are described in the following, by order of appearance in the calibration procedure.

- The LED system provides a first calibration of the gains from the photo-statistics. The gain G[3] is extracted from the ratio $(\sigma^2_{\text{LED}} - \sigma^2_{\text{noise}})/(A_{\text{LED}} - A_{\text{noise}}) = \kappa \frac{q}{S} f G$, where $\kappa = 1/3$ is the clipping factor introduced in chapter II, $q = 1.6 \cdot 10^{-19}$ C is the elementary charge, $S = 0.0195$ pC per ADC is the PMT sensitivity and $f \simeq 1.2$ is the Fano factor [78]. The σ^2_{noise} and A_{noise} take into account for the pedestal subtraction procedure and the influence of the noise and are known, in average, from Fig. III.1. This procedure provided calibration constants with an accuracy of 8-10 % [79].

- The calibration gains are then smoothed out by using the energy flow [80] over the calorimeter surface. This method is described in details in the following document. It provides a more precise inter-calibration of the cells of the ECAL and can provide an accurate cross-check of the calibration of the PS and HCAL.

- The absolute energy scale (and further inter-calibration, if needed) is obtained using reconstructed π^0's. One of the approaches consists in fitting the $\gamma\gamma$ invariant mass distribution for each ECAL cell, combining a photon that hits the cell to be calibrated and another reconstructed photon. The relative position of the peak compared to the known PDG [38] value provides a calibration constant. Doing this iteratively allows to calibrate the ECAL down to 2 %. Another independent method consists in subtracting the combinatorial $\gamma\gamma$ pairs by using the x and y symmetry of the detector, in minimizing a *cost function* to find the calibration constants for some group of cells, and in iterating.

- Finally, it is demonstrated in this document that the energy flow method can be used to further improve the inter-calibration of the ECAL, by doing a second pass of energy flow procedure after the π^0 calibration. This essentially allows to further improve the inter-calibration of the cells, but can not certainly improve the absolute scale.

III.2 Monte Carlo studies for the Energy Flow calibration

III.2.1 Overview

The energy flow is the cumulative energy[4] deposit over many events. In principle, for a perfectly calibrated calorimeter, the energy flow is expected to behave monotonically in each quadrant and smoothly in each of the two dimensions x and y (the z axis corresponds to the beam axis). The closest to the beam pipe, the highest energy a cell receives in average. If a relative miscalibration exists among the channels, the cumulative deposit is expected to fluctuate, breaking monotony and smoothness. The calibration is then performed by smoothing the energy flow, possibly using

[3] The different terms contributing to the gain are the quantum efficiency (the probability to produce an electron from a single photon in the photocathode), the collection efficiency (the probability that the produced electron is collected by the first dynode) and the amplification factor of the dynodes.

[4] The word *e*nergy is used as a generic term, transverse energy can be used as well.

different complementary methods. As the ECAL is made of three areas corresponding to three different cell sizes, these zones are always treated independently in this study. The method also applies to the PS and the HCAL, taking care of the different cell sizes and the different number of areas in the HCAL.

In section section III.2.1.1 the procedure of miscalibration and the selection of the hits is described in detail while in section III.2.1.2 and section III.2.1.3 the normalization of the flow and the intrinsic loss of sensitivity are emphasized. The procedure to compute the calibration coefficients is then explained in section III.2.1.4 and the data sample used for the Monte Carlo studies is described in section III.2.1.5.

III.2.1.1 Miscalibration procedure

In the work described here, the skeleton of the procedure given in [80] is used although some differences exist. By default 10 % of miscalibration is introduced by randomizing one *miscalibration coefficient* $c_{i,j}^{\text{miscalibration}}$ for each cell (i, j) on a Gaussian function centred at 1 and with a standard deviation of 0.1. These coefficients are then applied to the digits in the software. For a more convenient simulation, although approximative, the study is mainly done with a miscalibration applied in Brunel (reconstruction software). The coefficients are applied after the transcription of the ADC (well calibrated) in energies (miscalibrated) and thus after the zero-suppression.

The zero-suppression consists in removing the insignificant energy deposit, by decoding only the hits that are above a certain threshold. In the standard versions of the software, this procedure uses a "2D" approach in the sense that hits with a significant hit (above 50 MeV) in the neighbourhood are decoded anyway, in order to avoid biasing the energy reconstruction of physics signals. In the reconstruction that we use in this study, the "2D" zero-suppression is not applied and a basic "1D" cut is applied instead. Hits above 25 MeV of transverse energy (corresponding to 10 ADC counts) are selected for the calibration procedure. This cut allows to remove the intrinsic noise of the ECAL/HCAL full electronic chain and the value is chosen to be $5\sigma_{\text{noise}}$ to which is added a safety margin. Some parasitic effects due to this procedure are then observed. It is shown in section III.2.5 that with a proper simulation (the miscalibration done before the digitization performed in Boole) the results are at the same level of accuracy and validate those obtained with the approximative approach. The situation is different in the PS, since the zero suppression is hardware. By default it is applied at the level of 0.5 MIP, 1 MIP corresponding to 2.7 MeV). Although this threshold is already applied during the digitization (in Boole), a cut at 1 MIP is re-applied (this allows to perform the sensitivity study of the section III.2.1.3. The noise in the PS is expected to be of 1 ADC, 10 ADC corresponding to 1 MIP.

The effect of removing high (transverse) energy deposits (to avoid saturated digits for instance) does not influence the result and thus is not considered any more in the following, as expected since the events are minimum bias events.

Once the digits are miscalibrated and the selection is applied, the energy flow is cumulated over a relatively big amount of data of ten million of minimum bias events. In the following the starting point of the calibration procedure is referred as the *miscalibrated* energy flow. The energy flow without miscalibration is referred as *perfectly calibrated*.

The main difference with the procedure applied in [80] is that, here, the miscalibration is applied before offline selection cuts. This aspect is found to be one of the dominant limitations of the energy flow method, as emphasized in section III.2.1.3.

III.2.1.2 Normalization of the deposit

If the perfectly calibrated energy flow contains sizeable cell to cell variations, it is more difficult to disentangle between these intrinsic variations and the fluctuations due to the miscalibration. This section aims at finding the *best* normalization, in the sense that it should provide the best perfectly calibrated deposit.

The transverse energy deposit is expected to be proportional to the number of hits in each region of the calorimeter, because of the gain dependency with rapidity (see Fig. III.2). The correlation factor depends on the area since the sensitivity of the PMTs in the three areas are different (due to the fact that the WLS fibre densities and the cell sizes are different in the three areas [68]). The transverse energy normalized by the number of hits in each cell is then expected to be flat in first approximation and thus a good candidate for the energy flow calibration.

Two effects have to be taken into account to understand the departure with respect to this simple approximation. The former is motivated by physics arguments while the latter is purely technical and have not been corrected on the Monte Carlo studies due to time constraints (the study on real data is not sensitive to this effect).

- It is first noteworthy that the LHCb magnetic field plays a role in the shape at $|y| < 300$ mm (see Figs. III.3-III.4) with a striking effect in the outer ECAL (see Fig. III.3 top left). Charged particles are deviated by the magnetic field and in particular more energetic particles coming from larger rapidity regions are deviated to smaller rapidity. It follows that the energy deposit is higher in the cells located at $|y| < 300$ mm compared to cells at the same x but larger y. The magnetic field also modifies the shape of the normalized deposit in the inner HCAL, close to the beam pipe (see Fig. III.4 right). In this region the normalized deposit increases significantly. The effect of possible saturating digits is found to be negligible, looking at the spectra of some particular cells located in this region (see Fig. III.5), and this is due to the more important density of particles, maybe due to the beam plug located around the beam pipe (with the large HCAL cell size the pile-up is not

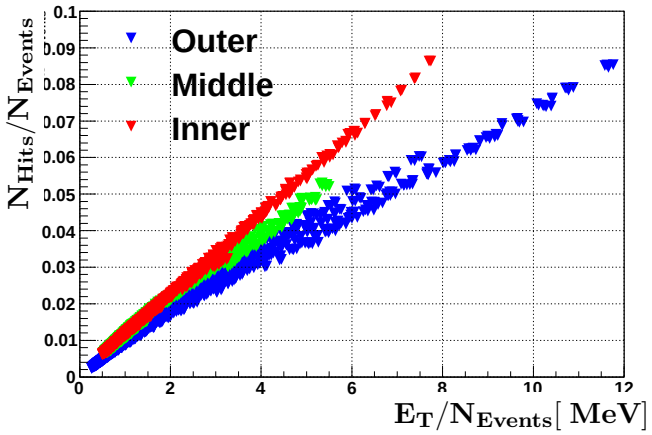

Figure III.2: Correlation of the occupancy and the average E_T per event in the ECAL for 10 Million of minimum bias events. The three areas have different correlation factors due to the different cell sizes and PMT sensitivities. Different regions are also distinguished in the outer ECAL due to the influence of the magnetic field.

negligible any more). Since, in one third of the events, more than one particle hit one cell of the HCAL at the same time, this results in an increased normalized transverse energy flow. The fact that this effect is not seen in the ECAL is due to the smaller cell size of the ECAL inner (HCAL inner cells are larger by a factor 3).

- The second effect on the flow is a circle with a radius of almost 1.5 m in the middle of the ECAL, which is due to the fact that the cut is applied on the transverse energy. Since the calibration is not exactly constant in E_T but varies smoothly on the calorimeter surface at the level of 10 %, the sharp cut in E_T introduces a threshold in the energy flow. This problem is solved on real data and on properly miscalibrated data by applying a cut on the ADC value rather than transverse energy. This effect also explains the discontinuities of the sensitivity loss emphasized in section III.2.1.3 where one also shows that the intrinsic limitation of the procedure depends on the choice of the normalization.

III.2.1.3 Sensitivity loss

As shown on Fig. III.3, the mean transverse energy deposit is of the order 80 MeV (110 MeV in the outer area) in the ECAL. Assuming that the spectrum in each cell follows roughly an exponential distribution, this means that the RMS of the deposit is of the same order of magnitude. Hence the mean transverse energy deposit is three to four times larger than the energy of the first bin above the threshold of 25 MeV. Recalling that the cut is applied at the level of 25 MeV, the bin in energy located near the cut represents almost one third of the total energy deposit in a typical cell. It is important to insist here on the fact that the simulation is not

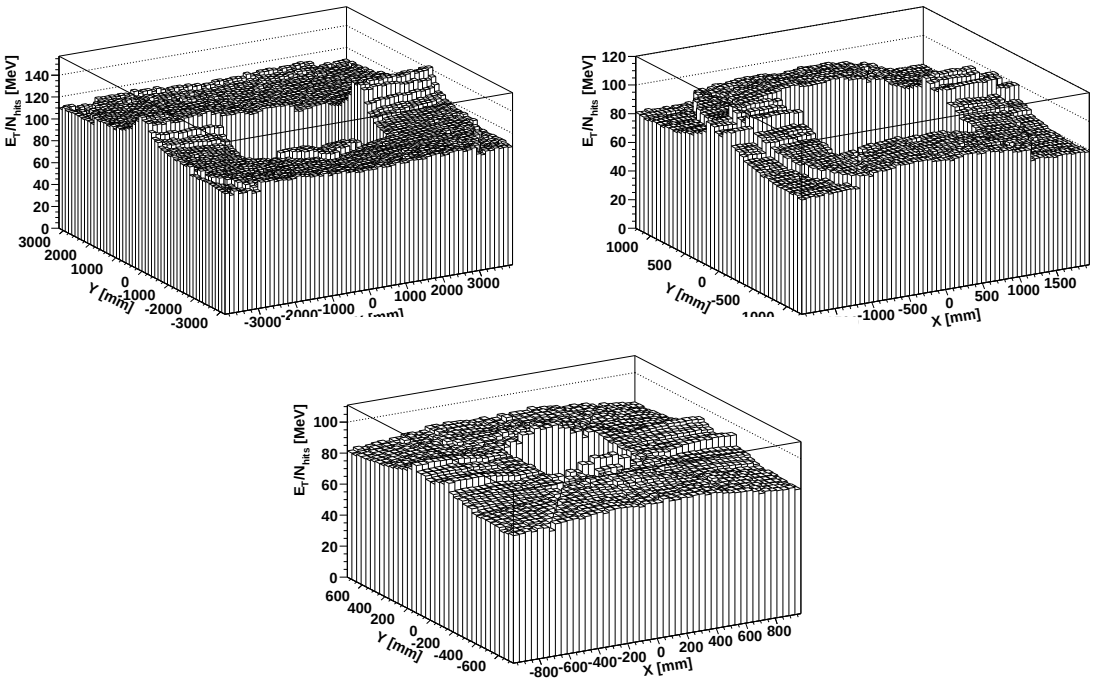

Figure III.3: Normalized perfectly calibrated transverse energy flow in the outer (top left), middle (top right) and inner (bottom) areas of the ECAL. The effect of the magnetic field is clearly visible in the outer but less in the inner, where the distribution is almost flat. The thresholds in the middle and outer are due to the cut in transverse energy, as explained in the text.

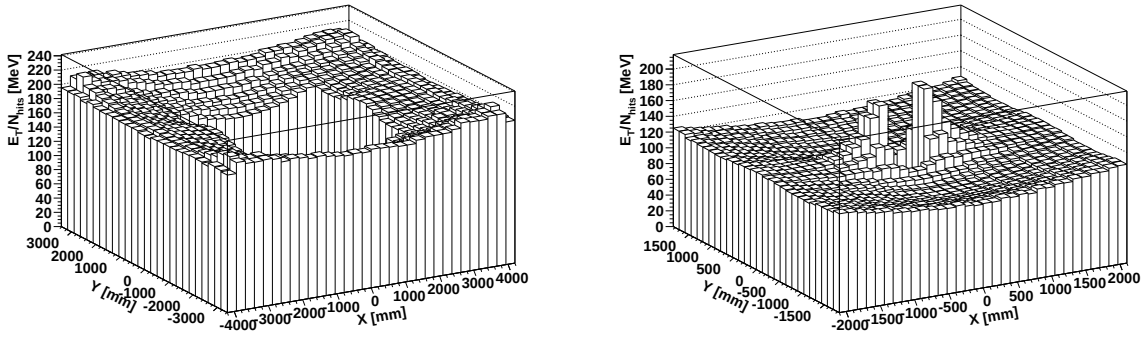

Figure III.4: Normalized perfectly calibrated transverse energy flow in the outer (left) and inner (right) areas of the HCAL. The distribution is peaked near the beam pipe due to a saturating occupancy as explained in section III.2.1.2.

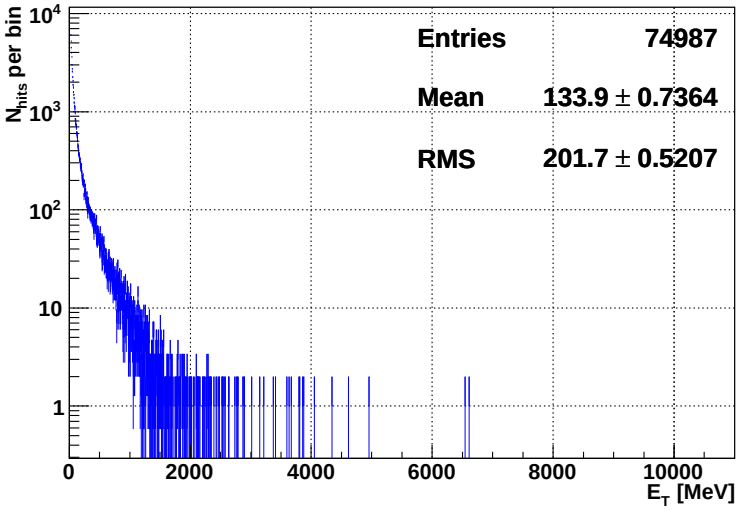

Figure III.5: Transverse energy spectrum in the HCAL inner cell ($\text{row} = 14, \text{column} = 13$) for 300 k events. This cell is located at the limit on the left of the innermost dead zone, close to $y = 0$. No saturated digit is found out of 300 k events, supporting the hypothesis of a saturating occupancy rather than a saturating energy deposit to explain the peak in the innermost region of the HCAL.

realistic in the sense that the miscalibration is not applied before the digitization but after the ADC's are decoded. Nevertheless it will be very difficult to perform the study on the sensitivity with a realistic simulation[5] since it is necessary to have both the miscalibrated and the perfectly calibrated information at the same time.

Some parasitic effects are nevertheless due to the improper miscalibration and are expected to disappear in the case of a realistic simulation and in the real data. In the unrealistic simulation, the ADC bins are well calibrated but the energies are miscalibrated. This means that each 2.5 MeV bin in energy is shifted by a certain quantity equal to the miscalibration times the energy corresponding to this bin. It results that if no cut is applied the mean energy deposit in the cell is strictly equal to the product of the miscalibration by the mean energy deposit without miscalibration (see Eq. III.5). But a cut is applied to remove the noise contribution at small ADC values and then it happens sometimes that the miscalibration is big enough[6] to remove or add a bin in the spectrum (see Eq. III.7). The Fig. III.6 shows the spectra in ECAL for these two typical situations where a bin is lost or not. This introduces, as one explains in the following, a sensitivity loss which depends on the choice of the normalization.

[5] A realistic simulation require to miscalibrate before the digitization and thus the true and non miscalibrated information is definitively lost.

[6] Typically the level of 10 % miscalibration, for a bin corresponding to 25 MeV, the shift is of 2.5 MeV which corresponds to the difference between two bins (10 GeV coded on a 12 bits ADC gives approximately 2.5 MeV per ADC count).

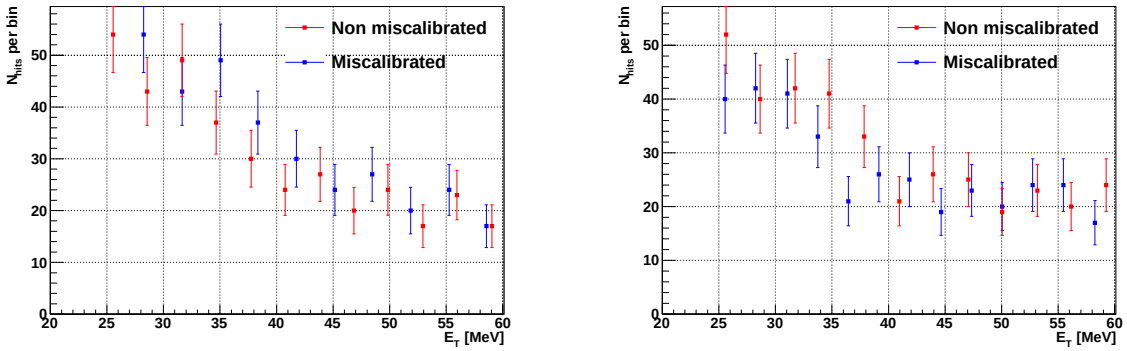

Figure III.6: The spectra for two different cells where no bin is lost (left) and one bin is lost (right) with the improper miscalibration procedure. The second case (right) will induce a non negligible sensitivity loss which depends on the normalization choice (see text). In the left the miscalibrated (blue) distribution is shifted on the right. In the right plot, the miscalibrated (blue) distribution is shifted on the left and the first bin in red close to 25 MeV is not present any more in the blue histogram. This effect results in a sensitivity loss, in the second case, described in section III.2.1.3.

Formally, defining ϵ_k and ν_k respectively the energy and the number of entries in a bin k above the threshold of an arbitrary cell of implicit coordinates (i, j), the number of hits, the normalized and the not normalized energy are:

$$e_{\text{true}} = e_{\text{true}}^{\text{not normalized}} = \sum_{k=1}^{N_{\text{bins}}} \nu_k \epsilon_k, \tag{III.2}$$

$$N_{\text{true}} = \sum_{k=1}^{N_{\text{bins}}} \nu_k, \tag{III.3}$$

$$e_{\text{true}}^{\text{normalized}} = \frac{e_{\text{true}}}{N_{\text{true}}}. \tag{III.4}$$

As a result, if no bin is lost

$$e_{\text{miscalibrated}}^{\text{not normalized}} = c^{\text{miscalibration}} e_{\text{true}}, \tag{III.5}$$

$$e_{\text{miscalibrated}}^{\text{normalized}} = c^{\text{miscalibration}} e_{\text{true}}^{\text{normalized}}, \tag{III.6}$$

and if one bin is lost

$$e_{\text{miscalibrated}}^{\text{not normalized}} = c^{\text{miscalibration}} e_{\text{true}} \left(1 - \frac{\nu_1 \epsilon_1}{e_{\text{true}}}\right), \tag{III.7}$$

$$e_{\text{miscalibrated}}^{\text{normalized}} = c^{\text{miscalibration}} e_{\text{true}}^{\text{normalized}} \frac{1 - \frac{\nu_1 \epsilon_1}{e_{\text{true}}}}{1 - \frac{\nu_1}{N_{\text{true}}}}. \tag{III.8}$$

The same expressions with opposite signs stand in the case where one bin is added in the spectrum. The analysis is also correct in the case of more than one lost or added bin. In those cases, $\nu_1 \epsilon_1$ and ν_1 are replaced by the corresponding sums over the lost or added bins

(*problematic* ones) $e_{\text{problematic}}$ and $N_{\text{problematic}}$ respectively (see Eq. III.10), and the sensitivity loss will increase. The sensitivity loss S, defined as

$$S = \frac{c^{\text{visible miscalibration}}}{c^{\text{miscalibration}}} \tag{III.9}$$

is thus written in the most general case as :

$$\epsilon_{c^{\text{miscalibration}}} = \frac{c^{\text{miscalibration}} - 1}{|c^{\text{miscalibration}} - 1|} = \text{sign}\left(c^{\text{miscalibration}} - 1\right), \tag{III.10}$$

$$S^{\text{not normalized case}} = 1 + \epsilon_{c^{\text{miscalibration}}} \frac{e_{\text{problematic}}}{e_{\text{true}}}, \tag{III.11}$$

$$S^{\text{normalized case}} = \frac{S^{\text{not normalized case}}}{1 + \epsilon_{c^{\text{miscalibration}}} \frac{N_{\text{problematic}}}{N_{\text{true}}}}, \tag{III.12}$$

$$\text{where } e_{\text{problematic}} = \sum_{k \in \{\text{problematic bins}\}} \nu_k \epsilon_k \tag{III.13}$$

$$\text{and } N_{\text{problematic}} = \sum_{k \in \{\text{problematic bins}\}} \nu_k. \tag{III.14}$$

In the case of no bin loss, the sensitivity is equal to unity.

This analysis shows that the sensitivity loss presents some discontinuities corresponding to different numbers of problematic bins. This will introduce non Gaussian effects in the calibration coefficients and then in the residuals of the calibration, as it will be shown in section III.2.2.2. These discontinuities are expected to disappear in the case of a realistic simulation since the bins are fixed in the energy range, only the content of the bin will be modified. As a result, the sensitivity loss is thus expected to be smoother and the effect slightly smaller, both with real data and a proper miscalibration procedure. This will be checked with a realistic miscalibration procedure in section III.2.5.

Fig. III.7 shows that the sensitivity loss is correlated with the miscalibration in the case of a not normalized procedure and anti-correlated in the normalized one. Expanding to the first order in ${}^{e_{\text{problematic}}}/_{e_{\text{true}}}$ and ${}^{N_{\text{problematic}}}/_{N_{\text{true}}}$ gives:

$$S^{\text{normalized case}} = 1 + \epsilon_{c^{\text{miscalibration}}} \left(\frac{e_{\text{problematic}}}{e_{\text{true}}} - \frac{N_{\text{problematic}}}{N_{\text{true}}} \right). \tag{III.15}$$

This shows that the ratio ${}^{N_{\text{problematic}}}/_{N_{\text{true}}}$ is larger than ${}^{e_{\text{problematic}}}/_{e_{\text{true}}}$ reflecting that the spectrum has a tail at high energies and is peaky at low energies.

The Tab. III.1 summaries the sensitivity loss as a function of the normalization and the sub-detector. It is important here to recall that these values are only estimates with the unrealistic miscalibration procedure. It should also be noted that these values are *absolute*. Starting from 10 % miscalibration, one cannot reach less that 7 % residual miscalibration after the procedure. If 20 % miscalibration was applied, one would get at least 14 % residuals, since the number of lost bins would increase.

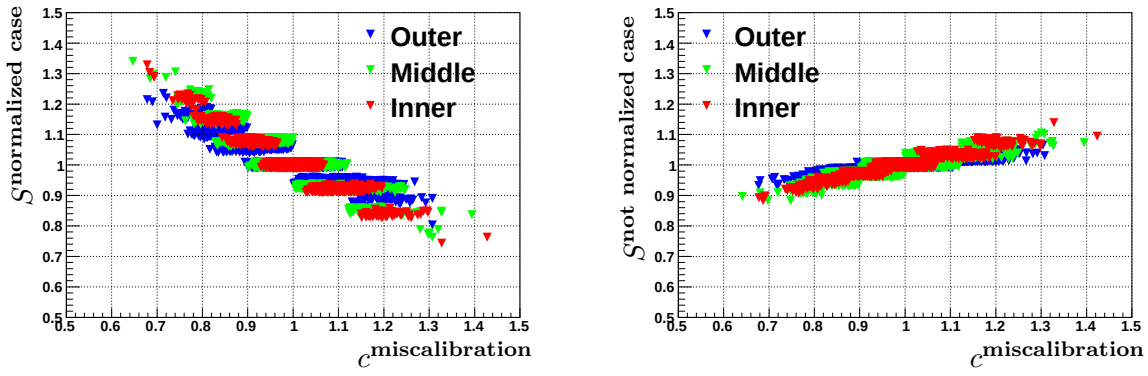

Figure III.7: The sensitivity as a function of the applied miscalibration for each cell of the ECAL in the normalized (left) and the not normalized case (right). The discontinuities are due to the procedure of miscalibration and will not be present in the real data (see text), for which one expects a smoother effect. The sensitivity loss is larger in the inner than in the outer due to different spectra.

Normalization	ECAL	HCAL	PS
Yes	7 %	5 %	5 %
No	2.5 %	1.5 %	1.5 %

Table III.1: The order of magnitude of the RMS of the absolute sensitivity loss for different normalizations (normalized or not by the number of hits) and for the three sub-detectors when 10 % miscalibration is applied.

Conclusion The most sensitive way to calibrate with the energy flow is to use the not normalized energy deposits. The normalized procedure will be limited to the *absolute* level of 5 % to 7 % depending on the sub-detector (and also of the considered area). As the not normalized transverse energy deposits will be used for the procedure for ECAL and HCAL, the limitation to the calibration procedure will come from the shapes shown on Figs. III.8-III.9, as stated in section III.2.2. Concerning the PS, the energy deposit (not the transverse one) is used for the calibration (see Fig. III.10), since the transverse energy deposit is not meaningful for the PS. In fact, since the relation between energy and transverse energy is a constant for each cell (i, j),

$$sin\,(\theta_{i,j}) = \frac{\sqrt{x_{i,j}^2 + y_{i,j}^2}}{\sqrt{x_{i,j}^2 + y_{i,j}^2 + z_{\text{ECAL}}^2}} = \frac{e_{i,j}^T}{e_{i,j}} \tag{III.16}$$

where $x_{i,j}$ and $y_{i,j}$ represent respectively the x and y coordinates of the cell (i, j) and z_{ECAL} is the ECAL z coordinate at the shower maximum, it is possible in principle to calibrate with energy or transverse energy equivalently. Since these two ways to calibrate give equivalent results, one only considers the one related to the ADC values (E_T for the ECAL and HCAL, E for the PS).

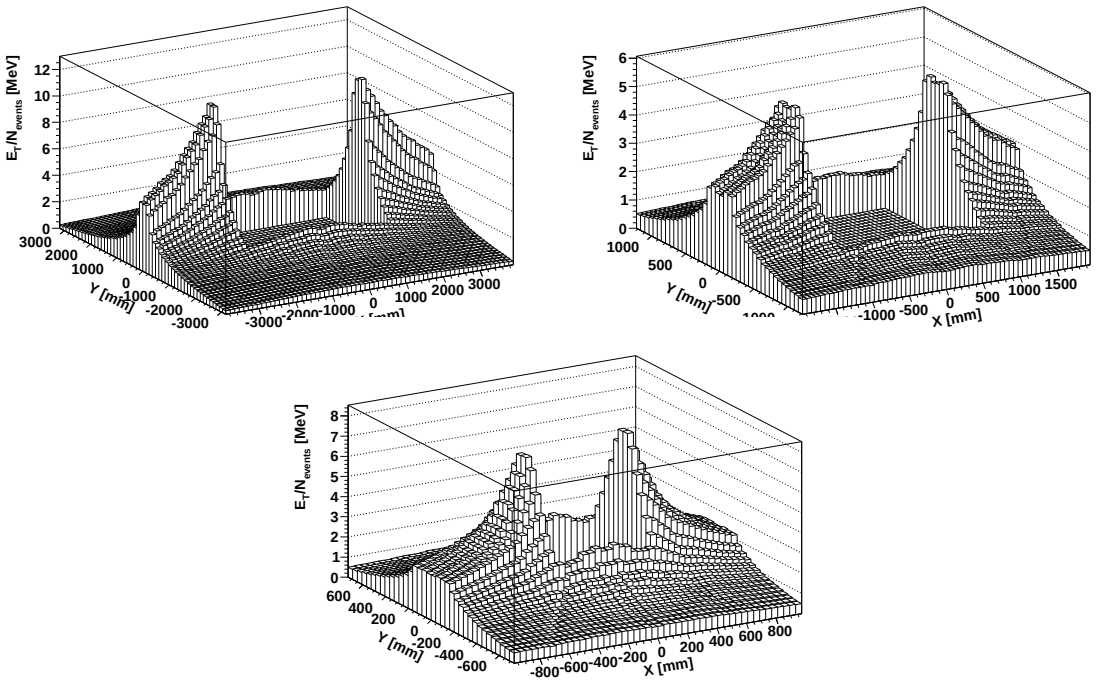

Figure III.8: Not normalized perfectly calibrated transverse energy deposit in the outer (top left), middle (top right) and inner (bottom) areas of the ECAL. The effect of the magnetic field is clearly visible in the three zones and is larger in the outer, where the relative difference in the energy flow between two extreme cells is bigger with respect to the other areas.

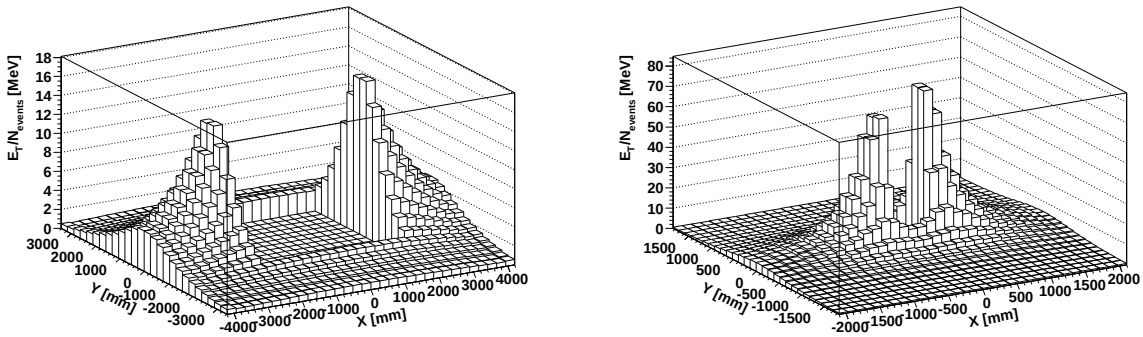

Figure III.9: Perfectly calibrated transverse energy deposit per event in the outer (left) and inner (right) areas of the HCAL. The effect of the magnetic field is important. Note that the amplitude of the peaks close to $y = 0$ is different at $x > 0$ and $x < 0$, due to the charge detection asymmetries, as expected from section III.2.3.

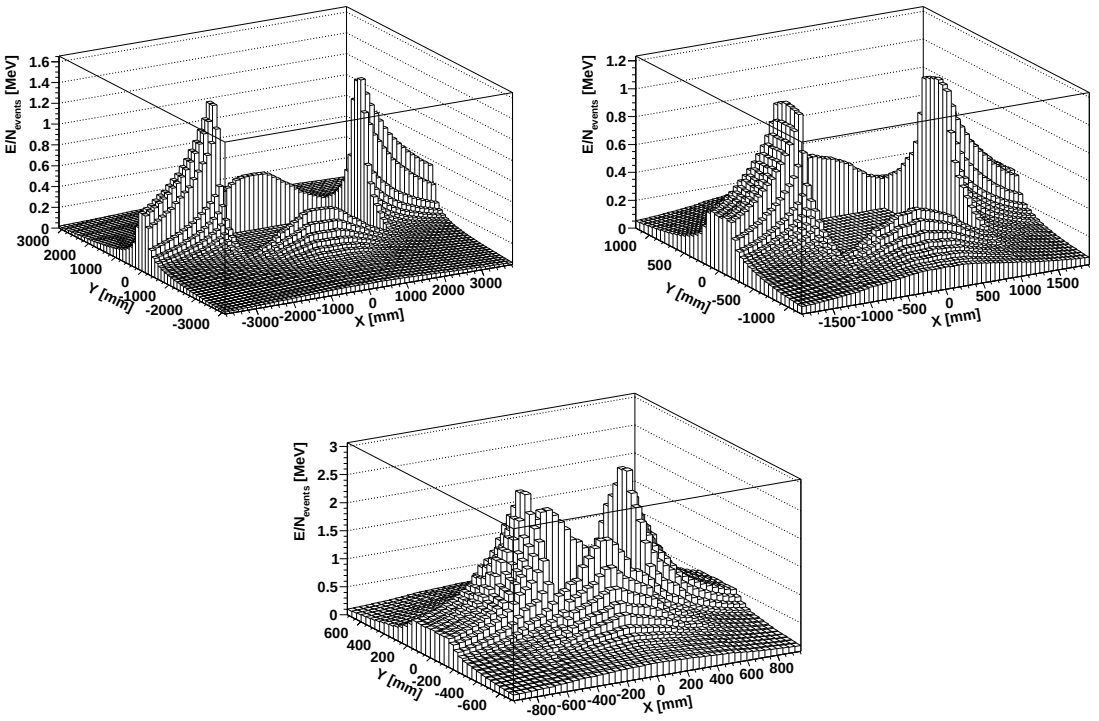

Figure III.10: Not normalized energy deposit in the outer (top left), middle (top right) and inner (bottom) areas of the PS. The effect of the magnetic field is clearly visible in the three regions as for the ECAL.

III.2.1.4 Extraction of the calibration coefficients

One of the smoothing methods described in section III.2.2 is applied in order to remove the fluctuations in the flow due to the miscalibration. The energy flow is corrected by the obtained calibration coefficient. The calibration coefficients are defined for each cell by the ratio of the *corrected* energy flow to the *miscalibrated* energy flow,

$$c_{i,j}^{\text{calibration}} = \frac{e_{i,j}^{\text{corrected}}}{e_{i,j}^{\text{miscalibrated}}}. \tag{III.17}$$

The results are given in terms of residuals of miscalibration $r_{i,j}$, defined as the relative difference between the *perfectly calibrated* deposit and the *corrected* one with respect to the *perfectly calibrated* one (see Eq. III.18), or as the product of the *miscalibration coefficient* (known in the simulation) by the calibration coefficient extracted from the calibration procedure. The residuals are not accessible in the case of real data taking. The sensitivity loss limits the calibration procedure by smearing the visible miscalibration

$$r_{i,j} = c_{i,j}^{\text{miscalibration}} c_{i,j}^{\text{calibration}} - 1 = c_{i,j}^{\text{visible miscalibration}} c_{i,j}^{\text{calibration}} \frac{1}{S_{i,j}} - 1 \tag{III.18}$$

$$= \frac{e_{i,j}^{\text{perfectly calibrated}} - e_{i,j}^{\text{corrected}}}{e_{i,j}^{\text{perfectly calibrated}}} \tag{III.19}$$

For a perfect calibration procedure, the residuals are $r_{i,j} = S_{i,j}^{-1} - 1$ and thus limited to the width of the sensitivity. The method consists in finding a procedure that reaches this bound.

III.2.1.5 Data sample and L0 requirement

The simulation conditions are summarized in Tab. III.2. All the results are presented here with 10 millions of minimum bias events. No specific requirement has been made on the L0 trigger for these events.

Parameter	Value
Beam Energy	5 TeV
β^*	2 m
Crossing angle	329 mrad
Magnetic Field	Down (-1)
Velo	Closed
Number of interactions per bunch crossing	$\nu = 1$
Spillover	No

Table III.2: Beam conditions for the generation of the events used in the following analysis.

The L0 trigger has an effect on the bi-dimensional shape of the energy flow. As the *not normalized* transverse energy flow is used in this study, the relative difference between 10 millions of events and 965 thousand other events passing the L0 filter is computed. Despite the limited statistics on the L0 data sample, the result is significant and two types of cells are clearly identified on Fig. III.11. As the L0 trigger selects the high energy deposits (the main requirement is on the HCAL energy deposit), a systematic shift in energy is found. The main lesson from this study is the difference between regions where the magnetic field plays a role and the others. The events without L0 requirement are less underestimated in the latter regions. This will induce that with L0 triggered events, the effect of the magnetic field will be less important. The relative difference is bigger in the case of a not normalized flow since for the same amount of events the total energy deposit is much bigger for L0 triggered events. The normalization by the number of hits tends to reduce this effect, which almost vanishes in the region at $|y| < 300$ mm, since the most contributing hits (to the mean deposit) are always contained in triggered events (not necessarily by the considered cell) since they are always sufficiently energetic. It happens more frequently in the other regions that the deposit does not belong to a triggered event and then the mean energy per hit is much bigger with the L0 requirement. The L0 trigger (HCAL mainly) seems to play a small role in the shape of ECAL energy flow and the method should then be fully tested on a L0 triggered data. That is why the results with a L0 requirement is also shown in the dedicated section III.2.5.3. Nevertheless, the effect on the calibration constants is not expected to be large since it will not introduce violent local variations.

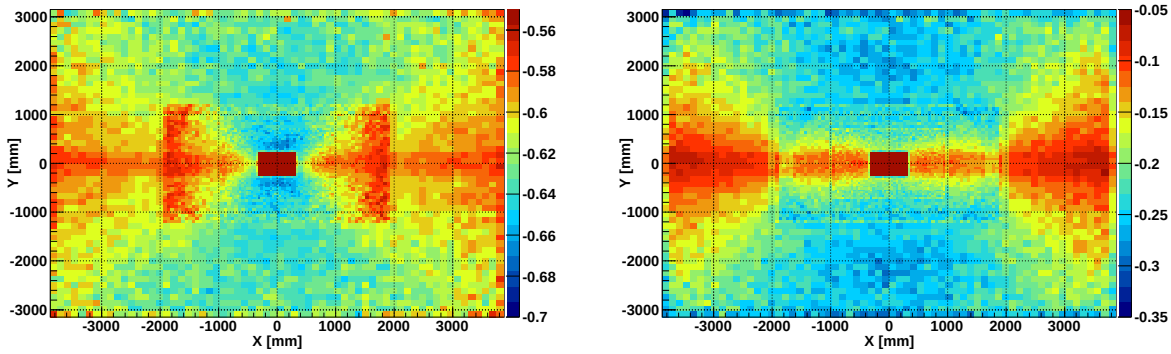

Figure III.11: Relative difference of the transverse energy deposit of events without requirement with respect to L0 triggered events for the not normalized case (left) and the normalized one (right) in the ECAL. Two types of cells are clearly identified. Cells where the magnetic field do not play a role are more underestimated than the others. Nevertheless, the magnitude of the effect depends on the normalization, since the number of hits is also different.

III.2.2 Energy flow calibration methods and results

The energy flow calibration is based on the smoothing of the transverse energy deposit. Despite the normalized energy flow is almost flat, it has already been stated in section III.2.1.3 that the sensitivity loss leads to prefer the not normalized distribution. This aspect is first emphasized on an example. Then the calibration study is performed on the not normalized transverse energy flow. To perform such a calibration, different ideas, based on different assumptions, are developed. These proposed methods and their expected strengths and weaknesses are presented before stating their results in a dedicated section.

III.2.2.1 Fit using an ad-hoc function

The first idea that came up when considering the smoothing of a 2D-histogram is to fit the energy flow by an ad-hoc function. However it is too restrictive to assume that the two dimensional shape of the deposit is well known for each region of each sub-calorimeter. Indeed it is difficult a priori to trust the Monte Carlo for the description of the shape of the energy flow, which also varies with external constraints as the trigger configuration or the pile-up and thus will not be robust. Moreover, such calibration method suffers from biases, since some regions on the calorimeter surface are particularized. Finally such fits are quite difficult to control, the result depending on the choice of "good" initial conditions in the parameters phase space. The convergence of the fit could also depend on the level of the initial miscalibration. For all of these reasons this method is not implemented in the following.

III.2.2.2 Mean over neighbours

To avoid a too strong hypothesis on the 2D shape of the deposit in each detector part, the idea is to relax the a priori by only assuming that the shape is locally plane. Although it is not really the case (in particular in the region where the field plays a role and where there are effects from the upstream material), a locally plane assumption is the simplest assumption that could be made. The full information of a 3×3 cluster is used for the computation of the mean over the neighbouring cells. The corrected deposit is then defined as the mean over nine miscalibrated cells (the deposit in the eight neighbours and the deposit in the considered cell, see Eq. III.20). In order not to propagate any bias from one cell of the calorimeter over all the ECAL, it is important not to use already corrected energies. In a previous study [80] of this method, a weight for the central cell was introduced. The present study does not use such a parameter in a first attempt. We will see that a weight can be introduced for geometrical reasons.

$$e_{i,j}^{\text{corrected}} = \frac{1}{9} \sum_{k=-1}^{k=+1} \sum_{k'=-1}^{k'=+1} e_{i+k,j+k'}^{\text{miscalibrated}} \tag{III.20}$$

Assuming that the deposit is perfectly plane, the residual miscalibration is expected to be reduced by a factor 3 due to the use of nine estimates of the same energy deposit. Nevertheless, this method is limited for the cells in regions with strongly non bi-linear variations of the flow (typically in the region at $|y| < 300$ mm influenced by the magnetic field). Moreover, this method is expected to fail when considering cells at the edge of the areas. The mean for such cells is not calculated over nine but over eight or less cells (depending on their position with respect to the boundaries). The expected result is then meaningful for the cells typically not at the edge of the areas and not in the regions where the deposit varies too much.

Results with normalization As already mentioned in section III.2.1.3, the sensitivity loss is important in the case of a normalized deposit. One gives here one example of what happens in this case, for illustration. The expected RMS of 3.3 % for the distribution of the residuals is not reached due to the loss in sensitivity explained in section III.2.1.3. As expected the residuals are at the level of 7 % and are not Gaussian distributions (see Fig. III.12). This is why the normalization is not used in the following document, for a first calibration.

Results without normalization As explained in section III.2.1.3 the normalization is removed in order to partly recover the sensitivity to the applied miscalibration. Doing this, the main limitation comes from the cells located at the edge of the areas (especially the bluish cells in the middle at the boundary with the outer and the yellowish and reddish cells in the inner at the limit with the central dead zone on Fig. III.13). Other limitations come from the effect of the magnetic field. The cells at the edge of this region are reddish in the outer part as shown in Fig. III.13. The coefficients are Gaussian distributed in the inner and the middle where the

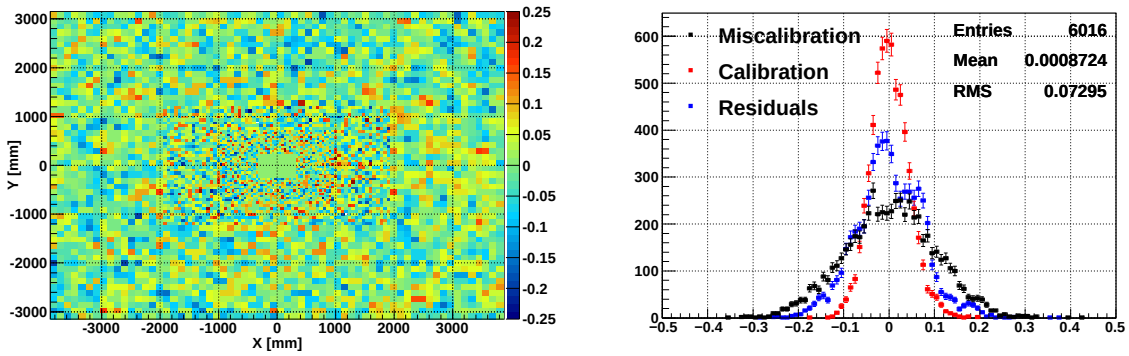

Figure III.12: Residuals of the calibration procedure when a normalization is applied to the energy flow, in the three areas of the ECAL after applying the mean over the neighbouring cells as a function of the cell position (left) and the corresponding cumulative distributions (right). There is no specifically particularized region due to the sensitivity loss (see section III.2.1.3) which is at the level of 7 % and non Gaussian.

residual miscalibration is nearly divided by a factor 2 compared to the initial one, see Fig. III.14. Part of outer ECAL diverges from the locally plane assumption. In this area the calibration of some cells is limited by the bar due to the magnetic field but the other cells, nearly 70 %, almost reach the intrinsic limit of the calibration procedure, since the deposit is more flat in this part of the calorimeter surface. This is not exactly the case due to the additional contribution of the sensitivity loss (2 %). The spread of the calibration residuals for these cells of the outer is 3.8 % which roughly equals to $\sqrt{3.3^2 + 2^2}$. Thus these cells behave as expected, only cells at $|y| < 300$ mm and at the borders are misbehaving.

An approximate bias of 1 % is introduced by the method (see Tab. III.3) and 70 % of the cells are calibrated at the level of 5 %. The result is clearly better than the one found with the normalized deposit since the sensitivity is recovered.

Area	Mean	RMS	< 20 %	< 10 %	< 5 %	< 4 %	< 3 %
Outer	0.7 %	4.6 %	99 %	95 %	74 %	64 %	52 %
Middle	1.1 %	5.1 %	99 %	94 %	65 %	54 %	43 %
Inner	1.6 %	5.4 %	99 %	91 %	64 %	54 %	42 %
Global	1.1 %	5.0 %	99 %	94 %	69 %	59 %	47 %

Table III.3: Calibration residuals in each area after mean over neighbours. The mean and RMS but also the percentage of cells calibrated at better than 20 %, 10 %, 5 %, 4 % and 3 % are given. Approximately 70 % of the cells are calibrated at better than 5 %.

Treatment of the boundaries In the previous method the boundaries are not well treated since the corresponding cells have less neighbours and then will be not as well calibrated. This is seen on the two dimensional view of the residuals. In principle such effect due to the edges of

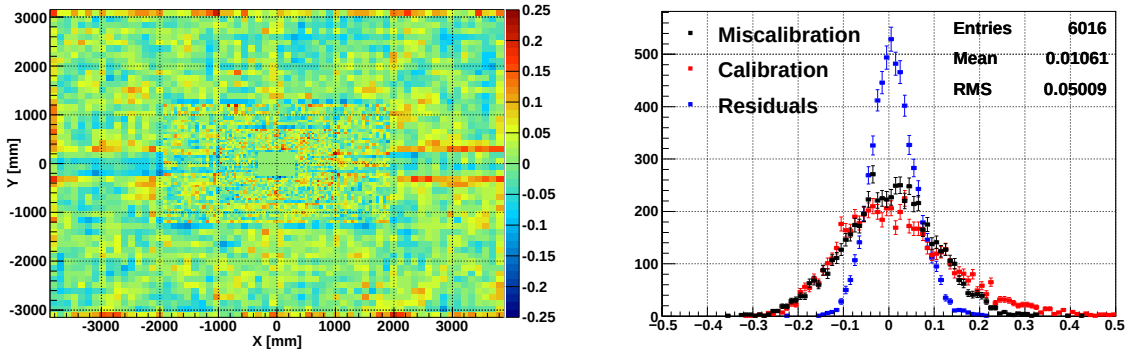

Figure III.13: Residuals of the calibration procedure without normalization of the energy flow, in the three areas of the ECAL after applying the mean over the neighbouring cells as a function of the cell position (left) and the corresponding cumulative distributions (right). The regions corresponding to energy thresholds in Fig. III.3 are clearly particularized as well as the boundaries of the areas.

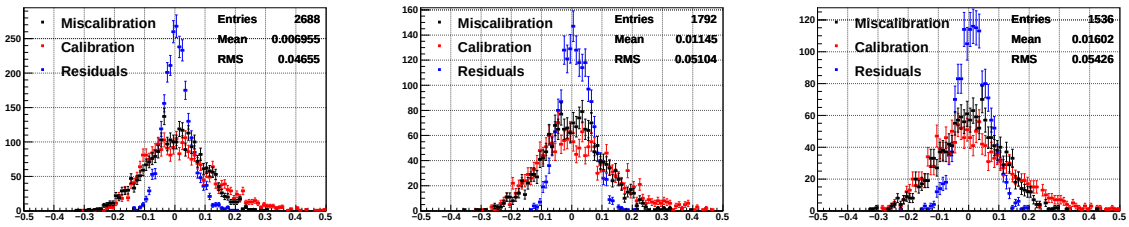

Figure III.14: Distribution of the miscalibration coefficients (black), the calibration coefficients (red) and the residual miscalibration (blue) in the outer (left), middle (centre) and inner (right) of the ECAL after applying the mean over the neighbouring cells. The result depends on the region where the procedure is applied. In particular the outer is better calibrated but less Gaussian due to larger variations of the deposit at $|y| < 300$ mm.

the areas could be reduced by extrapolating the deposit to fictive cells in the dead zones or in a different area. The result of the extrapolation is presented in this paragraph.

In order to extrapolate correctly the energy deposit in such cells, one has to ensure that the energy flow has the good sign for the gradient just before the edge. To ensure this, the corrected deposit using the mean over neighbours is used for all the cells except those at the edge of the area (this reduces the fluctuations and avoids an error on the sign of the slope). A linear extrapolation is made using all available cells, in particular the extrapolation is performed in the $\pm x$ and $\pm y$ directions. The extrapolation in the diagonal directions $\pm\frac{x+y}{\sqrt{2}}$ and $\pm\frac{x-y}{\sqrt{2}}$ diagonals was not found to improve significantly the extrapolation and is not used in the following. The extrapolation thus follows the Eq. III.21 in the case of an extrapolation in the $+x$ direction. If one also extrapolates in the diagonal, the value is the mean of 3 of such computations in most of the cases (one in x or y and two diagonal ones).

$$e_{i+1,j}^{\text{extrapolated}} = 2\left(e_{i-1,j}^{\text{corrected}} - e_{i-2,j}^{\text{corrected}}\right) + e_{i-1,j}^{\text{corrected}} \tag{III.21}$$

After that the extrapolated energies have all been calculated, the mean over the neighbours is computed using the extrapolation in fictive cells outside the area, the miscalibrated deposit in the cells at the edge, and the miscalibrated deposit in the cells just before the edge (to avoid taking twice into account the corrected deposits in the equipped region). The result is expected to correct the effect seen before and to avoid the under correction applied for the cells located at the edge of the areas. In practice the correction for the cells at the boundaries is effective but is a small effect on the global spread of the calibration coefficients since a few cells are concerned. The result is thus of the same order of magnitude than the previous result but always better as shown by Tab. III.4.

Area	Mean	RMS	< 20 %	< 10 %	< 5 %	< 4 %	< 3 %
Outer	0.5 %	4.3 %	100 %	97 %	76 %	66 %	54 %
Middle	1.1 %	5.0 %	99 %	95 %	65 %	54 %	42 %
Inner	1.6 %	5.3 %	100 %	92 %	65 %	55 %	42 %

Table III.4: Calibration residuals in each area after mean over neighbours with a special care at the borders. The mean and RMS but also the percentage of cells calibrated at better than 20 %, 10 %, 5 %, 4 % and 3 % are given. The result is slightly better than to the one without the extrapolation.

Choice of a kernel Until now the mean over the eight neighbouring cells and the one considered for the estimation of the calibration was done so that the nine contributions had the same weight (see Fig. III.15 left). Since the limitation is essentially due to the shape of the deposit for many of the cells in the inner and middle of the ECAL, weighting the contributions of the nine cells could be helpful. Attributing the same weight to all of the cells would be optimal for a flat energy flow. The first way of doing it is to give a null weight to the cells in the diagonal,

1	1	1
1	1	1
1	1	1

0	1	0
1	2	1
0	1	0

$\frac{1}{\sqrt{2}}$	1	$\frac{1}{\sqrt{2}}$
1	$2+\sqrt{2}$	1
$\frac{1}{\sqrt{2}}$	1	$\frac{1}{\sqrt{2}}$

Figure III.15: Different possible choices of kernels. On the left the *flat* kernel is the one used until now. The kernel given on the right is the one used in the following.

since they are farther, and to assume that the calibrated deposit should be the mean of three deposits in x and three others in y (see Fig. III.15 middle). Then it is also possible to keep the cells in the diagonals in order not to loose information, but giving to the mean with these cells a weight $1/\sqrt{2}$ (see Fig. III.15 right). These matrices of coefficients are called kernels in the following. Using the latter one, the result is significantly better (see Tab. III.5), especially in the middle and inner areas of ECAL.

Area	Mean	RMS	< 20 %	< 10 %	< 5 %	< 4 %	< 3 %
Outer	0.4 %	4.0 %	100 %	98 %	79 %	69 %	57 %
Middle	0.9 %	3.9 %	100 %	98 %	78 %	67 %	53 %
Inner	1.3 %	4.1 %	100 %	97 %	77 %	65 %	52 %

Table III.5: Calibration residuals in each area after mean over neighbours with a weighted kernel (see Fig. III.15 right). The mean and RMS but also the percentage of cells calibrated at better than 20 %, 10 %, 5 %, 4 % and 3 % are given.

Conclusion To conclude with this method based on a local assumption, the treatment of the borders does improve the calibration. A residual miscalibration of 5 % is obtained with a 1 % bias. About 40 % of the total amount of the cells, all located in the outer area, are nevertheless better calibrated, at the level of 3.8 % which corresponds to the best achievable result with this method, given the sensitivity loss and the expected reduction factor coming from the statistical power of the method. For the remaining 60 % of the cells, this limit is not reached due to borders effects or due to the non smooth deposit in the region where the magnetic field is playing an important role. All the cells in the inner and in the middle are concerned by such limitations. A different choice of the kernel is found to improve the result down to 4 % in the middle and in the inner with a smaller bias.

III.2.2.3 Symmetric mean

To avoid any assumption on the smoothness of the deposit, and in order to go further than the 4 % level obtained by the previous method another class of hypotheses is of interest. Considering

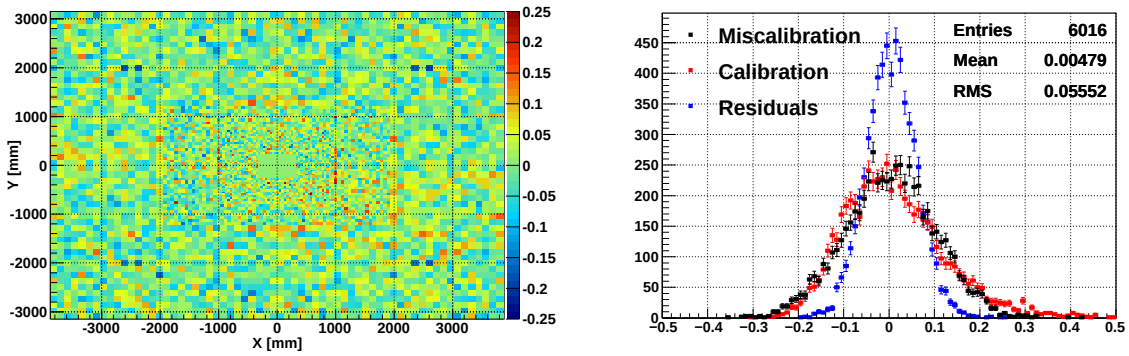

Figure III.16: Residuals of the calibration procedure without normalization of the energy flow, in the three areas of the ECAL after applying the mean over the four symmetric cells as a function of the cell position (left) and the corresponding cumulative distributions (right). No region is particularized which shows the interest and the robustness of the method against the shape of the energy flow.

the geometric symmetry of the detector, the energy flow can be considered as symmetric with respect to the beam axis z. In particular three assumptions are hidden behind this idea. First this means that there is no asymmetry (or at least negligible in first approximation) in the radiation length before the ECAL, and secondly, this assumes that the magnetic field is perfectly symmetric. Finally, this requires that the 3.6 mrad tilt in the (y, z) plane of the ECAL is negligible. The corrected energy is then calculated as in Eq. III.22, where N_x and N_y respectively denotes the number of cells in the x and y directions in the considered area of the sub-detector.

$$e_{i,j}^{\text{corrected}} = \frac{1}{4}\left(e_{i,j}^{\text{miscalibrated}} + e_{N_x-i,j}^{\text{miscalibrated}} + e_{i,N_y-j}^{\text{miscalibrated}} + e_{N_x-i,N_y-j}^{\text{miscalibrated}}\right) \tag{III.22}$$

Considering the fact that four different measurements are made for the same cell, the residual miscalibration is expected to be reduced by a factor 2 with respect to the starting point. This method is not as efficient as the previous one but nevertheless not limited by the boundaries or the non bi-linearity of the deposit. The limitation of this method is only due to the intrinsic asymmetry of the LHCb detector which is studied in section III.2.3.

Results The expected 5 % (see Fig. III.16 and Tab. III.6) of residual miscalibration is almost reached with less than 1 % of bias in all areas. Moreover any cell in the calorimeter is in principle as well calibrated as the others which is confirmed by the two dimensional view of the residuals. No visible structure due to the magnetic field or the boundaries exists which results in particularly Gaussian distributions for the residuals. This method is for this reason the more robust. This assertion is true only if the intrinsic limitations of the method are negligible, which is the case in first approximation on Monte Carlo studies.

Area	Mean	RMS	< 20 %	< 10 %	< 5 %	< 4 %	< 3 %
Outer	0.0 %	5.2 %	100 %	95 %	65 %	54 %	43 %
Middle	0.7 %	5.6 %	99 %	91 %	63 %	53 %	42 %
Inner	0.9 %	5.9 %	99 %	89 %	60 %	50 %	39 %
Global	0.5 %	5.5 %	99 %	92 %	63 %	53 %	43 %

Table III.6: Calibration residuals in each area applying the mean over the four symmetric cells without the hits normalization in the ECAL. The mean and RMS but also the percentage of cells calibrated at better than 20 %, 10 %, 5 %, 4 % and 3 % are given.

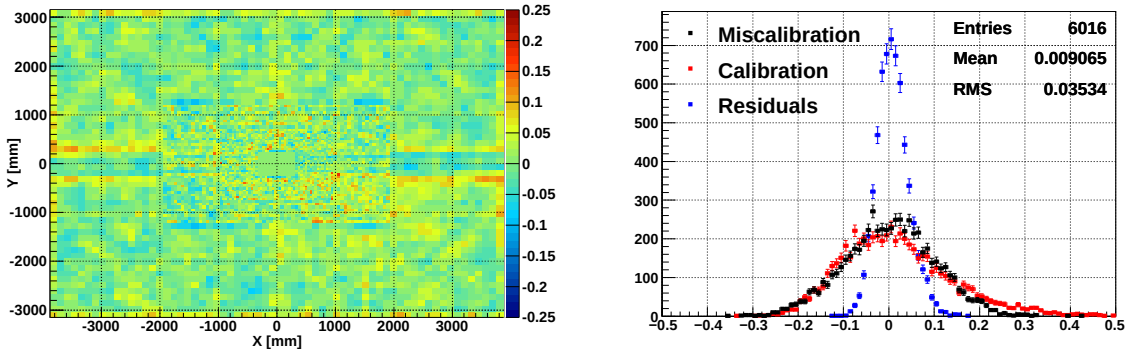

Figure III.17: Residuals of the calibration procedure without normalization of the energy flow, in the three areas of the ECAL after applying a combination of methods (see text), as a function of the cell position (left) and the corresponding cumulative distributions (right).

III.2.2.4 Summary of the results for the ECAL

As the *local* and the *symmetric* assumptions are independent (for the majority of the cells), the combination of these two methods should give a residual miscalibration of the order of 2 %. The order of application of the two methods does not have a sensitive effect. The results are summarized in Tab. III.7. The plot of the different distributions in the areas and for all the calorimeter is also given, see Fig. III.17 and Fig. III.18. It is noticeable that in the outer the expected level is reached for a significant part of the cells and the calibration is improved for the other cells regardless of the area. This is due to the too strong hypothesis on the local smoothness in the two most inner areas of the ECAL.

III.2.2.5 Results for the PS

As for the ECAL, the PS is quite well calibrated by the energy flow. The only difference between the two detectors is that we have chosen to work in terms of energies rather than in transverse energies. The same combined method as for the ECAL is used and the same precision is reached (see Figs. III.19-III.20 and Tab. III.8). This result is interesting to get a good inter-calibration

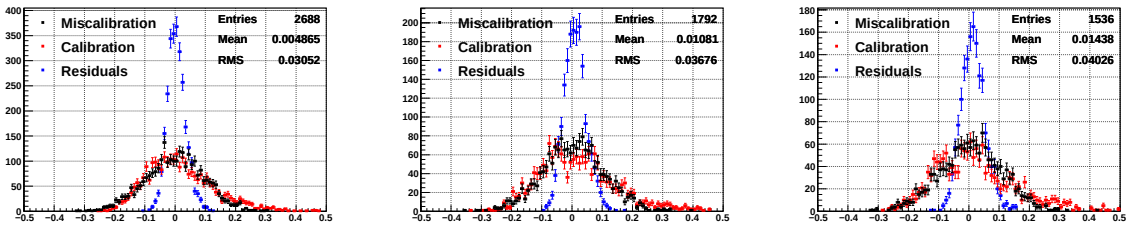

Figure III.18: Distribution of the miscalibration coefficients (black), the calibration coefficients (red) and the residual miscalibration (blue) in the outer (left), middle (centre) and inner (right) of the ECAL after applying a combination of methods (see text). The result depends on the region where the procedure is applied. In particular the outer is better calibrated.

Area	Mean	RMS	< 20 %	< 10 %	< 5 %	< 4 %	< 3 %
Outer	0.5 %	3.0 %	100 %	99 %	89 %	81 %	69 %
Middle	1.1 %	3.7 %	100 %	99 %	83 %	74 %	62 %
Inner	1.4 %	4.0 %	100 %	97 %	78 %	67 %	54 %
Global	0.9 %	3.5 %	100 %	98 %	84 %	75 %	62 %

Table III.7: Residuals in each area after applying a combination of methods (see text). The mean and RMS but also the percentage of cells calibrated at better than 20 %, 10 %, 5 %, 4 % and 3 % are given.

of the cells of the PS, the absolute scale of the visible energy being given by a MIP calibration. The non Gaussian tails are due to the region at $|y| < 300$ mm where the magnetic field plays an important role. For the other cells the calibration is at the 3 % level.

Area	Mean	RMS	< 20 %	< 10 %	< 5 %	< 4 %	< 3 %
Outer	0.8 %	3.6 %	99 %	98 %	85 %	78 %	66 %
Middle	1.3 %	3.3 %	100 %	99 %	83 %	74 %	62 %
Inner	0.8 %	3.1 %	100 %	99 %	87 %	78 %	66 %
Global	1.0 %	3.4 %	99 %	98 %	85 %	77 %	65 %

Table III.8: Calibration residuals in each area of the PS after applying a combination of methods (see text). The mean and RMS but also the percentage of cells calibrated at better than 20 %, 10 %, 5 %, 4 % and 3 % are given.

III.2.2.6 Results for the HCAL

Concerning the HCAL, the *symmetric* assumption of section III.2.2.3 is not useful for the reasons emphasized in section III.2.3. This problem could be solved by using two different data samples with opposite fields, or alternatively with a data sample with the magnetic field off. The HCAL is calibrated only using the smoothing method assuming a local bi-linearity of the deposit in the following. Nevertheless, the results (see figs. III.21 and III.22 and Tab. III.9) are worse than for

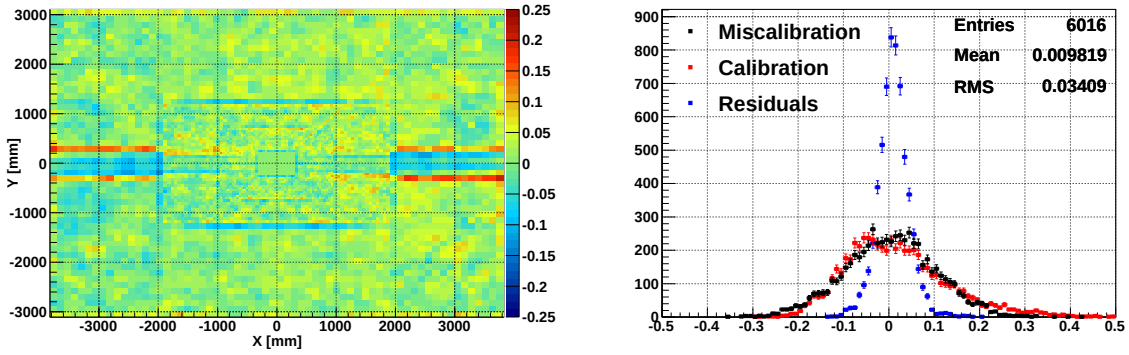

Figure III.19: Residuals of the calibration procedure without normalization of the energy flow, in the three areas of the PS after applying a combination of methods (see text), as a function of the cell position (left) and the corresponding cumulative distributions (right). The region influenced by the magnetic field at $|y| < 300$ mm is visible.

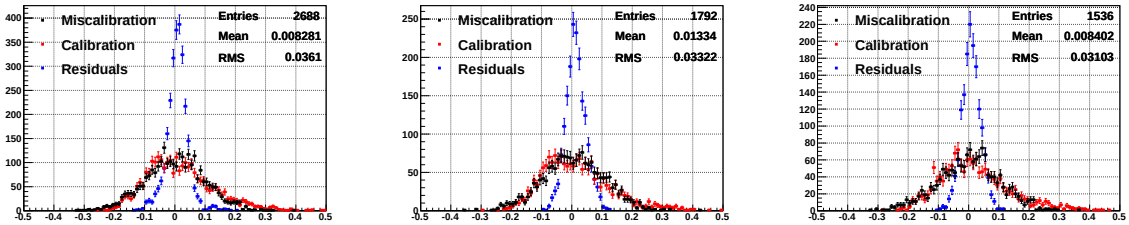

Figure III.20: Distribution of the miscalibration coefficients (black), the calibration coefficients (red) and the residual miscalibration (blue) in the outer (left), middle (centre) and inner (right) of the PS after applying a combination of methods (see text). The result depends on the region where the procedure is applied. In particular the outer is better calibrated.

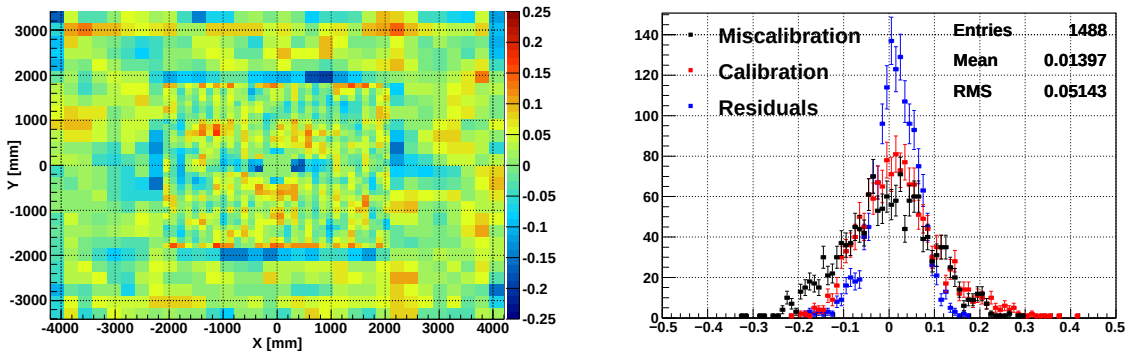

Figure III.21: Residuals of the calibration procedure without normalization of the energy flow, in the three areas of the HCAL after a local mean with a special kernel (see text) as a function of the cell position (left) and the corresponding cumulative distributions (right).

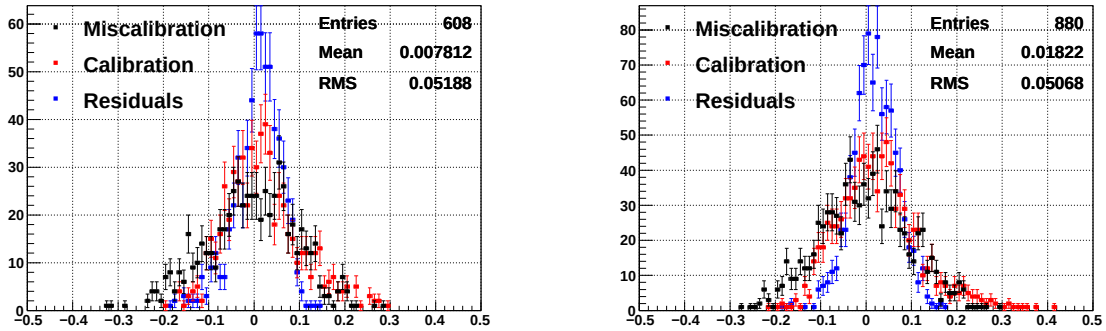

Figure III.22: Distribution of the miscalibration coefficients (black), the calibration coefficients (red) and the residual miscalibration (blue) in the outer (left) and inner (right) of the HCAL after applying a local mean with a special kernel (see text). The result depends on the region where the procedure is applied. In particular the outer is better calibrated but doubly Gaussian distributed due to more cells which do not follow the local smoothness assumption.

the two other sub-detectors of the calorimeter system due the fact that the cell sizes are bigger, and then the deposit is further away from the bi-linearity. Indeed, it results from the larger cell size that the shape of the energy flow is more peaky and thus that the smoothing of the energy flow by the mean over neighbours introduces a larger bias. To use the top-bottom symmetry in addition to the local mean could also help to improve the calibration residuals.

III.2.3 Asymmetries of the detector

In the procedure called *symmetric* (see section III.2.2.3), the detector is assumed to be symmetric in x and y and thus provides four measurements for the same energy deposit. In practice, this assumption is not exact since the LHCb detector has some inevitable asymmetries. This effect is

Area	Mean	RMS	< 20 %	< 10 %	< 5 %	< 4 %	< 3 %
Outer	0.8 %	5.2 %	100 %	95 %	67 %	57 %	43 %
Inner	1.8 %	5.1 %	100 %	93 %	65 %	56 %	45 %
Global	1.4 %	5.1 %	100 %	94 %	66 %	56 %	44 %

Table III.9: Calibration residuals in each area of the HCAL after applying a local mean with a special kernel (see text and Fig. III.15 right). The mean and RMS but also the percentage of cells calibrated at better than 20 %, 10 %, 5 %, 4 % and 3 % are given.

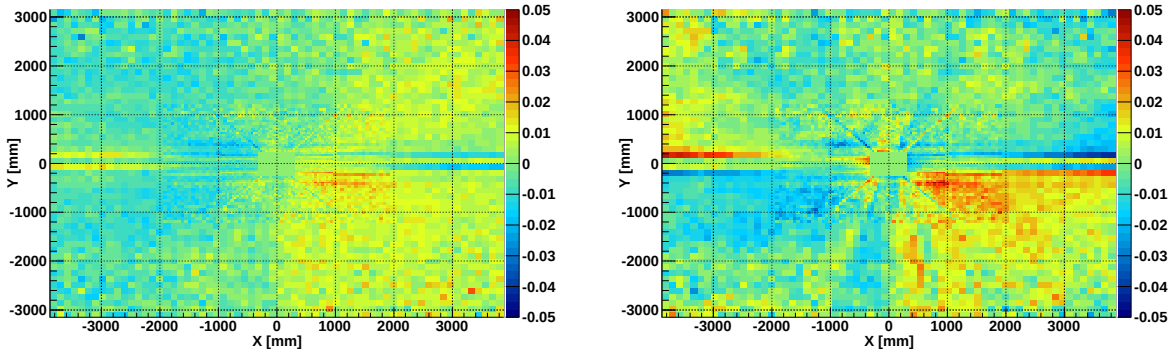

Figure III.23: Miscalibration introduced by the symmetric smoothing method evaluated on a *perfectly calibrated* transverse energy flow. The procedure is applied with the two cases (normalized on the left and not normalized on the right). Different types of asymmetries are visible.

estimated by applying this procedure on a perfectly calibrated (not miscalibrated) data sample. The result (see Fig. III.23) shows that the effect is of the order of 1 %, which intrinsically limits the calibration procedure. To reach a better calibration level, other methods like π^0 mass reconstruction should be used. It is interesting to observe that the asymmetry depends on the choice of the normalization. In the case of a normalization cell by cell, the dominant contribution is a *soft left right asymmetry* interpreted as a charge detection asymmetry. To that contribution a *local asymmetry* (interpreted as a material non uniformity before the calorimeters) is added in both cases but this second contribution is softer in the normalized case. The origin of these two asymmetries is inspected in this Section.

Charge detection asymmetry A soft global left-right asymmetry is clearly visible on the Fig. III.23. An explanation is that kaons of different electromagnetic charges interact in a different way with matter. It is expected that the K^- (the cross-section for K^-p is roughly equal to 20 m b at 10 GeV/c) interacts more than the K^+ (the cross-section for K^+p is approximately equal to 17 m b at 10 GeV/c), due to some forbidden baryonic resonances (like Λ which only exist with the -1 strangeness value) see Fig. III.25. As the ECAL is equivalent to 1.1 interaction length λ_{int}, the probability to have interactions in the ECAL for kaons is important and then

gives a non negligible contribution to the energy flow. The depletion of energy deposit on the left front view of the calorimeter (or right back view i.e. positive values of x since the z axis goes from the interaction point to the muon chambers through calorimeters and the y axis points upwards) is due to the fact that the K^+ are deviated to this side (this corresponds to the down polarity used in the Monte Carlo for this study). It follows that the deposit due to kaons is smaller on the right of the ECAL than on the left. As the $\sigma_{K^-p} \simeq 50$ m b and $\sigma_{K^+p} \simeq 15$ m b at 1 GeV/c, the effect is expected to be much larger in the outer zone (where kaons of smaller energy are located) than in the inner area. Let us assume that a kaon is emitted in the z direction of the calorimeter at the interaction point. If we assume that the magnetic field follows a step function in z and is equal to 1 T between $z_0 = 3$ m and $z_1 = 7$ m (these values are chosen in order to corresponds to the FWHM[7] of the field map [68] in z direction), the angle of flight of the kaon at z_1 is

$$\theta_d = -\frac{q}{|q|}\arcsin\left(\frac{z_1 - z_0}{R_c}\right) \quad \text{with } R_c = \frac{p}{|q|\,B}.$$

It results that the kaon hits the calorimeter at the position x_{kaon} given by

$$x_{\text{kaon}} = (z_{\text{ECAL}} - z_1)\tan(\theta_d) - \frac{q}{|q|}\left(R_c - \sqrt{R_c^2 - (z_1 - z_0)^2}\right) = 3.2 \text{ m}$$

for kaons of $p = 3$ GeV/c since it corresponds to a curvature radius of $R_c = \frac{p}{0.3B} = 10$ m. This effect is less visible in the other areas, due to the fact that the kaons that hit these areas are more energetic and then the difference between the two contributing cross-sections is smaller. The asymmetry is also seen in the PS and the HCAL (see Fig. III.24). The fact that the asymmetry is inverted in the HCAL is interpreted as follows. Since the ECAL represents $1.1\lambda_{int}$, 67 % of the charged hadronic particles interact in the ECAL, and 33 % in the HCAL. The ECAL asymmetry plot gives us that the energy deposit of positively charged particles is roughly 4 % smaller. Approximately 64 % of positively charged particles interact in the ECAL, and thus 36 % of the particles are interacting in the HCAL. This gives a 10 % asymmetry in the HCAL (in the number of interacting particles), and this asymmetry is reversed compared to the ECAL (the energy flow in the HCAL is bigger in the $x > 0$ region). This interpretation has been confirmed by looking at the truth information and identifying which kind of particle contribute to which energy deposit.

In order to convince ourselves, the combination of the same amount of data samples with two different polarities (or without magnetic field) should lead to a reduced contribution from such an effect. This also would permit a further calibration of the HCAL since the symmetric method could be applied in this case. This will be tested on real data.

[7] The FWHM is the Full Width at Half Maximum.

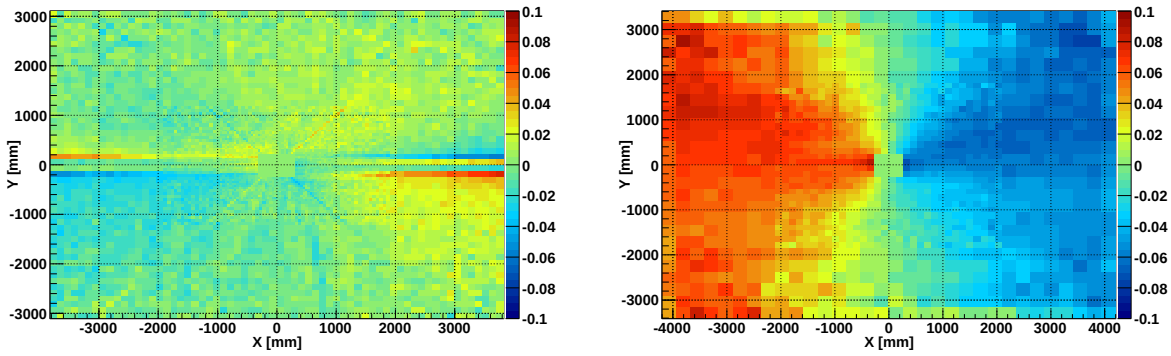

Figure III.24: Miscalibration introduced by the symmetric smoothing method evaluated on a *perfectly calibrated* transverse energy flow in the PS (left) and the HCAL (right). The not normalized procedure is applied. Different types of asymmetries are visible, the effect of the difference in cross-sections is striking in the HCAL. The PS is more sensitive to upstream material asymmetries.

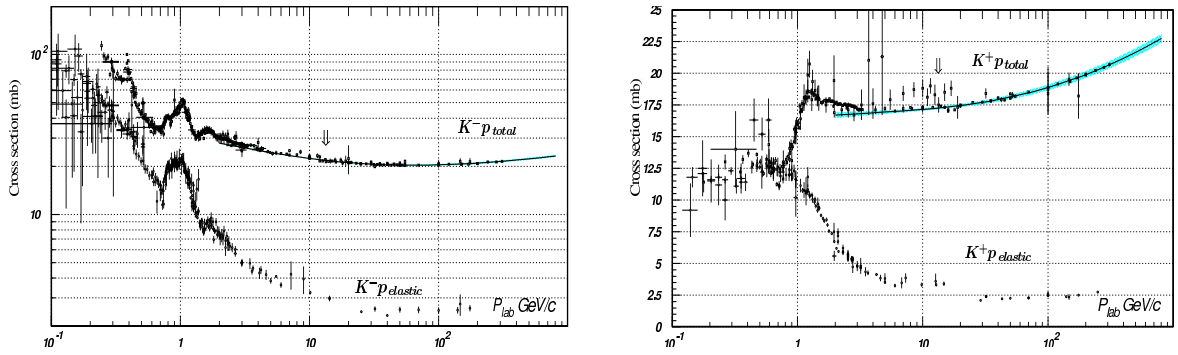

Figure III.25: Cross sections for the processes $K^- p$ (left) and $K^+ p$ (right) as a function of the momentum of the K (taken from [38]). The Λ peak is clearly absent in the $K^+ p$ cross section plot.

Material non uniformities before the calorimeters The energy flow is also asymmetric due to the number of radiation length seen by the particles before the ECAL. For example for neutral particles that fly from the interaction point to the calorimeter surface, the asymmetry (fully due to the geometry) seen is expressed in eq. III.23 where $\frac{X_{i,j}}{X_0}$ is the number of radiation lengths seen when the particle hits the center of the cell (i, j) and N_x, N_y are the number of cells in x and y directions respectively.

$$\left(\frac{X_{i,j}}{X_0}\right)_{\text{asymmetry}} = \frac{\frac{X_{i,j}}{X_0} - \frac{<X_{i,j}>}{X_0}}{\frac{X_{i,j}}{X_0}} \tag{III.23}$$

$$\frac{<X_{i,j}>}{X_0} = \frac{1}{4}\left(\frac{X_{i,j}}{X_0} + \frac{X_{N_x-i,j}}{X_0} + \frac{X_{i,Ny-j}}{X_0} + \frac{X_{N_x-i,N_y-j}}{X_0}\right) \tag{III.24}$$

The $\frac{X_{i,j}}{X_0}$ value is in fact calculated for the centre position of virtual cells of one half of the smallest cell size of the ECAL and then the mean over four, nine or thirty-six values (for inner, middle and outer respectively) is computed to estimate the contribution to one physical cell. This permits a smoothing of the asymmetries according to the geometry of the ECAL, and to have a better estimate of the contribution for each cell. The corresponding effect is of the order of 1 % as seen on Fig. III.26. An excess in radiation lengths corresponds to larger interactions before the ECAL and then smaller energy deposit in the calorimeters. Only local asymmetries are resulting from such an effect. Part of the asymmetries seen in the energy flow are present in this plot and were partly identified as cable routing in the trackers (see figures in [68]). But the relation between the radiation length plot and the energy deposit is not obvious since many particles contribute to the energy deposit, charged particles are deviated by the magnetic field, hadronic particles contribute and the radiation length is integrated in z over regions before and after the magnet. In particular the contribution is depending on the choice of the normalization. The normalization that provides the closest result to the map of the radiation length asymmetry is the *n*ot normalized energy flow. Normalizing by the number of hits in each cell reduces the contribution of the interactions before the ECAL, due to the fact that where the radiation lengths before ECAL are bigger, the number of hits in ECAL is also smaller.

Conclusion In practice the two contributions (charge detection asymmetry and material effects) are mixed and give the intrinsic energy flow asymmetry. Additional contributions to the asymmetry coming from magnetic field asymmetry, the tilt of the ECAL with respect to the beam axis could contribute or the crossing angle of the beams at the LHCb interaction point. A sample with the inverted field polarity could also help in disentangling these contributions.

III.2.4 Effect of the input of miscalibration

As the value of the miscalibration at the beginning of the experiment is not precisely known, different hypotheses have been studied in order to check the robustness of the method as a func-

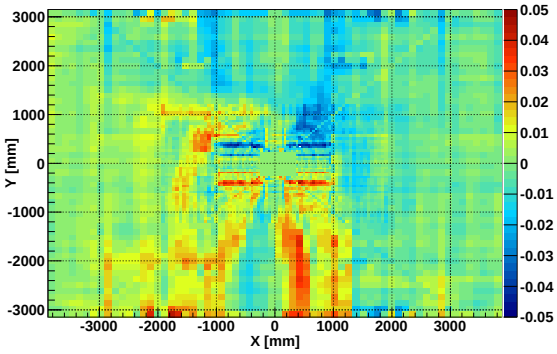

Figure III.26: Asymmetry in the number of radiation length before the ECAL.

tion of the initial miscalibration. The results are summarized in Tab. III.10. The combination of the mean over neighbours and the symmetric mean is used for the ECAL and the PS while only the method with the neighbours is used in the HCAL. Only the RMS and the mean value of the distribution noted respectively σ and μ are quoted. These numbers are only estimates due to the improper miscalibration procedure. The results for larger input miscalibration are systematically worse partly due to the more important sensitivity loss and partly due to the worse starting point.

Level of miscalibration	ECAL	HCAL	PS
10 %	$\mu = 0.9\ \%, \sigma = 3.5\ \%$	$\mu = 1.4\ \%, \sigma = 5.1\ \%$	$\mu = 1.2\ \%, \sigma = 4.1\ \%$
15 %	$\mu = 1.4\ \%, \sigma = 4.9\ \%$	$\mu = 1.4\ \%, \sigma = 6.6\ \%$	$\mu = 1.5\ \%, \sigma = 4.8\ \%$
20 %	$\mu = 2.0\ \%, \sigma = 6.5\ \%$	$\mu = 1.4\ \%, \sigma = 8.3\ \%$	$\mu = 1.9\ \%, \sigma = 5.8\ \%$

Table III.10: Mean and RMS of the calibration residuals as a function of the initial miscalibration for the ECAL, HCAL and PS.

III.2.4.1 Results without miscalibration

In order to estimate the intrinsic limitation of the calibration procedure, the calibration algorithm is applied to a non miscalibrated data sample. The result shows the limitation from the shape of the energy flow. It is found that a bias of 0.7 % is introduced in the ECAL and the PS while 1.6 % bias is observed in the HCAL. The HCAL is more problematic since the cells are much bigger and the energy flow is then intrinsically more subject to fluctuations from one cell to another. One concludes that the most important part of the bias comes from the sensitivity loss due to the threshold, in the ECAL and PS, while the bias is dominated by the shape in the HCAL. It also shows that without normalization of the energy flow it is not possible to obtain an inter-calibration better than 2.5 % (ECAL) or 3 % (HCAL and PS).

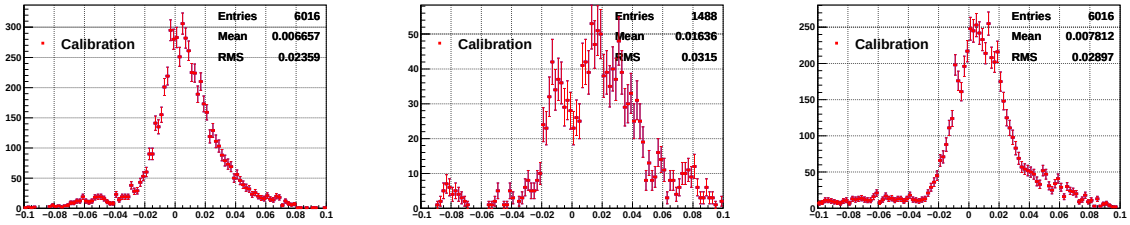

Figure III.27: Residuals in each subdetector (ECAL, HCAL and PRS from left to right) after applying the calibration procedure on a perfectly calibrated data sample.

III.2.5 Results with a more realistic miscalibration procedure

As mentioned in section III.2.1.1, the previous study was made with a not realistic miscalibration procedure. In this part, the miscalibration is applied at the level of the digitization. One not only shows the results for the procedures defined in Sections III.2.2.4, III.2.2.5 and III.2.2.6, but also the effect of the statistics, the threshold and the L0 trigger. In this exercise some cells (11 per sub-detector) were flagged as dead by the algorithm in order to estimate the robustness of the method to dead cells. These cells were correctly identified as dead (there was no hit above the threshold for these particular cells) and do not significantly bias the calibration of the neighbouring cells.

III.2.5.1 Effect of the available statistics

The amount of data needed for the energy flow calibration is expected to be small (less than ten millions of events). The results (mean and RMS) obtained for different statistics of (identically) miscalibrated data are given in Fig. III.28. With the proper miscalibration procedure the calibration residuals are similar than with the procedure used in the previous subsections. This study also shows that a plateau is reached with 1 million of minimum bias events, and with this amount of data the ECAL is calibrated at 4 %, the HCAL at 5.5 % and the PS at 4.5 %. Error bars are not given due to the fact that proper errors could only be given by generating different samples with different initial miscalibration sets, which is not manageable with the proper miscalibration procedure[8]. The statistical uncertainty on the first two moments of the residual miscalibration are always smaller than the size of the markers in the plot. Nevertheless a more important bias is introduced than for the previous study. This additional bias is identified to come from the threshold effect.

[8]This would require a time consuming event generation including a large fraction of the simulation chain from the detector response to reconstruction for an effect which would not impact significantly the final result.

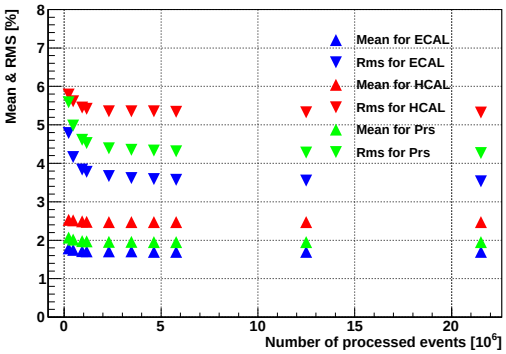

Figure III.28: Effect of the available statistics on the calibration residuals (mean and RMS).

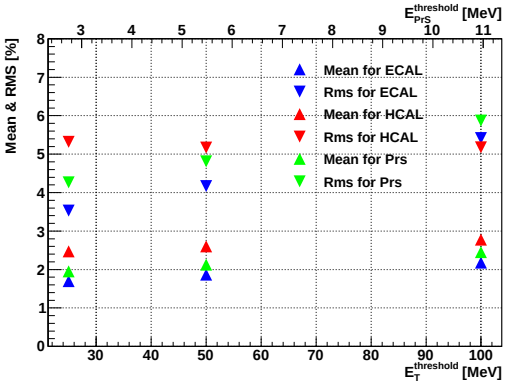

Figure III.29: Effect of the threshold on the calibration residuals (mean and RMS).

III.2.5.2 Effect of the threshold

In the case of the ECAL and PS the calibration residuals (see Fig. III.29), obtained with the full statistics, give a linear increase of the RMS and the mean with the threshold. The HCAL does not seem to be very sensitive to the threshold for the RMS of the residuals, reflecting the fact that the dominating limitation comes from the shape of the energy flow in the HCAL. The same remark concerning the error bars is also valid here. It is also observed that the bias is more important with the realistic procedure. Indeed, since the miscalibration is applied before the digitization, part of the information is definitively lost and the perfect calibration cannot be exactly recovered, introducing a larger bias than if the miscalibration was applied after the digitization.

III.2.5.3 Effect of the L0 trigger

As shown in section III.2.1.5 the L0 has a striking effect on the energy flow. Nevertheless the effect on the calibration coefficients extracted from the energy flow procedure has to be

estimated. Out of the full statistics (roughly 21 millions of events), 1.23 million survives the L0 trigger. The results obtained with these events for the three sub-detectors and for the "standard" calibration procedure are shown in Tab. III.11. These are of the same order of magnitude than for one million events without any requirement. This is due to the fact that the energy flow calibrates the low energies of the spectrum (typically 75 MeV), which is not very sensitive to the L0 trigger (roughly 1 GeV in ECAL but dominated by the HCAL requirement) and that the calibration is only sensitive to the small relative local modifications of the energy flow. This will also be checked on real data.

L0 prescription	ECAL	HCAL	PS
Yes	$\mu = 1.7\ \%, \sigma = 3.6\ \%$	$\mu = 2.3\ \%, \sigma = 5.2\ \%$	$\mu = 1.9\ \%, \sigma = 4.2\ \%$
No	$\mu = 1.7\ \%, \sigma = 3.8\ \%$	$\mu = 2.5\ \%, \sigma = 5.4\ \%$	$\mu = 1.9\ \%, \sigma = 4.5\ \%$

Table III.11: Calibration residuals (mean and RMS) for different assumptions concerning the L0 for the ECAL, HCAL and PS.

III.2.6 Cross check with π^0

The effect of the energy flow calibration on the width of the π^0 mass has been studied and allows to quantitatively show the impact of the method on physics. One reconstructs the π^0 in a calorimeter standalone procedure (especially without using the tracking information, this allows a very fast and private reconstruction with different calibration tags). The full reconstruction would only induce a better $^{S}/_{B}$ ratio. In order to have a reasonable $^{S}/_{B}$ one requires that the photons have $E_T > 500$ MeV, $E_{PS} > 10$ MeV and no hit in the 3×3 cluster of the SPD in front of the ECAL cluster. The PS energy is also estimated using the 3×3 cluster in front of the ECAL cluster. With these requirements, the π^0 mass distributions is obtained in each area (the two photons are reconstructed in the same area) for the properly miscalibrated data sample containing 10 millions of events. The black histograms represent the distribution of the mass containing 10 % miscalibration while the red represents the same after recalibration with the energy flow procedure. Since the energy flow procedure introduces a bias of the order of 2 %, the number of photons passing the selection is greater after recalibration by 2 %. In order to easily compare the distributions, the recalibrated distributions are rescaled by the ratio of the number of π^0 candidates (before and after calibration). Doing this, a fit of each distribution is performed with a function (given in Eq. III.25) which is a sum of a Gaussian and a polynomial. In order to decorrelate the polynomial coefficients, a Legendre expansion up to the third order is used (the coefficient of the fourth order was not found to be significantly different from zero and then fixed to zero). We also normalize by 250 MeV/c^2 the mass in the Legendre polynomial in order to have dimensionless coefficients of the same order of magnitude, allowing a direct

comparison of each term in the polynomial.

$$\begin{aligned} f\left(m_{\gamma\gamma}\right) &= \mathcal{G}\left(m_{\gamma\gamma}\right) + \mathcal{L}\left(m_{\gamma\gamma}\right), \\ \text{with} \quad & \mathcal{G}\left(m_{\gamma\gamma}\right) = A\exp\left(\frac{\left(m_{\gamma\gamma}-\mu\right)^2}{2\sigma^2}\right), \\ \text{and} \quad & \mathcal{L}\left(m_{\gamma\gamma}\right) = c_0 + c_1\frac{m_{\gamma\gamma}}{m_0} + \frac{c_2}{2}\left(3\frac{m_{\gamma\gamma}^2}{m_0^2}-1\right) + \frac{c_3}{2}\left(5\frac{m_{\gamma\gamma}^3}{m_0^3}-3\frac{m_{\gamma\gamma}}{m_0}\right), \\ \text{where} \quad & m_0 = 250\ \text{MeV}/c^2 \end{aligned} \tag{III.25}$$

The fit results are given on Fig. III.30. The total PDF of the fit is shown in plain lines while the background is shown is dashed lines. The background PDFs are always very well superimposed showing that the description of the background is robust. It is also observed that the signal width is reduced thanks to the calibration coefficients provided by the energy flow method. The signal peak seems to be distorted at 165 MeV/c^2 for the three curves (but it is more visible on the yellow and red curves, thanks to the better resolution). This feature was already visible in the re-optimized TDR [75] and is responsible for the bad goodness of fit, despite the obtained fit parameters for the Gaussian seem reasonable. The numerical results are given in table III.12.

The results show that the energy flow procedure is really able to reduce the width of the π^0 mass by 30 % from 10 % miscalibration without introducing a sensible bias on the mass reconstruction. With real data, the ECAL could be well calibrated with the energy flow procedure followed by an estimation area by area of the energy scale of the ECAL. The calibration of the fraction β of energy in the PS could also be calibrated by a method consisting in varying the β factor on a specific range and then minimizing the width of the π^0 mass peak [81].

III.2.6.1 Improved fit function

It is possible to get rid of the low p-value induced by the tail at high masses (> 165 MeV/c^2) and obtain a more reasonable goodness of fit, when modifying the Gaussian distribution by adding a tail. This tail is probably due to the pile-up in the clusters used to build the photon pairs. Hence the fit function becomes Eq. III.26. The evolution of this function with respect to the tail parameter is given in Fig. III.31.

$$\begin{aligned} f\left(m_{\gamma\gamma}\right) &= \mathcal{N}\left(m_{\gamma\gamma}\right) + \mathcal{L}\left(m_{\gamma\gamma}\right) \\ \text{with} \quad & \mathcal{N}\left(m_{\gamma\gamma}\right) = A\exp\left\{-\frac{1}{2}\left(\left(\frac{\ln t}{\text{tail}}\right)^2 + \text{tail}^2\right)\right\} \\ \text{where} \quad & t = 1 + \text{tail}\frac{\sinh\left(\text{tail}\sqrt{\ln 4}\right)}{\text{tail}\sqrt{\ln 4}}\frac{m_{\gamma\gamma}-\mu}{\sigma} \end{aligned} \tag{III.26}$$

The fitted resolution is consistent with the usual Gaussian result, as shown in Tab. III.13 and in Fig. III.32, giving confidence in the Gaussian description. The mean value is found to be lower by 1 % since the high mass region is now well fitted.

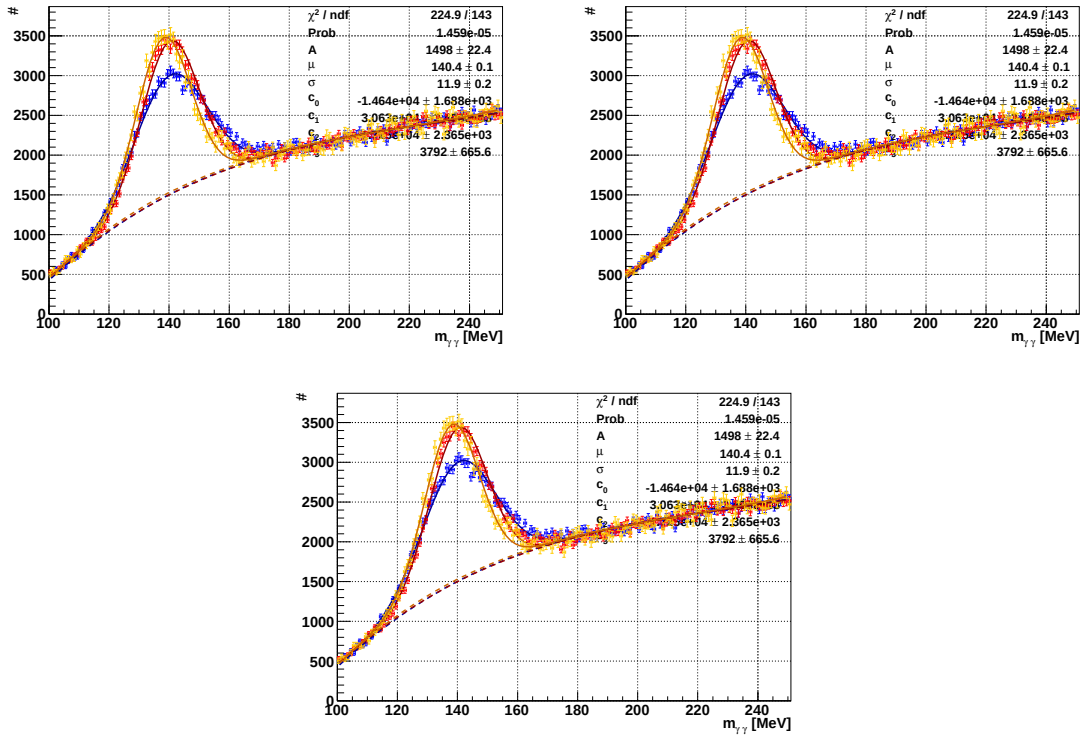

Figure III.30: Fit of the π^0 mass distribution in the three areas of the ECAL (outer on the top left, middle on the top right and inner on the bottom of the figure). The yellow/blue/red histograms represents the data without introduced miscalibration, with 10 % miscalibration and the same after recalibration with the energy flow respectively. The Fit function is also plotted in plain lines and the dashed lines represents the background contribution.

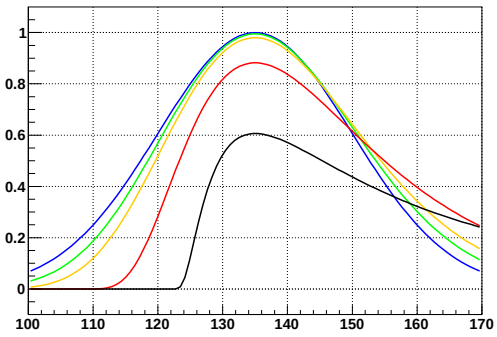

Figure III.31: Evolution of the Novosibirsk distribution as a function of the tail parameter. The usual Gaussian case is given in blue, while the Novosibirsk distribution is respectively given in green, orange, red and black for $\text{tail} = \{0.1, 0.2, 0.5, 1\}$.

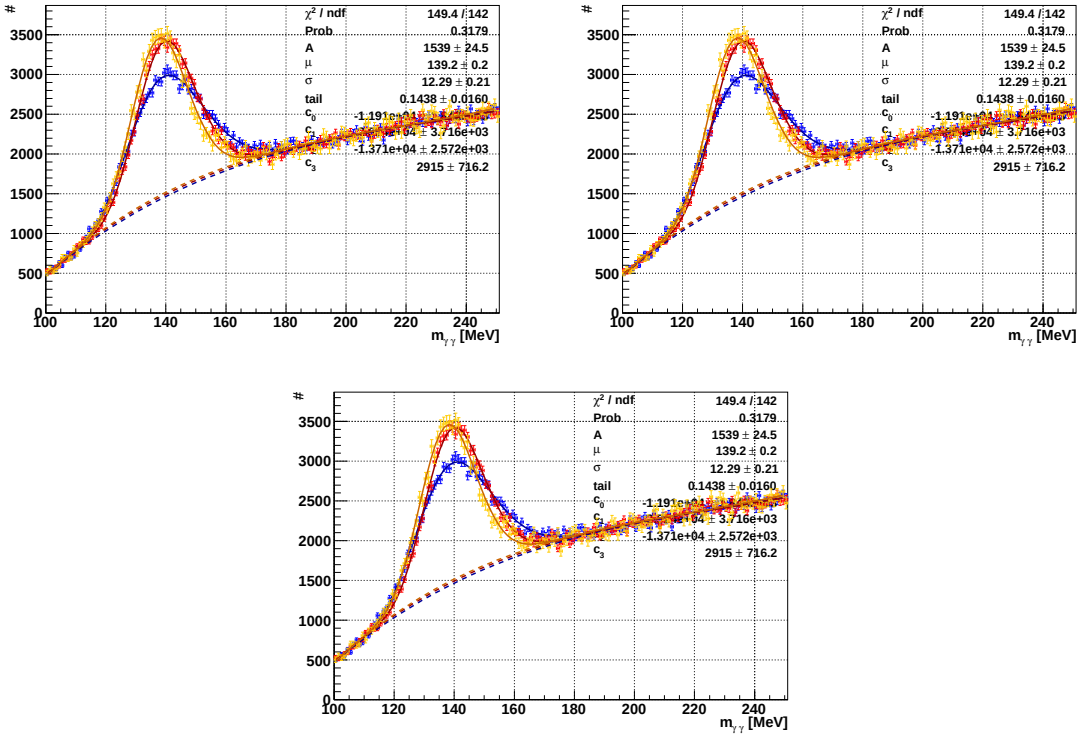

Figure III.32: Fit of the π^0 mass distribution in the three areas of the ECAL (outer to inner from left to right) with a modified Gaussian in order to parametrize the tail and a polynomial PDF for the background. The yellow/blue/red histograms represents the data without introduced miscalibration, with $10\ \%$ miscalibration and the same after recalibration with the energy flow respectively. The fit function is also plotted in plain lines and the dashed lines represents the background contribution.

OUTER	Before recalibration	After recalibration	Without miscalibration
p-value	$1.4 \cdot 10^{-5}$	0.15 %	13 %
A	1497 ± 22	1930 ± 19	1982 ± 29
μ [MeV/c^2]	140.41 ± 0.12	140.26 ± 0.08	138.12 ± 0.12
σ [MeV/c^2]	11.90 ± 0.19	9.62 ± 0.11	9.10 ± 0.16
c_0	$(-1.46 \pm 0.16) \cdot 10^4$	$(-1.34 \pm 0.13) \cdot 10^4$	$(-1.62 \pm 0.19) \cdot 10^4$
c_1	$(3.06 \pm 0.34) \cdot 10^4$	$(2.82 \pm 0.27) \cdot 10^4$	$(3.38 \pm 0.39) \cdot 10^4$
c_2	$(-1.72 \pm 0.23) \cdot 10^4$	$(-1.57 \pm 0.19) \cdot 10^4$	$(-1.95 \pm 0.27) \cdot 10^4$
c_3	$(0.37 \pm 0.06) \cdot 10^4$	$(0.33 \pm 0.05) \cdot 10^4$	$(0.45 \pm 0.07) \cdot 10^4$
MIDDLE	Before recalibration	After recalibration	Without miscalibration
p-value	0.14 %	$2.2 \cdot 10^{-7}$	$9.9 \cdot 10^{-6}$
A	813 ± 13	1084 ± 17	1141 ± 21
μ [MeV/c^2]	140.88 ± 0.14	140.75 ± 0.09	138.19 ± 0.14
σ [MeV/c^2]	10.02 ± 0.20	7.91 ± 0.11	7.43 ± 0.16
c_0	$(-0.91 \pm 0.09) \cdot 10^4$	$(-0.78 \pm 0.07) \cdot 10^4$	$(-0.90 \pm 0.11) \cdot 10^4$
c_1	$(1.88 \pm 0.18) \cdot 10^4$	$(1.63 \pm 0.15) \cdot 10^4$	$(1.88 \pm 0.22) \cdot 10^4$
c_2	$(-1.13 \pm 0.13) \cdot 10^4$	$(-0.96 \pm 0.10) \cdot 10^4$	$(-1.14 \pm 0.15) \cdot 10^4$
c_3	$(0.26 \pm 0.03) \cdot 10^4$	$(0.21 \pm 0.03) \cdot 10^4$	$(0.26 \pm 0.04) \cdot 10^4$
INNER	Before recalibration	After recalibration	Without miscalibration
p-value	0.53 %	$1.4 \cdot 10^{-5}$	5.3 %
A	327 ± 7	412 ± 7	465 ± 13
μ [MeV/c^2]	140.06 ± 0.19	139.89 ± 0.14	137.84 ± 0.18
σ [MeV/c^2]	9.16 ± 0.24	7.60 ± 0.16	6.48 ± 0.20
c_0	$(0.88 \pm 0.44) \cdot 10^3$	$(1.58 \pm 0.37) \cdot 10^3$	$(1.10 \pm 0.55) \cdot 10^3$
c_1	$(-1.66 \pm 0.90) \cdot 10^3$	$(-3.06 \pm 0.76) \cdot 10^3$	$(-2.10 \pm 0.11) \cdot 10^3$
c_2	$(2.02 \pm 0.63) \cdot 10^3$	$(2.99 \pm 0.53) \cdot 10^3$	$(2.34 \pm 0.78) \cdot 10^3$
c_3	$(-0.71 \pm 0.18) \cdot 10^3$	$(-0.99 \pm 0.15) \cdot 10^3$	$(-0.81 \pm 0.22) \cdot 10^3$

Table III.12: Results for the fit with a Gaussian and a polynomial, defined in Eq. III.25.

III.2.7 Conclusion on the Monte Carlo studies

The energy flow procedure suffers from an intrinsic loss of sensitivity, since it calibrates the low energies of the spectrum (around 30 ADC counts) compared to the cut (at 10 ADC counts) applied in order to remove the low energy background due to the noise of the electronic chain. It was shown that if the normalisation by the number of hits in each cell provides a very flat energy flow and is potentially of great interest for the calibration procedure, one cannot reach better than a 5 % miscalibration (combining all methods and starting from 10 % initial miscalibration). The choice of the not normalized energy flow is made to remove the effect of the sensitivity at the level of one to two per cent.

The results for different assumptions (local bi-linearity and left/right and up/down symmetries of the detector) are then given as well as the results for the combination of all the methods. The limitations (at the level of a few percent, comes from the shape of the energy flow

in the HCAL) of the symmetric method essentially come from intrinsic asymmetries, especially due to the charge detection asymmetry (which could be reduced to a negligible contribution using data samples with two different magnetic field polarities or data with field off) and to the material before the calorimeters. The combination of the sensitivity limitation and of the intrinsic limitation of the calibration procedure yields to calibration residuals of 3 % to 4 % in the ECAL and PS and of 5 % to 6 % in the HCAL with only one million events, starting from 10 % miscalibration. A bias of the order of 1 % to 2 % is found, which should be corrected by the absolute energy calibration and other complementary methods that use a physical input, like π^0 mass reconstruction. This bias is due to the shape of the energy flow but also partly due to the threshold effect that results in a sensitivity loss. Nevertheless, the method is able to give a good inter-calibration at the software level for the three sub-detectors and reduces by 30 % the width of the π^0 mass peaks in the three regions of the ECAL from a 10 % miscalibration. It was also checked that the two miscalibration procedures used in the study are consistent when looking at the results. The code was implemented as part of the standard LHCb software.

Different additional sources of limitations have been studied. In particular the effect of the charge detection asymmetry and the upstream material has been checked. it is found that the dominant systematics for the ECAL as well as for the PS comes from the shape of the deposit and the sensitivity loss. Concerning the HCAL, the main systematic uncertainty comes from the shape of the energy flow.

OUTER	Before recalibration	After recalibration	Without miscalibration
p-value	31 %	45 %	37 %
A	1539 ± 24	1940 ± 19	1988 ± 29
$\mu \left[\text{MeV}/c^2 \right]$	139.19 ± 0.17	139.50 ± 0.13	137.57 ± 0.18
$\sigma \left[\text{MeV}/c^2 \right]$	12.28 ± 0.21	9.71 ± 0.12	9.23 ± 0.17
tail	0.14 ± 0.01	0.09 ± 0.01	0.07 ± 0.02
c_0	$(-1.19 \pm 0.18) \cdot 10^4$	$(-1.31 \pm 0.13) \cdot 10^4$	$(-1.52 \pm 0.20) \cdot 10^4$
c_1	$(2.52 \pm 0.37) \cdot 10^4$	$(2.77 \pm 0.27) \cdot 10^4$	$(3.19 \pm 0.41) \cdot 10^4$
c_2	$(-1.37 \pm 0.25) \cdot 10^4$	$(-1.54 \pm 0.19) \cdot 10^4$	$(-1.83 \pm 0.28) \cdot 10^4$
c_3	$(0.29 \pm 0.07) \cdot 10^4$	$(0.33 \pm 0.05) \cdot 10^4$	$(0.42 \pm 0.08) \cdot 10^4$
MIDDLE	Before recalibration	After recalibration	Without miscalibration
p-value	74 %	14 %	0.4 %
A	833 ± 13	1100 ± 14	1156 ± 22
$\mu \left[\text{MeV}/c^2 \right]$	139.55 ± 0.14	139.65 ± 0.15	137.18 ± 0.21
$\sigma \left[\text{MeV}/c^2 \right]$	10.47 ± 0.21	8.13 ± 0.12	7.65 ± 0.17
tail	0.17 ± 0.02	0.16 ± 0.01	0.16 ± 0.02
c_0	$(-0.79 \pm 0.09) \cdot 10^4$	$(-0.72 \pm 0.07) \cdot 10^4$	$(-0.82 \pm 0.11) \cdot 10^4$
c_1	$(1.64 \pm 0.19) \cdot 10^4$	$(1.52 \pm 0.15) \cdot 10^4$	$(1.70 \pm 0.22) \cdot 10^4$
c_2	$(-0.98 \pm 0.13) \cdot 10^4$	$(-0.89 \pm 0.10) \cdot 10^4$	$(-1.02 \pm 0.15) \cdot 10^4$
c_3	$(0.22 \pm 0.03) \cdot 10^4$	$(0.20 \pm 0.03) \cdot 10^4$	$(0.24 \pm 0.04) \cdot 10^4$
INNER	Before recalibration	After recalibration	Without miscalibration
p-value	75 %	34 %	55 %
A	331 ± 7	417 ± 8	465 ± 13
$\mu \left[\text{MeV}/c^2 \right]$	138.41 ± 0.29	138.37 ± 0.22	136.64 ± 0.28
$\sigma \left[\text{MeV}/c^2 \right]$	9.89 ± 0.27	8.05 ± 0.17	7.06 ± 0.24
tail	0.23 ± 0.02	0.23 ± 0.02	0.22 ± 0.04
c_0	$(0.86 \pm 0.41) \cdot 10^3$	$(1.49 \pm 0.36) \cdot 10^3$	$(1.37 \pm 0.54) \cdot 10^3$
c_1	$(-1.61 \pm 0.84) \cdot 10^3$	$(-2.87 \pm 0.73) \cdot 10^3$	$(-2.62 \pm 0.11) \cdot 10^3$
c_2	$(1.93 \pm 0.59) \cdot 10^3$	$(2.82 \pm 0.51) \cdot 10^3$	$(2.67 \pm 0.77) \cdot 10^3$
c_3	$(-0.66 \pm 0.16) \cdot 10^3$	$(-0.91 \pm 0.14) \cdot 10^3$	$(-0.88 \pm 0.22) \cdot 10^3$

Table III.13: Results for the fit with a modified Gaussian in order to parametrize the tail and a polynomial for the background. Results similar to the previous fit are found.

III.3 Results on real data

The first collisions have been recorded with the LHCb detector during the short 2009 run. At that time some 400 thousand events were used to test the energy flow procedure on real data at $\sqrt{s} = 900$ GeV. These first results were obtained before the restart of the LHC for new collisions in 2010. As soon as first data were available in 2010, the calibration was applied on the 2010 real data, with a reasonable consistency with the results obtained on 2009 data. In 2010 the energy flow procedure was also used to improve the understanding of the calibration of the calorimeters, using different data samples and calibration samples. Finally the method was used to improve the situation with the first 2011 data.

III.3.1 First exercise with 2009 data

From Monte Carlo studies, typical residual calibration using the energy flow procedure is expected to be at the level of 5 %, combining different types of smoothing methods, already with 250 thousand events. In 2009, a first calibration exercise, pursued in early 2010, was performed.

III.3.1.1 Conditions

The trigger was required not to be in a Time Alignment Event (TAE) mode (see chapter II) and the VELO was in stable and closed position[9]. It was also required that the event was taken in time with a beam-beam interaction that fired the CALO triggers[10].

III.3.1.2 Protections

Some channels have an odd behaviour and need to be vetoed in the energy flow procedure. Indeed it was observed that some cells do not provide any (or a tiny) signal above the threshold of 25 MeV, due to a connection failure or a dead channel. These are easily found and vetoed in the analysis. Part of these also need to be vetoed in the calibration, because they correspond to significantly high transverse energy deposits. They could be either badly calibrated by the LED procedure or present some instabilities. Such cases are not investigated at this stage and are simply vetoed by requiring that the measured mean energy in each cell is not greater or smaller by 50 % than the average mean energy in the neighbouring or in the symmetric cells. Even if not ideal, this allows to remove problematic channels for a first energy flow analysis. Most of these problematic cells are also detected to misbehave with the LED system, because of instabilities, narrow pedestal distribution or dead channels.

[9] The VELO was not closed at its nominal position in 2009 but in the best case at 15 *mm* closing distance.

[10] CALO triggers in 2009 were part of the minimum bias triggers, looking for a rather low transverse energy deposit of 240 MeV.

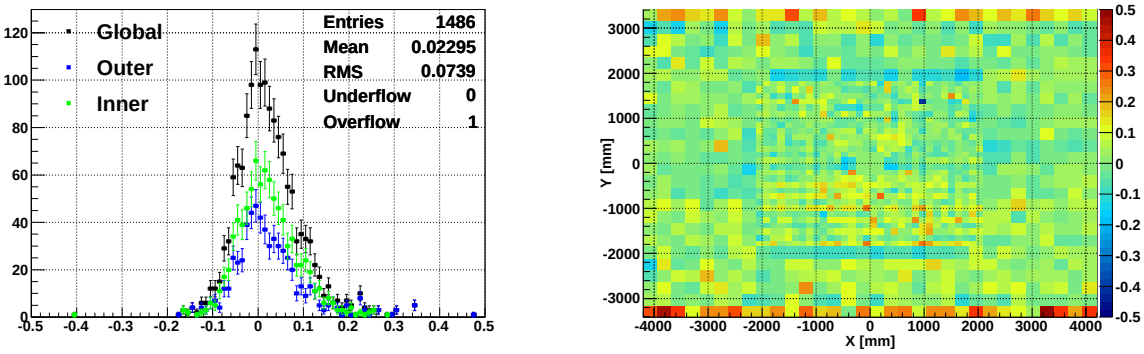

Figure III.33: Calibration coefficients (cumulative distribution on the left and 2D map on the right) extracted from the energy flow procedure using the method combining top-bottom symmetry and local smoothing in the HCAL with the 2009 data. The spread of the coefficients is found to be larger than expected, due to lack of statistics with the rather low multiplicity events used.

III.3.1.3 HCAL calibration

A first test was performed for the HCAL with the energy flow. It is in fact more a cross-check than a calibration since this was already performed at a typical 2–3 % level by ^{137}Cs sources. It is also noticeable that the energy flow procedure is sensitive to the asymmetries in the upstream material but also the different cross section for hadrons of two different charges, due to the magnetic field, as described in section III.2.3. The energy flow is found to be already very smooth and the spread of the calibration constants is found to be of 7.4 % using the mean over the neighbours and the up-down symmetry (see Fig. III.33).

III.3.1.4 PS calibration

The PS was first calibrated in 2009 using cosmic data by measuring the position of the MIP for charged tracks. The precision of the resulting calibration depends on the area considered in the calorimeter, since the statistics is different, due to the different cell sizes. This explains that the spread of calibration constants from the energy flow is much better in the outer region than the inner as shown in Tab. III.14. During this data taking period another calibration with the MIP was performed. The correlation between these two results is found to be better in the inner than in the outer due to the worse initial calibration in the inner (the 2009 statistics is less limiting in the inner), as shown in Fig. III.34.

III.3.1.5 ECAL calibration

As expected the situation for the ECAL is not as good as for the HCAL, since it is not expected that the LED system is able to deliver an inter-calibration at the level of a few percent. Depending on the considered region the spread of the calibration constant varies from 11 % to

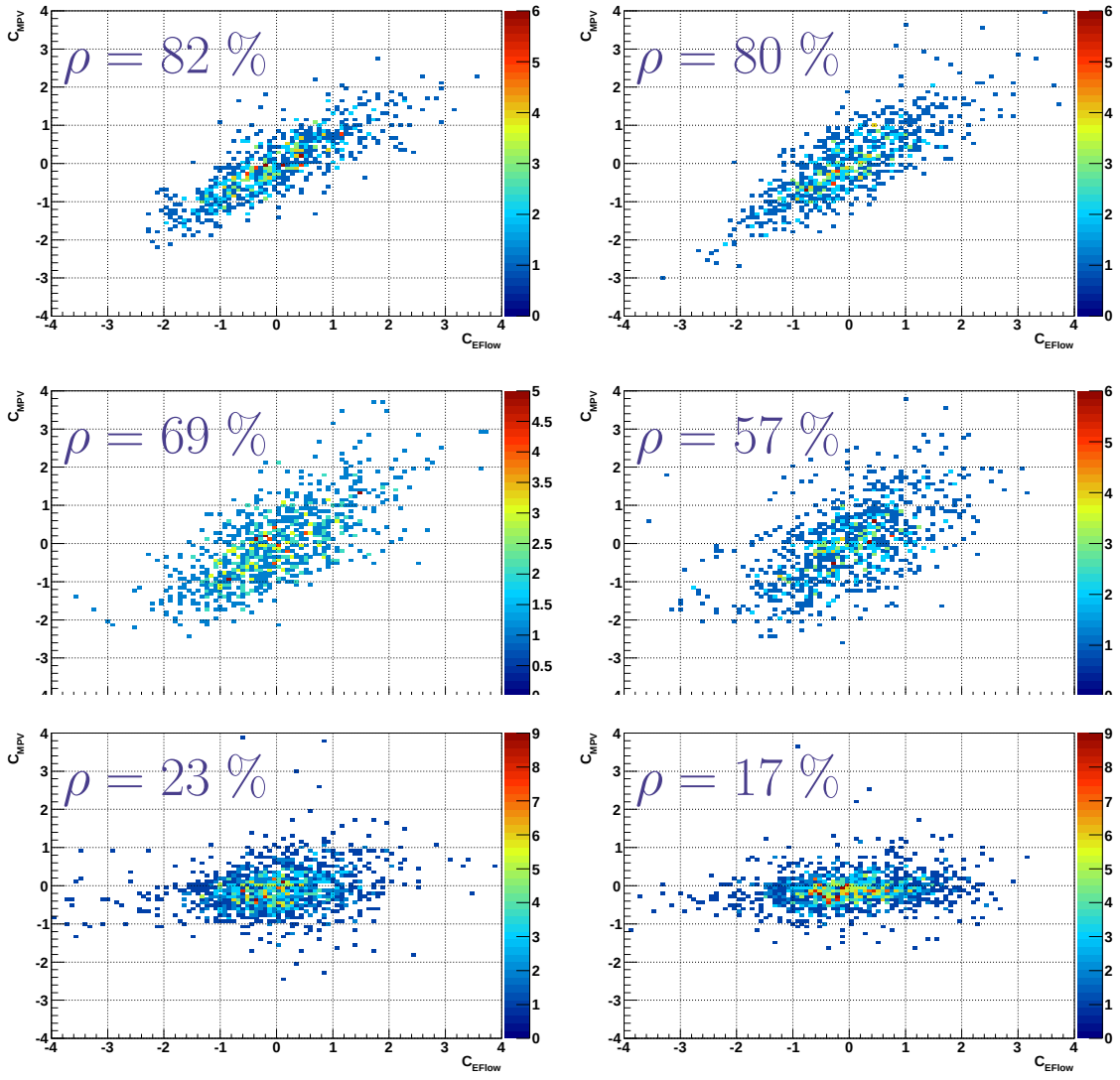

Figure III.34: Correlation of the calibration constants extracted from the energy flow (x-axis) or from the MIP measurements (y-axis) for the inner (top), middle (middle) and outer (bottom) of the A side (left) and the C side (right). Note that all of these coefficients are reduced to standard deviations: $c = (\text{coeff} - \langle\text{coeff}\rangle)/\sigma_{\text{coeff}}$. The correlation decreases from inner to outer which is explained by the fact that the inner was not as well calibrated as the outer due to lack of statistics in the previous calibration using cosmic data.

Area	Mean	RMS
Outer	1.2 %	8.0 %
Middle	1.5 %	10.1 %
Inner	2.6 %	14.8 %
Global	1.6 %	10.7 %

Table III.14: First two moments of the distribution of the calibration coefficients in each area of the PS after the mean over neighbours and the up-down symmetry. The outer is much better initially calibrated than the inner, as expected from the cosmic runs.

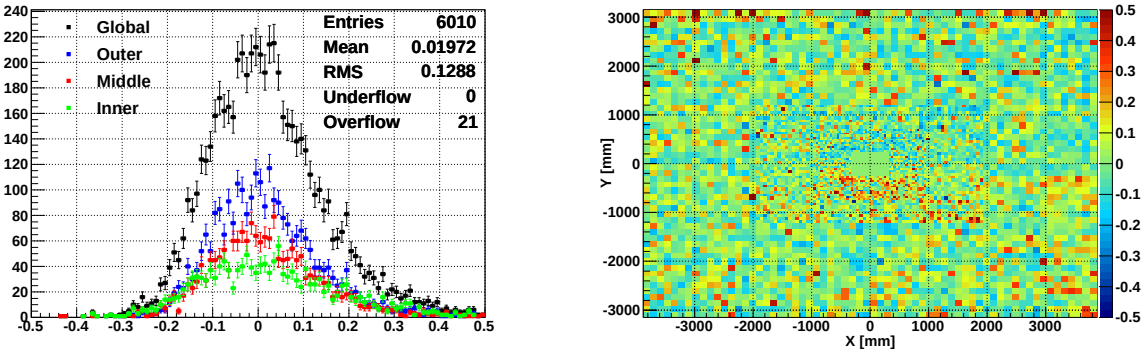

Figure III.35: Calibration coefficients (cumulative distribution on the left and 2D map on the right) extracted from the energy flow procedure using the method combining top-bottom symmetry and local smoothing in the ECAL with the 2009 real data.

15 % (see Fig. III.35). It is also observed on Fig. III.36 that the mass width of the π^0 peak is systematically reduced although the statistical uncertainty is of the order of 5 %.

III.3.2 First and fast offline ECAL calibration with the 2010 data

The calibration with the first 2010 data was performed rapidly after the beginning of data taking. The increase in accumulated statistics allowed to perform more accurate checks than in 2009 and the corresponding calibration constants were then applied in the database.

III.3.2.1 Conditions

The runs used to perform the calibration with the energy flow were runs where all the sub-detectors were ON and the events used are firing the CALO trigger in time with a beam-beam crossing. TAE are explicitly vetoed in the analysis. Data with the magnetic field off are used except otherwise stated. The cells which have a suspicious behaviour are also removed with the procedure defined with the 2009 data described in section III.3.1.2.

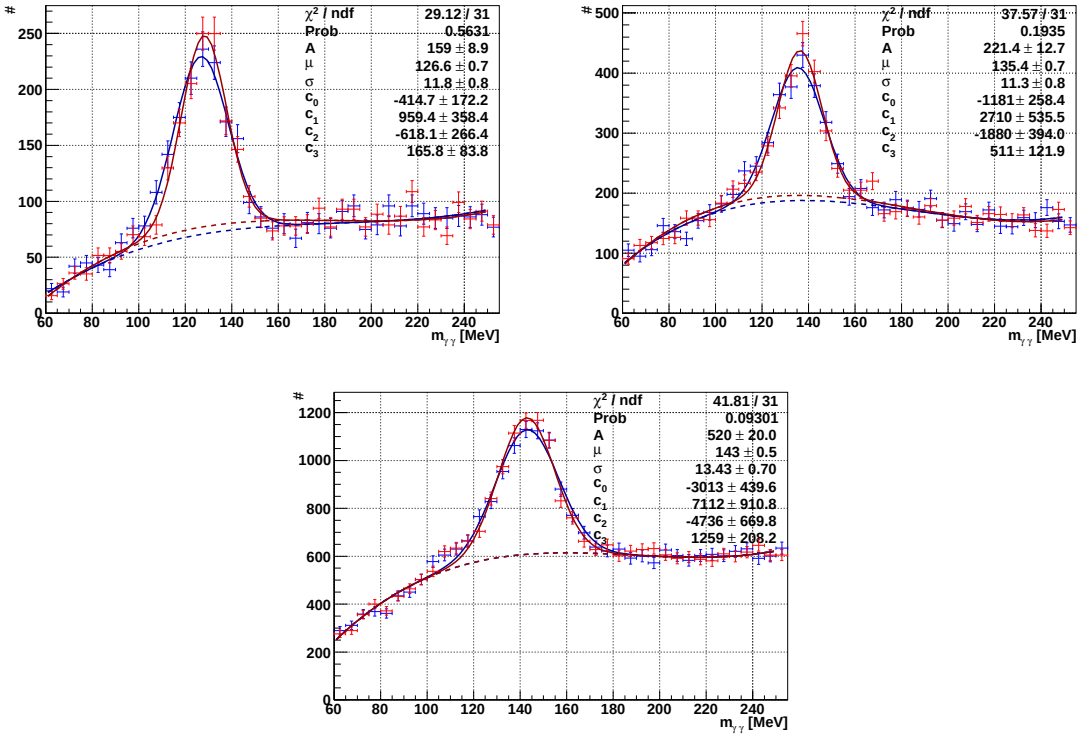

Figure III.36: Cross-check of the calibration using π^0 for the inner (top left), middle (top right) and outer (bottom). The distribution before recalibration is in blue and the distribution after calibration is in red. There is a slight improvement in the resolution on the di-photon invariant mass at the π^0 peak.

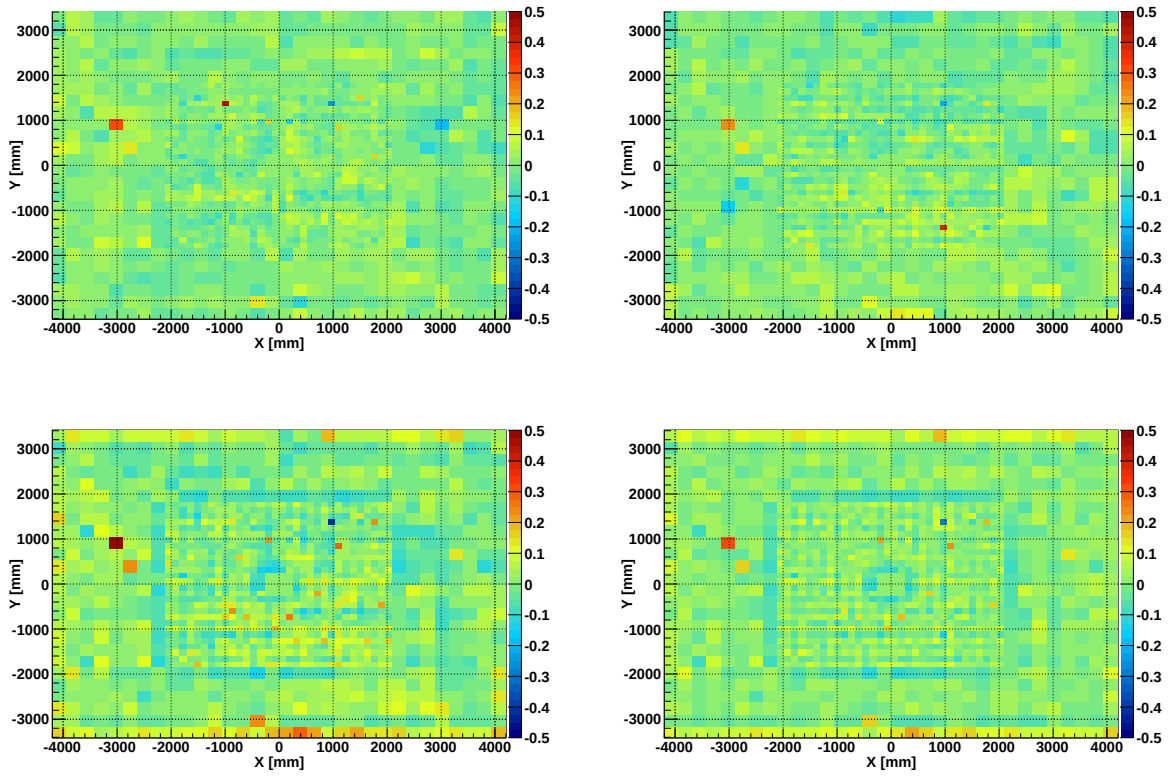

Figure III.37: Calibration coefficients extracted from the energy flow procedure based on the method using the left-right symmetry (top left), the top-bottom symmetry (top right), the mean over neighbours (bottom right) and the combination of all previous methods (bottom left) in the HCAL with the 2010 real data.

III.3.2.2 HCAL calibration

The HCAL is used as a benchmark sub-detector for the energy flow calibration since it is known to be already well calibrated at the level of 2-3 % by ^{137}Cs sources. The width of the coefficients extracted by the energy flow should be dominated by the limitation from the shape of the energy flow, at approximately 5 %. Using the different methods for the energy flow calibration, it is found that the geometrical symmetry of the detector is not ensured. This is indeed expected from Monte Carlo studies, especially in the HCAL where there is a strong influence from the difference in cross-sections for hadrons of opposite charges. Exploiting the local symmetry of the deposit provides a more robust estimate of the calibration constants and is found to be consistent with the expectations, see Fig. III.37 and Tab. III.15.

PS calibration After the 2009 data taking period, the electronic gains of the PS have been tuned to the calibration constants obtained with the MIP in 2009, where the statistic was big enough to supersede the calibration from cosmic data. If the spread of the calibration constants from the energy flow is stable in the middle and outer (where the statistics from cosmic was

Area	RMS (Local)	RMS (Local + Left-Right)	RMS (Local + Top-Bottom)
Outer	5.0 %	8.1 %	6.0 %
Inner	4.6 %	6.7 %	6.2 %
Global	4.8 %	7.3 %	6.2 %

Table III.15: RMS of the distribution of the calibration coefficients in each area of the HCAL after the mean over neighbours only, or combined with the left-right symmetry or the top-bottom symmetry. The results are not consistent and show an unexpected top-bottom asymmetry in the energy flow. The expected foreseen is reached with the local method alone.

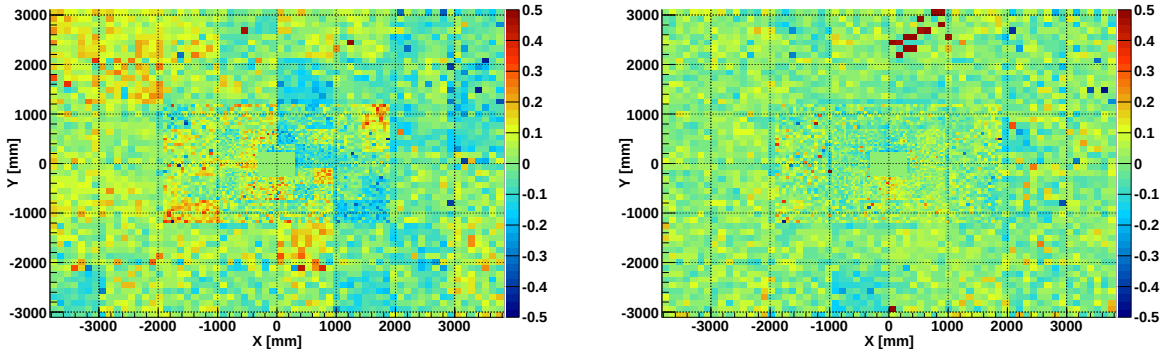

Figure III.38: Calibration coefficients extracted from the energy flow procedure using the method using the left-right symmetry and the top-bottom symmetry combined in the PS with the early 2010 data without (left) and with (right) applying the early 2010 calibration constants from the MIP.

sufficient), the RMS of the calibration constants in the inner are decreased to 9.9 %. As it is shown on Fig. III.38, using only the left-right and top-bottom symmetries of the detector, some patterns are observed in the map of the energy flow coefficients. This shows that the energy flow is sensitive, at a few percent level, to misalignments in time of half boards of the electronics, and to a global misalignment of one side with respect to the other. The correlation between a new MIP calibration extracted from the early 2010 data and the energy flow is found to be reasonable (see Fig. III.39), given the limited statistics and the precision of the time alignment. The RMS of the coefficients of the energy flow are reduced from 10 % to 7 % if the new MIP calibration is applied before the energy flow procedure, which gives confidence in the calibration provided by the MIP.

III.3.2.3 ECAL calibration

In the ECAL, the situations at the beginning of 2010 and at the end of 2009 were the same. The correlation between the calibration constants obtained in 2009 and 2010 is good and at the level of 83 %. This number does not vary significantly over the areas. Thus the two calibrations were found to be consistent with each other and the amount of statistics used in 2009 was enough to

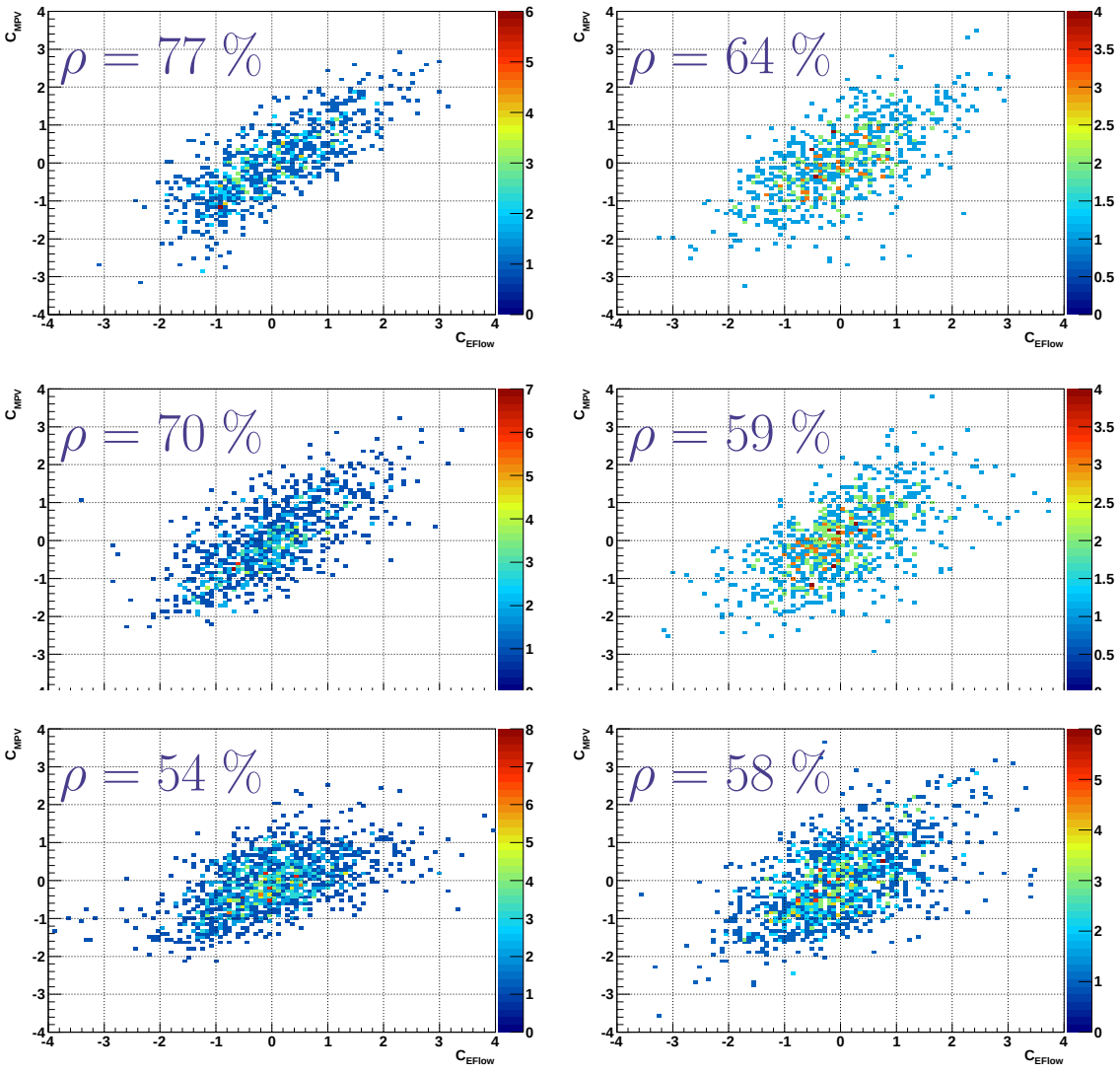

Figure III.39: Correlation of the calibration constants extracted from the energy flow (x-axis) or from the MIP measurements (y-axis) for the inner (top), middle (middle) and outer (bottom) of the A side (left) and the C side (right) with early 2010 data. Note that all of these coefficients are reduced to standard deviations: $c = (\text{coeff} - \langle\text{coeff}\rangle)/\sigma_{\text{coeff}}$. The correlation with the new calibration coefficients obtained by the MIP landau fit is now rather similar in all the areas.

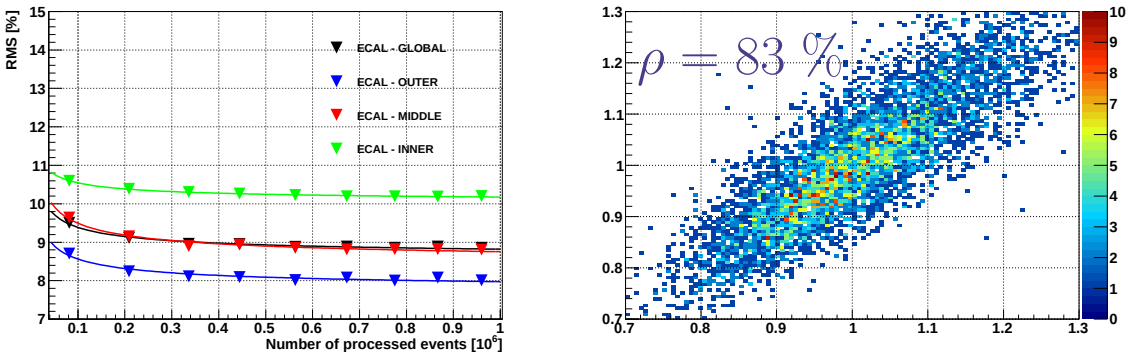

Figure III.40: Variation of the RMS of the calibration constants with the statistics (left) and correlation of the calibration constants extracted from 2009 (abscissa) and 2010 (ordinate) data (right).

calibrate the detector. This is confirmed by splitting the million of events used in sub-samples and performing a calibration on data samples of different sizes. Both the correlation with 2009 data and the scan over the statistics are shown on Fig. III.40. The mean and the RMS of the calibration constants are given in Tab. III.16. The calibration of the ECAL was at the level of 11 % to 15 % depending on the area. This energy flow calibration was used as a first offline

Area	Mean	RMS
Outer	1.3 %	11.1 %
Middle	1.5 %	12.4 %
Inner	2.6 %	15.3 %
Global	1.7 %	12.7 %

Table III.16: First two moments of the distribution of the calibration coefficients in each area of the ECAL after the mean over neighbours and the up-down symmetry with the early 2010 data.

calibration and as input for the fine π^0 calibration provided by another group. As a cross-check the calibration constants have been used to reconstruct π^0 and the result gives confidence in the usefulness of the energy flow to improve the energy resolution, as shown on Fig. III.41 and Tab. III.17.

III.3.3 Cross-check of the fine calibration and the LED system

The energy flow was also used in the summer 2010 to cross-check the π^0 calibration provided by two independent groups. For that the energy flow procedure was adapted. Taking advantage that the fine calibration provides a rather precise calibration at the level of 2.5 % it is necessary to reconsider the normalized energy flow. Indeed, once the π^0 calibration coefficients are applied, the ADC value if this coefficient had been taken into account to correct the HV gains, is computed. By doing this and cutting only on the "recalibrated" ADC is it possible to have an

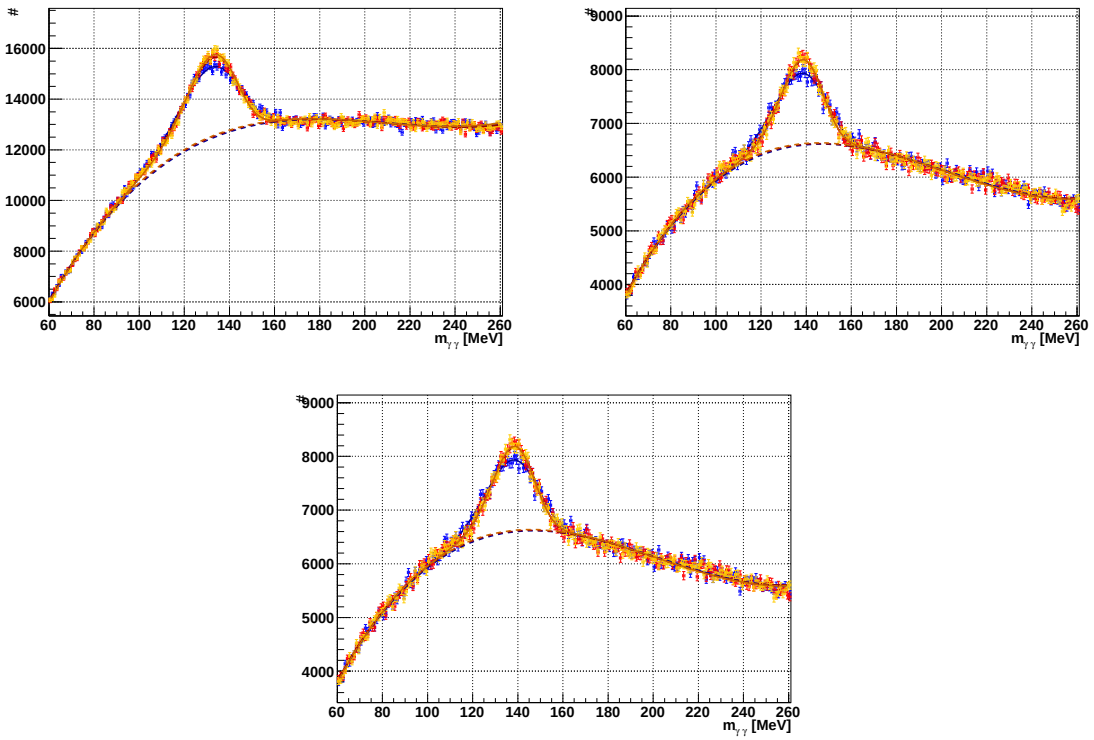

Figure III.41: Cross-check of the calibration using π^0 for the inner (top left), middle (top right) and outer (bottom) with early 2010 data. The distribution before calibration is in blue and the distribution after calibration is in red. There is a slight improvement in the resolution on the di-photon invariant mass at the π^0 peak. The blue curve corresponds to the non calibrated sample, the red curve corresponds to the recalibrated sample with the coefficients extracted from the use of the local method only and the yellow curve corresponds to the recalibrated sample with the coefficients extracted from the combination of the local and the symmetric methods. The result is slightly better with the combined method compared to the use of the mean over the neighbours only.

Before calibration	Mean	RMS
Outer	131.08 ± 0.13 MeV/c^2	12.73 ± 0.17 MeV/c^2
Middle	137.18 ± 0.16 MeV/c^2	10.46 ± 0.19 MeV/c^2
Inner	141.80 ± 0.17 MeV/c^2	12.04 ± 0.21 MeV/c^2
Global	135.04 ± 0.06 MeV/c^2	12.41 ± 0.08 MeV/c^2
After calibration	**Mean**	**RMS**
Outer	131.69 ± 0.11 MeV/c^2	10.66 ± 0.13 MeV/c^2
Middle	138.15 ± 0.13 MeV/c^2	8.99 ± 0.15 MeV/c^2
Inner	142.35 ± 0.13 MeV/c^2	9.81 ± 0.15 MeV/c^2
Global	135.72 ± 0.05 MeV/c^2	10.86 ± 0.07 MeV/c^2

Table III.17: Result of the Gaussian fit of the π^0 mass peak before calibration and after the energy flow calibration with the combination of the methods and the early 2010 data. The calibration by the energy flow systematically improves the width of the π^0 mass.

ideally flat normalized energy flow for which we are not limited any more by the intrinsic shape of the flow. The price to pay is to suffer from the sensitivity loss, which tends to underestimate the calibration by 30 %. Checking this procedure on Monte Carlo it is found that we are indeed sensitive to a 2.5 % miscalibration. The result is shown in Fig. III.42. Moreover it was found that the π^0 calibration, due to a missing protection against cells at the edge of the calorimeter, introduces a bias for the innermost and outermost cells of the calorimeter. This bias can be corrected very easily assuming that the inter-calibration was already rather good before the π^0 calibration. Averaging the π^0 calibration constants over the neighbouring cells of these belts allows to remove this annoying effect. The corresponding correction was applied in the database and the effect on the outermost belt is shown on Fig. III.43.

Another cross-check was performed when trying to understand the LED gain-shift correction. This correction is meant to follow the absolute gain of the ECAL cells by regularly flashing the LED. Due to bad time alignment of the LED cards until end of august, the gain shift correction is found, thanks to the energy flow, not to improve the calibration of the ECAL. However, after a correct time-alignment, the gain shift was well followed for the most luminous data taking period of October 2010. In this period the LED gain shift correction is found to improve slightly the smoothness of the energy flow, the effect being rather small since the energy flow constants are only sensitive to small-distance variations over which the multiplicity (and thus the ageing, and consequently the gain shift) is not expected to vary brutaly.

III.3.4 Robustness studies

There are potentially three important limitations to the energy flow. The first one is the effect of the trigger on the extraction of the calibration constants. It was shown on Monte Carlo studies that the effect on the coefficients of the energy flow should be small. Using late 2010 data, it is

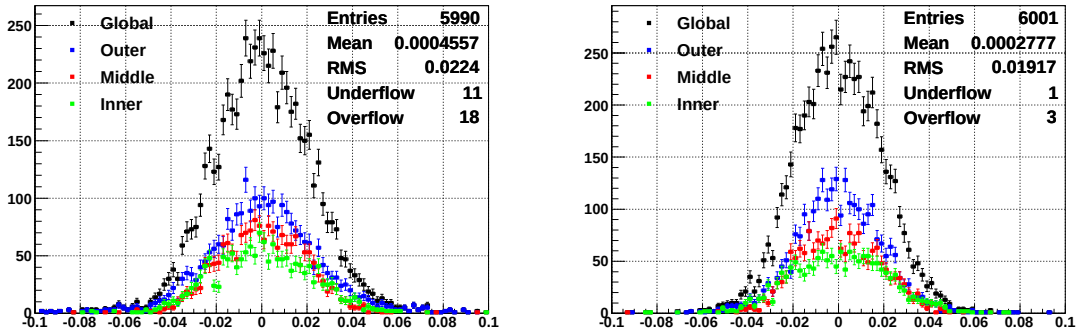

Figure III.42: Cross-check of the two fine π^0 calibration procedures (left the procedure involving background subtraction and weighting of the events, right the iterative fitting procedure, described in section III.1.2) using the energy flow method with the local averaging only and using data of beginning of June. The calibration of the calorimeters is of the order of 3 % and 2.5 % respectively, taking into account a relative sensitivity loss of 30 %.

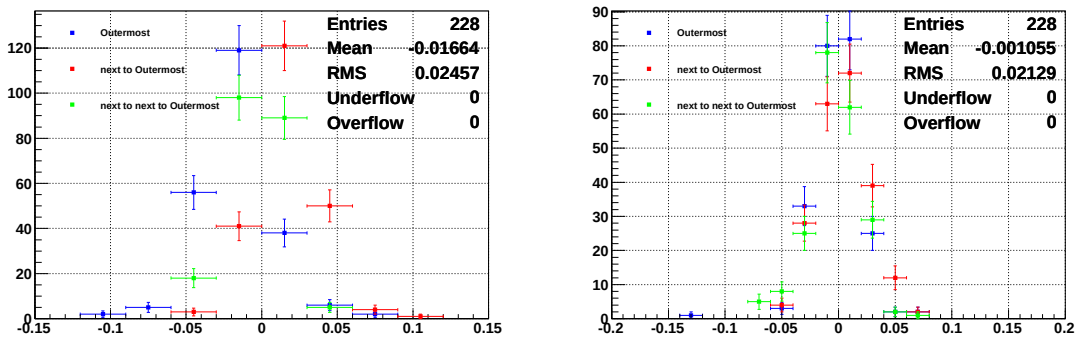

Figure III.43: Distribution of the calibration coefficients for the outermost (blue), the next to outermost (red) and the next to next to outermost (green) belt of cells and estimated by the energy flow when the coefficients for the fine π^0 calibration are in the database (left) and after the correction by averaging the π^0 coefficients over neighbouring cells (right). The systematic bias in the calibration constants is removed by the procedure.

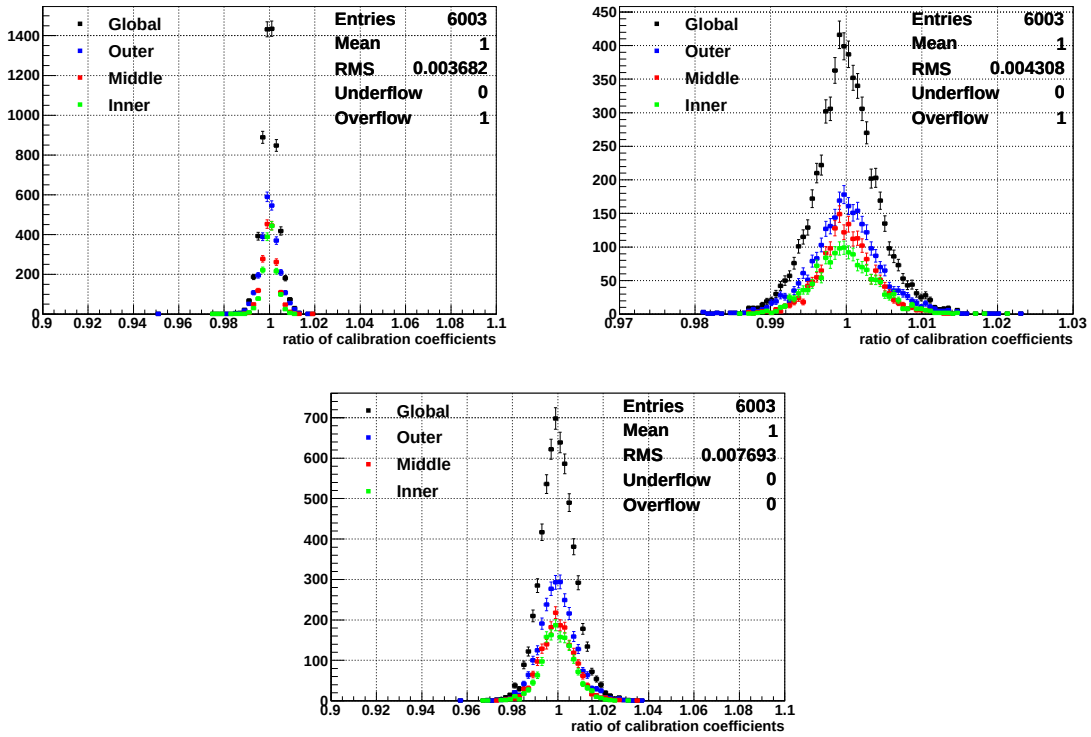

Figure III.44: Ratio of the calibration constants obtained for two different data sample. On the top left of the figure, the comparison for two different pile-up configurations is shown, on the top right of the figure the comparison of two different trigger configurations is given and on the bottom the effect due to the magnetic field is shown.

possible to compare two different physics triggers: the L0 muon and di-muon triggers and the L0 Hadron trigger ($E_T > 3.6$ GeV for the period considered here). The run 81619, for which the trigger configuration key (TCK) is `0x002e002a`, is used. This run was taken with a pile-up of 1.3 interactions per event in average. As shown on the Fig. III.44 the systematic uncertainty coming from the choice of a different trigger setting is smaller than 0.5 %. The effect of the pile-up, using the run 81596 (same fill of the LHC) taken with a pile-up of 2.2 is found to be smaller than 0.4 %, as shown on Fig. III.44. The effect of the magnetic field is found to be smaller than 0.8 % with 2011 data, by comparing data taken with the magnetic field off and magnetic field down (see Fig. III.44). Combining all these systematics shows that the energy flow is reliable at the level of 1 %.

III.3.5 Towards a fine Energy Flow inter-calibration

All the previous studies give a strong confidence that the energy flow is able to improve the calibration, even once the fine calibration was first applied, and at a smaller cost. Fig. III.45 shows on Monte Carlo that it is possible to reduce from 2.0 % to 1.1 % the residual miscalibration

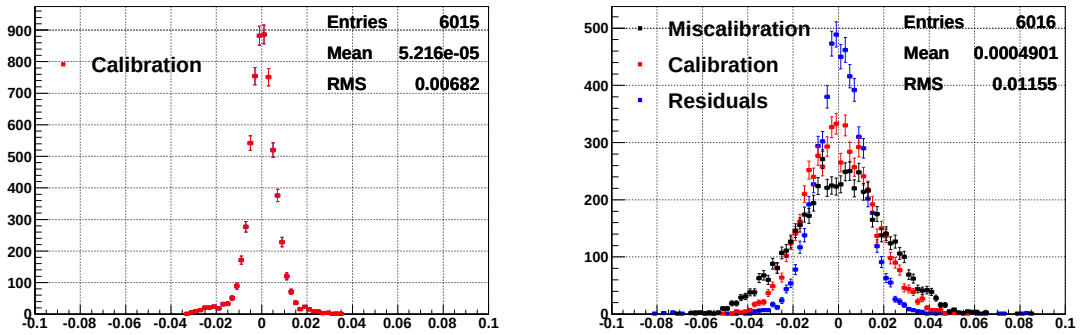

Figure III.45: Residuals applying the calibration procedure on the normalized transverse energy flow on Monte Carlo, without introducing a miscalibration on the left and introducing a 2 % miscalibration on the right. The 1 % level is almost reached by the energy flow.

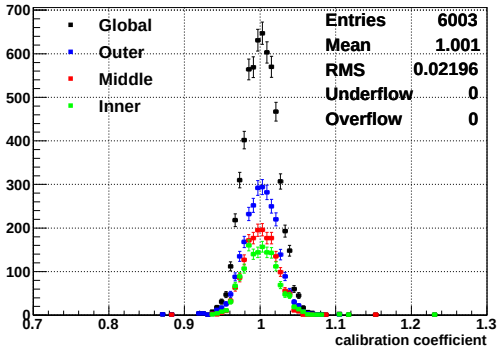

Figure III.46: Distribution of the 2011 recalibration coefficients applied in the database to reach the 1 % level of calibration.

by applying again the energy flow after the π^0 calibration. The intrinsic limitation of the energy flow using normalized distributions is found to be of 0.6 %.

This procedure was applied on real data, after having corrected for the bias introduced on the borders by the π^0 calibration, and the correction was put in the database in 2011. The corresponding coefficients are shown on Fig. III.46.

With early 2011 data, the calibration of the HCAL and the PS was cross checked. The result is shown on Fig. III.47. The calibration of the PS and the HCAL is excellent and found to be better than 4.5 % for the PS (the PS is still limited by the sensitivity loss and the shape of the energy deposit, the exact precision of the calibration cannot be precisely extracted by the energy flow) and 2 % for the HCAL (using the normalized energy flow for the HCAL and magnet off data allows to reach the same precision than for the ECAL, and to show that the expected precision is already obtained).

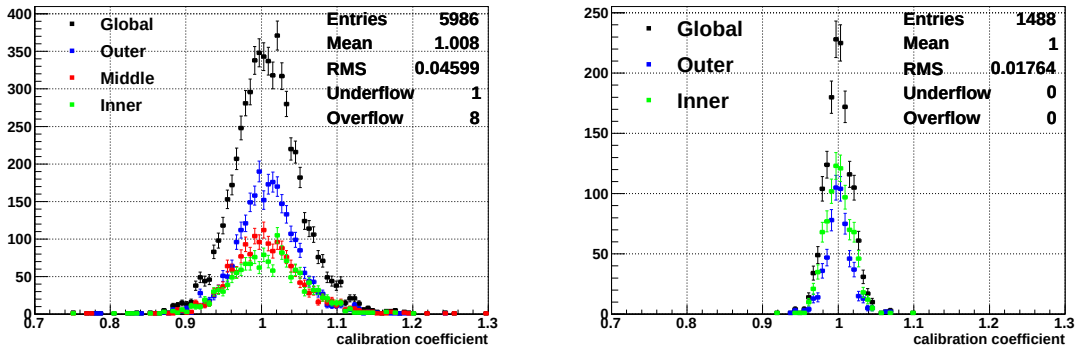

Figure III.47: Distribution of the 2011 energy flow coefficients for the PS (left) and the HCAL (right). The calibration has reached the desired level for these two sub-detectors. The result for the HCAL is obtained from a dataset for which the magnetic field is off.

III.4 Conclusion

III.4.1 Results

The energy flow inter-calibration has been demonstrated to be an efficient tool to calibrate and to cross-check the calibration of the calorimeters during the first year of data taking, and has been used as a standard tool in the calibration procedure. The results obtained in late 2010 and early 2011 show the ability of the energy flow to provide the required inter-calibration of the detector, the absolute scale being extracted from complementary methods. The applied procedure and the corresponding result for the different sub-detectors are the following.

- Due to the hardware zero suppression the energy flow is not normalized in the PS. The dominant limitation of the procedure then comes from a 3 % bias (from Monte Carlo) introduced by the shape of the energy flow. The energy flow procedure shows that, with 2011 data, the PS is calibrated at better than 4 % by the MIP measurements.

- Using the normalized energy flow and data without magnetic field, the energy flow demonstrated that the inter-calibration by the ^{137}Cs sources of the HCAL is better than 2 %.

- The energy flow procedure has been used twice for the calibration of the ECAL. A first energy flow calibration allowed to reach 5 % inter-calibration, by removing the normalization of the flow to be independent from the sensitivity loss. These coefficients were applied in the database at the end of April 2010. Then the technique was used a second time, after the calibration by the π^0 procedure, by normalizing the energy flow to be insensitive to the systematics from the shape of the flow. A typical 1.5 % inter-calibration is thus reached and was also applied in the database. A procedure, independent from the energy flow, was applied to correct for the bias introduced by the π^0 method for the borders. These

coefficients were also applied in the database. All these calibration constants have been used by default by analyses using neutral electromagnetic particles in the reprocessing of 2010 data and in the 2011 data sample. The energy flow was also used found to be useful to cross-check the π^0 calibration and the monitoring of the gains by the LED system.

III.4.2 Perspectives

Given the negligible impact of the trigger and the pile-up, it is possible to use the energy flow to follow the quality of the inter-calibration of the calorimeter cells. It was found that, thanks to the fact that the systematics from the shape of the flow cancel in the ratio, the energy flow can be precise at the percent level as a monitoring tool (of the inter-calibration) even using the not normalized method (the normalized method being too much sensitive to the threshold effect). Comparing the energy flow constants of two different runs would allow to monitor the inter-calibration at the level of a percent, assuming that the shape of of the energy flow is not or negligibly affected by the gain loss due to radiations. The impact of this effect on the calibration constants has still to be estimated.

Another improvement related to the threshold effect could also be implemented. Nothing was explicitly done to compensate for this effect in the current method. Since the exact ADC spectrum in each cell is not known, it is difficult to compensate the sensitivity loss by an ad-hoc function. However, it could be possible to compute a linear interpolation of the spectrum in between the real ADC bins. This would allow to smooth out the effect of the digitization and allow a better extraction of the calibration constants, that would be less influenced by the sensitivity loss. This would nevertheless take time to implement and would also require some careful realistic checks on Monte Carlo, and is not performed in the present study.

Chapter IV

Towards a γ measurement with $B^0 \to DK^{*0}$ at LHCb

- Non, mais arrêtez de nous baratiner avec vos chiffres là !
- Les chiffres, c'est pas une science exacte figurez-vous!

Franck Pitiot alias *Perceval* et Jean-Christophe Hembert alias *Karadoc*
in *Corvus Corone*, **Kaamelott, Livre V**, Tome 1, Épisode 1,
écrit par Alexandre Astier.

Contents

After the description of the formalism used to extract γ and some important considerations about the origin of the sensitivity to γ, a toy Monte Carlo sensitivity study of the angle γ is then described to show the ability of LHCb to provide a *CP* violation measurement. A Monte Carlo study of the channel of interest is then described, taking a special care to a potential dangerous background, a preliminary study of this background is then performed on real data in chapter V.

IV.1 γ measurement with the ADS method

IV.1.1 The interest of $B^0 \to DK^{*0}$ decays

The ADS [53, 54] method, see chapter I, consists in measuring γ using $B^{\pm} \to DK^{\pm}$ decays with the D decaying in a final state accessible by both the D^0 and the $\overline{D}^0$. In the original ADS method, the $b \to c$ transition which is a colour-favoured transition followed by a Cabibbo-suppressed D decay interfere with a $b \to u$ colour-favoured transition followed by a Cabibbo-suppressed D decay, so that the interference term contribution is rather small compared to the total number of events. To remedy this feature of the method, it was instead proposed [82] to use $B^0 \to DK^{*0}$ decays, for which both $b \to c$ and $b \to u$ transitions are colour-suppressed. For these decays, the b-meson flavour is self-tagged by the K^{*0} flavour and thus by the charge of the K of the K^{*0} decay. The interference term is thus enhanced by a factor 3, allowing for an increased sensitivity to the angle γ, the price to pay being an increased complexity (both on the theoretical and experimental side) due to the presence of a vector meson in the decay chain.

IV.1.2 Parametrisation of the observables

IV.1.2.1 Two body D decay

Due to the intrinsic width of the K^{*0}, the $B^0 \to DK^{*0}$ decays cannot be considered as monochromatic and the decay amplitudes have to be written as a function of M, an arbitrary point of the phase space. In particular, the modulus and the strong phases of the amplitudes will depend on the location in the phase space. In principle this should be a problem for the GLW and ADS methods, described in chapter I, but the usual formalism can be recovered by introducing an additional parameter in the equations [82]. The equations are in fact more general than the $B^0 \to DK^{*0}$ case, and we thus write the equations for $B^0 \to DX_s^0$ where the K^* has been replaced by an arbitrary light meson X_s^0 of strangeness ± 1, composed of one (like the K^{*0} case) or more particles ($K^+\pi^-$ for example, in a different region of the phase space than the K^{*0}). The modulus and the strong phase of the $b \to c$ and $b \to u$ amplitudes are depending on M and are respectively written $\mathcal{A}_c(M)$, $\mathcal{A}_u(M)$, $\delta_c(M)$ and $\delta_u(M)$. For a scalar X_s^0 meson, there is no dependence on M while for a vector X_s^0 meson or a multi-body X_s^0 the dependence on M is effective and depicts the interference of the final state particles ($K\pi$ in the case of K^{*0}). The

decay amplitudes of the B-meson are then parametrized as in Eq. IV.1, the weak angle γ of the CKM matrix appearing in the $b \to u$ transitions only.

$$\begin{aligned}
\mathcal{A}\left(B^0 \to \left(\overline{D}^0 X_s^0\right)_M\right) &= \mathcal{A}_c\left(M\right) e^{\imath\delta_c(M)} && \text{(IV.1a)}\\
\mathcal{A}\left(B^0 \to \left(D^0 X_s^0\right)_M\right) &= \mathcal{A}_u\left(M\right) e^{\imath\delta_u(M)+\gamma} && \text{(IV.1b)}\\
\mathcal{A}\left(\overline{B}^0 \to \left(D^0 \overline{X}_s^0\right)_M\right) &= \mathcal{A}_c\left(M\right) e^{\imath\delta_c(M)} && \text{(IV.1c)}\\
\mathcal{A}\left(\overline{B}^0 \to \left(\overline{D}^0 \overline{X}_s^0\right)_M\right) &= \mathcal{A}_u\left(M\right) e^{\imath\delta_u(M)-\gamma} && \text{(IV.1d)}
\end{aligned}$$

Assuming no *CP*-violation in the charm sector, the D decays are parametrized as in Eq. IV.2, where f denotes a two body final state[1] and $\mathcal{A}_f$, $\mathcal{A}_{\overline{f}}$, δ_f, $\delta_{\overline{f}}$ denote respectively the modulus and the strong phases of the $c \to s$ and $c \to d$ transitions respectively.

$$\begin{aligned}
\mathcal{A}\left(D^0 \to f\right) &= \mathcal{A}\left(\overline{D}^0 \to \overline{f}\right) = \mathcal{A}_f e^{\imath\delta_f} && \text{(IV.2a)}\\
\mathcal{A}\left(D^0 \to \overline{f}\right) &= \mathcal{A}\left(\overline{D}^0 \to f\right) = \mathcal{A}_{\overline{f}} e^{\imath\delta_{\overline{f}}} && \text{(IV.2b)}
\end{aligned}$$

It follows that the four amplitudes of interest are written as in Eq. IV.3, under the assumption of negligible mixing in the D sector [83].

$$\begin{aligned}
\mathcal{A}\left(B^0 \to \left(\overline{f} X_s^0\right)_M\right) &= \mathcal{A}\left(B^0 \to \left(\overline{D}^0 X_s^0\right)_M\right) \mathcal{A}\left(\overline{D}^0 \to \overline{f}\right) && \text{(IV.3a)}\\
&+ \mathcal{A}\left(B^0 \to \left(D^0 X_s^0\right)_M\right) \mathcal{A}\left(D^0 \to \overline{f}\right) && \text{(IV.3b)}\\
\mathcal{A}\left(\overline{B}^0 \to \left(f \overline{X}_s^0\right)_M\right) &= \mathcal{A}\left(\overline{B}^0 \to \left(D^0 \overline{X}_s^0\right)_M\right) \mathcal{A}\left(D^0 \to f\right) && \text{(IV.3c)}\\
&+ \mathcal{A}\left(\overline{B}^0 \to \left(\overline{D}^0 \overline{X}_s^0\right)_M\right) \mathcal{A}\left(\overline{D}^0 \to f\right) && \text{(IV.3d)}\\
\mathcal{A}\left(B^0 \to \left(f X_s^0\right)_M\right) &= \mathcal{A}\left(B^0 \to \left(D^0 X_s^0\right)_M\right) \mathcal{A}\left(D^0 \to f\right) && \text{(IV.3e)}\\
&+ \mathcal{A}\left(B^0 \to \left(\overline{D}^0 X_s^0\right)_M\right) \mathcal{A}\left(\overline{D}^0 \to f\right) && \text{(IV.3f)}\\
\mathcal{A}\left(\overline{B}^0 \to \left(\overline{f} \overline{X}_s^0\right)_M\right) &= \mathcal{A}\left(\overline{B}^0 \to \left(\overline{D}^0 \overline{X}_s^0\right)_M\right) \mathcal{A}\left(\overline{D}^0 \to \overline{f}\right) && \text{(IV.3g)}\\
&+ \mathcal{A}\left(\overline{B}^0 \to \left(D^0 \overline{X}_s^0\right)_M\right) \mathcal{A}\left(D^0 \to \overline{f}\right) && \text{(IV.3h)}
\end{aligned}$$

To remove the phase space dependence, these amplitudes are integrated out, defining the coherence factor κ_B [82] and the strong phase difference δ_B in the B^0 decays. These parameters are

[1] The convention used here is to choose that $D^0 \to f$ is a Cabibbo-favoured transition. A typical example is $f \equiv K^+\pi^-$.

written in Eq. IV.4 as a function of the previously defined parameters.

$$\delta(M) = \delta_u(M) - \delta_c(M) \tag{IV.4a}$$

$$\kappa_B e^{\imath\delta_B} = \frac{\int_M \mathcal{A}_c(M)\,\mathcal{A}_u(M)\,e^{\imath\delta(M)}\mathrm{d}M}{\sqrt{\int_M \mathcal{A}_c^2(M)\,\mathrm{d}M \int_M \mathcal{A}_u^2(M)\,\mathrm{d}M}} \tag{IV.4b}$$

$$r_B^2 = \frac{\int_M \mathcal{A}_u^2(M)\,\mathrm{d}M}{\int_M \mathcal{A}_c^2(M)\,\mathrm{d}M} = \frac{\Gamma\left(B^0 \to D^0 X_s^0\right)}{\Gamma\left(B^0 \to \overline{D}^0 X_s^0\right)} = \frac{\Gamma\left(\overline{B}^0 \to \overline{D}^0 \overline{X}_s^0\right)}{\Gamma\left(\overline{B}^0 \to D^0 \overline{X}_s^0\right)} \tag{IV.4c}$$

$$r_D = \frac{\mathcal{A}_{\overline{f}}}{\mathcal{A}_f} \tag{IV.4d}$$

$$\delta_D = \delta_f - \delta_{\overline{f}} \tag{IV.4e}$$

$$\Gamma_0 = \mathcal{A}_{\overline{f}}^2 \left(\int_M \mathcal{A}_c(M)\,\mathrm{d}M\right)^2 \tag{IV.4f}$$

The Schwartz inequality implies that $\kappa_B \in [0,1]$. If $\kappa_B = 1$ this means that the decay behaves as if there is no structure in the X_s^0 resonance and that the strong phase does not depend on M, this is equivalent to have a two body decay. On the contrary a very small value of κ_B indicates a poor coherence and a destructive interference between the different points M in the phase space of interest.

The expression of the partial rates, integrated over the phase space of interest, are written in Eq. IV.5.

$$\Gamma\left(B^0 \to \overline{f} X_s^0\right) = \Gamma_0\left(1 + r_B^2 r_D^2 + 2\kappa_B r_B r_D \cos\left(\delta_B - \delta_D + \gamma\right)\right) \tag{IV.5a}$$

$$\Gamma\left(\overline{B}^0 \to f \overline{X}_s^0\right) = \Gamma_0\left(1 + r_B^2 r_D^2 + 2\kappa_B r_B r_D \cos\left(\delta_B - \delta_D - \gamma\right)\right) \tag{IV.5b}$$

$$\Gamma\left(B^0 \to f X_s^0\right) = \Gamma_0\left(r_B^2 + r_D^2 + 2\kappa_B r_B r_D \cos\left(\delta_B + \delta_D + \gamma\right)\right) \tag{IV.5c}$$

$$\Gamma\left(\overline{B}^0 \to \overline{f X}_s^0\right) = \Gamma_0\left(r_B^2 + r_D^2 + 2\kappa_B r_B r_D \cos\left(\delta_B + \delta_D - \gamma\right)\right) \tag{IV.5d}$$

IV.1.2.2 Multi-body D decay

Eq. IV.5 is modified in the case of a multi-body D decay by introducing similar parameters than in the case of the B decay. A coherence factor κ_D and a strong phase difference δ_D are thus similarly introduced. The former definition of the strong phase δ_D is equivalent to the one defined in Eq. IV.6 in the case of a D decay in two scalar mesons, where $\kappa_D = 1$. The strong phases and amplitudes of the D decays now depend on the point M' in the phase space of the

D decay, as shown in Eq. IV.6.

$$\mathcal{A}\left(D^0 \to f_{M'}\right) = \mathcal{A}\left(\overline{D}^0 \to \overline{f}_{M'}\right) = \mathcal{A}_f\left(M'\right) e^{\imath\delta_f(M')} \tag{IV.6a}$$

$$\mathcal{A}\left(D^0 \to \overline{f}_{M'}\right) = \mathcal{A}\left(\overline{D}^0 \to f_{M'}\right) = \mathcal{A}^2_{\overline{f}}\left(M'\right) e^{\imath\delta_{\overline{f}}(M')} \tag{IV.6b}$$

$$\kappa_D e^{-\imath\delta_D} = \frac{\int_{M'} \mathcal{A}^2_{\overline{f}}\left(M'\right)\mathcal{A}_f\left(M'\right) e^{\imath\delta(M')}\mathrm{d}M'}{\sqrt{\int_{M'} \mathcal{A}_{\overline{f}}\left(M'\right)\mathrm{d}M' \int_{M'} \mathcal{A}^2_f\left(M'\right)\mathrm{d}M'}} \tag{IV.6c}$$

$$\delta\left(M'\right) = \delta_{\overline{f}}\left(M'\right) - \delta_f\left(M'\right) \tag{IV.6d}$$

$$\Gamma_0 = \left(\int_{M'} \mathcal{A}_{\overline{f}}\mathrm{d}M'\right)^2 \left(\int_M \mathcal{A}_c\left(M\right)\mathrm{d}M\right)^2 \tag{IV.6e}$$

The rates of Eq. IV.5 are thus accordingly modified to give Eq. IV.7.

$$\Gamma\left(B^0 \to \overline{f}X^0_s\right) = \Gamma_0\left(1 + r_B^2 r_D^2 + 2\kappa_B\kappa_D r_B r_D \cos\left(\delta_B - \delta_D + \gamma\right)\right) \tag{IV.7a}$$

$$\Gamma\left(\overline{B}^0 \to f\overline{X}^0_s\right) = \Gamma_0\left(1 + r_B^2 r_D^2 + 2\kappa_B\kappa_D r_B r_D \cos\left(\delta_B - \delta_D - \gamma\right)\right) \tag{IV.7b}$$

$$\Gamma\left(B^0 \to fX^0_s\right) = \Gamma_0\left(r_B^2 + r_D^2 + 2\kappa_B\kappa_D r_B r_D \cos\left(\delta_B + \delta_D + \gamma\right)\right) \tag{IV.7c}$$

$$\Gamma\left(\overline{B}^0 \to \overline{f}\overline{X}^0_s\right) = \Gamma_0\left(r_B^2 + r_D^2 + 2\kappa_B\kappa_D r_B r_D \cos\left(\delta_B + \delta_D - \gamma\right)\right) \tag{IV.7d}$$

IV.1.3 General strategy

The Eq. IV.5 contains one normalization factor Γ_0, three parameters for the B decay (κ_B, r_B and δ_B), two or three parameters for the D^0 decay (r_D and δ_D and, if the decay involves at least three bodies in the final state, κ_D), and the parameter of interest for this study, the unitarity triangle (UT) angle γ. Using only $D^0 \to K^\pm\pi^\mp$ and external measurements of the D decay parameters r_D and δ_D, from CLEO and soon from BES, the system of four equations is a closed problem as soon as κ_B is also taken from an external Monte Carlo study [50, 84].

Given the rather limited statistics ($b \to u$ transitions) and the ambiguities inherent to the determination of the angles δ_B and γ, a better convergence can be obtained by over-constraining the system of Eq. IV.5 by adding the decay modes $D^0 \to K^\pm\pi^\mp\pi^0$ and $D^0 \to K^\pm\pi^\mp\pi^+\pi^-$ that add two systems similar to Eq. IV.7. These three sets of equations contain in total, three normalization constants $\Gamma_{D^0\to K^\pm\pi^\mp}$, $\Gamma_{D^0\to K^\pm\pi^\mp\pi^0}$ and $\Gamma_{D^0\to K^\pm\pi^\mp\pi^+\pi^-}$ (the ratios of the normalization constants $\Gamma_{D^0\to K^\pm\pi^\mp\pi^0}$ and $\Gamma_{D^0\to K^\pm\pi^\mp\pi^+\pi^-}$ with respect to $\Gamma_{D^0\to K^\pm\pi^\mp}$ are also constrained from the Monte Carlo ratio of efficiencies, calibrated on real data), two B decay parameters r_B and δ_B and the UT angle γ. Eight D decay parameters (three ratios $r_{D^0\to K^\pm\pi^\mp}$, $r_{D^0\to K^\pm\pi^\mp\pi^0}$, $r_{D^0\to K^\pm\pi^\mp\pi^+\pi^-}$, three strong phases difference $\delta_{D^0\to K^\pm\pi^\mp}$, $\delta_{D^0\to K^\pm\pi^\mp\pi^0}$, $\delta_{D^0\to K^\pm\pi^\mp\pi^+\pi^-}$ and two coherence factors $\kappa_{D^0\to K^\pm\pi^\mp\pi^0}$, $\kappa_{D^0\to K^\pm\pi^\mp\pi^+\pi^-}$) are fixed from external measurements and one B decay parameter, κ_B, is taken from an external input.

Parameter	Value	Reference	Fit
$r_{D^0 \to K^\pm \pi^\mp}$	$(6.16 \pm 0.15)\,.10^{-2}$	[38]	fixed
$r_{D^0 \to K^\pm \pi^\mp \pi^0}$	$(4.69 \pm 0.11)\,.10^{-2}$	[38]	fixed
$r_{D^0 \to K^\pm \pi^\mp \pi^+ \pi^-}$	$5.68^{+0.22}_{-0.19}.10^{-2}$	[38]	fixed
$\kappa_{D^0 \to K^\pm \pi^\mp \pi^0}$	0.84 ± 0.07	[86]	fixed
$\kappa_{D^0 \to K^\pm \pi^\mp \pi^+ \pi^-}$	$0.33^{+0.20}_{-0.23}$	[86]	fixed
$\delta_{D^0 \to K^\pm \pi^\mp}$	$-151.5^\circ\ ^{+9.6^\circ}_{-9.5^\circ}$ (syst)	[85, 86]	fixed
$\delta_{D^0 \to K^\pm \pi^\mp \pi^0}$	$227^\circ\ ^{+14^\circ}_{-17^\circ}$	[86]	fixed
$\delta_{D^0 \to K^\pm \pi^\mp \pi^+ \pi^-}$	$114^\circ\ ^{+26^\circ}_{-23^\circ}$	[86]	fixed
γ	$70^\circ \pm 3^\circ$	[37]	free
δ_B	$62^\circ \pm 57^\circ\ [180^\circ]$	[50]	free
r_B	0.26 ± 0.08	[50, 88]	free
κ_B	0.95 ± 0.03	[50, 84]	fixed

Table IV.1: Summary of the constraints from various inputs on the parameters relative to the D decay and on the coherence factor of the K^{*0} in the B decay. The coherence factor of the $K^\mp \pi^\pm \pi^0$ decay mode is larger, and thus closer to a 2-body resonant decay, than the $K^\mp \pi^\pm \pi^+ \pi^-$ (for which there are large error bars). The ambiguity on the determination of δ_B is quoted in brackets. The value quoted for γ is the fit result from [37] assuming the Standard Model (only the central value is used for the generation of the events). The last column shows if the parameter is fixed or fitted (free) in the fit described in the following.

IV.1.4 Current experimental constraints

The D-factories have a crucial role in the determination of the D decay parameters, especially the phases. Some results have already been published by CLEO and measurements are planned at BES, that will improve the accuracy of the current determinations [85, 86]. The r_D values are taken from [38][2].

On the other hand, assuming a mass cut of ± 50 MeV/c^2 around the nominal K^{*0} mass, κ_B is estimated from Monte Carlo studies to be close to unity [50, 84]. It has been shown [87] that the main interfering contribution in the K^{*0} mass window is coming from D^* and can be vetoed without signal loss which increases the coherence factor. All these constraints are summarized in Tab. IV.1. These parameters will be fixed or constrained in the toy Monte Carlo study.

[2]There is two distinct values for the D decay parameters, depending on whether the fit allows for mixing in the charm or not. Since for the γ extraction the charm mixing has to be integrated out, the values for the D decay parameters allowing mixing in the D should be considered.

IV.1.5 First expectations

Assuming that there is neither detection[3] nor production asymmetry[4], the Eq. IV.5 can be written for the number of detected events. Using the values from Tab. IV.1 it is also possible to replace the known parameters (except the phases) by their values (the uncertainties on κ_B, r_B and r_D are used to compute the errors in the numbers of Eq. IV.8). Restricting ourselves to $f \equiv K^+\pi^-$, Eq. IV.8 shows quantitatively that the interference term is enhanced in the suppressed decay modes (Eqs. IV.8c-IV.8d), while the interference term is diluted in the favoured decay mode (Eqs. IV.8a-IV.8b). Using only the central values of the different terms, the size of the interference can be measured at 3 standard deviations with 100 events in the suppressed mode (charge conjugates added here), which is the typical number of suppressed mode events that can be observed in 2 fb^{-1} at $\sqrt{s} = 7$ TeV as shown in section IV.3. The same sensitivity on the interference term in the favoured mode cannot be obtained with less than 10000 observed favoured decays which corresponds to 7 times more integrated luminosity (which is beyond the scope of LHCb without an upgrade), and this term can be neglected. The other terms can as well be neglected.

$$\begin{aligned}
N\left(B^0 \to K^-\pi^+ X_s^0\right) &= N_0\,(1 + (0.026\ \% \pm 0.011\ \%) && \text{(IV.8a)}\\
&+ (3.2\ \% \pm 1.0\ \%)\cos\left(\delta_B - \delta_D + \gamma\right)) \\
N\left(\overline{B}^0 \to K^+\pi^-\overline{X}_s^0\right) &= N_0\,(1 + (0.026\ \% \pm 0.011\ \%) && \text{(IV.8b)}\\
&+ (3.2\ \% \pm 1.0\ \%)\cos\left(\delta_B - \delta_D - \gamma\right)) \\
N\left(B^0 \to K^+\pi^- X_s^0\right) &= N_0 r_B^2\,(1 + (5.6\ \% \pm 2.4\ \%) && \text{(IV.8c)}\\
&+ (45\ \% \pm 14\ \%)\cos\left(\delta_B + \delta_D + \gamma\right)) \\
N\left(\overline{B}^0 \to K^-\pi^+\overline{X}_s^0\right) &= N_0 r_B^2\,(1 + (5.6\ \% \pm 2.4\ \%) && \text{(IV.8d)}\\
&+ (45\ \% \pm 14\ \%)\cos\left(\delta_B + \delta_D - \gamma\right))
\end{aligned}$$

Taking into account these simplifications, the system of equations becomes Eq. IV.9, showing that two equations are identical. The normalization N_0 is thus precisely extracted from the number of favoured modes and the other parameters are extracted from the suppressed decay modes. There are three remaining parameters (r_B, δ_B and γ) for two equations which makes, in practice, the extraction impossible. Despite the extraction of the parameters N_0, r_B, δ_B and γ seems (with infinite statistics) feasible with only one D decay mode (section IV.1.3), the use of other D decay modes is mandatory to be able to measure γ and resolve the eight inherent

[3] This generic term gathers here geometrical acceptance, reconstruction, trigger and selection.

[4] These assumptions have to be discussed to perform an accurate CP-asymmetry measurement, but are meaningless for the present discussion.

ambiguities of Eq. IV.9c andEq. IV.9d.

$$
\begin{aligned}
N\left(B^0 \to K^-\pi^+ X_s^0\right) &\simeq N_{D^0\to K^\pm\pi^\mp} && \text{(IV.9a)}\\
N\left(\overline{B}^0 \to K^+\pi^- \overline{X}_s^0\right) &\simeq N_{D^0\to K^\pm\pi^\mp} && \text{(IV.9b)}\\
N\left(B^0 \to K^+\pi^- X_s^0\right) &\simeq N_{D^0\to K^\pm\pi^\mp}\left(r_B^2\right. && \text{(IV.9c)}\\
&+ \left. 2\kappa_B r_B r_{D^0\to K^\pm\pi^\mp}\cos\left(\delta_B + \delta_{D^0\to K^\pm\pi^\mp} + \gamma\right)\right)\\
N\left(\overline{B}^0 \to K^-\pi^+ \overline{X}_s^0\right) &\simeq N_{D^0\to K^\pm\pi^\mp}\left(r_B^2\right. && \text{(IV.9d)}\\
&+ \left. 2\kappa_B r_B r_{D^0\to K^\pm\pi^\mp}\cos\left(\delta_B + \delta_{D^0\to K^\pm\pi^\mp} - \gamma\right)\right)
\end{aligned}
$$

The same analysis can be performed for the other decay modes and the corresponding equations are given in Eqs. IV.10-IV.11. The complete system of equations gives 9 equations for 6 unknowns[5].

$$
\begin{aligned}
N\left(B^0 \to K^-\pi^+\pi^0 X_s^0\right) &\simeq N_{D^0\to K^\pm\pi^\mp\pi^0} && \text{(IV.10a)}\\
N\left(\overline{B}^0 \to K^+\pi^-\pi^0 \overline{X}_s^0\right) &\simeq N_{D^0\to K^\pm\pi^\mp\pi^0} && \text{(IV.10b)}\\
N\left(B^0 \to K^+\pi^-\pi^0 X_s^0\right) &\simeq N_{D^0\to K^\pm\pi^\mp\pi^0}\left(r_B^2\right. && \text{(IV.10c)}\\
&+ \left. 2\kappa_{D^0\to K^\pm\pi^\mp\pi^0}\kappa_B r_B r_{D^0\to K^\pm\pi^\mp\pi^0}\cos\left(\delta_B + \delta_{D^0\to K^\pm\pi^\mp\pi^0} + \gamma\right)\right)\\
N\left(\overline{B}^0 \to K^-\pi^+\pi^0 \overline{X}_s^0\right) &\simeq N_{D^0\to K^\pm\pi^\mp\pi^0}\left(r_B^2\right. && \text{(IV.10d)}\\
&+ \left. 2\kappa_{D^0\to K^\pm\pi^\mp\pi^0}\kappa_B r_B r_{D^0\to K^\pm\pi^\mp\pi^0}\cos\left(\delta_B + \delta_{D^0\to K^\pm\pi^\mp\pi^0} - \gamma\right)\right)
\end{aligned}
$$

$$
\begin{aligned}
N\left(B^0 \to K^-\pi^+\pi^+\pi^- X_s^0\right) &\simeq N_{D^0\to K^\pm\pi^\mp\pi^+\pi^-} && \text{(IV.11a)}\\
N\left(\overline{B}^0 \to K^+\pi^-\pi^+\pi^- \overline{X}_s^0\right) &\simeq N_{D^0\to K^\pm\pi^\mp\pi^+\pi^-} && \text{(IV.11b)}\\
N\left(B^0 \to K^+\pi^-\pi^+\pi^- X_s^0\right) &\simeq N_{D^0\to K^\pm\pi^\mp\pi^+\pi^-}\left(r_B^2 + 2\kappa_{D^0\to K^\pm\pi^\mp\pi^+\pi^-}\right. && \text{(IV.11c)}\\
&\times \left. \kappa_B r_B r_{D^0\to K^\pm\pi^\mp\pi^+\pi^-}\cos\left(\delta_B + \delta_{D^0\to K^\pm\pi^\mp\pi^+\pi^-} + \gamma\right)\right)\\
N\left(\overline{B}^0 \to K^-\pi^+\pi^+\pi^- \overline{X}_s^0\right) &\simeq N_{D^0\to K^\pm\pi^\mp\pi^+\pi^-}\left(r_B^2 + 2\kappa_{D^0\to K^\pm\pi^\mp\pi^+\pi^-}\right. && \text{(IV.11d)}\\
&\times \left. \kappa_B r_B r_{D^0\to K^\pm\pi^\mp\pi^+\pi^-}\cos\left(\delta_B + \delta_{D^0\to K^\pm\pi^\mp\pi^+\pi^-} - \gamma\right)\right)
\end{aligned}
$$

IV.1.6 Ambiguities in the determination of γ

With only the $D^0 \to K^\pm\pi^\mp$ decay mode, only two equations Eq. IV.9c and Eq. IV.9d are meaningful for the determination of γ. Assuming that $N_{D^0\to K^\pm\pi^\mp}$ is determined by the two other equations of the system Eq. IV.9, we have three parameters, r_B, δ_B and γ. Assuming that r_B is known thanks by adding the $D^0 \to K^\pm\pi^\mp\pi^+\pi^-$ decay mode (the coherence is rather small in this decay mode), we are left with a well defined system of two equations and two unknowns.

[5] If by misfortune, all the δ_D phases and δ_B and γ were such that the number of events in the suppressed modes are fully correlated for each D decay mode, there would still be 6 equations for 6 unknowns and the system would still be solvable (which is not completely true due to the small value of $\kappa_{D^0\to K^\pm\pi^\mp\pi^+\pi^-}$). But this case is very unlikely since the δ_D strong phases are different for the different D decay modes.

This system of equations Eq. IV.9c and Eq. IV.9d, with $N_{D^0\to K^\pm\pi^\mp}$ and r_B constrained from other equations, allow to determine γ and δ_B simultaneously. However, since the angles are only contributing through their cosine, there are inherent ambiguities in their extraction. Indeed, the eight different changes of variables (the first one is the identical solution) given in Eq. IV.12 let Eq. IV.9 unchanged:

$$(\delta_B + \delta_{D^0\to K^\pm\pi^\mp}, \gamma) \to (\delta_B + \delta_{D^0\to K^\pm\pi^\mp}, \gamma) \quad \text{(IV.12a)}$$
$$(\delta_B + \delta_{D^0\to K^\pm\pi^\mp}, \gamma) \to (-\delta_B - \delta_{D^0\to K^\pm\pi^\mp}, -\gamma) \quad \text{(IV.12b)}$$
$$(\delta_B + \delta_{D^0\to K^\pm\pi^\mp}, \gamma) \to (\gamma, \delta_B + \delta_{D^0\to K^\pm\pi^\mp}) \quad \text{(IV.12c)}$$
$$(\delta_B + \delta_{D^0\to K^\pm\pi^\mp}, \gamma) \to (-\gamma, -\delta_B - \delta_{D^0\to K^\pm\pi^\mp}) \quad \text{(IV.12d)}$$
$$(\delta_B + \delta_{D^0\to K^\pm\pi^\mp}, \gamma) \to (\delta_B + \delta_{D^0\to K^\pm\pi^\mp} + \pi, \gamma + \pi) \quad \text{(IV.12e)}$$
$$(\delta_B + \delta_{D^0\to K^\pm\pi^\mp}, \gamma) \to (-\delta_B - \delta_{D^0\to K^\pm\pi^\mp} + \pi, -\gamma + \pi) \quad \text{(IV.12f)}$$
$$(\delta_B + \delta_{D^0\to K^\pm\pi^\mp}, \gamma) \to (\gamma + \pi, \delta_B + \delta_{D^0\to K^\pm\pi^\mp} + \pi) \quad \text{(IV.12g)}$$
$$(\delta_B + \delta_{D^0\to K^\pm\pi^\mp}, \gamma) \to (-\gamma + \pi, -\delta_B - \delta_{D^0\to K^\pm\pi^\mp} + \pi) \quad \text{(IV.12h)}$$

The first one is the true solution. The second correspond to a simultaneous sign-flip of $\delta_B + \delta_{D^0\to K^\pm\pi^\mp}$ and γ. The next two are the first two equations but for which $\delta_B + \delta_{D^0\to K^\pm\pi^\mp}$ is taken for γ and vice-versa. The last four equations are the first four, under which a phase π is added both to $\delta_B + \delta_{D^0\to K^\pm\pi^\mp}$ and γ, which corresponds to a 2π or 0 radian change in the arguments of the two master equations. These last four equations are in any case not distinguishable from the first four and correspond to an irreducible ambiguity.

These eight equivalent solutions to the problem, are very poorly resolved, due to statistical fluctuations in the favoured B decay modes of Eq. IV.9a and Eq. IV.9b. Since in these later two equations there is a sign-flip of $\delta_{D^0\to K^\pm\pi^\mp}$, equations of type Eq. IV.12a and Eq. IV.12b are partially resolved and only four strong ambiguities remain. The ambiguity on the determination of which value is γ and $\delta_B + \delta_{D^0\to K^\pm\pi^\mp}$ is further reduced by adding an additional mode to the system, for example $D^0 \to K^\pm\pi^\mp\pi^0$. The resolution of this ambiguity is also improved by constraining the normalization factors $N_{D^0\to K^\pm\pi^\mp\pi^0}$ and $N_{D^0\to K^\pm\pi^\mp\pi^+\pi^-}$ by $N_{D^0\to K^\pm\pi^\mp}$ and the ratio of efficiencies.

These ambiguities on the determination of $(\delta_B + \delta_{D^0\to K^\pm\pi^\mp}, \gamma)$ can be translated in ambiguities on the determination of (δ_B, γ) and the resolution power depends on δ_B. Tab. IV.2 show the different values of the ambiguities as a function of δ_B.

IV.1.7 Conclusion

The previous analysis shows that the sensitivity to γ comes from the suppressed decay modes and that the significance of these modes (and not the favoured modes) has to be optimized for

Solution	$\delta_B = -90°$	$\delta_B = 0°$	$\delta_B = 62°$
(δ_B, γ)	$(-90°, 70°)$	$(0°, 70°)$	$(62°, 70°)$
$(-\delta_B - 2\delta_D, -\gamma)$	$(46°, -70°)$	$(-44°, -70°)$	$(-106°, -70°)$
$(\gamma - \delta_D, \delta_B + \delta_D)$	$(-132°, 112°)$	$(-132°, -158°)$	$(-132°, -96°)$
$(-\gamma - \delta_D, -\delta_B - \delta_D)$	$(88°, -112°)$	$(88°, +158°)$	$(88°, +96°)$
$(\delta_B + \pi, \gamma + \pi)$	$(90°, -110°)$	$(180°, -110°)$	$(-118°, -110°)$
$(-\delta_B - 2\delta_D + \pi, -\gamma + \pi)$	$(-134°, 110°)$	$(136°, 110°)$	$(74°, 110°)$
$(\gamma - \delta_D + \pi, \delta_B + \delta_D + \pi)$	$(48°, -68°)$	$(48°, 22°)$	$(48°, 84°)$
$(-\gamma - \delta_D + \pi, -\delta_B - \delta_D + \pi)$	$(-92°, 68°)$	$(-92°, -22°)$	$(-92°, -84°)$

Table IV.2: Values of (δ_B, γ) for the eight ambiguous solutions for different values of δ_B.

the γ extraction. After having discussed the Monte Carlo selection strategy, a sensitivity study is performed and the previous considerations will be of primary importance to understand the behaviour of the fit.

IV.2 Expected sensitivity

IV.2.1 Fit procedure

Instead of measuring the total rate and the *CP* asymmetries or ratios, and extracting the parameters of interest from these measurements an other approach consisting of a direct fit of the observables defined in Eq. IV.7 is developed here. In practice for each channel ($D^0 \to K^\pm\pi^\mp$, $D^0 \to K^\pm\pi^\mp\pi^0$, $D^0 \to K^\pm\pi^\mp\pi^+\pi^-$), the events are split in two flavour sub-categories : K^{*0} and $\overline{K}^{*0}$, depending on the charge of the kaon from the K^*. In these two categories all the parameters are identical, only the number of events differ. The events are also split in two *sign* categories, in order to distinguish the events with same or opposite sign kaons in the final state. The number of signal events in the opposite sign sub-categories are expected to be smaller by roughly a factor r_B^2 compared to the same sign. Combinatorial background is also added to the toy Monte Carlo simulation. It is not expected to have the same level of background in the two categories nor the same shape. So the fit is left free to find different values for the shapes of the backgrounds in these two set sub-categories.

The chosen procedure for the fit follows a simultaneous extended maximum likelihood fit on all of the sub-categories. The signal PDF is a Gaussian with the mass and the width of the B^0 peak as parameters. As provided by the extended maximum likelihood method, the number of signal and background events in each sub-category are also extracted from the fit, knowing that the number of signal events is a function of the parameters of interest. The resulting PDF has finally the form given in equation Eq. IV.13, but what differs from usual extended fits is that the number of signal events fully depends on the parameters of the fit (N_s is not directly fitted

but only through the physical parameters due to the equation Eq. IV.14). The splitting of the parameters in channels is here implicit.

$$\begin{aligned} f\left(m_i|\theta, m_{Bd}, \sigma_{Bd}, p_{\text{sign}}, \text{sign, flavour}\right) &= \frac{N_s\left(\theta\right)}{N_s\left(\theta\right) + N_{b;\text{sign, flavour}}} G\left(m_i|m_{Bd}, \sigma_{Bd}\right) \\ &+ \frac{N_{b;\text{sign, flavour}}}{N_s\left(\theta\right) + N_{b;\text{sign, flavour}}} P\left(m_i|p_{\text{sign}}\right) \end{aligned} \tag{IV.13}$$

Where θ represent the set of parameters of interest which are fitted. This set contains at least γ, r_B, δ_B and N_0. Optionally the parameters coming from the decay of the D are added in this set.

$$\begin{aligned} N_s\left(\theta\right) &= N_0 \left(\frac{1+\epsilon_{\text{sign}}}{2}\left(1 + r_B^2 r_D^2\right) + \frac{1-\epsilon_{\text{sign}}}{2}\left(r_B^2 + r_D^2\right) \right. \\ &+ \left. 2\kappa_B r_B \kappa_D r_D \cos\left(\delta_B + \epsilon_{\text{sign}}\delta_D + \epsilon_{\text{flavour}}\gamma\right)\right) \end{aligned} \tag{IV.14}$$

Where ϵ_{sign} (resp. $\epsilon_{\text{flavour}}$) is fixed to $+1$ for the opposite sign (resp. B^0) sub-categories and to -1 for the same sign (resp. $\overline{B^0}$) sub-categories. Then the likelihood function is given by the equation IV.15, where we recall that the number of signal events in each sub-category depends on fitted parameters via the equation IV.14.

$$\mathcal{L} = \mathcal{P}_{\text{extended}} \prod_{\text{sign, flavour}} \prod_{i=1}^{N_{\text{bins}}} f\left(\theta, m_{Bd}, \sigma_{Bd}, p_{\text{sign}}|m_i, \text{sign, flavour}\right) \tag{IV.15}$$

$$\mathcal{P}_{\text{extended}} = \prod_{\text{sign, flavour}} \frac{\left(N_s\left(\theta\right) + N_{b;\text{sign, flavour}}\right)^{N_{\text{observed}}} e^{-\left(N_s(\theta) + N_{b;\text{sign, flavour}}\right)}}{N_{\text{observed}}!} \tag{IV.16}$$

The Poissonian multiplicative term $\mathcal{P}_{\text{extended}}$ of Eq. IV.16 tends to vary the numbers of signal and background events such that their sum is equal to the number of observed events in each sub-category. In our case, the number of signal events strongly depends on the values of the parameters of interest. Then this constraint interferes with the one coming from the PDF, and the equality cannot always be exactly verified. In simple terms, the fitter has to choose between adjusting the statistical fluctuations of signal events or the physical contribution of the PDF (the one due to γ and the strong phases). Nevertheless, the pull of the difference of the observed and fitted number of events will be plotted in the following as a crucial sanity check of the extended fitting method.

Alternatively, the fit can be performed by fitting the R_{ADS} and A_{ADS} parameters instead of the parameters of interest δ_B, r_B and γ. This allows to extract numbers independently for all the channels studied and thus provide useful input for further combination with other B decay modes.

Parameter	Value	Comment
$c^{\text{comb. background OS}}$	-1	free
$c^{\text{comb. background SS}}$	-1	free
μ_{B^0}	5.279	free
σ^{B^0}	0.015	free

Table IV.3: Summary of the shape parameters for the invariant mass distributions.

IV.2.2 Inputs to the fit

IV.2.2.1 Physical parameters

The physical parameters fixed and floated in the fit are summarized in the Tab. IV.1. Only r_B, δ_B and γ are let free in the fit. The r_D, δ_D and κ_D parameters are fixed in the present analysis, as if they would be perfectly known. Since this is not true (especially for the coherence factor in $D^0 \to K^{\pm}\pi^{\mp}\pi^{+}\pi^{-}$), they could also be let free to vary but constrained with Gaussians to the expected values (summarized in Tab. IV.1). The input value used for r_B is 0.26.

IV.2.2.2 Shape parameters

The parameters used to describe the invariant mass distributions are summarized in the Tab. IV.3. The combinatorial background slope is taken from the Monte Carlo simulation as well as the resolution of the B^0. The mean value for the B^0 is free to vary and the B_s^0 Gaussian mean value is constrained to be equal to the B^0 mass plus the mass difference between the B_s^0 and the B^0 from PDG [38].

IV.2.2.3 Number of events

The input values for the yields are summarized in the Tab. IV.4 and are taken from the Monte Carlo study developed in section IV.3. The number of favoured signal events is given to the fitter, that splits this number in two flavour categories and computes the number of suppressed mode yields using the physical value of r_B, δ_B and γ. The number of signal $D^0 \to K^-\pi^+\pi^0$ events is computed from the expected yield of resolved candidates (we neglect the contributions from merged π^0 for simplicity). The level of combinatorial background is assumed to be the same in favoured and suppressed modes, since no important difference was observed with the small amount of real data collected so far, see chapter V.

IV.2.3 Fit result

An example of fit result for an integrated luminosity of 1 fb^{-1} at $\sqrt{s} = 7$ TeV is shown in Figs. IV.1-IV.3. As described in the next subsection, the uncertainty on the determination of γ is

Parameter	Input value
$N_{B^0 \to \bar{D}^0 K^{*0}}$, with $D^0 \to K^-\pi^+$	468
$N_{B^0 \to \bar{D}^0 K^{*0}}$, with $D^0 \to K^-\pi^+\pi^0$	144
$N_{B^0 \to \bar{D}^0 K^{*0}}$, with $D^0 \to K^-\pi^+\pi^+\pi^-$	270
$N_{\text{comb. } D^0 \to K^-\pi^+}$	1779
$N_{\text{comb. } D^0 \to K^-\pi^+\pi^0}$	4979
$N_{\text{comb. } D^0 \to K^-\pi^+\pi^+\pi^-}$	1738

Table IV.4: Summary of the event yields as input of the fit.

rather large while the uncertainty on r_B is rather small (determination at better than 10 % with 5 fb^{-1}). This result was expected since it is a characteristic of the ADS method, see chapter I.

IV.2.4 Toy Monte Carlo study for 1 fb^{-1}

IV.2.4.1 Fitting r_B, δ_B and γ

Fig. IV.4 shows the fit result and the pull distributions for 400 toys assuming 1 fb^{-1} and taking into account for the combinatorial background, and Fig. IV.5 shows the same distributions for 900 toys assuming 5 fb^{-1} and no background. As mentioned in Tab. IV.2, there are two sets of four ambiguities separated by 180° in γ and δ_B. These two sets of solutions cannot be distinguished and an irreducible 180° ambiguity on γ remains in any case.

The four ambiguities, that can be distinguished by the use of other D decay modes, are located at 70°, 84°, 96°, 110°. These values are rather close to each other and difficult to resolve at low statistics. This is in particular the case with 1 fb^{-1}, for which the fit result is given in Fig. IV.4. The most probable value of γ is not located at the generated value of 70°, but between 80° and 90°, because the fit cannot resolve the ambiguities and fall in a minimum that tries to cope with the four possible solutions. The resulting errors of the fit are not well estimated due to the multiple local minima and the pull is not well behaved with a bias in addition to the not properly estimated uncertainties. Adding the two additional $D^0 \to K^\pm\pi^\mp\pi^+\pi^-$ and $D^0 \to K^\pm\pi^\mp\pi^0$ channels is not sufficient to resolve the ambiguities for two reasons: their statistical accuracy is not as good as $D^0 \to K^\pm\pi^\mp$ and they do provide similar constraints than $D^0 \to K^\pm\pi^\mp$ in the (δ_B, γ) plane, because of the similar values for δ_D, see section IV.2.5. The measurement of the δ_B parameter is problematic as well. The determination of r_B is rather good, but the errors are not well determined, as shown on Fig. IV.4.

Increasing the statistics by a factor 5 and assuming there is no background shows that the behaviour of the fit is better. Indeed, if the ambiguities are not fully resolved, the fit falls more frequently in the *good* solution, as shown on Fig. IV.5 in the distribution of the fit value for γ. It is also noticeable that δ_B is also better determined.

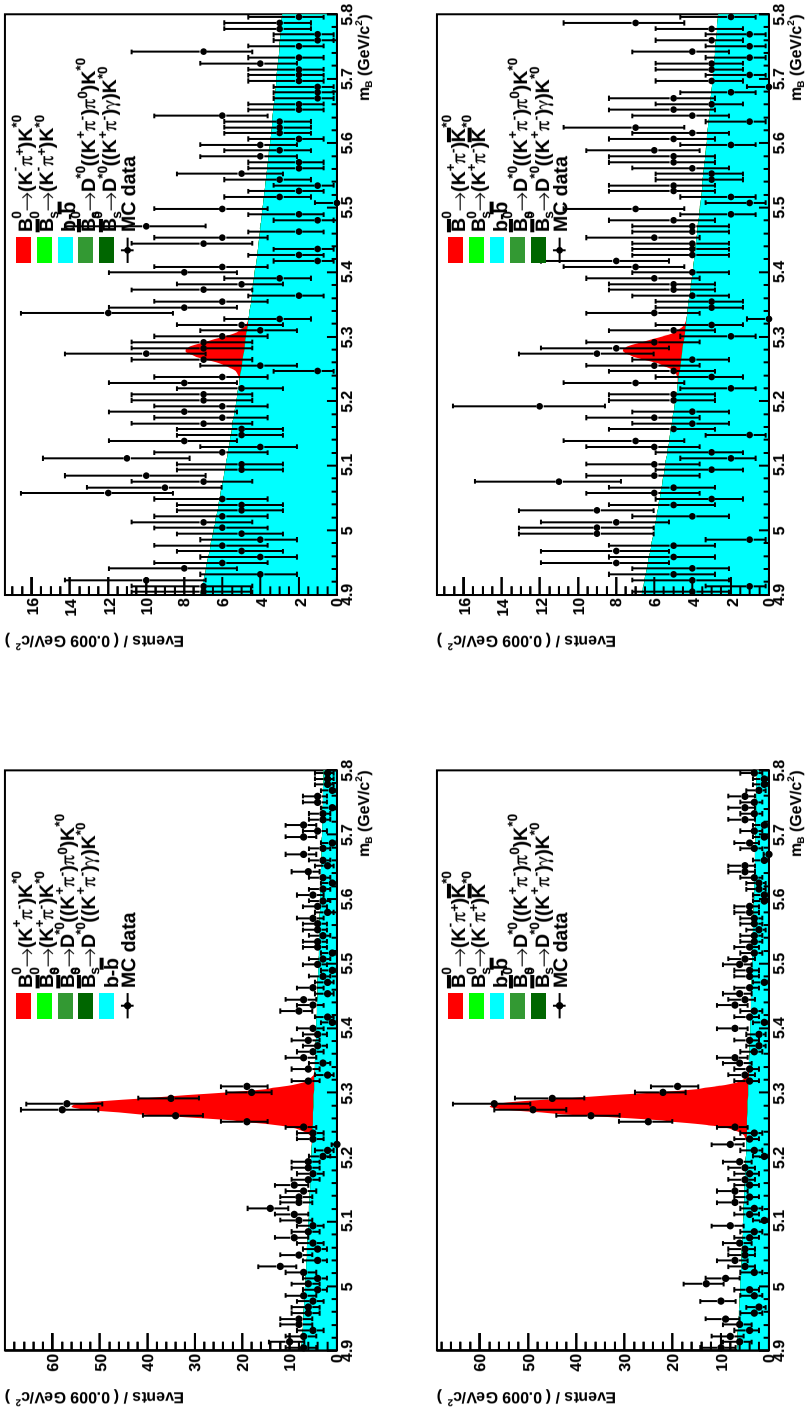

Figure IV.1: Fit result for 1 fb^{-1} for the $D^0 \to K^{\pm}\pi^{\mp}$ decay mode, only B^0 and $b\overline{b}$ inclusive background have been generated (the B_s^0 modes are not present in the figure).

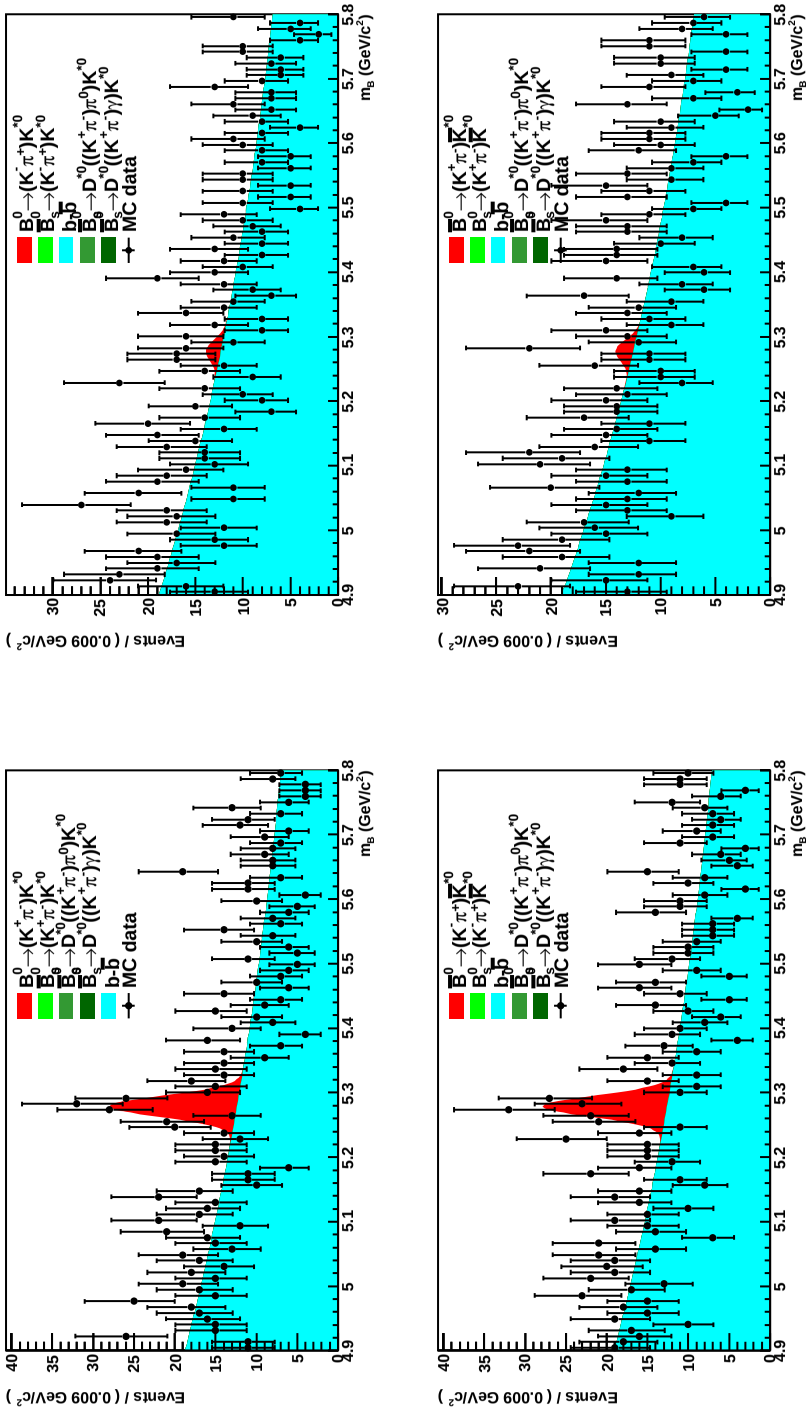

Figure IV.2: Fit result for 1 fb^{-1} for the $D^0 \to K^{\pm}\pi^{\mp}$ decay mode, only B^0 and $b\bar{b}$ inclusive background have been generated (the B^0_s modes are not present in the figure).

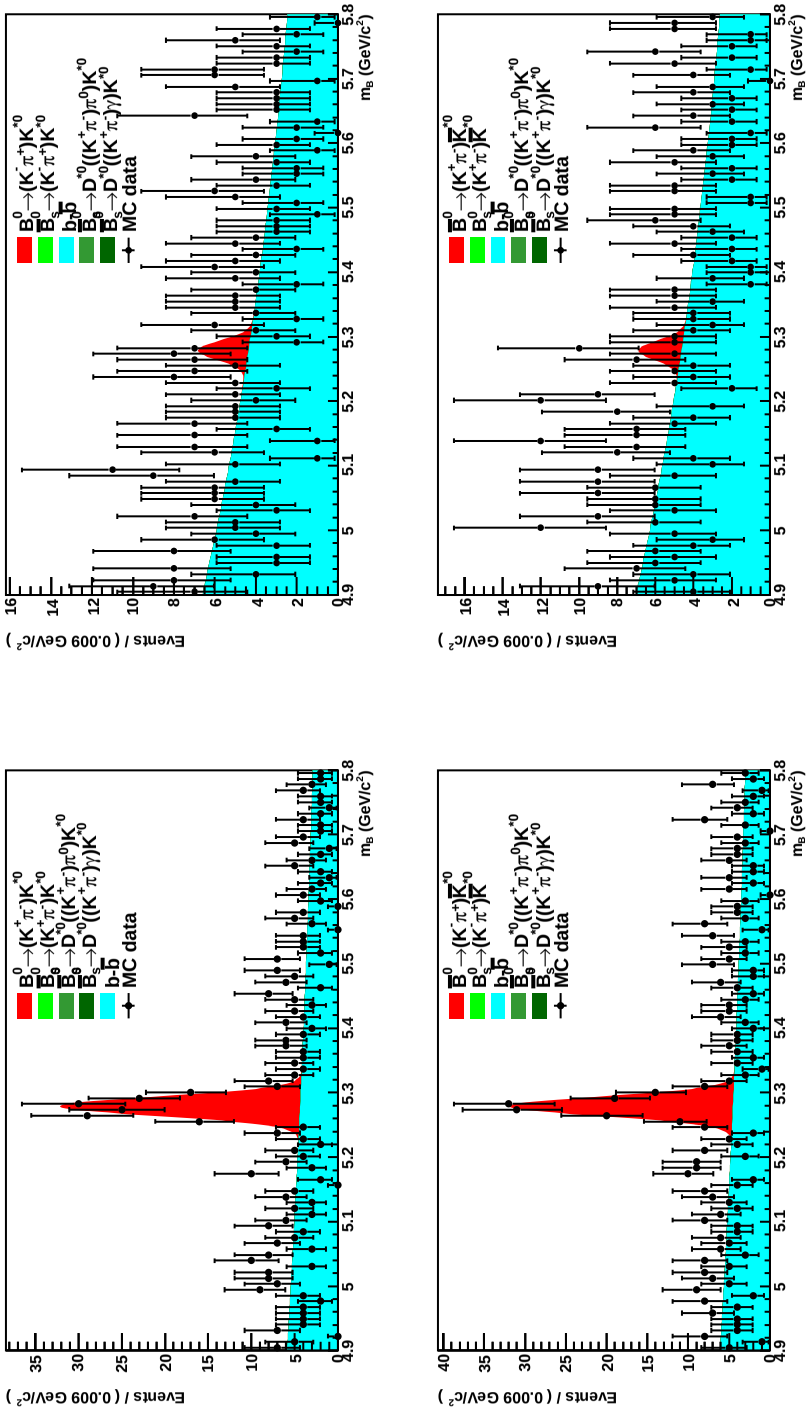

Figure IV.3: Fit result for 1 fb^{-1} for the $D^0 \to K^{\pm}\pi^{\mp}$ decay mode, only B^0 and $b\overline{b}$ inclusive background have been generated (the B_s^0 modes are not present in the figure).

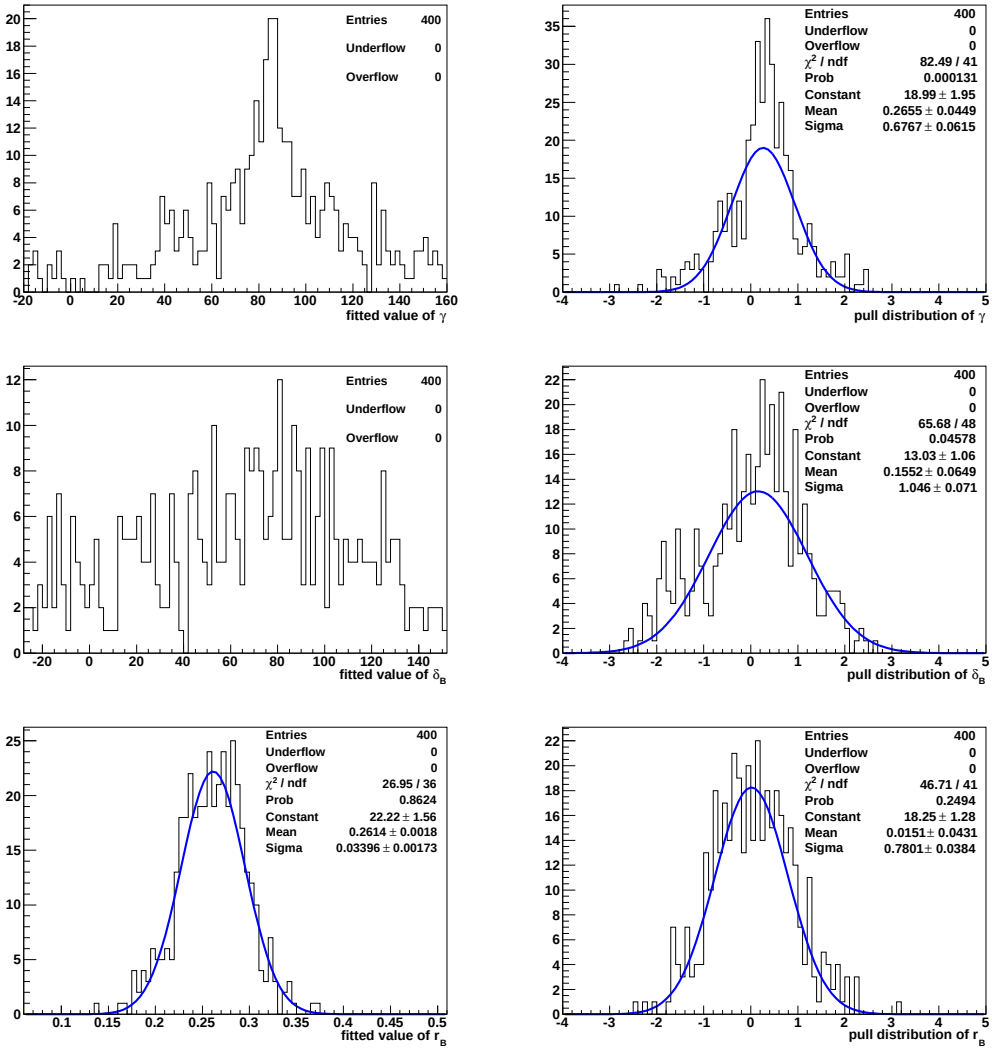

Figure IV.4: The fitted value and the pull distribution of γ (top), δ_B (middle) and r_B (bottom) for 1 fb^{-1}. Due to the irreducible 180° degree ambiguity the fitted value is shifted by 180° when out of the range $\gamma_{\text{generated}} \pm 90^\circ$, and as well for δ_B. The distributions are not well behaved as explained in the text.

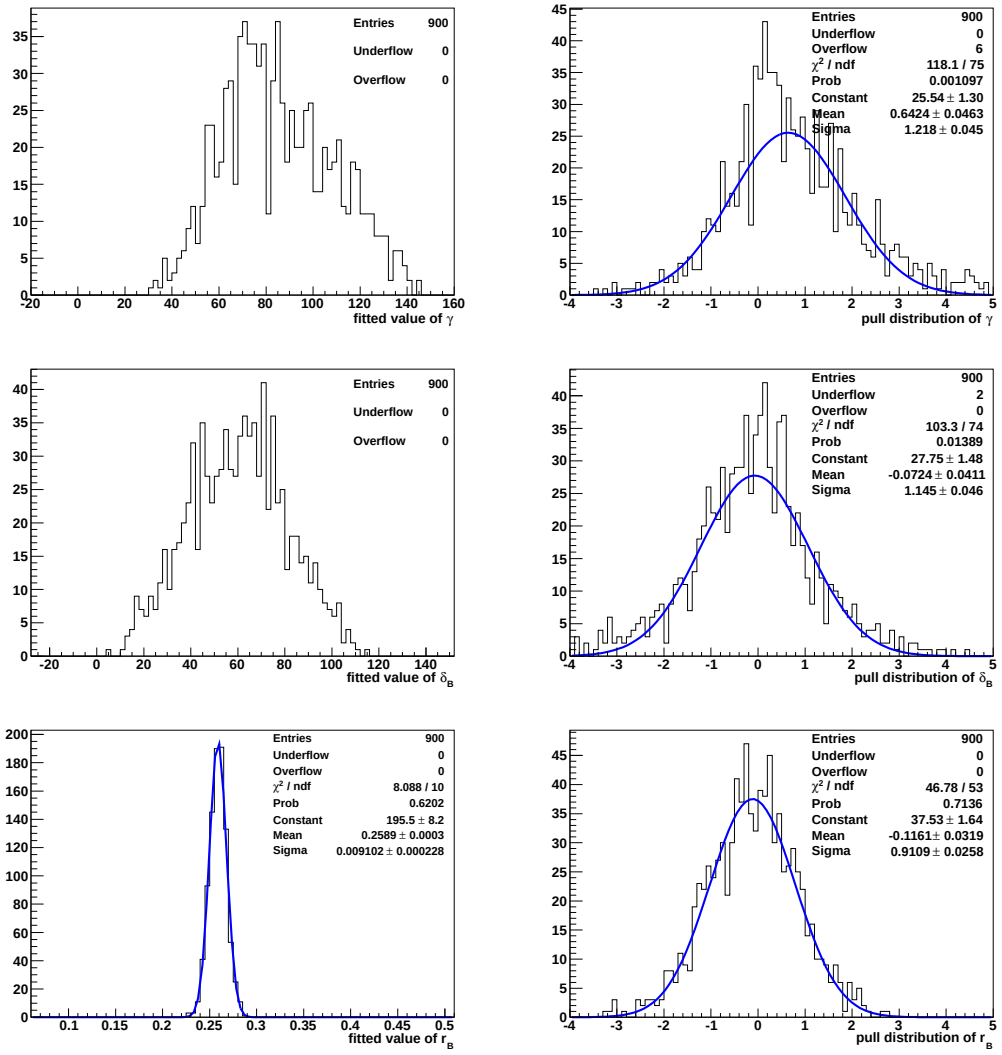

Figure IV.5: The fitted value and the pull distribution of γ (top), δ_B (middle) and r_B (bottom) for 5 fb^{-1} without background. Due to the irreducible 180° degree ambiguity the fitted value is shifted by 180° when out of the range $\gamma_{\text{generated}} \pm 90^\circ$, and as well for δ_B. The distributions are better behaved than at low statistics but ambiguities are still difficult to resolve as explained in the text.

This shows that it seems difficult to use this fitting procedure to give a constraint in the (γ, δ_B, r_B) hyperspace. As discussed in chapter I and section IV.2.5 it is necessary to add a constraint from the GLW method, at least to be able to *measure* γ. However, constraints on the R_{ADS} and A_{ADS} variables can be given, allowing to decorrelate the different D decay channels. An interesting alternative solution, not exploited here, is to provide constraints in the $(x_\pm, y_\pm)$ plane, as discussed in chapter I.

IV.2.4.2 Fitting R_{ADS}, A_{ADS}

Fitting R_{ADS}, A_{ADS} instead of the physics parameters, the result is much better behaved, thanks to the decorrelation of the different channels. The pulls are all well behaved and in particular for the asymmetries in Opposite Sign and R_{ADS}, as shown on Fig. IV.6.

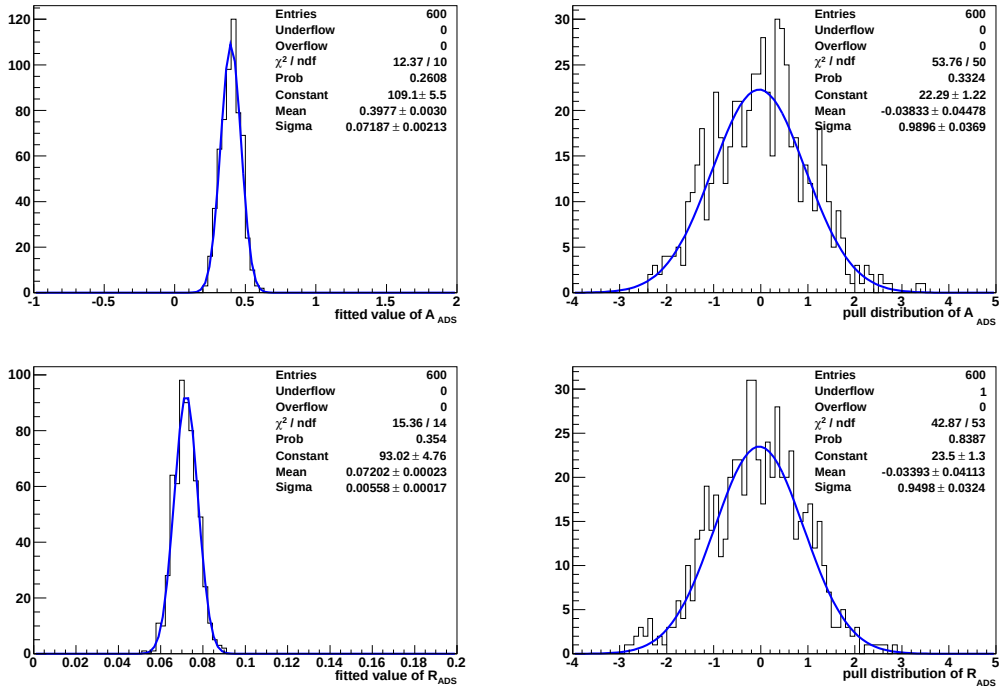

Figure IV.6: The fitted value and the pull distribution of A_{ADS} (top), and R_{ADS} (bottom) for 5 fb^{-1} without background for the $D^0 \to K^\pm\pi^\mp$ channel. The distributions are well behaved as explained in the text.

The fit results with 1 fb^{-1} are shown on Fig. IV.7. The A_{ADS} is not measured in the $D^0 \to K^\pm\pi^\mp$ channel (the relative uncertainty is of the order of 100 %). The result cannot be better for the other D modes. However R_{ADS} is measured at 2.5σ, which means that the suppressed modes (sensitive to γ) are seen. Note that this result scales with the statistics and previous measurement made in [50] for $B^0 \to DK^{*0}$ with $D^0 \to K^\pm\pi^\mp$ with the BABAR experiment.

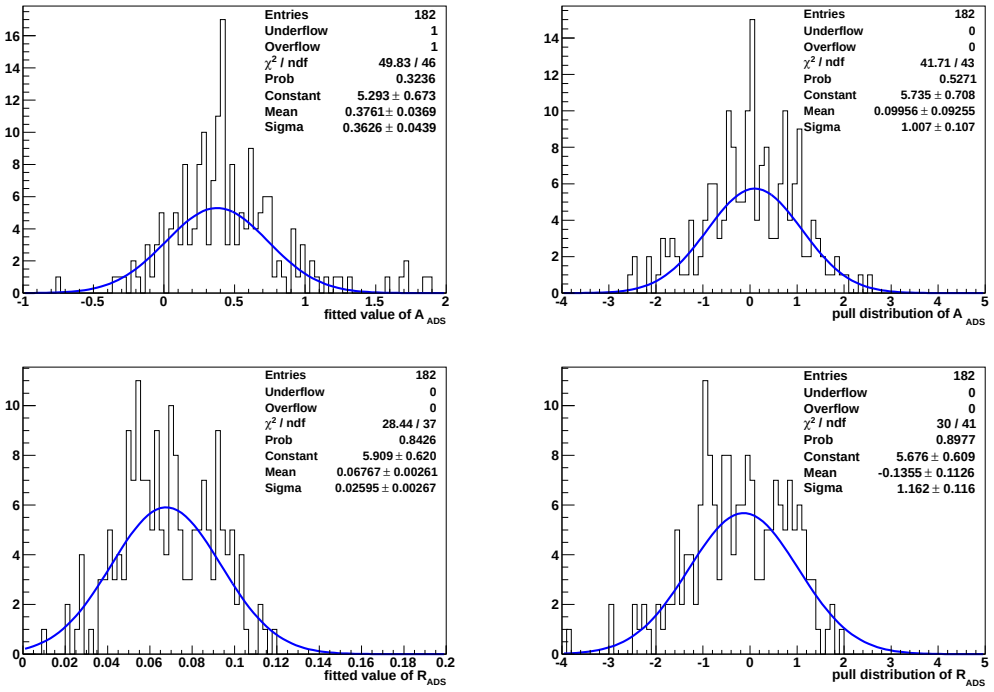

Figure IV.7: The fitted value and the pull distribution of A_{ADS} (top), and R_{ADS} (bottom) for 1 fb^{-1} with background for the $D^0 \to K^{\pm}\pi^{\mp}$ channel. The distributions are well behaved as explained in the text.

In order to provide a determination of γ, these decay channels will be combined with GLW channels as $D^0 \to K^{\pm}K^{\mp}$ and $D^0 \to \pi^{\pm}\pi^{\mp}$.

IV.2.5 Interpretation in Cartesian coordinates

The fact that $D^0 \to K^{\pm}\pi^{\mp}\pi^0$ and $D^0 \to K^{\pm}\pi^{\mp}\pi^+\pi^-$ do not provide significant information to the measurement of γ can be explained by looking at the constraints in the (x, y) plane, introduced in chapter I. The three constraints coming from the three different decay channels with the ADS method do not determine precisely $x_{\pm}$ and $y_{\pm}$, as illustrated (in the absence of background) on Fig. IV.8 for 1 fb^{-1} and 5 fb^{-1} in the (x_+, y_+) plane (similar constraints are available in the (x_-, y_-) plane). This representation is made assuming $\gamma = 70°$, $\delta_B = 62°$ and $r_B = 0.25$. The D decay parameters are assumed to be perfectly known and fixed to the central values summarized in Tab. IV.1. Each channel corresponds to one circle in the (x_+, y_+) plane with central values that depend on the coherence factor κ_D, the ratio of branching fractions of suppressed to favoured D decays r_D and the strong phase δ_D. The radius of each circle also depends on these parameters, but also on r_B, δ_B and γ. The drawing is made taking only into account the statistical uncertainty on the yields, that translates into an uncertainty on the radius of the circle. From the superimposition of the three circles one observes that x_+ and y_+

are poorly constrained even with 5 fb^{-1}. As shown in chapter I, the addition of GLW channels, help to resolve the degenerate solutions of $x_\pm$ and $y_\pm$.

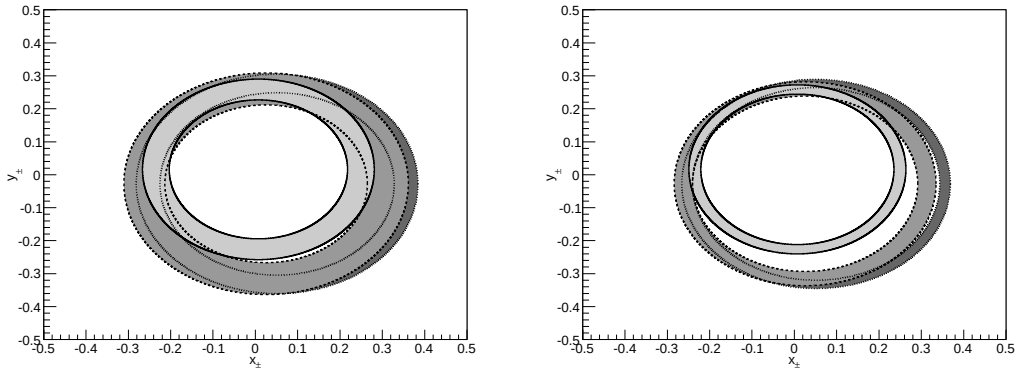

Figure IV.8: The constraints from ADS analysis with $D^0 \to K^\pm\pi^\mp$ (dark gray), $D^0 \to K^\pm\pi^\mp\pi^0$ (intermediate gray) and $D^0 \to K^\pm\pi^\mp\pi^+\pi^-$ (light gray) assuming 1 fb^{-1} and no background (left) or 5 fb^{-1} and no background (right) in the x_+, y_+ plane (similar curves are also valid for the x_-, y_- plane). The Cartesian parameter are poorly constrained by the ADS method alone.

IV.3 Monte Carlo studies for $B^0 \to DK^{*0}$

IV.3.1 Background from $\overline{B}{}^0_s \to D^{(*)}K^{*0}$ decays

When considering suppressed $B^0 \to D^0K^{*0}$ decays, for which $\mathcal{B}(B^0 \to D^0K^{*0}) < 1.1 \cdot 10^{-5}$ at 90 % C.L. [89], the potential backgrounds have to be looked at carefully. Apart from the combinatorial background[6], a significant part of the background comes from the partially reconstructed $B^0 \to DK^\pm\pi^\mp X$ decays. Their B invariant mass distribution is generally more peaky than the random association and dedicated analyses have to be performed. One of the potentially most dangerous background, not present at B factories, can come from partially reconstructed B^0_s decays such as $B^0_s \to D^*\overline{K}{}^{*0}$, indeed the B^0_s is only 90 MeV/c^2 above the B^0 mass, and the misreconstructed B^0_s can potentially lie in the B^0 signal mass window, that would reduce the significance of the $B^0 \to D^0K^{*0}$ signal and strongly modify the shape of the background.

Let us first consider the $B^0_s \to \overline{D}{}^0\overline{K}{}^{*0}$ decay which is of interest for two reasons that can be observed on the diagrams of Fig. IV.9:

- the final state is strictly identical to the final state of our channel of interest,
- the $B^0_s \to \overline{D}{}^0\overline{K}{}^{*0}$ is Cabibbo-allowed while $B^0 \to D^0K^{*0}$ is Cabibbo-suppressed.

[6]This background comes from random associations of tracks and is generally flat or exponentially distributed in B invariant mass.

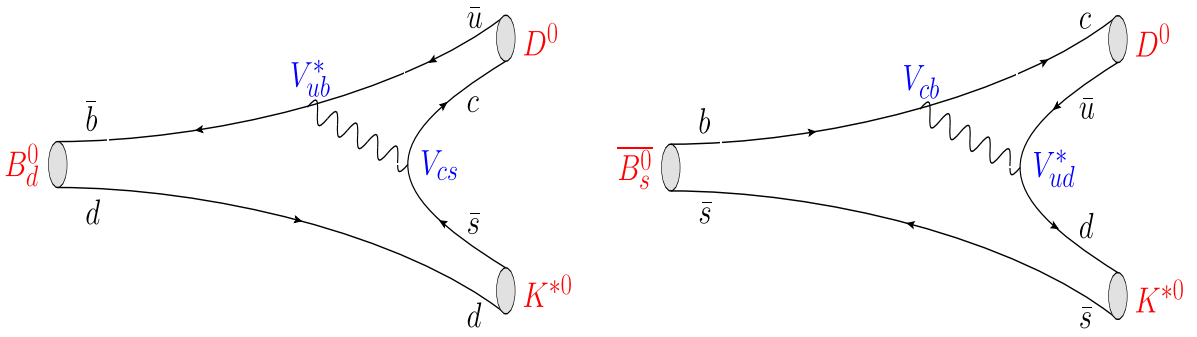

Figure IV.9: Feynman diagrams for the $B^0 \to D^0 K^{*0}$ decay (left) and the $\overline{B}^0_s \to D^0 K^{*0}$ decay (right) in the same final state. The B^0_s decay corresponds to a $b \to c$ transition while the B^0 decay occurs through a $b \to u$ transition and is the place where the sensitivity to γ comes from.

This channel has not yet been observed and thus the estimation of the pollution is difficult to estimate reliably. The branching fraction of this decay can however be estimated by using the current experimental constraints on $B^0 \to DK^{*0}$ decays and the CKM matrix elements. Up to λ^4 in the Wolfenstein parametrization [28, 35],

$$\left|\frac{\mathcal{A}\left(\overline{B}^0_s \to D^0 K^{*0}\right)}{\mathcal{A}\left(B^0 \to D^0 K^{*0}\right)}\right|^2 = \left|\frac{V^*_{cb} V_{ud}}{V_{ub} V^*_{cs}}\right|^2 = \frac{1}{\lambda^2\left(\overline{\rho}^2 + \overline{\eta}^2\right)} \simeq 120 \tag{IV.17}$$

which gives, taking into account for the fragmentation fractions $\frac{f_d}{f_s} = 3.71 \pm 0.47$ the ratio of number of produced events :

$$\frac{N_{\text{produced}}(\overline{B}^0_s \to D^0 K^{*0})}{N_{\text{produced}}(B^0 \to D^0 K^{*0})} = \left|\frac{\mathcal{A}(\overline{B}^0_s \to D^0 K^{*0})}{\mathcal{A}(B^0 \to D^0 K^{*0})}\right|^2 \frac{f_s}{f_d} = 32 \pm 4, \tag{IV.18}$$

where the error only takes into account the uncertainty on the ratio of fragmentation fractions. An alternative way to estimate the number of produced $B^0_s \to \overline{D}^0 \overline{K}^{*0}$ events is to use $\mathcal{B}(B^0 \to \overline{D}^0 \rho^0) = (3.2 \pm 0.5) \cdot 10^{-4}$ [38, 90], $\mathcal{B}(B^0 \to \overline{D}^0 K^{*0}) = (4.2 \pm 0.6) \cdot 10^{-5}$ [38, 89, 91] and to assume that $\mathcal{B}(B^0 \to \overline{D}^0 \rho^0) = \mathcal{B}(B^0_s \to \overline{D}^0 \overline{K}^{*0})$, since only the *spectator quark* changes and to take $\frac{\mathcal{B}(B^0 \to \overline{D}^0 K^{*0})}{\mathcal{B}(B^0 \to D^0 K^{*0})} = \frac{1-\lambda^2}{\lambda^2} \simeq 18$. This leads to

$$\frac{N_{\text{produced}}(\overline{B}^0_s \to D^0 K^{*0})}{N_{\text{produced}}(B^0 \to D^0 K^{*0})} = \frac{\mathcal{B}(\overline{B}^0_s \to D^0 K^{*0})}{\mathcal{B}(B^0 \to \overline{D}^0 \rho^0)} \frac{\mathcal{B}(B^0 \to \overline{D}^0 \rho^0)}{\mathcal{B}(B^0 \to \overline{D}^0 K^{*0})} \frac{\mathcal{B}(B^0 \to \overline{D}^0 K^{*0})}{\mathcal{B}(B^0 \to D^0 K^{*0})} \frac{f_s}{f_d} \simeq 37 \pm 8, \tag{IV.19}$$

where the error is only the error due the measured branching fractions. Both estimates are consistent. Therefore, assuming identical detection efficiencies for these two decays, one expects to observe a peak about 30 times larger than B^0 mass peak and 90 MeV/c^2 above it. With a B mass resolution of the order of 15 MeV/c^2, the $B^0_s \to \overline{D}^0 \overline{K}^{*0}$ pollution under the B^0 peak is not a drawback for the measurement but the validation of the signal B^0 invariant mass distributions will require a careful validation on data.

However the decay mode $B_s^0 \to \overline{D}^{*0}\overline{K}^{*0}$ where a γ or a π^0 from the D^{*0} decay is not reconstructed can induce a significant deterioration of the S/B of the signal $B^0 \to D^0 K^{*0}$ decay. The polarisation will be assumed in the following to be equally distributed on the three different polarisation amplitudes. This assumption may be wrong and is correlated with the invariant mass distribution, and thus would affect the shape of the background under the signal and the amount of background. Using the existing limits $\mathcal{B}(B^0 \to \overline{D}^{*0}\rho^0) < 5.1 \cdot 10^{-4}$ [92] and $\mathcal{B}(B^0 \to \overline{D}^{*0}K^{*0}) < 6.9 \cdot 10^{-5}$ [91][7], we obtain

$$\mathcal{B}(B_s^0 \to \overline{D}^{*0}\overline{K}^{*0}) = \mathcal{B}(B^0 \to \overline{D}^{*0}K^{*0}) \left|\frac{V_{ud}^*}{V_{us}}\right|^2 < 1.2 \cdot 10^{-3} \text{ at } 90\ \% \text{ C.L} \quad \text{(IV.20a)}$$

$$\mathcal{B}(B_s^0 \to \overline{D}^{*0}\overline{K}^{*0}) = \mathcal{B}(B^0 \to \overline{D}^{*0}\rho^0) < 5.1 \cdot 10^{-4} \text{ at } 90\ \% \text{ C.L.} \quad \text{(IV.20b)}$$

$$\mathcal{B}(B^0 \to D^0 K^{*0}) \simeq r_B^2 \mathcal{B}(B^0 \to \overline{D}^0 K^{*0}) \simeq 2.6 \cdot 10^{-6} \quad \text{(IV.20c)}$$

$$\frac{\mathrm{N}_{\text{produced}}(B_s^0 \to \overline{D}^{*0}\overline{K}^{*0})}{\mathrm{N}_{\text{produced}}(B^0 \to D^0 K^{*0})} = \frac{f_s}{f_d}\frac{\mathcal{B}(B_s^0 \to \overline{D}^{*0}\overline{K}^{*0})}{\mathcal{B}(B^0 \to D^0 K^{*0})} \quad \text{(IV.20d)}$$

$$< 130 \text{ at } 90\ \% \text{ C.L. using } \mathcal{B}(B^0 \to \overline{D}^{*0}K^{*0}) \quad \text{(IV.20e)}$$

$$< 55 \text{ at } 90\ \% \text{ C.L. using } \mathcal{B}(B^0 \to \overline{D}^{*0}\rho^0). \quad \text{(IV.20f)}$$

In the following, the detection efficiencies will be estimated for these decays and the invariant mass distributions on Monte Carlo will be described. This will provide a more accurate estimate of the level of this background.

IV.3.2 Monte Carlo study with $D^0 \to K^-\pi^+$

The selection is meant to optimize $S/\sqrt{S+B}$ keeping in mind reasonable values for the cuts. The optimization is performed on the $B^0 \to \overline{D}^0 K^{*0}$ decay mode, assuming that the $B_s^0 \to \overline{D}^0\overline{K}^{*0}$ mode has the same distributions[8]. In the following the D^0 is always reconstructed in $K^-\pi^+$, the DCS $K^+\pi^-$ mode is neglected since it will only contribute for less than 1 % (which is far below the expected systematic uncertainties). The K^{*0} is always reconstructed in $K^+\pi^-$. The charge conjugate modes are always implied.

IV.3.2.1 Software and Monte Carlo samples

The analysis uses the standard LHCb software (see section II.2.4). We have used 201008 simulated $B^0 \to \overline{D}^0 K^{*0}$ signal events (where the $\overline{D}^0$ and K^{*0} are both forced to decay in $K^+\pi^-$) and 1445257 $b\bar{b}$-inclusive stripped background events corresponding to 52 millions of events[9]. The stripping efficiency was found to be (2.770 ± 0.002) %. We have also generated privately 91047

[7] This analysis sets an upper limit from the observation of $8.6^{+4.2}_{-3.6}$ events using 85 millions $B\overline{B}$ pairs. There is no published update of this upper limit.

[8] This can be checked by looking at the distributions shown in chapter V.

[9] 1444659 of these events have been processed, and then selection efficiencies are quoted according to this number in the following. The yields will be computed from the selection efficiency and the stripping efficiency.

and 94002 specific $\overline{B}{}^0_s \to D^{*0}K^{*0}$ events with $D^{*0} \to D^0\gamma$ and $D^{*0} \to D^0\pi^0$ respectively. For both of these data samples, the $\overline{D}{}^0$ and K^{*0} were both forced to decay in $K^+\pi^-$. These events are also generated with equiprobable helicity states.

IV.3.2.2 Stripping preselection

Once the reconstruction is made a preselection (called stripping) is applied to reduce the data sample prior to the offline analysis. The main request for the preselection is to achieve a good background rejection, without removing too much the signal. This is achieved by selecting good tracks (low χ^2_{track}) with high momentum ($p > 2$ GeV/c) and large minimal impact parameter[10] (IP) with respect to all reconstructed primary vertices (PV). Then the D^0 and K^{*0} candidates are built requiring a large transverse momentum (p_T) and good fit quality for the decay vertexes of these resonances. The D^0 decay vertex is also required to be well separated from the PV, by 6 standard deviations. The K^{*0} preselection is rather tight compared to the D^0 to reduce the amount of combinatorics under this broad resonance. Then the B candidate is reconstructed by requiring a small IP with respect to the PV, a good decay vertex fit quality, a good collinearity of its line of flight and its reconstructed momentum ($\cos\theta_{\text{pointing}} = \frac{\vec{p}_{B_d} \cdot (\vec{v}_{\text{vertex}} - \vec{v}_{\text{PV}})}{|\vec{p}_{B_d}||\vec{v}_{\text{vertex}} - \vec{v}_{\text{PV}}|}$ where $\vec{v}$ is a $3D$ position vector, see Fig. IV.10), and a very good separation of the decay vertex position with respect to the PV. Mass window cuts are applied on all resonances, but are kept quite loose. The one for the B is asymmetric in order to keep 500 MeV/c margin under the B^0 and above the B^0_s masses.

After the stripping, summarized in the table IV.5, 14610 signal events, 6876 $b\overline{b}$-inclusive events, 6686 and 7896 $B^0_s \to \overline{D}{}^{*0}\overline{K}{}^{*0}$ events with $D^{*0} \to D^0\gamma$ and $D^{*0} \to D^0\pi^0$ respectively are preselected.

IV.3.2.3 Selection

The selection, aimed at achieving the best $B^0 \to DK^{*0}$ signal significance $S/\sqrt{S+B}$[11], is summarized in table IV.6 and the corresponding figures are IV.11-IV.18. The mass window is given in section IV.3.3 with the parametrization of the shapes. It is based on adding particle identification cuts (differences $\text{DLL}_{\text{K}\pi}$ in logarithms of likelihood for kaons and pions hypotheses) to the preselected candidates, tightening some preselection cuts and adding requirements on the helicity[12] and mass windows of the D^0 and the K^{*0}. The number quoted for $b\overline{b}$ inclusive events does not contain neither B^0 signal nor the specific $\overline{B}{}^0_s \to D^{*0}K^{*0}$ decays considered in

[10] Defined as the distance of minimal approach with respect to some $3D$ point, here the primary vertex.

[11] This selection has been optimized comparing signal and background distributions, without using a dedicated algorithm, and is thus probably suboptimal

[12] In $B \to PV$ decays the vector meson is produced in a specific helicity state, and thus the decay $V \to PP$ exhibits a specific helicity distribution. The helicity angle θ^* is defined as the angle made by the line of flight of the K meson in the K^{*0} mother reference frame with respect to the direction of flight of the K^{*0}.

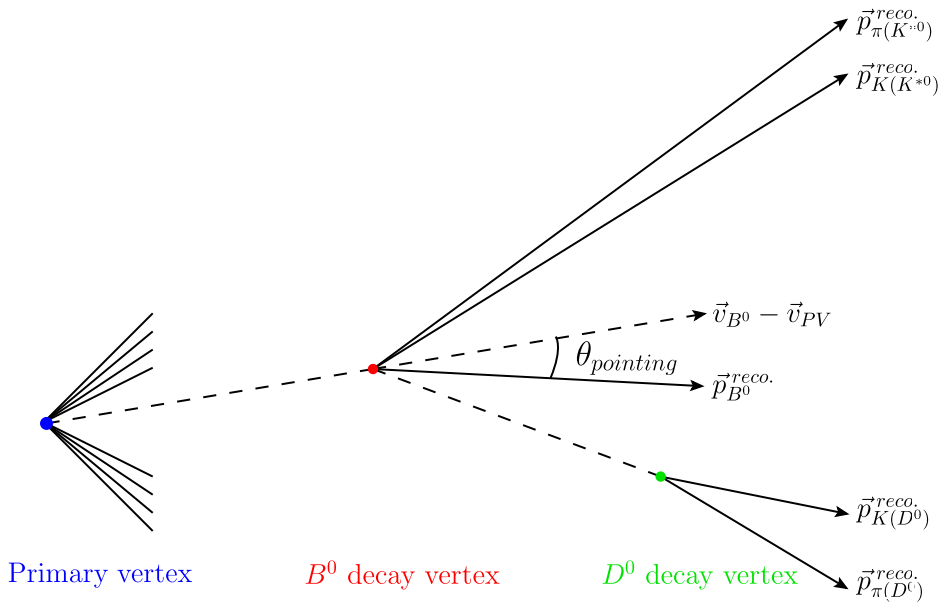

Figure IV.10: Schematic describing how the *pointing angle* is computed.

Particle	Variable	Cut value
π_{D^0} or K_{D^0}	χ^2_{track} per d.o.f.	< 10
	p_T	> 250 MeV/c
	p	> 2 GeV/c
	min $\chi^2_{\text{IP to PV}}$	> 4
D^0	$\lvert m_{\text{reco}} - m_{\text{pdg}}\rvert$	< 50 MeV/c^2
	p_T	> 1000 MeV/c
	χ^2_{vertex} per d.o.f.	< 10
	$\chi^2_{\text{vertex distance to PV}}$	> 36
$\pi_{K^{*0}}$ or $K_{K^{*0}}$	χ^2_{track} per d.o.f.	< 10
	p_T	> 300 MeV/c
	p	> 2 GeV/c
	min $\chi^2_{\text{IP to PV}}$	> 6.25
K^{*0}	$\lvert m_{\text{reco}} - m_{\text{pdg}}\rvert$	< 150 MeV/c
	p_T	> 600 MeV/c
	χ^2_{vertex} per d.o.f.	< 12
	min $\chi^2_{\text{IP to PV}}$	> 4
B^0	m_{reco}	> 4800 MeV/c^2 and < 5900 MeV/c^2
	$\chi^2_{\text{IP to PV}}$	< 12.25
	$\cos\theta_{\text{pointing}}$	> 0.9997
	χ^2_{vertex} per d.o.f.	< 10
	$\chi^2_{\text{vertex distance to PV}}$	> 100

Table IV.5: Summary of the stripping selection applied on the events, prior to the offline analysis.

Parameter	Cut Value	$B^0 \to \overline{D}^0 K^{*0}$	$b\overline{b}$	$\overline{B}^0_s \to D^{*0}K^{*0}$ $D^{*0} \to D^0\gamma$	$D^{*0} \to D^0\pi^0$
Candidates	before selection	17441	11066	7991	9559
$\mathrm{DLL}_{K\pi}$ of $K_{K^{*0}}$	> 2	15951	3133	7353	8770
$\mathrm{DLL}_{K\pi}$ of K_{D^0}	> 2	14474	934	6676	7983
$\mathrm{DLL}_{K\pi}$ of $\pi_{K^{*0}}$	< 2 and $\neq -1000$	12928	520	5992	7153
$\mathrm{DLL}_{K\pi}$ of π_{D^0}	< 2 and $\neq -1000$	11550	330	5405	6368
p_T of $K_{K^{*0}}$	> 400 MeV/c	11288	305	5339	6291
p_T of K_{D^0}	> 400 MeV/c	10923	249	5138	6067
χ^2_{vertex}per d.o.f. of B^0	< 4	10548	122	4977	5855
χ^2_{vertex}per d.o.f. of D^0	< 5	10165	100	4782	5639
$\min \chi^2_{\mathrm{IP\ to\ PV}}$ of D^0	> 2	10121	94	4757	5617
$\chi^2_{\mathrm{IP\ to\ PV}}$ of $K_{K^{*0}}$	> 3	10013	76	4725	5553
$\chi^2_{\mathrm{IP\ to\ PV}}$ of $\pi_{K^{*0}}$	> 3	9878	65	4658	5475
$\lvert m^{\mathrm{reco}}_{K^{*0}} - m^{\mathrm{PDG}}_{K^{*0}} \rvert$	< 75 MeV/c^2	8836	25	4167	4882
$\lvert m^{\mathrm{reco}}_{D^0} - m^{\mathrm{PDG}}_{D^0} \rvert$	< 15 MeV/c^2	8357	9	3933	4600
$\lvert \cos\theta^*_{K_{K^{*0}}} \rvert$	> 0.4	7634	3	2072	2529
$\cos\theta_{\mathrm{pointing}B^0}$	> 0.99995	7208	0	1925	2374
$\lvert m^{\mathrm{reco}}_{B^0} - m^{\mathrm{PDG}}_{B^0} \rvert$	< 50 MeV/c^2	7130	0	518	3

Table IV.6: Summary of the selection cuts applied on the preselected events with the number of events remaining after each cut. The number of $\overline{B}^0_s \to D^{*0}K^{*0}$ with $D^{*0} \to D^0\pi^0$ is extremely small in the invariant mass region of the signal since this, in this decay, the π^0 is rather monochromatic, which is not the case of the γ. The approximate integrated luminosity corresponding to the number of generated $b\overline{b}$ events used for this study is approximately 0.4 pb^{-1} assuming $\sigma_{b\overline{b}} = 280$ µb .

this document. In order to compute the yields, one has removed the multiple candidates by keeping the candidate that minimizes χ^2 given in eq. IV.21. 2 % of the selected signal events had more than one candidate after the full selection.

$$\chi^2 = \frac{\left(m_{D^0} - m^{\mathrm{PDG}}_{D^0}\right)^2}{\sigma^2_{D^0}} + \frac{\left(m_{K^{*0}} - m^{\mathrm{PDG}}_{K^{*0}}\right)^2}{\sigma^2_{K^{*0}}} \tag{IV.21}$$

The number of selected events (after having removed the multiple candidates) is given in table IV.7. The L0 and HLT1 (described in section II.2.3) combined efficiency is taken from reference [93] where the setting is described.

IV.3.2.4 Expected yields and S/B estimate

The estimate of the number of events for $\overline{B}^0 \to D^0\overline{K}^{*0}$ signal and $\overline{B}^0_s \to D^0K^{*0}$, $B^0_s \to \overline{D}^{*0}\overline{K}^{*0}$ with $D^{*0} \to D^0\gamma$ and $D^{*0} \to D^0\pi^0$, and $b\overline{b}$-inclusive backgrounds are given for different invariant mass windows. The computation of $N_{B^0 \to \overline{D}^0 K^{*0}}$ is directly done from the selection. Then $N_{B^0 \to \overline{D}^0(K^+\pi^-)K^{*0}}$ (contribution of the DCS decay of the D^0 to the favoured B^0 decay) and

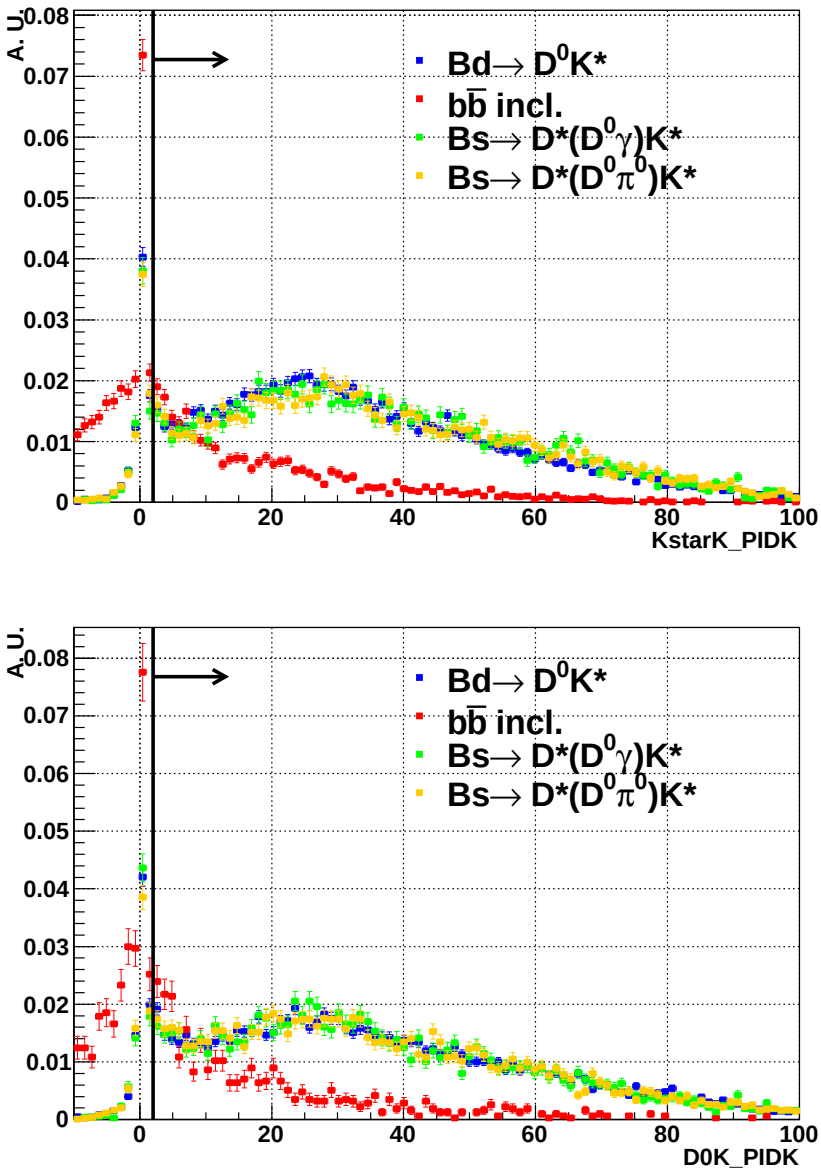

Figure IV.11: Distribution of the $\mathrm{DLL}_{\mathrm{K}\pi}$ variable for the kaons coming from the K^{*0} (top) and D^0 (bottom). The final selection cut is materialized by the vertical bar and the arrow showing the events kept after the cut. In each plot, the red points corresponds to $b\bar{b}$-inclusive background, the blue points correspond to the $B^0 \to \overline{D}^0 K^{*0}$ events and the green and yellow points respectively correspond to the $\overline{B}^0_s \to D^{*0} K^{*0}$ with $D^{*0} \to D^0\gamma$ and $D^{*0} \to D^0\pi^0$ respectively. The $\overline{B}^0_s \to D^{*0} K^{*0}$ and $B^0 \to \overline{D}^0 K^{*0}$ are compatible within statistical uncertainties.

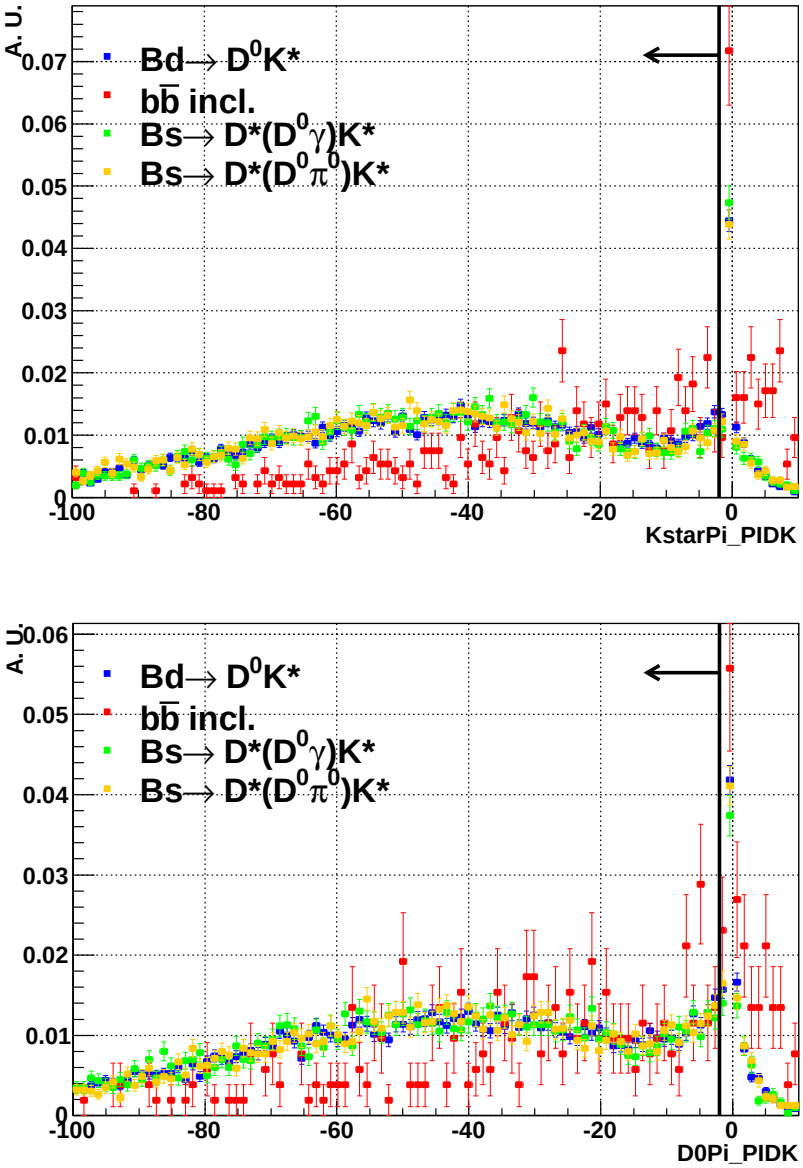

Figure IV.12: Distribution of the $\mathrm{DLL}_{\mathrm{K}\pi}$ variable for the pions coming from the K^{*0} (top) and D^0 (bottom). The final selection cut is materialized by the vertical bar and the arrow showing the events kept after the cut. In each plot, the red points corresponds to $b\bar{b}$-inclusive background, the blue points correspond to the $B^0 \to \overline{D}^0 K^{*0}$ events and the green and yellow points respectively correspond to the $\overline{B}^0_s \to D^{*0}K^{*0}$ with $D^{*0} \to D^0\gamma$ and $D^{*0} \to D^0\pi^0$ respectively. The $\overline{B}^0_s \to D^{*0}K^{*0}$ and $B^0 \to \overline{D}^0 K^{*0}$ are compatbile within statistical uncertainties.

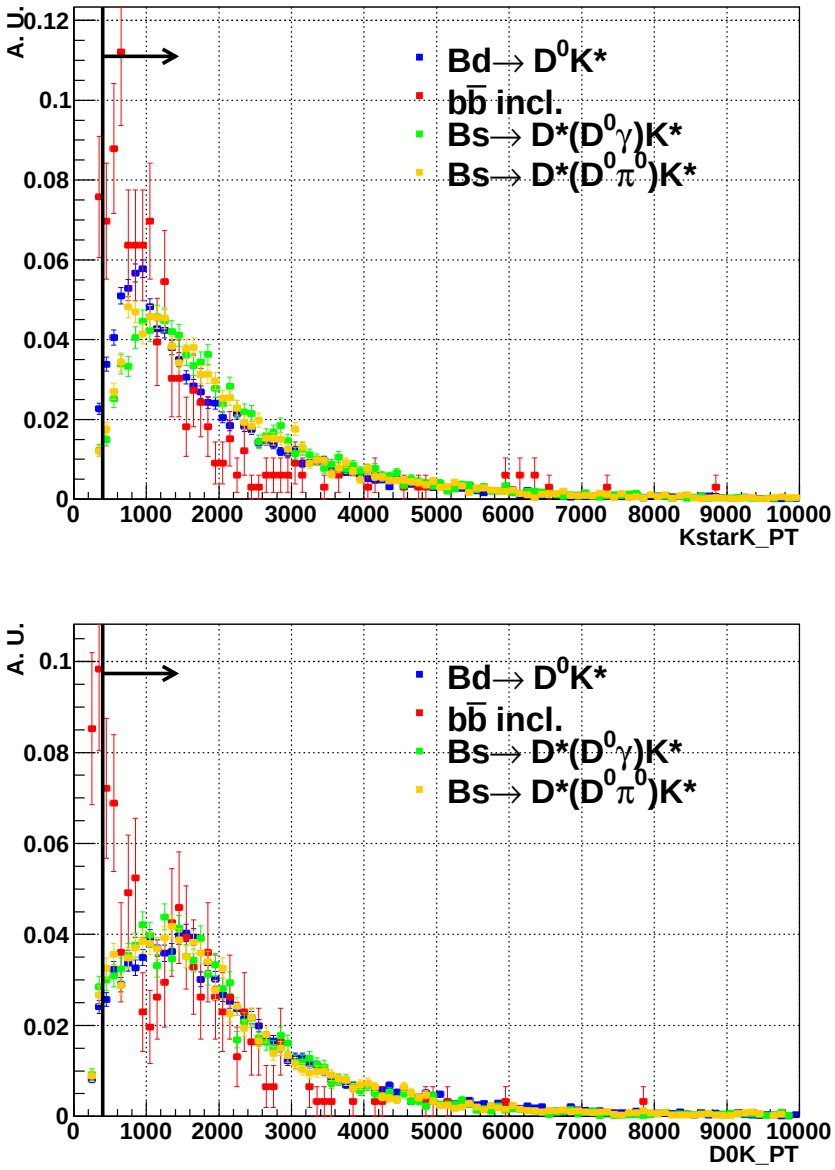

Figure IV.13: Distributions of the transverse momenta of the kaon from the K^{*0} (top) and D^0 (bottom) decays. The final selection cut is materialized by the vertical bar and the arrow showing the events kept after the cut. In each plot, the red points corresponds to $b\bar{b}$-inclusive background, the blue points correspond to the $B^0 \to \overline{D}^0 K^{*0}$ events and the green and yellow points respectively correspond to the $\overline{B}^0_s \to D^{*0} K^{*0}$ with $D^{*0} \to D^0\gamma$ and $D^{*0} \to D^0\pi^0$ respectively. The slightly harder p_T distributions of the K^{*0} daughter for the $\overline{B}^0_s \to D^{*0} K^{*0}$ decays should be noticed.

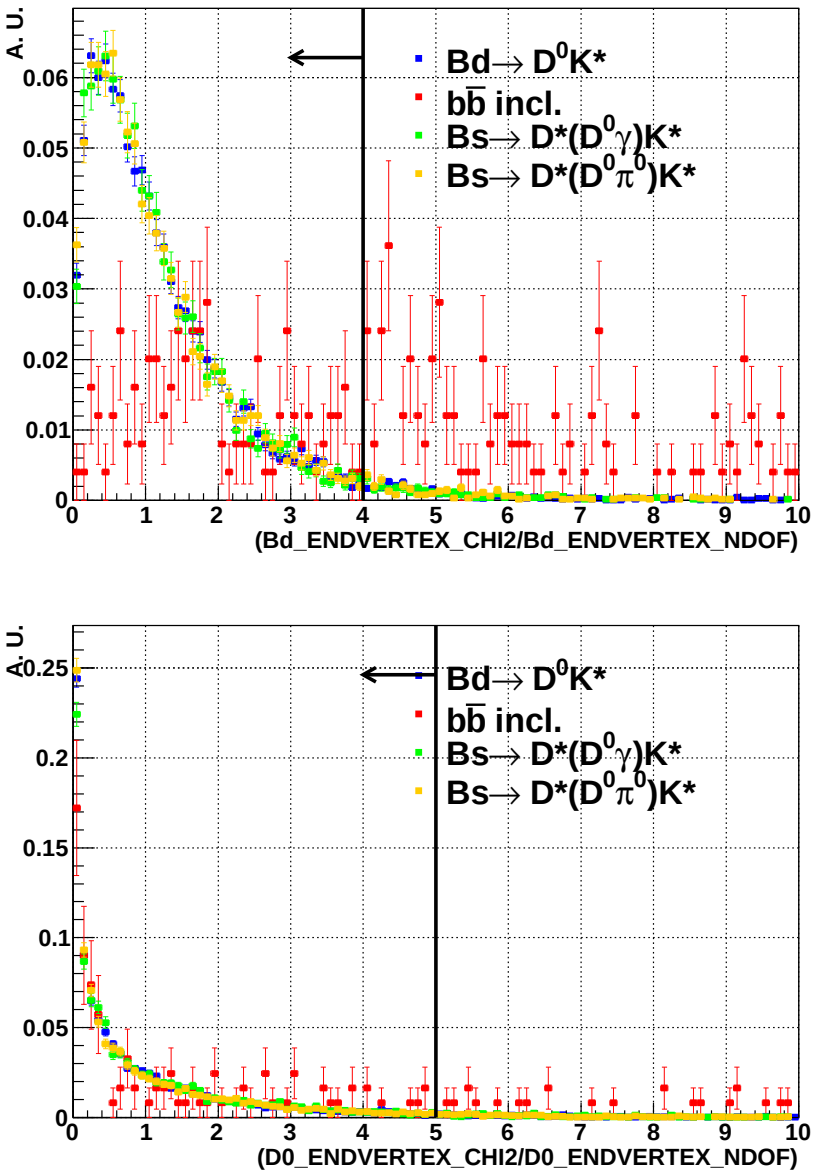

Figure IV.14: Distributions for the vertex fit quality of the D^0 (top) and B^0 (bottom). The final selection cut is materialized by the vertical bar and the arrow showing the events kept after the cut. In each plot, the red points corresponds to $b\bar{b}$-inclusive background, the blue points correspond to the $B^0 \to \overline{D}^0 K^{*0}$ events and the green and yellow points respectively correspond to the $\overline{B}^0_s \to D^{*0} K^{*0}$ with $D^{*0} \to D^0\gamma$ and $D^{*0} \to D^0\pi^0$ respectively. The $\overline{B}^0_s \to D^{*0} K^{*0}$ and $B^0 \to \overline{D}^0 K^{*0}$ are compatible within statistical uncertainties.

	$B^0 \to \overline{D}^0 K^{*0}$	$b\bar{b}$	$\overline{B}^0_s \to D^{*0} K^{*0}$ $D^{*0} \to D^0\gamma$	$\overline{B}^0_s \to D^{*0} K^{*0}$ $D^{*0} \to D^0\pi^0$
	In the full $[m_{B^0} - 500\ \text{MeV}/c^2, m_{B^0_s} + 500\ \text{MeV}/c^2]$ mass window			
$N_{\text{sel. events}}$	7057	<2.44 at 90 % C.L.	1886	2330
$\epsilon_{\text{selection}}$	(3.51 ± 0.04) %	$< 1.7.10^{-6}$ at 90 % C.L.	(2.07 ± 0.04) %	(2.47 ± 0.05) %
	In the restricted $[m_{B_d} - 50\ \text{MeV}/c^2, m_{B_d} + 50\ \text{MeV}/c^2]$ B_d mass window			
$N_{\text{sel. events}}$	6980	< 0.22 at 90 % C.L.	507	3
$\epsilon_{\text{selection}}$	(3.47 ± 0.04) %	$< 1.5.10^{-7}$ at 90 % C.L.	(0.55 ± 0.02) %	(0.003 ± 0.002) %
	In the restricted $[m_{B_s} - 50\ \text{MeV}/c^2, m_{B_s} + 50\ \text{MeV}/c^2]$ B_s mass window			
$N_{\text{sel. events}}$	40	< 0.22 at 90 % C.L.	22	1
$\epsilon_{\text{selection}}$	(0.019 ± 0.003) %	$< 1.5.10^{-7}$ at 90 % C.L.	(0.024 ± 0.005) %	(0.001 ± 0.001) %

Table IV.7: Summary of the number of selected events (multiple candidates are removed) and the corresponding efficiencies. A flat background is assumed for the computation of the $b\bar{b}$ inclusive background efficiency estimate.

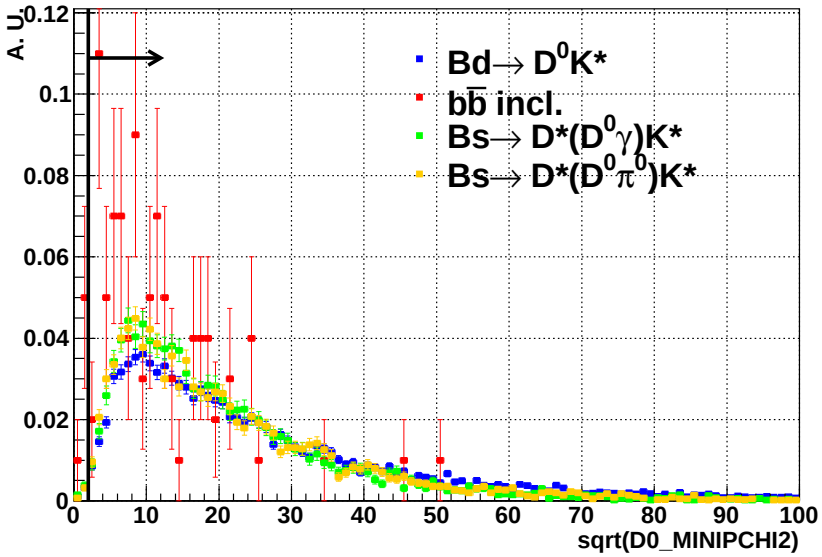

Figure IV.15: Distributions for the impact parameter significance of the D^0. The final selection cut is materialized by the vertical bar and the arrow showing the events kept after the cut. In each plot, the red points corresponds to $b\bar{b}$-inclusive background, the blue points correspond to the $B^0 \to \overline{D}^0 K^{*0}$ events and the green and yellow points respectively correspond to the $\overline{B}^0_s \to D^{*0} K^{*0}$ with $D^{*0} \to D^0\gamma$ and $D^{*0} \to D^0\pi^0$ respectively.

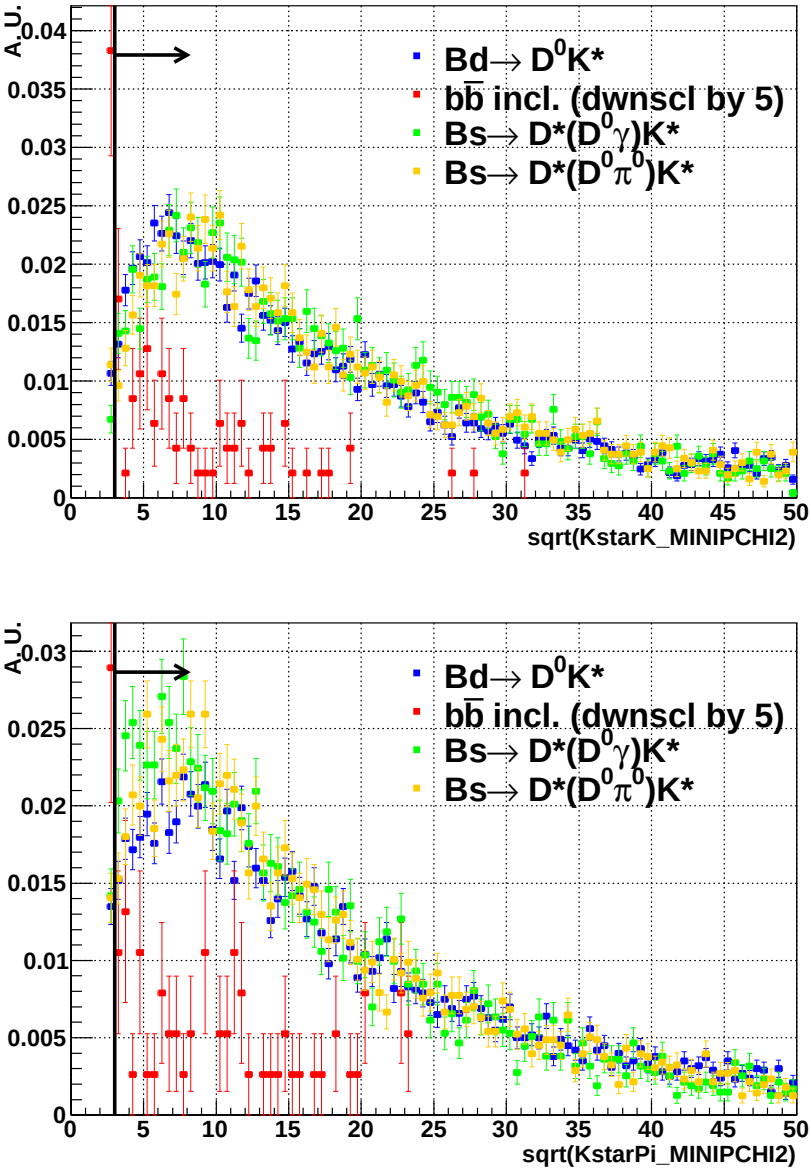

Figure IV.16: Distributions for the impact parameter significance of the daughters (K on the top, π on the bottom) of the K^{*0}. In both cases the $b\overline{b}$ inclusive background is downscaled by a factor 5 to ease the representation. The final selection cut is materialized by the vertical bar and the arrow showing the events kept after the cut. In each plot, the red points corresponds to $b\overline{b}$-inclusive background, the blue points correspond to the $B^0 \to \overline{D}^0 K^{*0}$ events and the green and yellow points respectively correspond to the $\overline{B}^0_s \to D^{*0} K^{*0}$ with $D^{*0} \to D^0\gamma$ and $D^{*0} \to D^0\pi^0$ respectively.

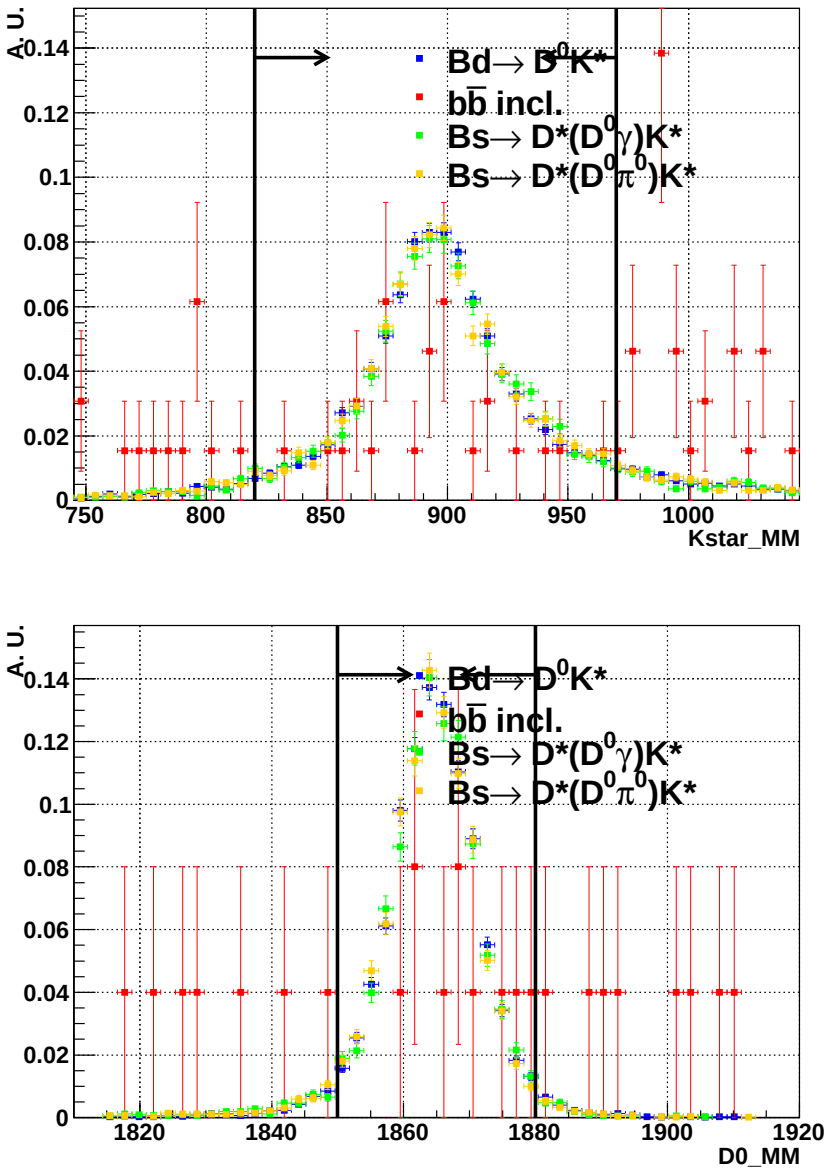

Figure IV.17: Distributions of the K^{*0} mass (top) and the D^0 mass (bottom). The final selection cut is materialized by the vertical bar and the arrow showing the events kept after the cut. In each plot, the red points corresponds to $b\bar{b}$-inclusive background, the blue points correspond to the $B^0 \to \overline{D}^0 K^{*0}$ events and the green and yellow points respectively correspond to the $\overline{B}^0_s \to D^{*0} K^{*0}$ with $D^{*0} \to D^0\gamma$ and $D^{*0} \to D^0\pi^0$ respectively. The $\overline{B}^0_s \to D^{*0} K^{*0}$ and $B^0 \to \overline{D}^0 K^{*0}$ are compatible within statistical uncertainties.

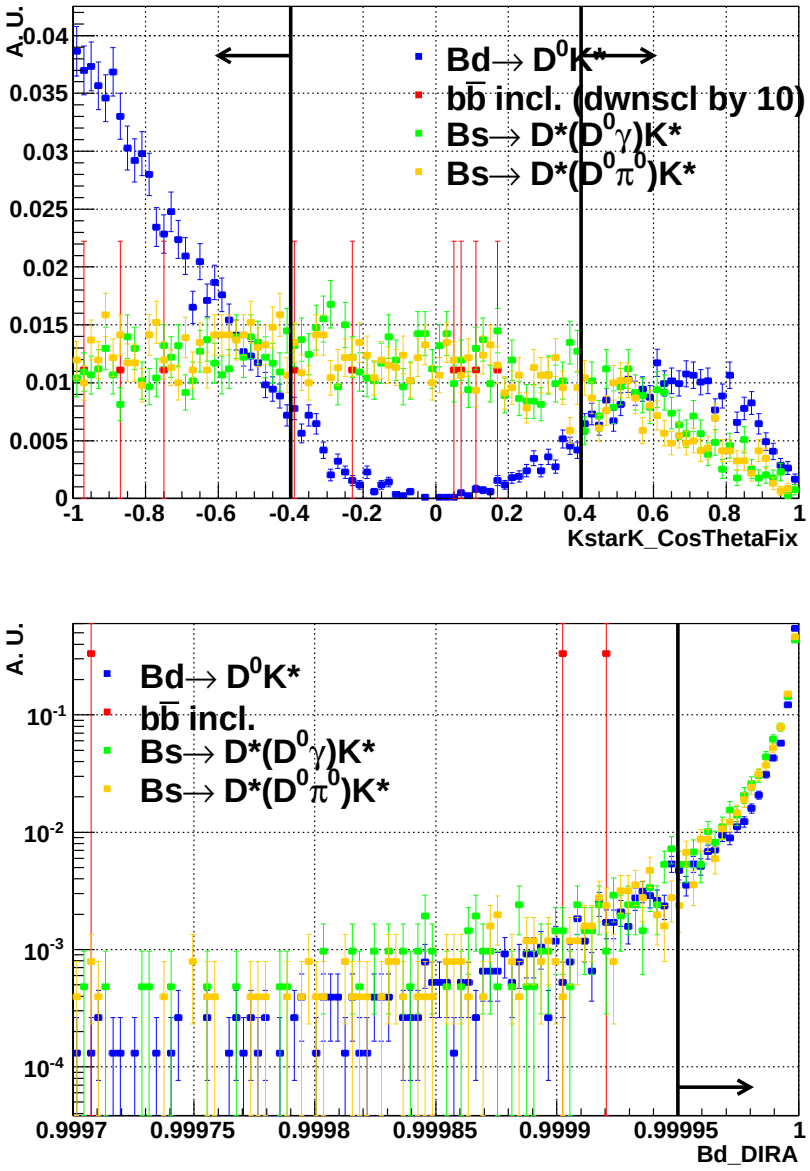

Figure IV.18: Distributions of the helicity angle (top) of the kaon coming from the K^{*0} (the $b\bar{b}$ inclusive background is downscaled by a factor 10 to ease the representation) and on the pointing angle of the B^0 (bottom). The final selection cut is materialized by the vertical bar and the arrow showing the events kept after the cut. In each plot, the red points corresponds to $b\bar{b}$-inclusive background, the blue points correspond to the $B^0 \to \overline{D}^0 K^{*0}$ events and the green and yellow points respectively correspond to the $\overline{B}^0_s \to D^{*0} K^{*0}$ with $D^{*0} \to D^0\gamma$ and $D^{*0} \to D^0\pi^0$ respectively. The loss of events at high helicity angle is due to the p_T cut on the kaons.

$N_{B^0 \to D^0 K^{*0}}$ (suppressed B^0 decay) are derived using the estimates of r_D and r_B given in Tab. IV.1. The contribution of the DCS D^0 decay is negligible as expected. The numbers of B_s^0 events are estimated using the expected ratio of branching fraction (see Eq. IV.18) neglecting kinematic terms and SU(3) flavour breaking. We also neglect in these estimates the possible difference in efficiencies in between the $B^0 \to DK^{*0}$ and $B_s^0 \to D\overline{K}^{*0}$ decays, this assumption being confirmed by the analysis performed in chapter V. The estimates of DCS D^0 and B_s^0 suppressed decays are also given for completeness. The contribution of these modes is also negligible. The number of events in $\overline{B}_s^0 \to D^{*0}K^{*0}$ decays are computed using the efficiencies extracted from the Monte Carlo simulation and using the upper limit given in Eq. IV.20f. The number of B_s^0 events in the B_s^0 and B^0 mass windows respectively are computed from the number of B^0 events in the B^0 and B_s^0 mass windows respectively. $N_{b\overline{b}}$ is simply taken from the upper limit expected number of $N_{b\overline{b}}$ events from the selection. The distribution of these events in the mass window is conservatively assumed to be flat, which corresponds to a reduction factor of $1/11$ (already present in Tab. IV.7).

Among the first measurements performed by LHCb, the measurement of the $b\overline{b}$ cross-section is of interest to confirm (and extend to an higher energy) the agreement between the TEVATRON experimental data and theoretical predictions [94]. Two measurements have been performed at $\sqrt{s} = 7$ TeV, both compatible within statistical uncertainties, the most (statistically) precise giving $\sigma\left(pp \to b\overline{b}X\right) = 288 \pm 4 \pm 48$ µb. This value is used to compute the expected yields for 1 fb^{-1} and 5 fb^{-1}.

The trigger efficiencies are taken from the analysis performed in chapter V. We will assume 43 % efficiency for the L0, 80 % for the HLT1 and 85 % for the HLT2 (on selected events). The accumulative trigger efficiency is 30 %.

The yields are computed using Eq. IV.22 and the values quoted in table IV.8, the results is given in Tab. IV.9. We assume that all the geometrical acceptance for B^0 and B_s^0 decays are

identical.

$$
\begin{aligned}
N_{B^0\to\overline{D}^0K^{*0}} &= \int \mathcal{L}\sigma_{b\overline{b}} 2 f_d \mathcal{B}\left(B^0 \to \overline{D}^0 K^{*0}\right) \mathcal{B}\left(D^0 \to K^-\pi^+\right) && \text{(IV.22a)}\\
&\times \mathcal{B}\left(K^{*0} \to K^+\pi^-\right) A_{\text{sig.}} \epsilon_{B^0\to\overline{D}^0K^{*0}} \\
N_{B^0\to\overline{D}^0(K^+\pi^-)K^{*0}} &= N_{\overline{B}^0\to D^0\overline{K}^{*0}} r_D^2 && \text{(IV.22b)}\\
N_{B^0\to D^0K^{*0}} &= N_{\overline{B}^0\to D^0\overline{K}^{*0}} r_B^2 && \text{(IV.22c)}\\
N_{\overline{B}^0_s\to D^0K^{*0}} &= \int \mathcal{L}\sigma_{b\overline{b}} 2 f_s \mathcal{B}\left(\overline{B}^0_s \to D^0 K^{*0}\right) \mathcal{B}\left(D^0 \to K^-\pi^+\right) && \text{(IV.22d)}\\
&\times \mathcal{B}\left(K^{*0} \to K^+\pi^-\right) A_{\text{sig.}} \epsilon_{\overline{B}^0_s\to D^0K^{*0}} \\
N_{\overline{B}^0_s\to D^0(K^-\pi^+)K^{*0}} &= N_{\overline{B}^0_s\to D^0K^{*0}} r_D^2 && \text{(IV.22e)}\\
N_{\overline{B}^0_s\to\overline{D}^0K^{*0}} &= N_{\overline{B}^0_s\to D^0K^{*0}} \left|\frac{|V_{ub}||V_{cd}|^*}{|V_{cb}||V_{ud}|^*}\right|^2 \simeq N_{\overline{B}^0_s\to D^0K^{*0}} \lambda^4\left(\rho^2+\eta^2\right) && \text{(IV.22f)}\\
N_{b\overline{b}} &= \int \mathcal{L}\sigma_{b\overline{b}} A_{b\overline{b}} \epsilon_{\text{stripping}} \epsilon_{b\overline{b}} && \text{(IV.22g)}\\
N_{B^0_s\to\overline{D}^{*0}\overline{K}^{*0},\ D^{*0}\to D^0\pi^0} &= \int \mathcal{L}\sigma_{b\overline{b}} 2 f_s \mathcal{B}\left(\overline{B}^0_s \to D^{*0} K^{*0}\right) \mathcal{B}\left(D^{*0} \to D^0\pi^0\right) && \text{(IV.22h)}\\
&\times \mathcal{B}\left(D^0 \to K^-\pi^+\right) \mathcal{B}\left(K^{*0} \to K^+\pi^-\right) \\
&\times A_{\text{sig.}} \epsilon_{B^0_s\to\overline{D}^{*0}\overline{K}^{*0},\ D^{*0}\to D^0\pi^0} \\
N_{B^0_s\to\overline{D}^{*0}\overline{K}^{*0},\ D^{*0}\to D^0\gamma} &= \int \mathcal{L}\sigma_{b\overline{b}} 2 f_s \mathcal{B}\left(\overline{B}^0_s \to D^{*0} K^{*0}\right) \mathcal{B}\left(D^{*0} \to D^0\gamma\right) && \text{(IV.22i)}\\
&\times \mathcal{B}\left(D^0 \to K^-\pi^+\right) \mathcal{B}\left(K^{*0} \to K^+\pi^-\right) \\
&\times A_{\text{sig.}} \epsilon_{B^0_s\to\overline{D}^{*0}\overline{K}^{*0},\ D^{*0}\to D^0\gamma}
\end{aligned}
$$

More sophisticated background estimate Figs. IV.19-IV.20 show the remaining background after having applied all the cuts except the last three: the helicity cut on the kaon from the K^{*0}, the pointing angle cut, and the B mass cut. Figure IV.21 shows the correlation between the helicity angle of the kaon coming from the K^{*0} and on the pointing angle of the B^0, for signal and background candidates. The $b\overline{b}$ background does not include the candidates corresponding to the specific backgrounds considered in this document[13]. Assuming that the background is flat in the helicity angle variable, in pointing angle and in B_d mass window, one gets 0.2 background event which corresponds to 143 and 714 events in 1 fb^{-1} and 5 fb^{-1} respectively. This result, compatible with the previous approach, is summarized in table IV.10, where only the significantly contributing backgrounds are quoted.

IV.3.3 Parametrization of the backgrounds

[13] Before applying the last three cuts, only one candidate corresponds to a $\overline{B}^0_s \to D^{*0}K^{*0}$ decay.

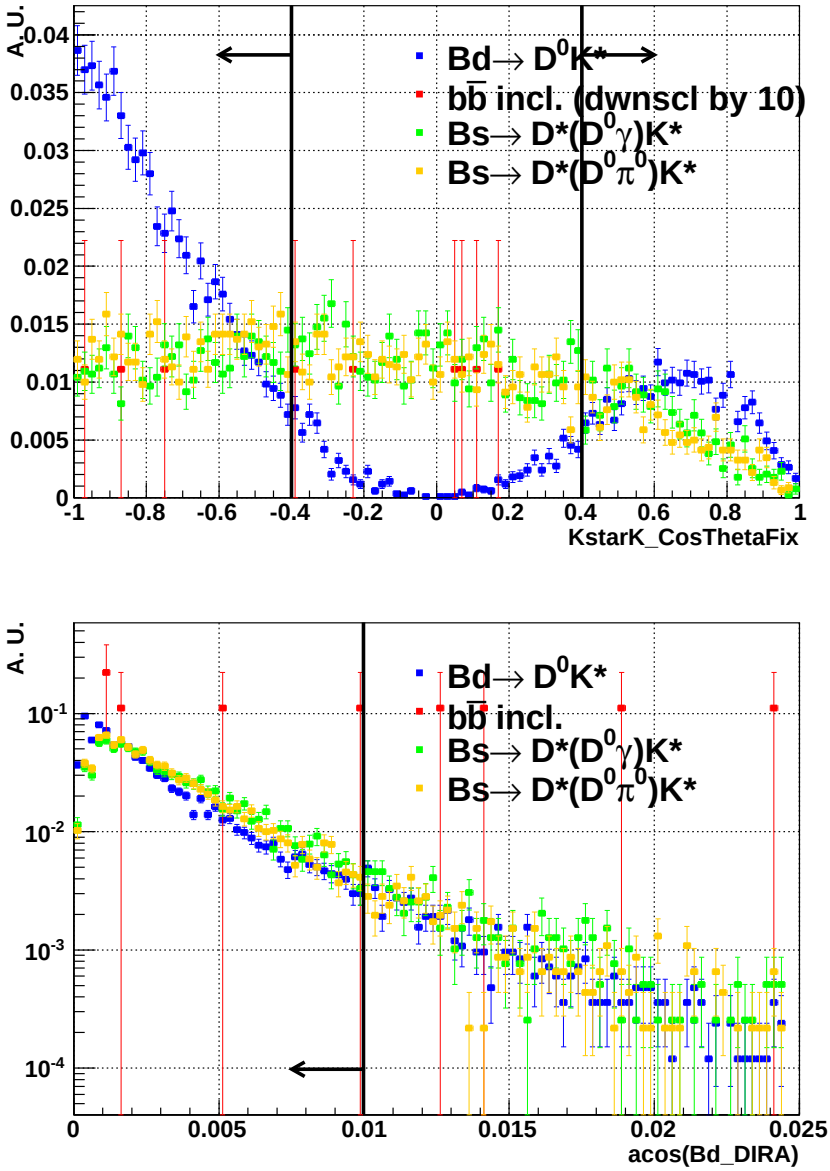

Figure IV.19: Distributions of the helicity angle (top) of the kaon coming from the K^{*0} (the $b\overline{b}$ inclusive background is downscaled by a factor 10 to ease the representation) and on the pointing angle of the B^0 (bottom), after all the cuts except the last three: the helicity cut on the kaon from the K^{*0}, the pointing angle cut, and the B mass cut. The final selection cut is materialized by the vertical bar and the arrow showing the events kept after the cut. In each plot, the red points correspond to $b\overline{b}$-inclusive background, the blue points correspond to the $B^0 \to \overline{D}^0 K^{*0}$ events and the green and yellow points respectively correspond to the $\overline{B}^0_s \to D^{*0} K^{*0}$ with $D^{*0} \to D^0\gamma$ and $D^{*0} \to D^0\pi^0$ respectively. The loss of events at high helicity angle is due to the p_T cut on the kaons. The $B^0_s \to \overline{D}^{*0}\overline{K}^{*0}$ backgrounds have been generated flat in helicity and thus helicity angle distribution may differ on real data for these backgrounds.

parameter	value	reference or comment
λ	0.2253 ± 0.0007	[38]
$\bar{\rho}$	$0.132^{+0.022}_{-0.014}$	[38]
$\bar{\eta}$	0.341 ± 0.013	[38]
r_B	0.26 ± 0.08	[38]
r_D	0.0616 ± 0.015	[38]
f_d	0.402 ± 0.013	[44]
f_s	0.112 ± 0.013	[44]
$\mathcal{B}\left(B^0 \to \overline{D}^0 K^{*0}\right)$	$(4.2 \pm 0.6)\,.10^{-5}$	[38]
$\mathcal{B}\left(D^0 \to K^- \pi^+\right)$	$(3.89 \pm 0.05)\,.10^{-2}$	[38]
$\mathcal{B}\left(K^{*0} \to K^+ \pi^-\right)$	$\frac{2}{3}$	isospin
$\mathcal{B}\left(B^0 \to \overline{D}^{*0} K^{*0}\right)$	$< 6.9 \cdot 10^{-5}$ at 90 % C.L.	[38]
$\mathcal{B}\left(D^{*0} \to D^0 \pi^0\right)$	(61.9 ± 2.9) %	[38]
$\mathcal{B}\left(D^{*0} \to D^0 \gamma\right)$	(38.1 ± 2.9) %	[38]
$A_{\text{sig.}}$	0.1784	Monte Carlo
$A_{b\bar{b}}$	0.437	Monte Carlo

Table IV.8: Values of the parameters used to compute the yields.

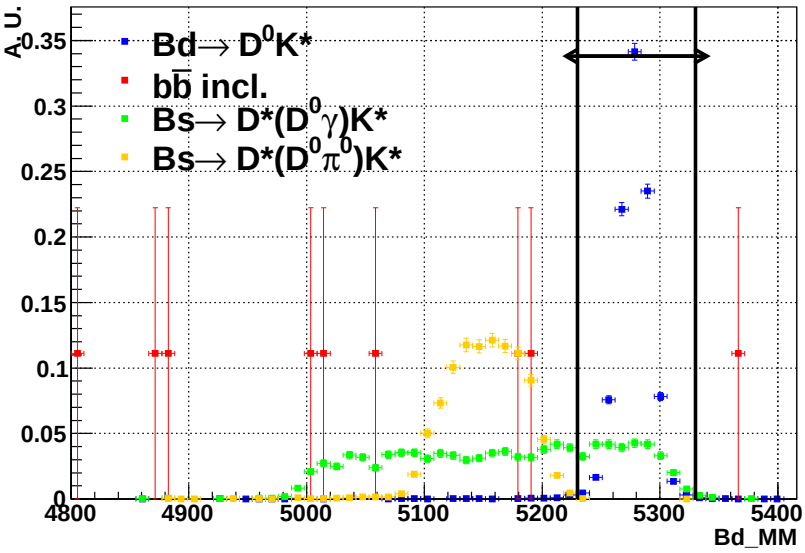

Figure IV.20: Distribution of the B^0 invariant mass, after all the cuts except the last three: the helicity cut on the kaon from the K^{*0}, the pointing angle cut, and the B mass cut. The relative size of the different contributions are not scaled to their expected levels. The final selection cut is materialized by the vertical bar and the arrow showing the events kept after the cut. In each plot, the red points correspond to $b\bar{b}$-inclusive background, the blue points correspond to the $B^0 \to \overline{D}^0 K^{*0}$ events and the green and yellow points respectively correspond to the $\overline{B}^0_s \to D^{*0} K^{*0}$ with $D^{*0} \to D^0 \gamma$ and $D^{*0} \to D^0 \pi^0$ respectively.

	1 fb^{-1}	5 fb^{-1}
In the full $[m_{B_d} - 500$ MeV/$c^2, m_{B_s} + 500$ MeV/$c^2]$ mass window		
$N_{B^0 \to \overline{D}^0 K^{*0}}$	474	2369
$N_{B^0 \to \overline{D}^0 (K^+\pi^-) K^{*0}}$	1.8	8.9
$N_{B^0 \to D^0 K^{*0}}$	32	160
$N_{\overline{B}^0_s \to D^0 K^{*0}}$	2294	11471
$N_{\overline{B}^0_s \to D^0 (K^-\pi^+) K^{*0}}$	8.7	43.5
$N_{\overline{B}^0_s \to \overline{D}^0 K^{*0}}$	0.8	4.1
$N_{b\bar{b}}$	< 1779 at 90 % C.L.	< 8897 at 90 % C.L.
$N_{B^0_s \to \overline{D}^{*0} \overline{K}^{*0},\ D^{*0} \to D^0 \pi^0}$	< 1643 at 90 % C.L.	< 8214 at 90 % C.L.
$N_{B^0_s \to \overline{D}^{*0} \overline{K}^{*0},\ D^{*0} \to D^0 \gamma}$	< 847 at 90 % C.L.	< 4237 at 90 % C.L.
In the restricted $[m_{B_d} - 50$ MeV$, m_{B_d} + 50$ MeV$]$ B_d mass window		
$N_{\overline{B}^0 \to D^0 \overline{K}^{*0}}$	468	2343
$N_{B^0 \to \overline{D}^0 (K^+\pi^-) K^{*0}}$	1.8	8.9
$N_{B^0 \to D^0 K^{*0}}$	32	158
$N_{\overline{B}^0_s \to D^0 K^{*0}}$	12	62
$N_{\overline{B}^0_s \to D^0 (K^-\pi^+) K^{*0}}$	0.05	0.23
$N_{\overline{B}^0_s \to \overline{D}^0 K^{*0}}$	0.004	0.02
$N_{b\bar{b}}$	< 157 at 90 % C.L.	< 785 at 90 % C.L.
$N_{B^0_s \to \overline{D}^{*0} \overline{K}^{*0},\ D^{*0} \to D^0 \pi^0}$	< 2 at 90 % C.L.	< 10 at 90 % C.L.
$N_{B^0_s \to \overline{D}^{*0} \overline{K}^{*0},\ D^{*0} \to D^0 \gamma}$	< 225 at 90 % C.L.	< 1125 at 90 % C.L.
In the restricted $[m_{B_s} - 50$ MeV$, m_{B_s} + 50$ MeV$]$ B_s mass window		
$N_{\overline{B}^0 \to D^0 \overline{K}^{*0}}$	2.6	13
$N_{B^0 \to \overline{D}^0 (K^+\pi^-) K^{*0}}$	0.01	0.05
$N_{B^0 \to D^0 K^{*0}}$	0.2	0.9
$N_{\overline{B}^0_s \to D^0 K^{*0}}$	2268	11339
$N_{\overline{B}^0_s \to D^0 (K^-\pi^+) K^{*0}}$	8.6	43
$N_{\overline{B}^0_s \to \overline{D}^0 K^{*0}}$	0.8	3.9
$N_{b\bar{b}}$	< 157 at 90 % C.L.	< 785 at 90 % C.L.
$N_{B^0_s \to \overline{D}^{*0} \overline{K}^{*0},\ D^{*0} \to D^0 \pi^0}$	< 0.7 at 90 % C.L.	< 3.3 at 90 % C.L.
$N_{B^0_s \to \overline{D}^{*0} \overline{K}^{*0},\ D^{*0} \to D^0 \gamma}$	< 9.82 at 90 % C.L.	< 49 at 90 % C.L.

Table IV.9: Expected yields for integrated luminosities of 1 fb^{-1} and 5 fb^{-1} at $\sqrt{s} = 7$ TeV. The values are given for different invariant mass regions. The same trigger efficiency is assumed for all the channels and is taken from chapter V. The branching fractions are the most conservative limits taken from section IV.3.1.

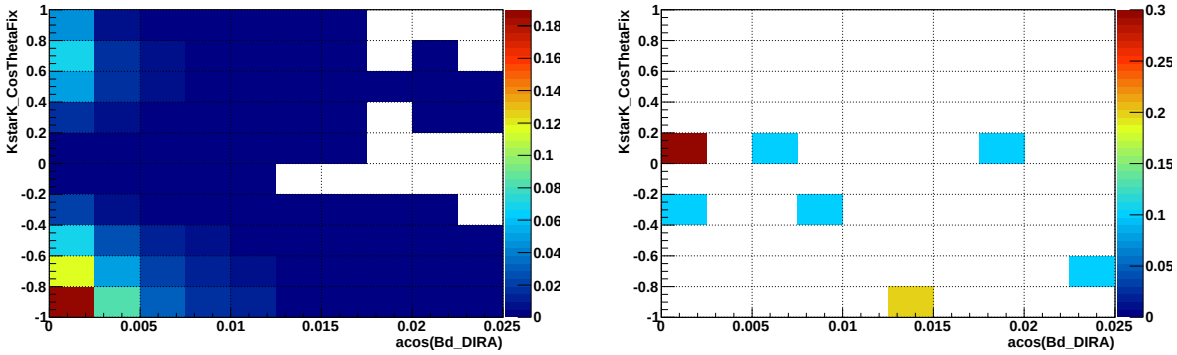

Figure IV.21: Correlation of the helicity angle (y-axis) of the kaon coming from the K^{*0} and on the pointing angle of the B^0 (x-axis), after all the cuts except the last three (the helicity cut on the kaon from the K^{*0}, the pointing angle cut, and the B mass cut), for the signal (left) and the $b\bar{b}$-inclusive background (right).

	1 fb^{-1}	5 fb^{-1}
$N_{\overline{B}^0 \to D^0 \overline{K}^{*0}}$ in B_d mass region	468	2343
$N_{\overline{B}^0_s \to D^0 K^{*0}}$ in B^0_s mass region	2268	11339
$N_{b\bar{b}}$ in B mass region	143	714
$N_{B^0_s \to \overline{D}^{*0} \overline{K}^{*0},\ D^{*0} \to D^0 \gamma}$ in B_d mass region	< 225 at 90 % C.L.	< 1125 at 90 % C.L.
$\frac{N_{\overline{B}^0 \to D^0 \overline{K}^{*0}}}{N_{b\bar{b}}}$ in B_d mass region	3.3	3.3

Table IV.10: Expected yields of signal and dominant backgrounds for integrated luminosities of 1 fb^{-1} and 5 fb^{-1} at $\sqrt{s} = 7$ TeV. The values are quoted in B invariant mass signal window of ± 50 MeV/c^2.

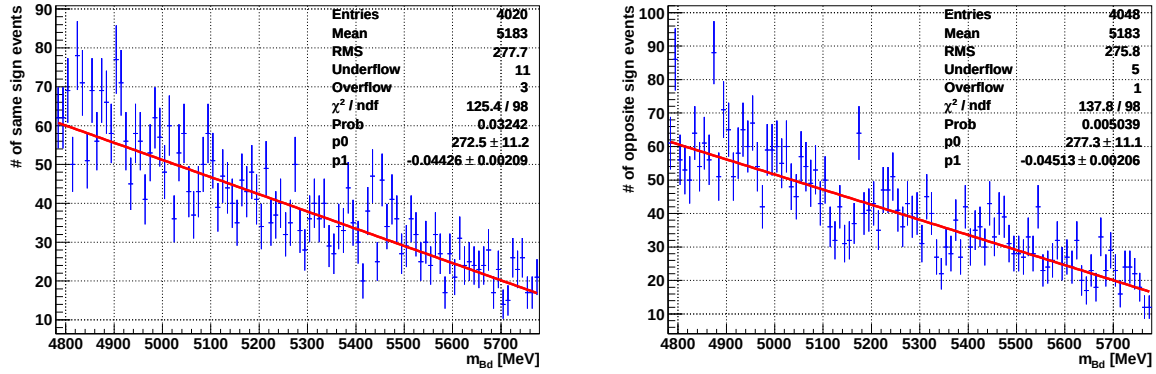

Figure IV.22: Shape of the background after the preselection but before the final selection for the same (resp. opposite) sign events in the left (resp. right) plot. A linear fit is performed and the value of the slope is used in the fit. No significant difference is seen between these two categories.

IV.3.3.1 Parametrization of combinatorial background

It has been seen on the limited Monte Carlo sample after the preselection that the shape of the combinatorial background is roughly linear (see figure IV.22) and will have to be validated on real data after the selection cuts in chapter V.

IV.3.3.2 Parametrization of $B_s^0 \to \overline{D}^{*0}\overline{K}^{*0}$ with $D^{*0} \to D^0\gamma$

The parametrization of the $B_s^0 \to \overline{D}^{*0}\overline{K}^{*0}$ with $D^{*0} \to D^0\gamma$ background is done with a function based on a sum of two generalized ARGUS function (see eq. IV.23).

$$\begin{aligned} f(t) &= K_{\text{norm}}((m_B - M_{\text{min}})\left(1-t^2\right)^{p_1} e^{c_1\left(1-t^2\right)} \\ &+ f\,(M_{\text{max}} - m_B)\left(1-t'^2\right)^{p_2} e^{c_2\left(1-t'^2\right)}) \text{ if t } \in [0,1] \\ f(t) &= 0 \text{ if } t < 0 \text{ or } t > 1 \\ \text{with } t &= \frac{m_B - M_{\text{min}}}{M_{\text{max}} - M_{\text{min}}} \\ \text{and } t' &= 1 - t \end{aligned} \tag{IV.23}$$

The result of the fit on the MC data sample after the selection, given in fig. IV.23, is used for the radiative decay of the D^{*0}. The normalization coefficient K_{norm} is numerically computed.

IV.3.3.3 Parametrization of the $B_s^0 \to \overline{D}^{*0}\overline{K}^{*0}$ with $D^{*0} \to D^0\pi^0$ background

The parametrization of the $B_s^0 \to \overline{D}^{*0}\overline{K}^{*0}$ with $D^{*0} \to D^0\pi^0$ background is done with a generalized Gaussian distribution (see eq. IV.24 where K_{norm} is a normalization factor), where the β

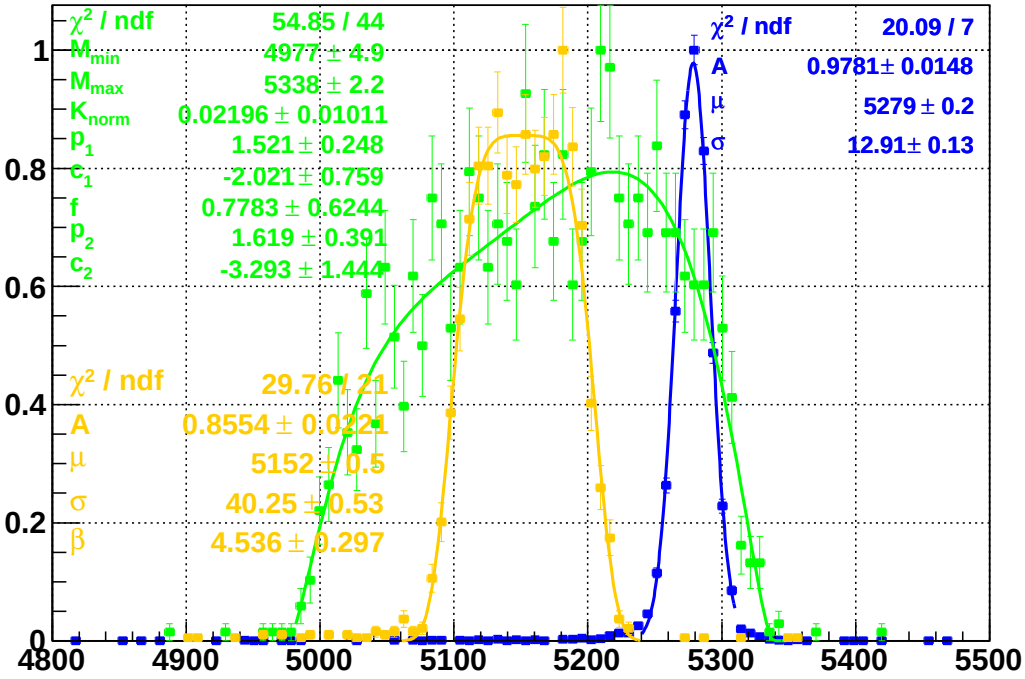

Figure IV.23: Result of the fit of the B_s^0 backgrounds and the B^0 signal peak in the region of interest. The function defined in eq. IV.23 has been used for the $B_s^0 \to \overline{D}^{*0}\overline{K}^{*0}$ with $D^{*0} \to D^0\gamma$ background and the one defined in eq. IV.24 for the $D^{*0} \to D^0\pi^0$ partially reconstructed decay. A simple Gaussian is used for the signal. All the distributions are scaled to unity, to ease the representation. The $B_s^0 \to \overline{D}^{*0}\overline{K}^{*0}$ backgrounds have been generated flat in helicity and thus the distributions that will be observed on real data may differ, since those ditributions are the sum of three different distributions.

exponent generalize the Gaussian $\beta = 2$ case. $\beta \to \infty$ parametrizes a flat-top function.

$$f(t) = K_{\text{norm}} \exp\left(-\left|\frac{m_B - \mu}{\sqrt{2}\sigma}\right|^{\beta}\right) \tag{IV.24}$$

The result of the fit on the MC data sample after the selection, given in fig. IV.23, is used for the decay of the D^{*0} through $D^0\pi^0$.

IV.3.4 Monte Carlo study for $D^0 \to K^-\pi^+\pi^+\pi^-$ and $D^0 \to K^-\pi^+\pi^0$

The previous analysis can be adapted to the two other D decays $D^0 \to K^-\pi^+\pi^+\pi^-$ and $D^0 \to K^-\pi^+\pi^0$. The difference in the selection thresholds is first emphasized and the expected yields are then infered.

IV.3.4.1 Software and Monte Carlo sample

504877 $B^0 \to \overline{D}^0 K^{*0}$ with $D^0 \to K^-\pi^+\pi^0$ and 504947 $B^0 \to \overline{D}^0 K^{*0}$ with $D^0 \to K^-\pi^+\pi^+\pi^-$ signal Monte Carlo events have been generated with a Dalitz Model for both of the decay modes. 45.5 million $b\overline{b}$-inclusive events are used for the background in the $D^0 \to K^-\pi^+\pi^0$ selection and 35.0 million $b\overline{b}$-inclusive events are used for the background in the $D^0 \to K^-\pi^+\pi^+\pi^-$.

IV.3.4.2 General strategy

When this study was performed there was no pre-existing stripping selection. The first piece of work was to implement a preselection that was corresponding to the requirements (low retention rate, low CPU consumption). These decays are 5 and 6 body final states, thus the measured particles have rather soft transverse momentum distributions, which make the task more difficult.

- In the case of $K^\pm\pi^\mp\pi^0$, 60 % of the π^0 are not reconstructible since they have at least one photon under the threshold of $p_T > 200$ MeV/c. This gives a strong argument to cut as loose as possible on the p_T of the π^0. Moreover half of the photons are converted before reaching the calorimeter system and among them half of these are converted before the magnet and thus not reconstructed. For the remaining half of the photons, the efficiency is reduced due to the conversion (their signal looks more like electrons than photons).
- The D decay in four tracks also implies to keep the kinematic cuts as low as possible, to preserve signal efficiency.

IV.3.4.3 Preselection

When this analysis was performed, the stripping selection for $D^0 \to K^-\pi^+$ was updated to meet some new requirements. Thus some "robust" cuts (against error calculations) have been added to the $D^0 \to K^-\pi^+$ preselection compared to what is presented is section IV.3.2. A loose selection on the kinematics of the π^0, a tighter K^{*0} selection (this was then also updated later on for the $D^0 \to K^-\pi^+$) and a wider D^0 invariant mass are required. The cuts are summarized in Tab. IV.11 for the $D^0 \to K^\pm\pi^\mp\pi^0$ decay and in Tab. IV.12 for the $D^0 \to K^\pm\pi^\mp\pi^+\pi^-$ decay.

IV.3.4.4 Selection

The selection strategy is similar to the selection used for $D^0 \to K^\pm\pi^\mp$ and is mainly based on applying PID cuts. Additional cuts in the phase space of the $D^0 \to K^\pm\pi^\mp\pi^0$ are also applied to remove more background. Another cut, consisting in cutting on the signed significance of the distance projected positions of the D^0 and the K^{*0} vertex on the z-axis is applied to remove combinations that confuse these two vertices. Finally a cut on the angular separation between

Particle	Variable	Cut value
π_{D^0} or K_{D^0}	χ^2_{track} per d.o.f.	< 10
	P_T	> 250 MeV
	P	> 2 GeV
	$\min \chi^2_{\text{IP to PV}}$	> 4
	$\min$ IP to PV	> 0.05 mm
$\pi^0_{D^0}$	P_T	> 250 MeV
	P	> 2 GeV
D^0	$\lvert m_{\text{reco}} - m_{\text{pdg}} \rvert$	< 150 MeV
	P_T	> 1000 MeV
	χ^2_{vertex} per d.o.f.	< 12
	$\chi^2_{\text{vertex distance to PV}}$	> 36
	vertex distance to PV	> 1 mm
	vertex distance to PV in ρ	> 0.2 mm
$\pi_{K^{*0}}$ or $K_{K^{*0}}$	χ^2_{track} per d.o.f.	< 10
	P_T	> 300 MeV
	P	> 2 GeV
	$\min \chi^2_{\text{IP to PV}}$	> 6.25
	$\min$ IP to PV	> 0.05 mm
K^{*0}	$\lvert m_{\text{reco}} - m_{\text{pdg}} \rvert$	< 150 MeV
	P_T	> 1000 MeV
	χ^2_{vertex} per d.o.f.	< 12
	$\min \chi^2_{\text{IP to PV}}$	> 4
	$\min$ IP to PV	> 0.05 mm
B^0	m_{reco}	> 4800 MeV and < 5900 MeV
	$\chi^2_{\text{IP to PV}}$	< 12.25
	$\cos\theta_{\text{pointing}}$	> 0.9997
	χ^2_{vertex} per d.o.f.	< 10
	$\chi^2_{\text{vertex distance to PV}}$	> 100
	vertex distance to PV	> 1 mm
	impact parameter w.r.t PV	< 0.07 mm

Table IV.11: Summary of the preselection cuts applied on the $D^0 \to K^{\pm}\pi^{\mp}\pi^0$ candidates.

Particle	Variable	Cut value
π_{D^0} or K_{D^0}	χ^2_{track} per d.o.f.	< 10
	P_T	> 150 MeV
	P	> 1 GeV
	$\min \chi^2_{\text{IP to PV}}$	> 4
	$\min$ IP to PV	> 0.05 mm
D^0	$\lvert m_{\text{reco}} - m_{\text{pdg}} \rvert$	< 50 MeV
	P_T	> 1000 MeV
	χ^2_{vertex} per d.o.f.	< 12
	$\chi^2_{\text{vertex distance to PV}}$	> 36
	vertex distance to PV	> 1 mm
	vertex distance to PV in ρ	> 0.2 mm
$\pi_{K^{*0}}$ or $K_{K^{*0}}$	χ^2_{track} per d.o.f.	< 10
	P_T	> 300 MeV
	P	> 2 GeV
	$\min \chi^2_{\text{IP to PV}}$	> 6.25
	$\min$ IP to PV	> 0.05 mm
K^{*0}	$\lvert m_{\text{reco}} - m_{\text{pdg}} \rvert$	< 150 MeV
	P_T	> 1000 MeV
	χ^2_{vertex} per d.o.f.	< 12
	$\min \chi^2_{\text{IP to PV}}$	> 4
	$\min$ IP to PV	> 0.05 mm
B^0	m_{reco}	> 4800 MeV and < 5900 MeV
	$\chi^2_{\text{IP to PV}}$	< 12.25
	$\cos\theta_{\text{pointing}}$	> 0.9997
	χ^2_{vertex} per d.o.f.	< 10
	$\chi^2_{\text{vertex distance to PV}}$	> 100
	vertex distance to PV	> 1 mm
	impact parameter w.r.t PV	< 0.07 mm

Table IV.12: Summary of the preselection cuts applied on the $D^0 \to K^{\pm}\pi^{\mp}\pi^{+}\pi^{-}$ candidates.

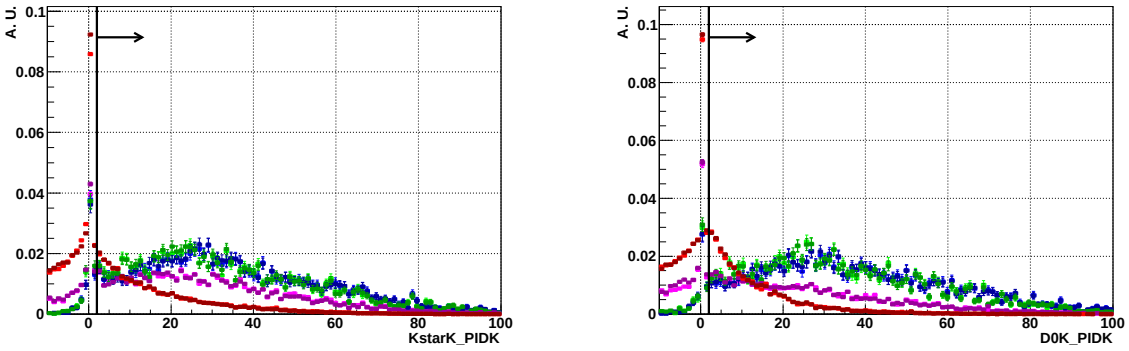

Figure IV.24: Distribution of the $\mathrm{DLL}_{\mathrm{K}\pi}$ variable for the kaons coming from the K^{*0} (left) and D^0 (right). The final selection cut is materialized by the vertical bar and the arrow showing the events kept after the cut. In each plot, the red points corresponds to $b\overline{b}$-inclusive background, the blue points correspond to the properly reconstructed (and matched) $B^0 \to \overline{D}^0 K^{*0}$ events, the green points correspond to partially reconstructed signal for which one of the two photons used to construct the π^0 is from the underlying event and the pink points correspond to the combinatorial background in the signal Monte Carlo data sample. The light and dark points respectively correspond to the events without and with a constraint on the D^0 invariant mass.

the two photons originating from the π^0 is performed, since for combinatorial combinations of photons it is not expected to be strongly correlated with the π^0 mass, contrary to signal. The selection is summarized in Tab. IV.13 and in Figs. IV.24-IV.34 in the case of resolved π^0[14].

To constrain the D^0 mass to its nominal value helps in reducing the amount of background (in particular by reducing the width of the B signal invariant mass window). This constraint will be used in the following, while this constraint is not yet working for merged π^0.

IV.3.4.5 Expected yields

After the selection, multiple candidates are removed with the same procedure than for $D^0 \to K^-\pi^+$. The expected number of events are then computed with similar equations than for $D^0 \to K^-\pi^+$, the selection efficiencies and the branching fractions being different. For simplicity, the trigger efficiency is assumed to be the same (which would tend to be slightly optimistic for $D^0 \to K^\pm\pi^\mp\pi^0$ and $D^0 \to K^\pm\pi^\mp\pi^+\pi^-$ compared to $D^0 \to K^\pm\pi^\mp$). The results are given in Tab. IV.17 and Tab. IV.18.

[14]Resolved π^0 are π^0 for which the energy deposits of the two photons are resolved by the calorimeter. Merged π^0 are π^0 for which it is not the case, they have thus on average a larger energy.

Parameter	Cut Value	$B^0 \to \overline{D}^0 K^{*0}$ with $D^0 \to K^\pm\pi^\mp\pi^0$			$b\bar{b}$
		signal	partially reconstructed	combinatorial	
candidates		4750	6137	112101	973380
$\Delta_{K-\pi}\mathcal{L}$ of $K_{K^{*0}}$	> 2	4402	5627	61444	278743
$\Delta_{K-\pi}\mathcal{L}$ of K_{D^0}	> 2	4156	5282	26681	82748
$\Delta_{K-\pi}\mathcal{L}$ of $\pi_{K^{*0}}$	< 2 and $\neq -1000$	3746	4674	22023	44263
$\Delta_{K-\pi}\mathcal{L}$ of π_{D^0}	< 2 and $\neq -1000$	3292	4109	15163	22666
P_T of $K_{K^{*0}}$	> 400 MeV	3228	4050	15003	21694
χ^2_{vertex}per d.o.f. of D^0	< 5	3091	3865	13313	16173
χ^2_{vertex}per d.o.f. of B^0	< 4	2986	3711	11611	7489
min $\chi^2_{\text{IP to PV}}$ of D^0	> 4	2963	3688	11497	7103
min $\chi^2_{\text{IP to PV}}$ of $K_{K^{*0}}$	> 9	2940	3646	11271	5992
min $\chi^2_{\text{IP to PV}}$ of $\pi_{K^{*0}}$	> 9	2899	3601	10972	5050
$\lvert m^{\text{reco}}_{K^*} - m^{\text{pdg}}_{K^*}\rvert$	< 75 MeV	2589	3184	9477	2912
$\lvert\cos\theta^*_{K_{K^{*0}}}\rvert$	> 0.4	2365	2876	8375	1786
theta pi0	< 0.05 rad	2122	1828	4024	790
$m^{\text{reco}}_{\pi^0}$	> 120 and < 160	1946	1244	2867	567
P_T of $\pi^0_{D^0}$	> 600 MeV	1877	952	1608	404
m_ρ	$< 950 \lvert\rvert > 1200$	1703	825	1242	275
$m_{K^{*0}}$	$< 1200 \lvert\rvert > 1400$	1583	761	1112	193
m_{K^*}	$< 1100 \lvert\rvert > 1400$	1458	671	843	133
$m^{\text{reco}}_{D^0}$	> 1810 and < 1930	1353	424	426	53
P_T of D^0	> 2 GeV	1283	404	394	26
$\frac{V_{z,D^0} - V_{z,K^{*0}}}{\sqrt{\sigma^2_{z,D^0} + \sigma^2_{z,K^{*0}}}}$	> -2	1278	403	387	18
$\cos\theta_{\text{pointing}B_d}$	> 0.99995	1225	388	330	12
IP wrt PV of B^0	< 0.07	1222	388	327	8
$\lvert m^{\text{reco}}_{B_d} - m^{\text{pdg}}_{B_d}\rvert$	< 150 MeV	1219	388	327	3

Table IV.13: Summary of the selection cuts applied on the preselected events with the number of resolved $D^0 \to K^\pm\pi^\mp\pi^0$ candidates remaining after each cut.

Parameter	Cut Value	$B^0 \to \overline{D}^0 K^{*0}$ with $D^0 \to K^\pm\pi^\mp\pi^0$ signal	combinatorial	$b\bar{b}$
candidates		1154	1793	1371
$\Delta_{K-\pi}\mathcal{L}$ of $K_{K^{*0}}$	> 2	1025	761	373
$\Delta_{K-\pi}\mathcal{L}$ of K_{D^0}	> 2	920	213	107
$\Delta_{K-\pi}\mathcal{L}$ of $\pi_{K^{*0}}$	< 2 and $\neq -1000$	824	165	67
$\Delta_{K-\pi}\mathcal{L}$ of π_{D^0}	< 2 and $\neq -1000$	742	98	37
P_T of $K_{K^{*0}}$	> 400 MeV	730	97	37
χ^2_{vertex}per d.o.f. of D^0	< 5	684	86	30
χ^2_{vertex}per d.o.f. of B^0	< 4	663	68	18
min $\chi^2_{\text{IP to PV}}$ of D^0	> 4	649	67	13
min $\chi^2_{\text{IP to PV}}$ of $K_{K^{*0}}$	> 9	649	67	11
min $\chi^2_{\text{IP to PV}}$ of $\pi_{K^{*0}}$	> 9	640	64	10
$\lvert m^{\text{reco}}_{K^*} - m^{\text{pdg}}_{K^*}\rvert$	< 75 MeV	583	59	6
$\lvert\cos\theta^*_{K_{K^{*0}}}\rvert$	> 0.4	537	49	5
$m^{\text{reco}}_{\pi^0}$	> 120 and < 160	256	18	1
$m^{\text{reco}}_{D^0}$	> 1820 and < 1960	228	14	0
$\frac{V_{z,D^0}-V_{z,K^{*0}}}{\sqrt{\sigma^2_{z,D^0}-\sigma^2_{z,K^{*0}}}}$	> -2	228	14	0
$\cos\theta_{\text{pointing}B_d}$	> 0.99995	222	14	0
$\lvert m^{\text{reco}}_{B_d} - m^{\text{pdg}}_{B_d}\rvert$	< 150 MeV	219	14	0

Table IV.14: Summary of the selection cuts applied on the preselected events with the number of $D^0 \to K^\pm\pi^\mp\pi^0$ merged candidates remaining after each cut.

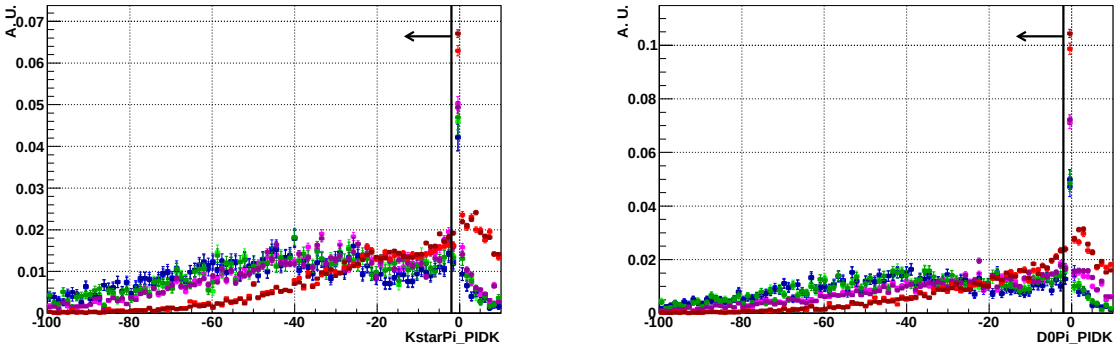

Figure IV.25: Distribution of the $\text{DLL}_{K\pi}$ variable for the pions coming from the K^{*0} (left) and D^0 (right). The final selection cut is materialized by the vertical bar and the arrow showing the events kept after the cut. In each plot, the red points corresponds to $b\bar{b}$-inclusive background, the blue points correspond to the properly reconstructed (and matched) $B^0 \to \overline{D}^0 K^{*0}$ events, the green points correspond to partially reconstructed signal for which one of the two photons used to construct the π^0 is from the underlying event and the pink points correspond to the combinatorial background in the signal Monte Carlo data sample. The light and dark points respectively correspond to the events without and with a constraint on the D^0 invariant mass.

Parameter	Cut Value	$B^0 \to \overline{D}^0 K^{*0}$ with $D^0 \to K^\pm\pi^\mp\pi^0$			$b\overline{b}$
		signal	partially reconstructed	combinatorial	
candidates		4750	6137	112101	973380
$\Delta_{K-\pi}\mathcal{L}$ of $K_{K^{*0}}$	> 2	4402	5627	61444	278743
$\Delta_{K-\pi}\mathcal{L}$ of K_{D^0}	> 2	4156	5282	26681	82748
$\Delta_{K-\pi}\mathcal{L}$ of $\pi_{K^{*0}}$	< 2 and $\neq -1000$	3746	4674	22023	44263
$\Delta_{K-\pi}\mathcal{L}$ of π_{D^0}	< 2 and $\neq -1000$	3292	4109	15163	22666
P_T of $K_{K^{*0}}$	> 400 MeV	3228	4050	15003	21694
χ^2_{vertex}per d.o.f. of D^0	< 5	3091	3865	13313	16173
χ^2_{vertex}per d.o.f. of B^0	< 4	2986	3711	11611	7489
min $\chi^2_{\text{IP to PV}}$ of D^0	> 4	2963	3688	11497	7103
min $\chi^2_{\text{IP to PV}}$ of $K_{K^{*0}}$	> 9	2940	3646	11271	5992
min $\chi^2_{\text{IP to PV}}$ of $\pi_{K^{*0}}$	> 9	2899	3601	10972	5050
$\lvert m^{\text{reco}}_{K^*} - m^{\text{pdg}}_{K^*}\rvert$	< 75 MeV	2589	3184	9477	2912
$\lvert\cos\theta^*_{K_{K^{*0}}}\rvert$	> 0.4	2365	2876	8375	1786
Reffiting status	successful	2365	2875	8373	1783
theta pi0	< 0.05 rad	2110	1639	3307	653
$m^{\text{reco}}_{\pi^0}$	> 120 and < 160	1916	641	1191	252
P_T of $\pi^0_{D^0}$	> 600 MeV	1847	494	665	184
m_ρ	$< 950 \lvert\rvert > 1200$	1688	457	562	124
$m_{K^{*0}}$	$< 1200 \lvert\rvert > 1400$	1570	424	505	89
m_{K^*}	$< 1100 \lvert\rvert > 1400$	1455	396	430	62
$m^{\text{reco}}_{D^0}$	> 1810 and < 1930	1318	305	303	38
P_T of D^0	> 2 GeV	1247	294	283	19
$\frac{V_{z,D^0}-V_{z,K^{*0}}}{\sqrt{\sigma^2_{z,D^0}+\sigma^2_{z,K^{*0}}}}$	> -2	1240	294	277	13
$\cos\theta_{\text{pointing}B_d}$	> 0.99995	1188	283	241	8
IP wrt PV of B^0	< 0.07	1185	283	239	5
$\lvert m^{\text{reco}}_{B_d} - m^{\text{pdg}}_{B_d}\rvert$	< 50 MeV	1162	283	239	1

Table IV.15: Summary of the selection cuts applied on the preselected events with the number of resolved $D^0 \to K^\pm\pi^\mp\pi^0$ candidates remaining after each cut, using a constraint on the D^0 invariant mass.

Parameter	Cut Value	$B^0 \to \overline{D}^0 K^{*0}$ with $D^0 \to K^\pm\pi^\mp\pi^+\pi^-$		$b\overline{b}$
		signal	partially reconstructed	
candidates		15722	172185	398272
$\Delta_{K-\pi}\mathcal{L}$ of K_{D^0}	> 2	14720	52997	110210
$\Delta_{K-\pi}\mathcal{L}$ of $K_{K^{*0}}$	> 2	13366	25603	33429
$\Delta_{K-\pi}\mathcal{L}$ of $\pi_{K^{*0}}$	< 2 and $\neq -1000$	11941	21489	17144
$\Delta_{K-\pi}\mathcal{L}$ of $\pi_{D^0 extrm,OS1}$	< 2 and $\neq -1000$	10868	14486	9535
$\Delta_{K-\pi}\mathcal{L}$ of $\pi_{D^0 extrm,OS2}$	< 2 and $\neq -1000$	8563	7309	4078
$\Delta_{K-\pi}\mathcal{L}$ of $\pi_{D^0 extrm,SS}$	< 2 and $\neq -1000$	7318	4229	1966
P_T of $K_{K^{*0}}$	> 400 MeV	7193	4164	1872
χ^2_{vertex}per d.o.f. of D^0	< 5	6923	2383	682
χ^2_{vertex}per d.o.f. of B^0	< 4	6685	2104	316
min $\chi^2_{\text{IP to PV}}$ of D^0	> 4	6652	2086	298
min $\chi^2_{\text{IP to PV}}$ of $K_{K^{*0}}$	> 9	6598	2063	268
min $\chi^2_{\text{IP to PV}}$ of $\pi_{K^{*0}}$	> 9	6517	2010	233
$\lvert m^{\text{reco}}_{K^*} - m^{\text{pdg}}_{K^*}\rvert$	< 75 MeV	5803	1703	108
$\lvert\cos\theta^*_{K_{K^{*0}}}\rvert$	> 0.4	5299	1524	68
$\lvert m^{\text{reco}}_{D^0} - m^{\text{pdg}}_{D^0}\rvert$	< 15 MeV	5055	569	8
P_T of D^0	> 2 GeV	4709	518	2
$\frac{V_{z,D^0}-V_{z,K^{*0}}}{\sqrt{\sigma^2_{z,D^0}-\sigma^2_{z,K^{*0}}}}$	> -2	4687	513	2
$\cos\theta_{\text{pointing}B_d}$	> 0.99995	4570	493	2
IP wrt PV of B^0	< 0.07	4561	490	2
$\lvert m^{\text{reco}}_{B_d} - m^{\text{pdg}}_{B_d}\rvert$	< 50 MeV	4510	490	0

Table IV.16: Summary of the selection cuts applied on the preselected events with the number of $D^0 \to K^\pm\pi^\mp\pi^+\pi^-$ candidates remaining after each cut.

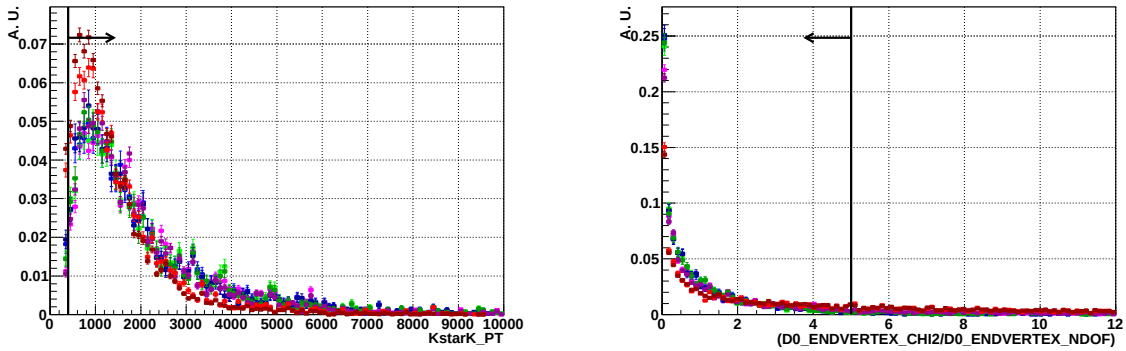

Figure IV.26: Distributions of the transverse momenta of the kaon from the K^{*0} (left) the vertex fit quality of the D^0 (right). The final selection cut is materialized by the vertical bar and the arrow showing the events kept after the cut. In each plot, the red points corresponds to $b\bar{b}$-inclusive background, the blue points correspond to the properly reconstructed (and matched) $B^0 \to \overline{D}^0 K^{*0}$ events, the green points correspond to partially reconstructed signal for which one of the two photons used to construct the π^0 is from the underlying event and the pink points correspond to the combinatorial background in the signal Monte Carlo data sample. The light and dark points respectively correspond to the events without and with a constraint on the D^0 invariant mass.

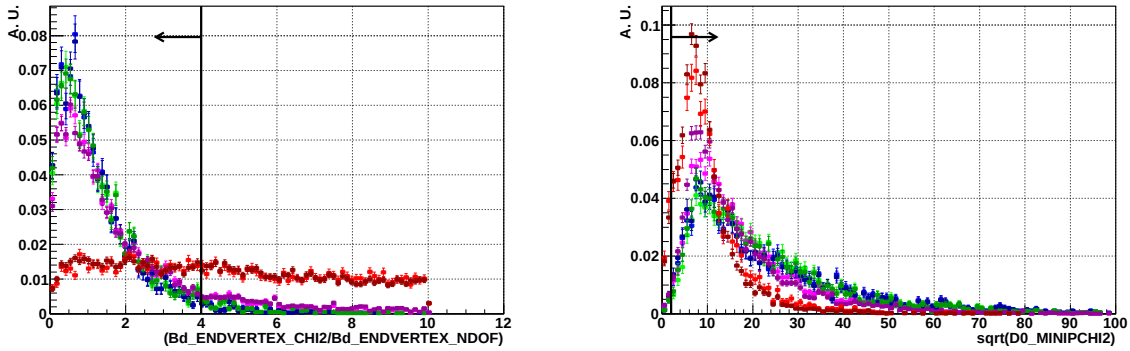

Figure IV.27: Distributions for the vertex fit quality of the B^0 (left) and the impact parameter significance of the D^0 (right). The final selection cut is materialized by the vertical bar and the arrow showing the events kept after the cut. In each plot, the red points corresponds to $b\bar{b}$-inclusive background, the blue points correspond to the properly reconstructed (and matched) $B^0 \to \overline{D}^0 K^{*0}$ events, the green points correspond to partially reconstructed signal for which one of the two photons used to construct the π^0 is from the underlying event and the pink points correspond to the combinatorial background in the signal Monte Carlo data sample. The light and dark points respectively correspond to the events without and with a constraint on the D^0 invariant mass.

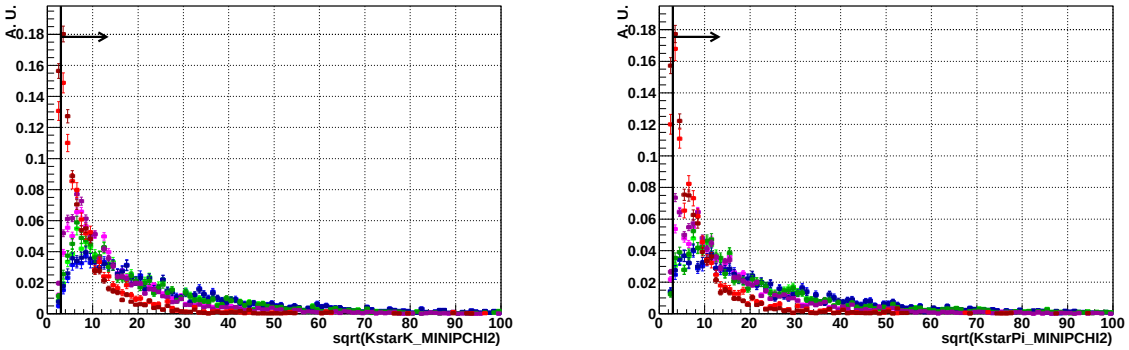

Figure IV.28: Distributions for the impact parameter significance of the daughters (K on the left, π on the right) of the K^{*0}. In both cases the $b\overline{b}$ inclusive background is downscaled by a factor 5 to ease the representation. The final selection cut is materialized by the vertical bar and the arrow showing the events kept after the cut. In each plot, the red points corresponds to $b\overline{b}$-inclusive background, the blue points correspond to the properly reconstructed (and matched) $B^0 \to \overline{D}^0 K^{*0}$ events, the green points correspond to partially reconstructed signal for which one of the two photons used to construct the π^0 is from the underlying event and the pink points correspond to the combinatorial background in the signal Monte Carlo data sample. The light and dark points respectively correspond to the events without and with a constraint on the D^0 invariant mass.

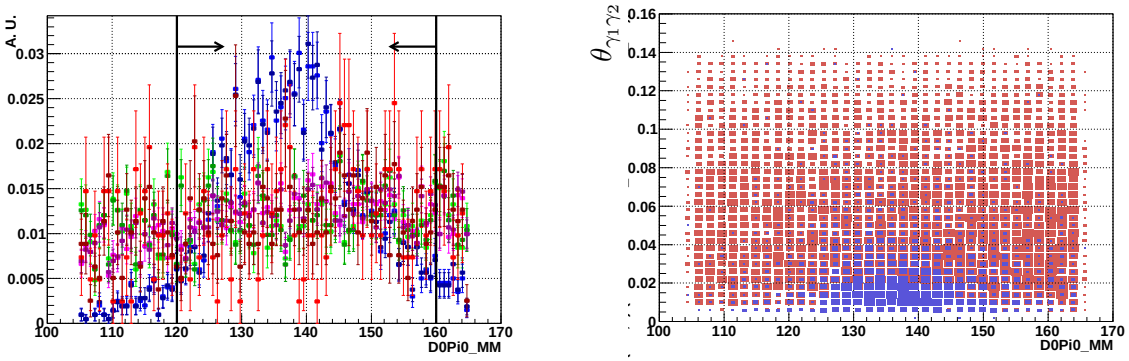

Figure IV.29: Distributions of the π^0 mass (left) and correlation of the π^0 mass and the angle between the tow photons (right). The final selection cut is materialized by the vertical bar and the arrow showing the events kept after the cut. In the left plot, the red points corresponds to $b\overline{b}$-inclusive background, the blue points correspond to the properly reconstructed (and matched) $B^0 \to \overline{D}^0 K^{*0}$ events, the green points correspond to partially reconstructed signal for which one of the two photons used to construct the π^0 is from the underlying event and the pink points correspond to the combinatorial background in the signal Monte Carlo data sample. The light and dark points respectively correspond to the events without and with a constraint on the D^0 invariant mass. In the plot on the right, the red boxes correspond to $b\overline{b}$-inclusive background and the blue boxes correspond to signal.

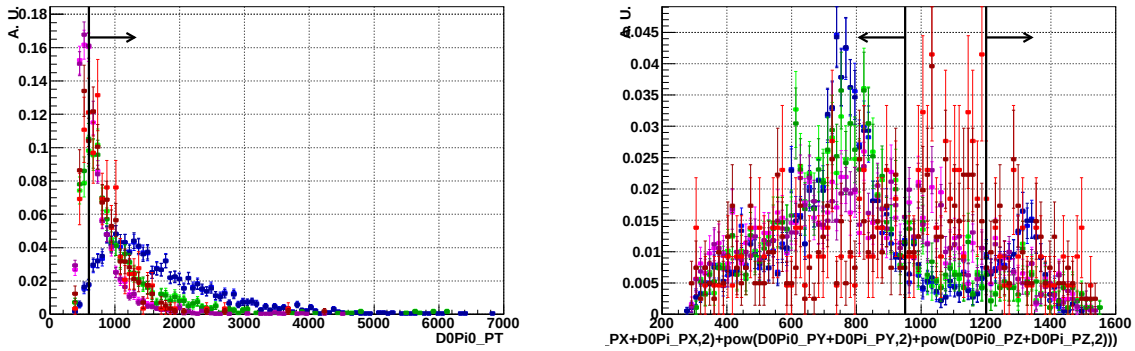

Figure IV.30: Distributions of p_T of the π^0 (left) and invariant $\pi^{\pm}\pi^0$ mass (right). The final selection cut is materialized by the vertical bar and the arrow showing the events kept after the cut. In each plot, the red points corresponds to $b\overline{b}$-inclusive background, the blue points correspond to the properly reconstructed (and matched) $B^0 \to \overline{D}^0 K^{*0}$ events, the green points correspond to partially reconstructed signal for which one of the two photons used to construct the π^0 is from the underlying event and the pink points correspond to the combinatorial background in the signal Monte Carlo data sample. The light and dark points respectively correspond to the events without and with a constraint on the D^0 invariant mass.

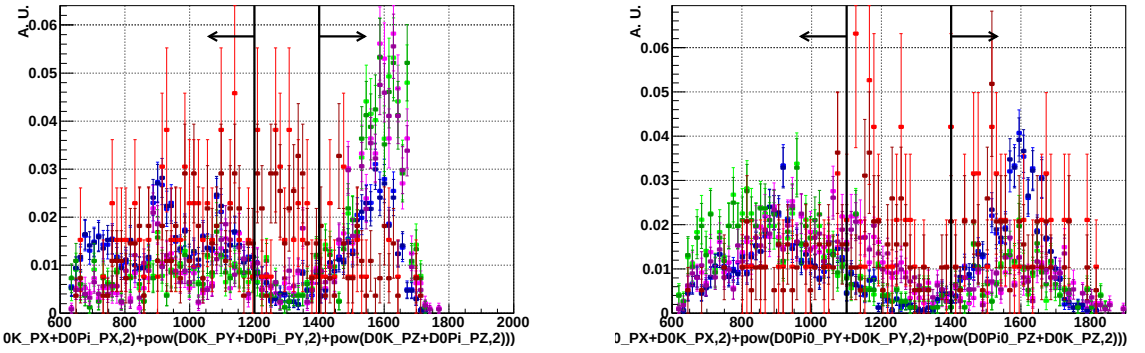

Figure IV.31: Distributions of the $K^{\pm}\pi^{\mp}$ (left) and $K^{\pm}\pi^0$ (right) invariant masses. The final selection cut is materialized by the vertical bar and the arrow showing the events kept after the cut. In each plot, the red points corresponds to $b\overline{b}$-inclusive background, the blue points correspond to the properly reconstructed (and matched) $B^0 \to \overline{D}^0 K^{*0}$ events, the green points correspond to partially reconstructed signal for which one of the two photons used to construct the π^0 is from the underlying event and the pink points correspond to the combinatorial background in the signal Monte Carlo data sample. The light and dark points respectively correspond to the events without and with a constraint on the D^0 invariant mass.

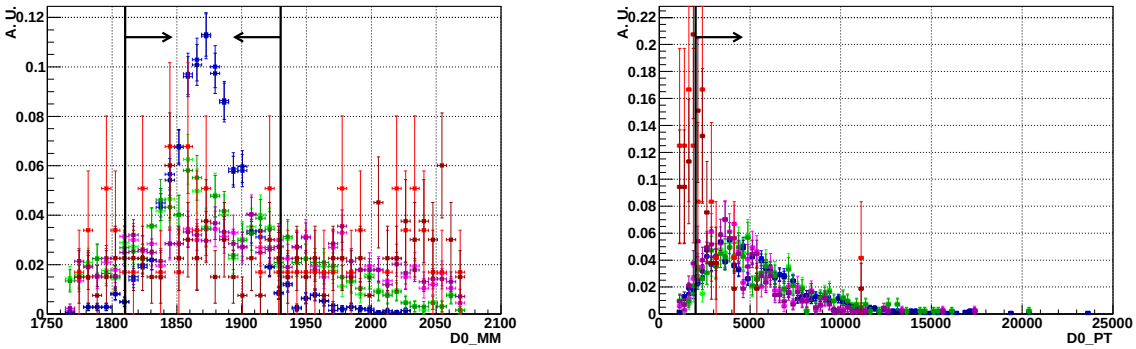

Figure IV.32: Distributions of the D^0 invariant mass (left) and p_T of D^0 (right). The final selection cut is materialized by the vertical bar and the arrow showing the events kept after the cut. In each plot, the red points corresponds to $b\overline{b}$-inclusive background, the blue points correspond to the properly reconstructed (and matched) $B^0 \to \overline{D}^0 K^{*0}$ events, the green points correspond to partially reconstructed signal for which one of the two photons used to construct the π^0 is from the underlying event and the pink points correspond to the combinatorial background in the signal Monte Carlo data sample. The light and dark points respectively correspond to the events without and with a constraint on the D^0 invariant mass.

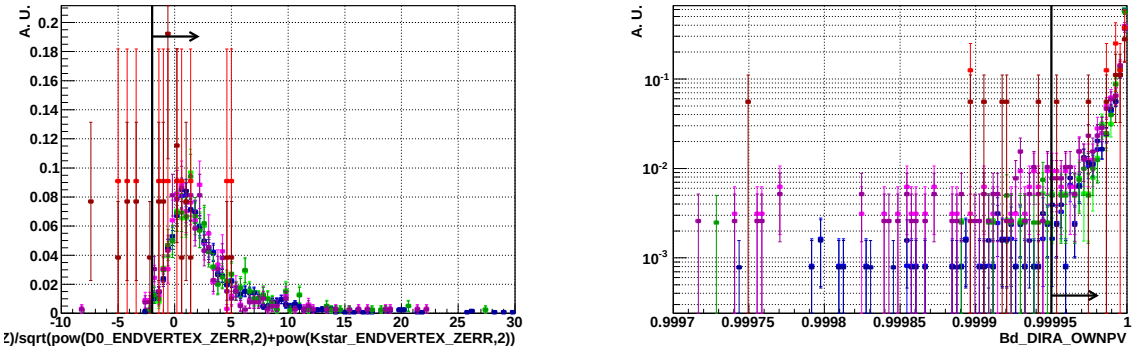

Figure IV.33: Distributions of the signed significance of the distance between the D^0 and K^{*0} positions of the vertex projected on the z-axis (left) and pointing angle of the B^0 (right). The final selection cut is materialized by the vertical bar and the arrow showing the events kept after the cut. In each plot, the red points corresponds to $b\overline{b}$-inclusive background, the blue points correspond to the properly reconstructed (and matched) $B^0 \to \overline{D}^0 K^{*0}$ events, the green points correspond to partially reconstructed signal for which one of the two photons used to construct the π^0 is from the underlying event and the pink points correspond to the combinatorial background in the signal Monte Carlo data sample. The light and dark points respectively correspond to the events without and with a constraint on the D^0 invariant mass.

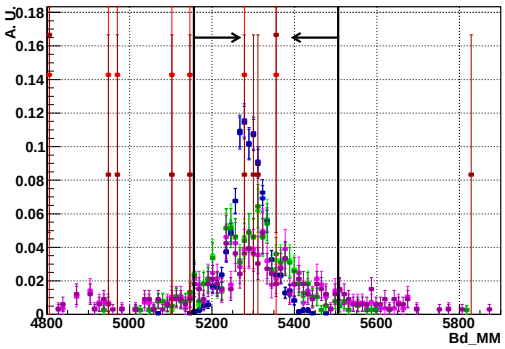

Figure IV.34: Distributions of the B^0 invariant mass. The final selection cut is materialized by the vertical bar and the arrow showing the events kept after the cut. In each plot, the red points corresponds to $b\overline{b}$-inclusive background, the blue points correspond to the properly reconstructed (and matched) $B^0 \to \overline{D}^0 K^{*0}$ events, the green points correspond to partially reconstructed signal for which one of the two photons used to construct the π^0 is from the underlying event and the pink points correspond to the combinatorial background in the signal Monte Carlo data sample. The light and dark points respectively correspond to the events without and with a constraint on the D^0 invariant mass.

numbers in B_d mass region	1 fb^{-1}	5 fb^{-1}
$N_{\overline{B}^0 \to D^0 \overline{K}^{*0}}$, with $D^0 \to K^-\pi^+\pi^0$ resolved.	112	562
$N_{\overline{B}^0 \to D^0 \overline{K}^{*0}}$, with $D^0 \to K^-\pi^+\pi^0$ resolved, including part. reco.	141	705
$N_{\overline{B}^0 \to D^0 \overline{K}^{*0}}$, with $D^0 \to K^-\pi^+\pi^0$ merged.	42	211
$N_{\overline{B}^0 \to D^0 \overline{K}^{*0}}$, with $D^0 \to K^-\pi^+\pi^0$ all.	183	917
$N_{b\overline{b}}$ resolved. in B mass region	1463	7314
$N_{b\overline{b}}$ merged. in B mass region	< 446 at 90 % C.L.	< 2230 at 90 % C.L.
$\frac{N_{\overline{B}^0 \to D^0 \overline{K}^{*0}} \text{ resolved.}}{N_{b\overline{b}} \text{ resolved.}}$ in B_d mass region	0.097	0.097
$\frac{N_{\overline{B}^0 \to D^0 \overline{K}^{*0}} \text{ merged.}}{N_{b\overline{b}} \text{ merged.}}$ in B_d mass region	> 0.094 at 90 % C.L.	> 0.094 at 90 % C.L.
$N_{\overline{B}^0 \to D^0 \overline{K}^{*0}}$, with $D^0 \to K^-\pi^+\pi^0$ resolved with D mass constraint.	110	549
$N_{\overline{B}^0 \to D^0 \overline{K}^{*0}}$, with $D^0 \to K^-\pi^+\pi^0$ resolved including part. reco.	130	653
$N_{b\overline{b}}$ resolved. in B mass region	304	1524
$\frac{N_{\overline{B}^0 \to D^0 \overline{K}^{*0}} \text{ resolved.}}{N_{b\overline{b}} \text{ resolved.}}$ in B_d mass region	0.4	0.4

Table IV.17: Expected yields of $B^0 \to \overline{D}^0 K^{*0}$ with $D^0 \to K^-\pi^+\pi^0$ signal and dominant backgrounds for integrated luminosities of 1 fb^{-1} and 5 fb^{-1} at $\sqrt{s} = 7$ TeV. The values are quoted in an invariant mass window of ± 150 MeV/c^2 centered on the PDG B^0 invariant mass, w/o D^0 mass constraint for the merged π^0, and ± 50 MeV/c^2, w/ D^0 mass constraint for the resolved π^0.

numbers in B_d mass region	1 fb^{-1}	5 fb^{-1}
$N_{\overline{B}^0 \to D^0 \overline{K}^{*0}, \text{ with } D^0 \to K^-\pi^+\pi^+\pi^-}$, in B_d mass region	246	1231
$N_{\overline{B}^0 \to D^0 \overline{K}^{*0}, \text{ with } D^0 \to K^-\pi^+\pi^+\pi^- \text{ including part. reco.}}$, in B_d mass region	270	1351
$N_{b\overline{b}}$ in B mass region	158	792
$\frac{N_{\overline{B}^0 \to D^0 \overline{K}^{*0}}}{N_{b\overline{b}}}$ in B_d mass region	1.5	1.5

Table IV.18: Expected yields of $B^0 \to \overline{D}^0 K^{*0}$ with $D^0 \to K^-\pi^+\pi^+\pi^-$ signal and dominant backgrounds for integrated luminosities of 1 fb^{-1} and 5 fb^{-1} at $\sqrt{s} = 7$ TeV. The values are quoted iin an invariant mass window of ± 50 MeV/c^2 centered on the PDG B^0 invariant mass.

IV.4 Conclusion and necessary steps towards a γ measurement

IV.4.1 Conclusion

In this chapter we have demonstrated that a selection of $B^0 \to DK^{*0}$ with $D^0 \to K^\pm\pi^\mp$ can be performed with a good signal over background, and this selection has been extended to the $D^0 \to K^\pm\pi^\mp\pi^0$ and $D^0 \to K^\pm\pi^\mp\pi^+\pi^-$. The study of the impact on the γ extraction is performed, showing that γ is difficult to extract with an ADS method only, but provides useful constraints that can be combined to a GLW analysis of $B^0 \to DK^{*0}$. An important potential background to the suppressed modes, from partially reconstructed $B_s^0 \to D^*\overline{K}^{*0}$ decays is pointed out. This channel and the fully reconstructed $B_s^0 \to D\overline{K}^{*0}$ have not yet been observed, making this channel interesting as a first study, performed in chapter V.

IV.4.2 Steps towards γ

The necessary steps towards the measurement of γ to understand the backgrounds in the $B^0 \to DK^{*0}$ decays are the following (40 pb^{-1} is the integrated luminosity collected in 2010 and used for winter 2011 analyses, 200 pb^{-1} is the integrated luminosity used for the summer 2011 conferences, 1 fb^{-1} is the expected integrated luminosity by the end of 2011):

- first observation of the favoured $B_s^0 \to \overline{D}^0\overline{K}^{*0}$ decay mode (see chapter V) and evidence for $B^0 \to \overline{D}^0 K^{*0}$, with 40 pb^{-1},
- observation of the favoured $B^0 \to \overline{D}^0 K^{*0}$ decay mode with 100 pb^{-1},
- search for the $B_s^0 \to \overline{D}^0\overline{K}^{*0}$ decay mode with other D decays ($D^0 \to K^\pm K^\mp$, $D^0 \to K^\pm\pi^\mp\pi^0$, $D^0 \to K^\pm\pi^\mp\pi^+\pi^-$) 200 pb^{-1},
- optimization of the analysis on real data and for the suppressed modes with 200 pb^{-1} and more,
- understanding of the partially reconstructed background with 200 pb^{-1} and more,

- search for the suppressed $B^0 \to D^0 K^{*0}$ decay mode with 500 pb^{-1},
- γ (R_{ADS} and A_{ADS}) measurements with 1 fb^{-1} and more.

Chapter V

Observation of $\overline{B}^0_s \to D^0 K^{*0}$ and measurement of its branching fraction

- Sur une échelle de 5 à 10 [...], de 5 à 6 c'est une époque qui est loin derrière nous, de 7 à 9 du passé faisons table en marbre et à 10 on est beaucoup plus pris au sérieux qu'avant, j'ai bon ?
- Non c'est n'importe quoi mais ça ne fait rien. Le principal, c'est d'essayer, c'est ça qui compte.

Jean-Christophe Hembert alias *Karadoc* et Franck Pitiot alias *Perceval* in *L'échelle de Perceval*, **Kaamelott, Livre IV**, Tome 1, Épisode 25, écrit par Alexandre Astier.

Contents

As pointed out in chapter IV, the first step towards a γ measurement with $B^0 \to D^0 K^{*0}$ decays at LHCb consist in the observation of the $\overline{B}^0_s \to D^0 K^{*0}$ decay. The first observation of this decay mode of the B^0_s is performed in this chapter. The result is compared with theoretical predictions and the expectations for 2011 are summarized.

V.1 Theoretical motivation

Different theoretical approaches are available for the estimation of the branching fractions of $B \to DV$ decays. These approaches differ in their assumptions on the breaking of SU(3) symmetry. Applying SU(3) symmetry and neglecting effects that could break it, Colangelo and Ferrandes [95] obtained $\mathcal{BR}(\overline{B}^0_s \to D^0 K^{*0}) = (9.6 \pm 2.4)\,10^{-4}$. It should be noted that this value is obtained with a rather imprecise value of $\mathcal{BR}(\overline{B}^0 \to D^0 \overline{K}^{*0}) = (4.8 \pm 1.2)\,10^{-5}$, the experimental status being now $\mathcal{BR}(\overline{B}^0 \to D^0 \overline{K}^{*0}) = (4.2 \pm 0.6)\,10^{-5}$ [38].

Another approach consists in a global fit of a class of decays (a complete description of decays of B mesons to two-body hadronic final states in the context of $SU(3)_F$ symmetry breaking is given in ref. [96]). Doing this for $B \to DP$ and $B \to D^*P$ decays, Chiang and Senaha [97] perform a fit (including $SU(3)_F$ symmetry breaking parameters) and are able to extract predictions on many undiscovered B_s channels. When they apply their method to the $B \to DV$ decays, things are less convincing due to an inconsistency in the data at the 1.7σ level, between DK^* and $D\rho$ decays. They have to fix the $SU(3)_F$ symmetry breaking parameters to the values obtained from naive factorization in order to get a convergent fit. With such an approximation they obtained $\mathcal{BR}(\overline{B}^0_s \to D^0 K^{*0}) = (5.6 \pm 0.5)\,10^{-4}$ assuming $\mathcal{BR}(\overline{B}^0 \to D^0 \overline{K}^{*0}) = (3.8 \pm 0.4)\,10^{-5}$. The result assuming no $SU(3)_F$ breaking, gives a consistent result of $\mathcal{BR}(\overline{B}^0_s \to D^0 K^{*0}) = (5.8 \pm 0.5)\,10^{-4}$, but the fit is worse. A solution to this problem is to get a direct measurement of one of the $SU(3)_F$ symmetry breaking parameters which directly appears in the comparison of branching fractions $\mathcal{BR}(\overline{B}^0_s \to D^0 K^{*0})$ and $\mathcal{BR}(\overline{B}^0 \to D^0 \overline{K}^{*0})$. In the framework developed in [97], only one $SU(3)_F$ breaking parameter appears for each topology and each class of decay. We obtain (p^* is the momentum of the D^0 or K^{*0} in the center of mass of the B, ϵ_{C_V} is a $SU(3)_F$ breaking parameter):

$$\frac{\mathcal{BR}(\overline{B}^0_s \to D^0 K^{*0})}{\mathcal{BR}(B^0 \to D^0 K^{*0})} = \left(\frac{p^*_{\overline{B}^0_s \to D^0 K^{*0}}}{p^*_{B^0 \to D^0 K^{*0}}}\right)^3 \left(\frac{m_{B_s}}{m_{B_d}}\right)^2 \frac{\tau_{B_s}}{\tau_{B_d}} \left(\frac{1 - \frac{\lambda^2}{2}}{\lambda}\right)^2 \left(\frac{1}{\epsilon_{C_V}}\right)^2. \qquad \text{(V.1)}$$

Another approach is to estimate rescattering effects in the final state (final state interactions, FSI). Such an approach, developed by Chua and Hou [98] yields to predictions for FSI in $B \to DP$ decays, which are not consistent with the factorization approach. The ratio $\frac{\mathcal{BR}(\overline{B}^0_s \to D^0 K^{*0})}{\mathcal{BR}(B^0 \to D^0 K^{*0})}$ could give insights to the order of magnitude of FSI in the $B \to DV$ decays.

Finally a pQCD calculation of $\mathcal{BR}(\overline{B}^0_s \to D^0 K^{*0})$ is performed in [99] and provides, from more fundamental principles than the previous predictions, $\mathcal{BR}(\overline{B}^0_s \to D^0 K^{*0}) =$

$\left(4.36^{+1.84+1.21+0.13}_{-1.31-1.14-0.13}\right) 10^{-4}$ where the first uncertainty comes from the hadronic parameters of the B^0 meson wave function, the second from higher order perturbative QCD corrections and the last (negligible) one comes from the uncertainty on the CKM matrix elements.

The understanding of low energy QCD and in particular the order of magnitude of $SU(3)_F$ symmetry breaking effects could be improved by the proposed measurement.

V.2 Measurement

V.2.1 Accumulated statistics

Since the favoured $B^0 \to \overline{D}^0 K^{*0}$ decays are colour suppressed in neutral B decays, they are more difficult to observe than the charged $B^\pm \to DK^\pm$ modes. Typical branching fractions for the colour suppressed $B \to DV$ (where V^0 denotes either ρ^0 or K^{*0}) decays are in the range of 10^{-4} to 10^{-5}. The branching fractions for these channels are listed in Tab. V.1, where the total branching fraction takes into account the subdecays of the D^0 into $K^-\pi^+$, of the K^{*0} into $K^+\pi^-$ and of the ρ^0 into $\pi^+\pi^-$. Given the approximate 36 pb^{-1} collected in the 2010 run at LHCb, approximate numbers of events produced in the LHCb acceptance are given in the same table, using the cross-section measurements described in early LHCb publications [100, 101, 102]. These last numbers do not take into account the reconstruction, selection and trigger efficiencies. This shows that the number of $B^0 \to \overline{D}^0 K^{*0}$ will be too small to use this mode as a normalization for the $\overline{B}^0_s \to D^0 K^{*0}$ observation. Instead the $\overline{B}^0 \to D^0 \rho^0$ mode is used in the following for the normalization.

channel	B decay $\mathcal{B}$(in 10^{-5})	total $\mathcal{B}$(in 10^{-6})	number of produced events
$\overline{B}^0 \to D^0 \rho^0$	32 ± 5	12 ± 2	20000
$B^0 \to \overline{D}^0 K^{*0}$	4.2 ± 0.6	1.1 ± 0.2	1800
$\overline{B}^0_s \to D^0 K^{*0}$	32 to 87	8 to 23	3000 to 9600
$B^0 \to D^0 K^{*0}$	$\simeq 0.26$	$\simeq 0.07$	110

Table V.1: Branching fractions [38] for colour suppressed $B \to DV$ decays where V denotes a vector meson resonance (either ρ^0 or K^{*0}). The last column gives the approximate number of events produced within the LHCb acceptance for an integrated luminosity of 36 pb^{-1} at the centre of mass energy of $\sqrt{s} = 7\ TeV$, using the measured $b\bar{b}$ cross-section $\sigma\left(pp \to b\bar{b}X\right) = (284 \pm 20 \pm 49)$ µ b [100, 101, 102]. The values quoted for the $\overline{B}^0_s \to D^0 K^{*0}$ are extrapolated from $\overline{B}^0 \to D^0 \rho^0$ (lower value) and $B^0 \to \overline{D}^0 K^{*0}$ (higher value) branching fractions, taking into account for CKM matrix elements only. The value quoted for $B^0 \to D^0 K^{*0}$ is calculated from the branching fraction of $B^0 \to \overline{D}^0 K^{*0}$ taking into account for a factor r_B^2.

V.2.2 Datasets and trigger settings

V.2.2.1 Data samples

The Monte Carlo samples have been produced with the latest production versions of the software that are summarized in Tab. V.2. The full statistics mentioned in Tab. V.2 is split in two halves corresponding to the two polarities of the magnetic field. This Monte Carlo sample has been generated with $\nu = 2.5$, that roughly corresponds to the average number of visible interactions in the 2010 real data sample. The whole 2010 run at $\sqrt{s} = 7$ TeV of the LHC, corresponding to (35.7 ± 3.5) pb^{-1}, is used and is dominated by the data taken since the end of September. The so-called Stripping 12*b* version of the stripping is used. All samples are then processed with version v26r4 of DaVinci to produce the tuples used in this analysis.

channel	model	Gauss	Boole	Brunel	Moore	DaVinci	stat.
$\overline{B}^0 \to D^0 \rho^0$	SVS	v39r0	v21r9	v37r8p5	v10r2	v26r3p2	510k evts
$\overline{B}^0 \to D^0 \overline{K}^{*0}$	SVS	v39r0	v21r9	v37r8p5	v10r2	v26r3p2	114k evts
$\overline{B}^0_s \to D^0 K^{*0}$	SVS	v39r0	v21r9	v37r8p5	v10r2	v26r3p2	510k evts

Table V.2: All of the channels are generated using the center-of-mass energy of $\sqrt{s} = 7$ TeV and the stripping version used for the reprocessing. The SVS model is the EvtGen standard to generate decays of a spin-0 particle to a spin-1 particle and a spin-0 particle [103].

V.2.2.2 Trigger settings

Different trigger settings have been used during the data-taking period. The most significant contributions to the whole data sample are summarized in Tab. V.3 which gives the main characteristics of each trigger setting but also the corresponding integrated luminosity. At the trigger level four Global Event Cuts (GECs) are applied to fulfill online and offline timing requirements. These GECs are the following

- number of VELO clusters < 3000,
- number of OT hits < 10000,
- number of IT hits < 3000,
- SPD multiplicity, that depends on the trigger setting (see Tab. V.3).

The first three GECs are independently applied in most of the contributing trigger settings to the total statistics. The analysis is not sensitive to the SPD multiplicity cut, that depends on the trigger setting, for two reasons. On the one hand another GEC is applied at the stripping level at 120 long tracks, which is similar to the tightest SPD multiplicity cut (< 450). On the second hand the effect of any GEC cancels in the ratio of numbers of events that is computed to extract the ratio of branching fractions.

TCK	SPD mult.	L0 Hadron	$\int \mathcal{L}$	stat.
0x19001f	disabled	$E_T > 2.26$ GeV/c^2	1.4 pb^{-1}	63
0x190024	< 600	$E_T > 2.26$ GeV/c^2	1.0 pb^{-1}	38
0x1e0030	< 900	$E_T > 2.6$ GeV/c^2	2.1 pb^{-1}	72
0x1f0029	< 900	$E_T > 3.6$ GeV/c^2	3.1 pb^{-1}	44
0x24002a	< 900	$E_T > 3.6$ GeV/c^2	1.2 pb^{-1}	19
0x24002c	< 450	$E_T > 3.6$ GeV/c^2	1.3 pb^{-1}	13
0x25002c	< 450	$E_T > 3.6$ GeV/c^2	1.9 pb^{-1}	21
0x2b002a	< 900	$E_T > 3.6$ GeV/c^2	1.8 pb^{-1}	21
0x2a002a	< 900	$E_T > 3.6$ GeV/c^2	4.2 pb^{-1}	62
0x2e002a	< 900	$E_T > 3.6$ GeV/c^2	8.7 pb^{-1}	119
0x2e002c	< 450	$E_T > 3.6$ GeV/c^2	8.9 pb^{-1}	122

Table V.3: The main trigger settings used are summarised here with a special emphasis on the SPD multiplicity and the L0 hadron threshold. The last two columns contain the integrated luminosity collected [104] and the number of events in the `D0Rho0` fit mass window for the given TCK.

The HLT trigger is made of the single HLT1 track algorithm [74] for all the data used here except the first 2.4 pb^{-1} and the HLT2 topological trigger [105]. In the first 2.4 pb^{-1} the HLT1 single hadron and di-hadron lines are used.

V.2.2.3 Requirements on the trigger settings

In order to extract the ratio of branching fractions (see section V.2.5) the events triggering the L0 level by the `L0HadronTOS` or the `OtherB` (see section V.2.5.2) are used. 94 ± 8 % are thus kept for the analysis. No specific requirement is made on the HLT.

V.2.3 Selection

As mentioned above, the analysis strategy is to benefit from the cancellation of most of the systematic uncertainties in the ratio of branching fractions. In particular the difference in selection efficiencies is minimised by adopting the same selection strategy for both channels. Hence common cuts will be used as far as possible, especially for building a D^0 candidate. However, some inevitable differences appear in the selection of the vector meson candidate, especially in the particle identification requirements and in the mass window cuts.

In the current analysis, we use a cut-based selection aiming at optimizing the significance $\frac{S}{\sqrt{S+B}}$ (where S and B respectively denote the number of signal and background events) but keeping in mind reasonable values for the cuts. This optimization was performed using $B^0 \to$

$D^0 K^{*0}$ MC09 for the signal and inclusive $b\bar{b}$ MC09 for the background. In the future, we anticipate moving to a multivariate analysis in order to further improve the statistical significance of the signal of interest.

V.2.3.1 Common cuts

Stripping and Global Event Cuts After having been triggered and stored by the LHCb apparatus, the dataset is stripped in order to keep under control the computing time spent by users and limit the needed storage capacity. Stripping selections were intended to be loose with respect to offline analysis selection cuts but had to cope with an increased CPU time consumption and retention rate compared to the design due to the higher pile-up.

In order to reduce correlations between channels of similar topologies a very inclusive $B \to DX$ stripping for hadronic channels has been developed. The cuts are summarised in Tab. V.4 and also in [106].

A single GEC is applied in the stripping at 120 reconstructed long tracks – this mainly removes busy events for which too many candidates are built in the reconstruction. The threshold is motivated by time constraints and retention rates.

Selection cuts The selection strategy is to build a common clean D^0 candidate that is then combined with a vector meson candidate to construct the B candidate. The selection thresholds are summarised in Tab. V.5. The distributions after the stripping but before any additional cut are shown in Figs. V.1-V.13. We systematically show, on the left the distributions for the $D^0 K^{*0}$ selection and on the right the distributions for the $\overline{D}{}^0 \rho^0$ selection. In all plots, the red distribution corresponds to the real data. In the $D^0 K^{*0}$ plots (on the left), the blue and green distributions respectively correspond to the Monte Carlo distributions for signal $B^0 \to D^0 K^{*0}$ and $\overline{B}{}^0_s \to D^0 K^{*0}$. These two distributions are in any case consistent within the statistical uncertainty, meaning that kinematic effects due to the exchange of a B^0 by a B^0_s are negligible. In the $\overline{D}{}^0 \rho^0$ plots (on the right), the blue distributions correspond to the Monte Carlo distributions for signal $\overline{B}{}^0 \to D^0 \rho^0$. All distributions are normalized to the same area.

particle	variable	threshold
$\text{track}_{K^{*0}}$	χ^2_{track}	< 5
	p_T	> 300 MeV/c
	p	> 2 GeV/c
	$\min_{\text{PVs}} \chi^2_{\text{IP}}$	> 4
track_{ρ^0}	χ^2_{track}	< 5
	p_T	> 250 MeV/c
	p	> 2 GeV/c
	$\min_{\text{PVs}} \chi^2_{\text{IP}}$	> 4
K^{*0} or ρ^0	$\left(\chi^2/n_{\text{D.O.F.}}\right)$ vertex	< 12
	p_T	> 1 GeV/c
	$\min_{\text{PVs}} \chi^2_{\text{IP}}$	> 4
track_{D^0}	χ^2_{track}	< 5
	p_T	> 250 MeV/c
	p	> 2 GeV/c
	$\min_{\text{PVs}} \chi^2_{\text{IP}}$	> 4
D^0	$\left(\chi^2/n_{\text{D.O.F.}}\right)$ vertex	< 12
	$\left(\chi^2\right)$ flight wrt best PV	> 36
	p_T	> 1 GeV/c
	$\cos$ (Dir. Angle wrt own PV)	> 0.9
	$\max_{\text{daughters}}$ (D.O.C.A.)	< 1.5 mm
	$\max_{\text{daughters}} \chi^2_{\text{IP wrt PV}}$	> 40
	$\left\lvert m^{\text{reconstructed}}_{D^0} - m^{\text{PDG}}_{D^0} \right\rvert$	< 100 MeV/c^2
B^0 or B^0_s	$\cos$ (Dir. Angle wrt own PV)	> 0.9998
	$\left(\chi^2/n_{\text{D.O.F.}}\right)$ vertex	< 12
	$\min_{\text{PVs}} \chi^2_{\text{IP}}$	< 25
	$\tau_{\text{reconstructed}}$	> 0.2 ps
	$m^{\text{reconstructed}}_{B^0}$	$< m^{\text{PDG}}_{B^0_s} + 500$ MeV/c^2
	$m^{\text{reconstructed}}_{B^0}$	$> m^{\text{PDG}}_{B^0} - 500$ MeV/c^2
Global Event Cut	$N_{\text{long tracks}}$	< 120

Table V.4: Summary of the stripping selection cuts applied in the Stripping 12b.

particle	variable	threshold
$K_{K^{*0}}$	$\Delta\mathrm{LL}_{K-\pi}$	> 3
	p_T	> 300 MeV/c
$\pi_{K^{*0}}$ or π_{ρ^0}	$\Delta\mathrm{LL}_{K-\pi}$	< 3
	p_T	> 300 MeV/c
K^{*0}	$\lvert\cos\theta^*\rvert$	> 0.4
	$\min_{\mathrm{PVs}} \chi^2_{\mathrm{IP}}$	> 25
	$\lvert m^{\mathrm{reconstructed}}_{K^{*0}} - m^{\mathrm{PDG}}_{K^{*0}}\rvert$	< 50 MeV/c^2
ρ^0	$\lvert\cos\theta^*\rvert$	> 0.4
	$\min_{\mathrm{PVs}} \chi^2_{\mathrm{IP}}$	> 25
	$\lvert m^{\mathrm{reconstructed}}_{\rho^0} - m^{\mathrm{PDG}}_{\rho^0}\rvert$	< 150 MeV/c^2
K_{D^0}	$\Delta\mathrm{LL}_{K-\pi}$	> 0
	P_T	> 400 MeV/c
π_{D^0}	$\Delta\mathrm{LL}_{K-\pi}$	< 4
D^0	$\left(\chi^2/n_{\mathrm{D.O.F.}}\right)$ vertex	< 5
	$\min_{\mathrm{PVs}} \chi^2_{\mathrm{IP}}$	> 4
	$\lvert m^{\mathrm{reconstructed}}_{D^0} - m^{\mathrm{PDG}}_{D^0}\rvert$	< 20 MeV/c^2
B^0 or B^0_s	$\frac{z_{D^0\ \mathrm{vertex}} - z_{V\ \mathrm{vertex}}}{\sqrt{\sigma_{z,\ D^0\ \mathrm{vertex}} + \sigma_{z,\ V\ \mathrm{vertex}}}}$	> -2
	$\cos$ (Dir. Angle wrt own PV)	> 0.99995
	$\left(\chi^2/n_{\mathrm{D.O.F.}}\right)$ vertex	< 4
	$\min_{\mathrm{PVs}} \chi^2_{\mathrm{IP}}$	< 9

Table V.5: Summary of the selection cuts used. The V particle denotes either a ρ^0 or a K^{*0}. The PID cuts found after the optimization described in section V.2.3.4 are shown.

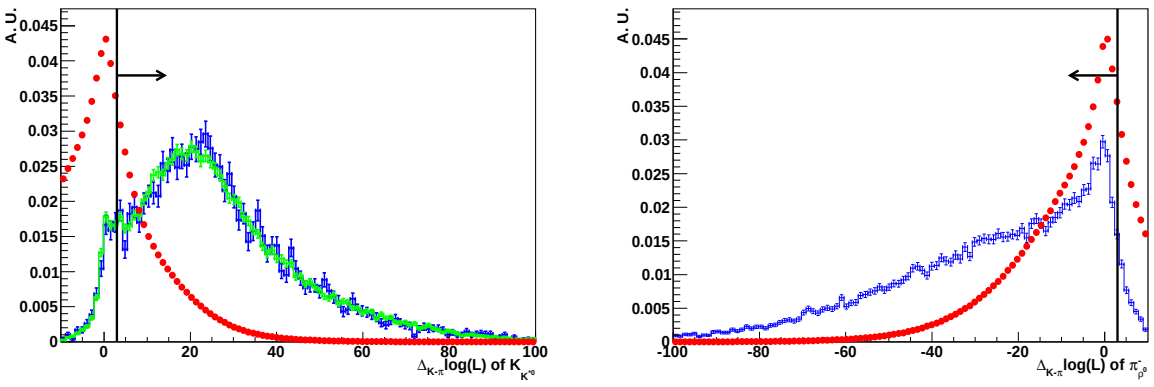

Figure V.1: Particle identification variables for the K from the K^{*0} and the π^+ from the ρ^0 respectively on the left and the right after the stripping only. The full red circles (black in black and white printing) correspond to the real data in both plots. On the left plot, the blue and green histograms (respectively black and grey in black and white printing) correspond to $B^0 \to D^0 K^{*0}$ and $\overline{B}^0_s \to D^0 K^{*0}$ Monte Carlo respectively. On the right plot, the blue histogram (black in black and white printing) corresponds to $\overline{B}^0 \to D^0 \rho^0$ Monte Carlo. The black vertical lines indicate the final selection cuts.

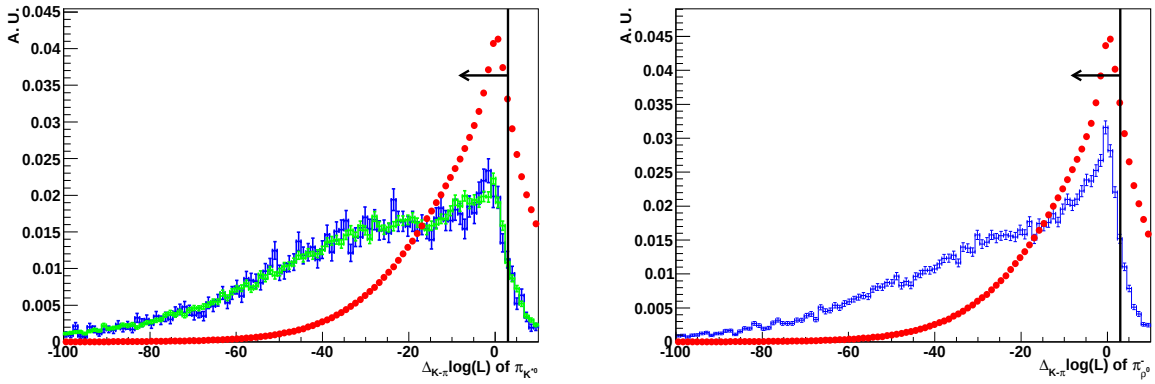

Figure V.2: Particle identification variables for the π from the K^{*0} and the π^- from the ρ^0 respectively on the left and the right after the stripping only. The full red circles (black in black and white printing) correspond to the real data in both plots. On the left plot, the blue and green histograms (respectively black and grey in black and white printing) correspond to $B^0 \to D^0 K^{*0}$ and $\overline{B}^0_s \to D^0 K^{*0}$ Monte Carlo respectively. On the right plot, the blue histogram (black in black and white printing) corresponds to $\overline{B}^0 \to D^0 \rho^0$ Monte Carlo. The black vertical lines indicate the final selection cuts.

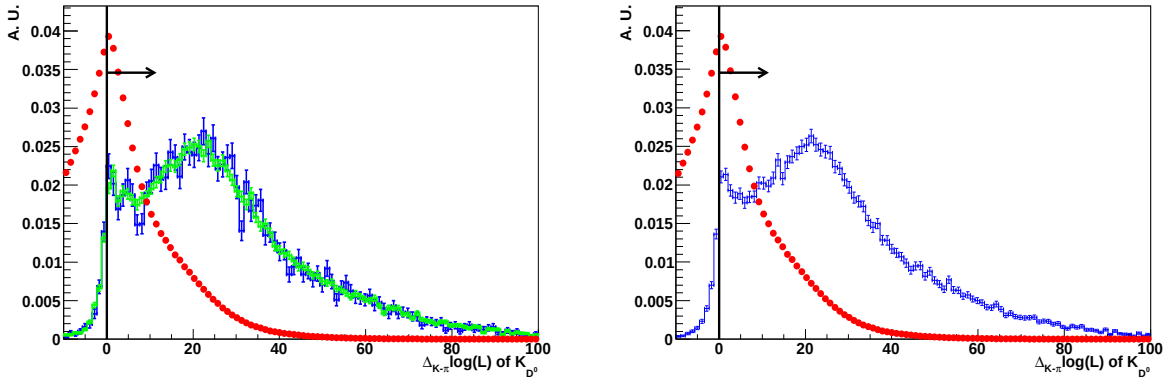

Figure V.3: Particle identification variables for the K from the D^0 on the left and the right after the stripping only. The full red circles (black in black and white printing) correspond to the real data in both plots. On the left plot, the blue and green histograms (respectively black and grey in black and white printing) correspond to $B^0 \to D^0 K^{*0}$ and $\overline{B}^0_s \to D^0 K^{*0}$ Monte Carlo respectively. On the right plot, the blue histogram (black in black and white printing) corresponds to $\overline{B}^0 \to D^0 \rho^0$ Monte Carlo. The black vertical lines indicate the final selection cuts.

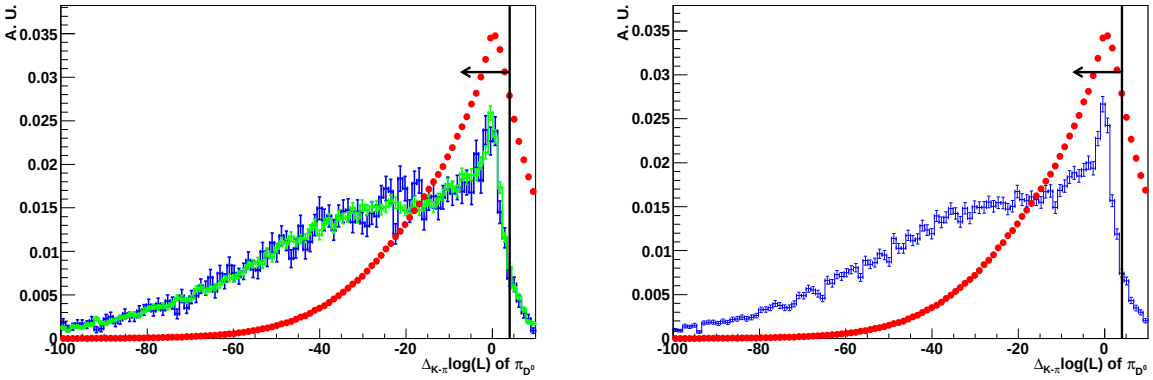

Figure V.4: Particle identification variables for the π from the D^0 on the left and the right after the stripping only. The full red circles (black in black and white printing) correspond to the real data in both plots. On the left plot, the blue and green histograms (respectively black and grey in black and white printing) correspond to $B^0 \to D^0 K^{*0}$ and $\overline{B}^0_s \to D^0 K^{*0}$ Monte Carlo respectively. On the right plot, the blue histogram (black in black and white printing) corresponds to $\overline{B}^0 \to D^0 \rho^0$ Monte Carlo. The black vertical lines indicate the final selection cuts.

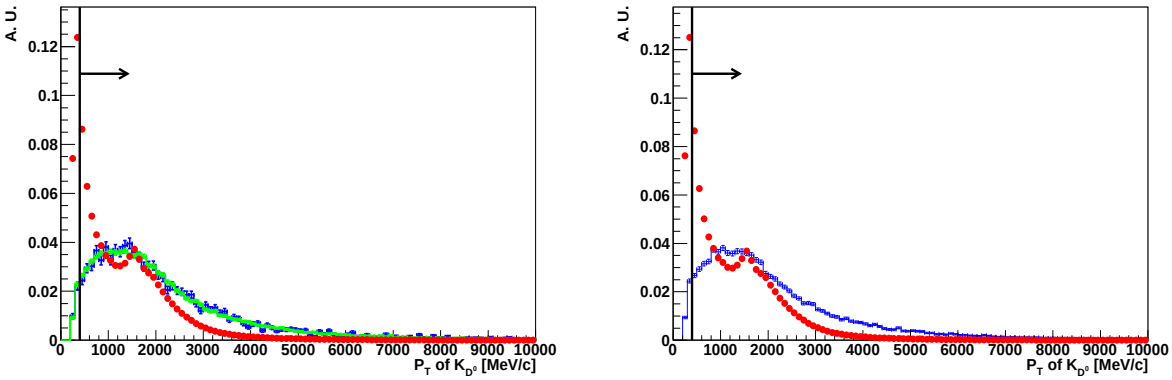

Figure V.5: Transverse momentum distribution of the K of the D^0 meson. The full red circles (black in black and white printing) correspond to the real data in both plots. On the left plot, the blue and green histograms (respectively black and grey in black and white printing) correspond to $B^0 \to D^0 K^{*0}$ and $\overline{B}^0_s \to D^0 K^{*0}$ Monte Carlo respectively. On the right plot, the blue histogram (black in black and white printing) corresponds to $\overline{B}^0 \to D^0 \rho^0$ Monte Carlo. The black vertical lines indicate the final selection cuts.

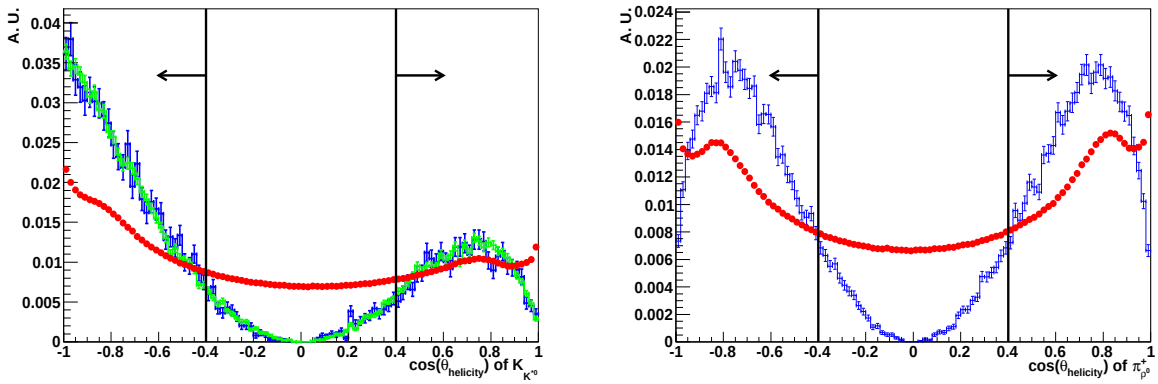

Figure V.6: Distributions for the cosine of the helicity angle of the K from the K^{*0} and the π^+ from the ρ^0 respectively on the left and the right. The full red circles (black in black and white printing) correspond to the real data in both plots. On the left plot, the blue and green histograms (respectively black and grey in black and white printing) correspond to $B^0 \to D^0 K^{*0}$ and $\overline{B}^0_s \to D^0 K^{*0}$ Monte Carlo respectively. On the right plot, the blue histogram (black in black and white printing) corresponds to $\overline{B}^0 \to D^0 \rho^0$ Monte Carlo. The black vertical lines indicate the final selection cuts.

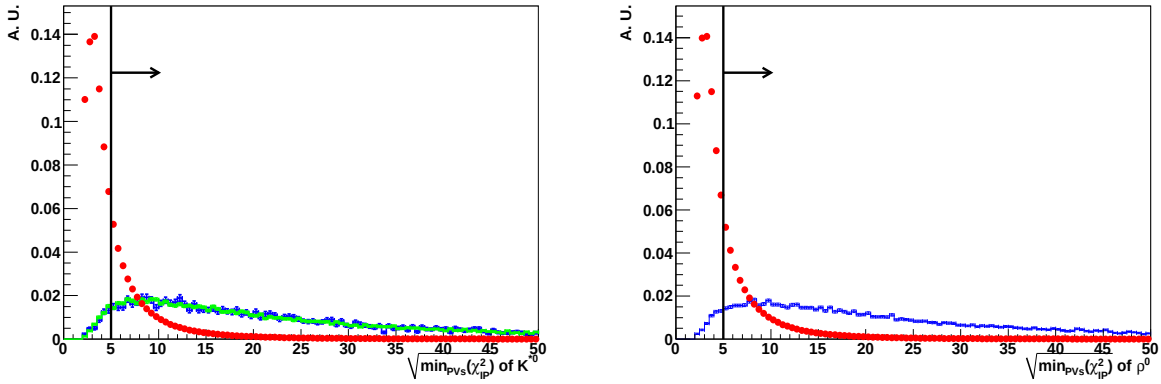

Figure V.7: Square root of the minimum impact parameter χ^2 of the vector meson (K^{*0} on the left and ρ^0 on the right) among all the reconstructed primary vertices. The full red circles (black in black and white printing) correspond to the real data in both plots. On the left plot, the blue and green histograms (respectively black and grey in black and white printing) correspond to $B^0 \to D^0 K^{*0}$ and $\overline{B}^0_s \to D^0 K^{*0}$ Monte Carlo respectively. On the right plot, the blue histogram (black in black and white printing) corresponds to $\overline{B}^0 \to D^0 \rho^0$ Monte Carlo. The black vertical lines indicate the final selection cuts.

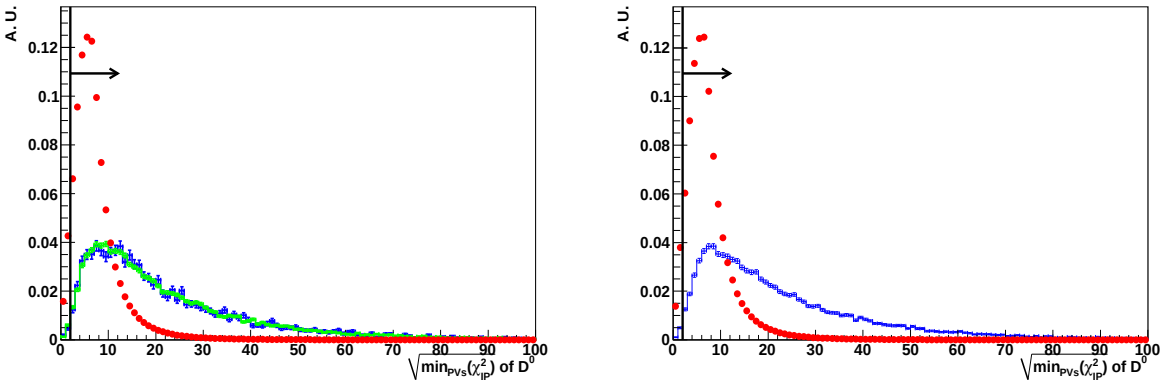

Figure V.8: Square root of the minimum impact parameter χ^2 of the D^0 meson among all the reconstructed primary vertices. The full red circles (black in black and white printing) correspond to the real data in both plots. On the left plot, the blue and green histograms (respectively black and grey in black and white printing) correspond to $B^0 \to D^0 K^{*0}$ and $\overline{B}{}^0_s \to D^0 K^{*0}$ Monte Carlo respectively. On the right plot, the blue histogram (black in black and white printing) corresponds to $\overline{B}{}^0 \to D^0 \rho^0$ Monte Carlo. The black vertical lines indicate the final selection cuts.

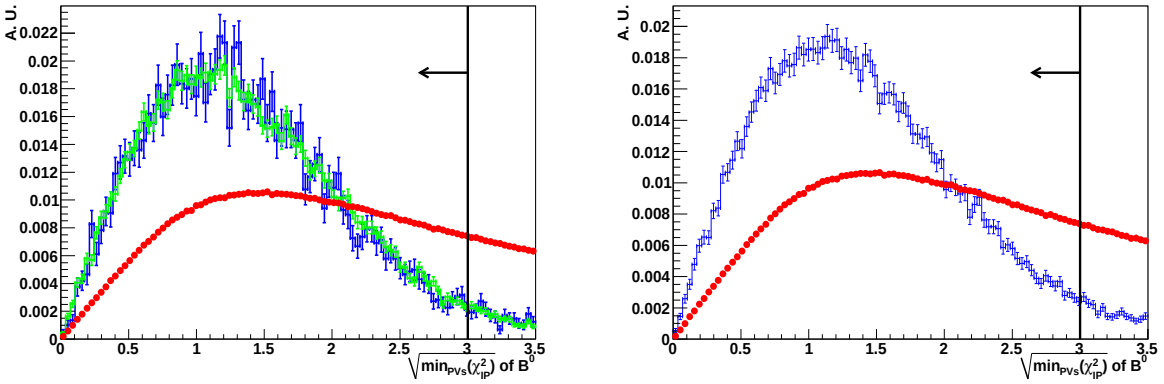

Figure V.9: Square root of the minimum impact parameter χ^2 of the B^0 meson among all the reconstructed primary vertices. The full red circles (black in black and white printing) correspond to the real data in both plots. On the left plot, the blue and green histograms (respectively black and grey in black and white printing) correspond to $B^0 \to D^0 K^{*0}$ and $\overline{B}{}^0_s \to D^0 K^{*0}$ Monte Carlo respectively. On the right plot, the blue histogram (black in black and white printing) corresponds to $\overline{B}{}^0 \to D^0 \rho^0$ Monte Carlo. The black vertical lines indicate the final selection cuts.

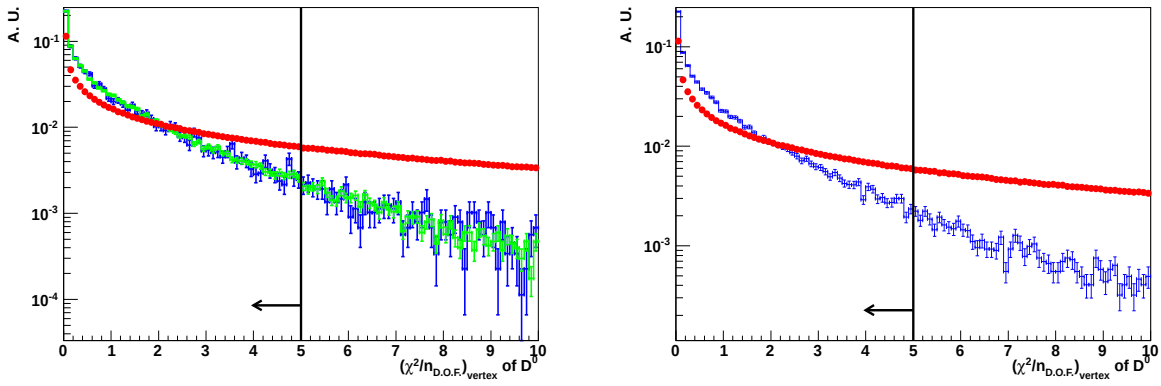

Figure V.10: Distributions for the χ^2 per degree of freedom for the D^0 vertex fit. The full red circles (black in black and white printing) correspond to the real data in both plots. On the left plot, the blue and green histograms (respectively black and grey in black and white printing) correspond to $B^0 \to D^0 K^{*0}$ and $\overline{B}^0_s \to D^0 K^{*0}$ Monte Carlo respectively. On the right plot, the blue histogram (black in black and white printing) corresponds to $\overline{B}^0 \to D^0 \rho^0$ Monte Carlo. The black vertical lines indicate the final selection cuts.

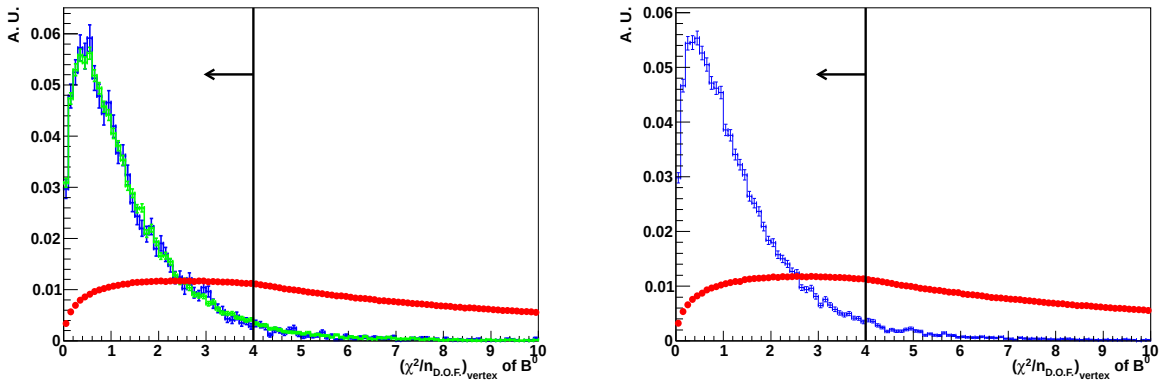

Figure V.11: Distributions for the χ^2 per degree of freedom for the B^0 vertex fit. The full red circles (black in black and white printing) correspond to the real data in both plots. On the left plot, the blue and green histograms (respectively black and grey in black and white printing) correspond to $B^0 \to D^0 K^{*0}$ and $\overline{B}^0_s \to D^0 K^{*0}$ Monte Carlo respectively. On the right plot, the blue histogram (black in black and white printing) corresponds to $\overline{B}^0 \to D^0 \rho^0$ Monte Carlo. The black vertical lines indicate the final selection cuts.

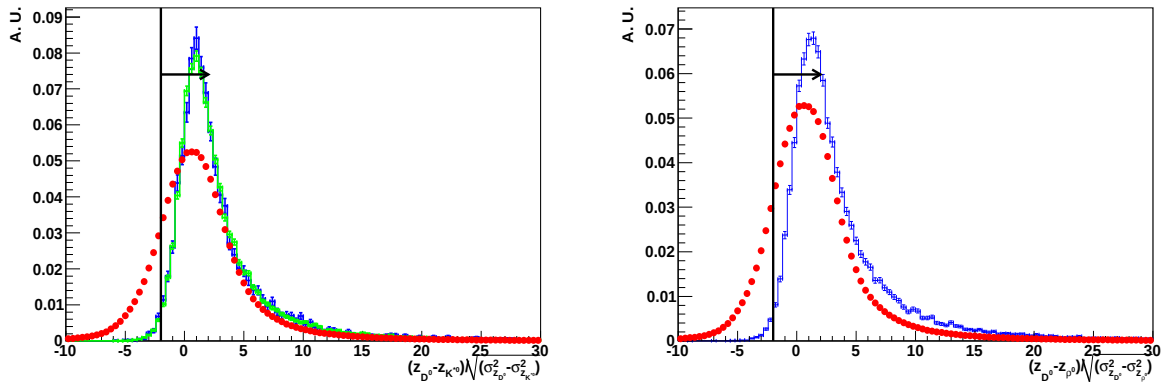

Figure V.12: Distributions for the signed significance of the distance between the z position of the D^0 vertex and the vector meson vertex (K^{*0} on the left, ρ^0 on the right) given by the formula in the Tab. V.5. The full red circles (black in black and white printing) correspond to the real data in both plots. On the left plot, the blue and green histograms (respectively black and grey in black and white printing) correspond to $B^0 \to D^0 K^{*0}$ and $\overline{B}^0_s \to D^0 K^{*0}$ Monte Carlo respectively. On the right plot, the blue histogram (black in black and white printing) corresponds to $\overline{B}^0 \to D^0 \rho^0$ Monte Carlo. The black vertical lines indicate the final selection cuts.

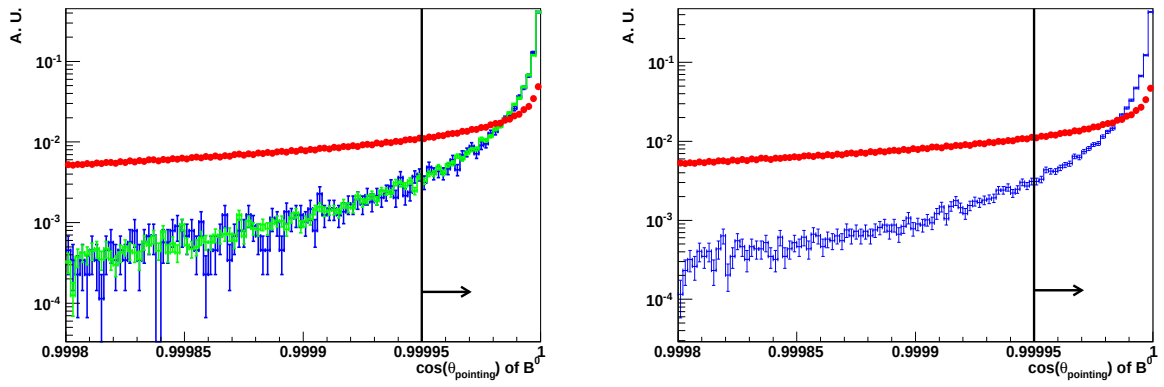

Figure V.13: Distribution for the cosine of the pointing angle (the angle between the reconstructed 3-momentum of the B^0 and the flight distance vector of the B^0. On the left plot, the blue and green full circles (respectively black and grey in black and white printing) correspond to $B^0 \to D^0 K^{*0}$ and $\overline{B}^0_s \to D^0 K^{*0}$ Monte Carlo respectively. On the right plot, the blue full circles (black in black and white printing) corresponds to $\overline{B}^0 \to D^0 \rho^0$ Monte Carlo. The black vertical lines indicate the final selection cuts.

V.2.3.2 ρ^0 and K^{*0} specific cuts

The only difference between the ρ^0 and K^{*0} hypotheses is the particle identification cut on one of the tracks (obtained from an optimization described in the next section) and the mass requirements on the vector meson. A difference exists at the stripping level in the p_T cuts on the daughters of of the vector resonances ($p_T > 250$ MeV/c for the ρ^0 daughters and $p_T > 300$ MeV/c for the K^{*0} daughters), but in the offline selection the requirement is the same, as shown in Tab. V.5. In order to reduce the ρ^0 pollution by resonant or non resonant $\pi^+\pi^-$ contributions, the mass window on the ρ^0 is taken to be equal to the full Breit-Wigner width (± 150 MeV/c^2). The K^{*0} mass window is chosen to be $\left|m^{\text{reconstructed}}_{K^{*0}} - m^{\text{PDG}}_{K^{*0}}\right| < 50$ MeV/c^2. The mass window requirements applied in the selection together with the mass distribution of the vector meson are shown in Fig. V.14.

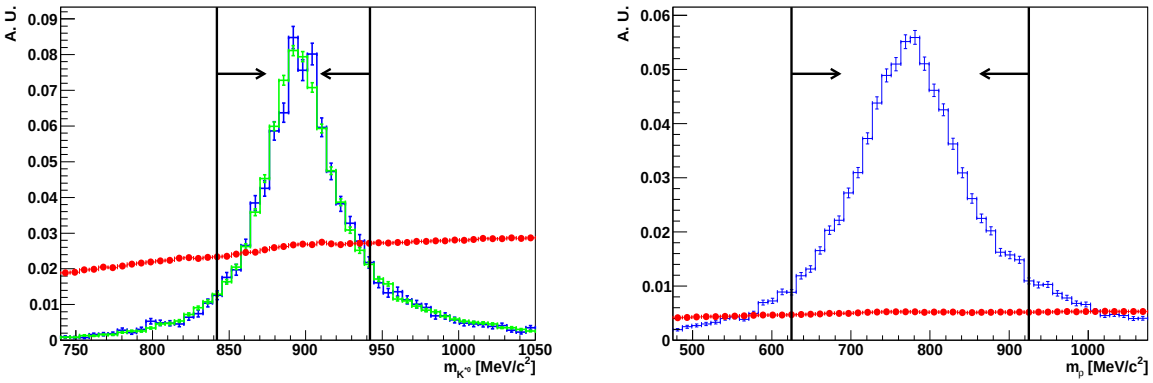

Figure V.14: Distributions of the vector meson mass (K^{*0} on the left hand side and ρ^0 on the right hand side). The red histogram (black in black and white printing printing) corresponds to the real data in both plots. On the left plot, the blue and green points correspond to $B^0 \to D^0 K^{*0}$ and $\overline{B}^0_s \to D^0 K^{*0}$ Monte Carlo respectively. On the right plot, the blue full circles (black in black and white printing) corresponds to $\overline{B}^0 \to D^0 \rho^0$ Monte Carlo. The black vertical lines indicate the final selection cuts.

V.2.3.3 Veto on $D^+_{(s)} \to \overline{K}^{*0} K^+$

In order to remove background from $B^0 \to D^+\pi^-$ or $B^0_s \to D^+_s \pi^-$ decays with the D^+ (or D^+_s) reconstructed in $\overline{K}^{*0}K^+$, a veto is applied on the $\overline{K}^{*0}K^+$ invariant mass window at 15 MeV around the nominal D^+_s and D^+ masses. These two vetoes are more than 99.5 % efficient on the signal $\overline{B}^0_s \to D^0 K^{*0}$ simulated data sample.

V.2.3.4 PID cuts optimization

The particle identification requirements were initially set based on previous Monte Carlo studies [107, 63]. In the 2010 data, the particle identification distributions are different than expected

from MC10 and thus the corresponding cuts need optimization. The PID efficiency is calculated on the whole data sample of Stripping 12*b*, after all the selection cuts except the particle identification and mass window requirements, using the large D^0 peak for both kaon and pion hypotheses. The D^0 peak is first fitted using the whole data sample (see Fig. V.16). The fit results are consistent for the different trigger settings, listed in Tab. V.3 and magnetic field configurations. The signal is described with a sum of two Gaussians with identical mean values, and a linear background shape is used. The fit parameters are then fixed to those obtained using the full data sample and the number of signal and background events are fitted for each threshold on the optimised cut. The efficiency is then simply calculated as the ratio of the number of fitted signal events with and without a given $\Delta\mathrm{LL}_{K-\pi}$ cut. See Eq. V.2 for the expression of the efficiency as a function of the PID cut x on the K from the D^0 and Eq. V.3 for the expression of the misidentification rate as a function of x. In these calculations candidates for which there is no particle identification information associated are explicitely removed. Similar formulas hold for the π efficiency and misidentification rate. The procedure is applied for both the K and the π from the D^0.

$$\epsilon^{K\to K}(x) = \frac{N_{D^0}\left(\Delta\mathrm{LL}_{K-\pi}\left(K_{D^0}\right) > x\right)}{N_{D^0}^{\mathrm{total}}} \tag{V.2}$$

$$\epsilon^{K\to \pi}(x) = \frac{N_{D^0}\left(\Delta\mathrm{LL}_{K-\pi}\left(K_{D^0}\right) < x\right)}{N_{D^0}^{\mathrm{total}}} \tag{V.3}$$

The result as a function of the threshold shown in Fig. V.15 gives the particle identification efficiencies and misidentification for the tracks combined to form a D^0. Since the same procedure cannot be applied to the broad vector resonances (the peak being not clean enough), the same efficiencies are assumed for the tracks from the vector meson (both the ρ^0 and the K^{*0}). This assumption does not bias the selection, and can only lead to a not fully optimised cut. The previous working point, defined on Monte Carlo studies in Refs. [107] and [63], was only (80.6 ± 0.8) % and (89.2 ± 1.0) % efficient on the real data for pions and kaons respectively. It is chosen to set the thresholds to $\Delta\mathrm{LL}_{K-\pi} > 0$, corresponding to (94.6 ± 1.0) % efficiency, and $\Delta\mathrm{LL}_{K-\pi} < 4$, corresponding to (95.9 ± 0.7) % efficiency, respectively for the kaon and the pion from the D^0. In order to keep the misidentification rate low, the thresholds for the vector meson daughters are set to $\Delta\mathrm{LL}_{K-\pi} > 3$, corresponding to (86.6 ± 1.0) % efficiency, and $\Delta\mathrm{LL}_{K-\pi} < 3$, corresponding to (94.4 ± 0.7) % efficiency or (5.6 ± 0.7) % misidentification rate.

We also provide the D^0 mass plot before the particle identification scan in Fig. V.16, and the same plots after having applied one of the optimal PID cuts found by the procedure described above are given in Figs. V.17-V.18. All the parameters of the fit have been fixed to the result of the full fit and only the number of events is free to vary.

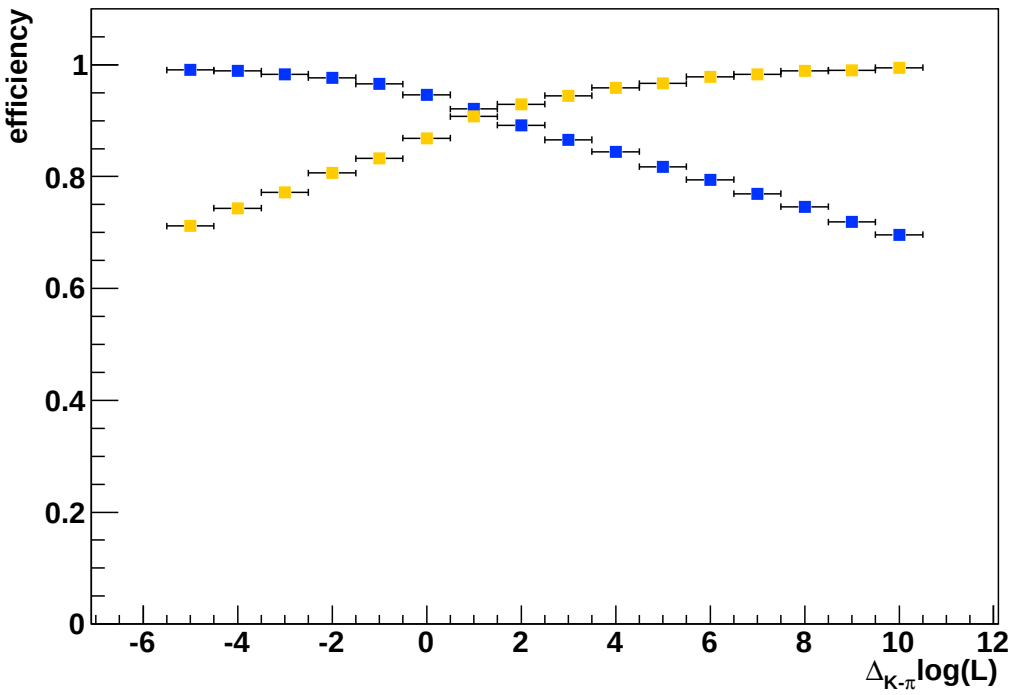

Figure V.15: Variation of the particle identification efficiency as a function of the threshold on $\Delta_{K-\pi}\log L$. This as been produced from the full data sample of D^0 candidates. The blue (dark grey in black and white printing) curve corresponds to the kaon efficiency and the orange (light grey in black and white printing) curve to the pion efficiency.

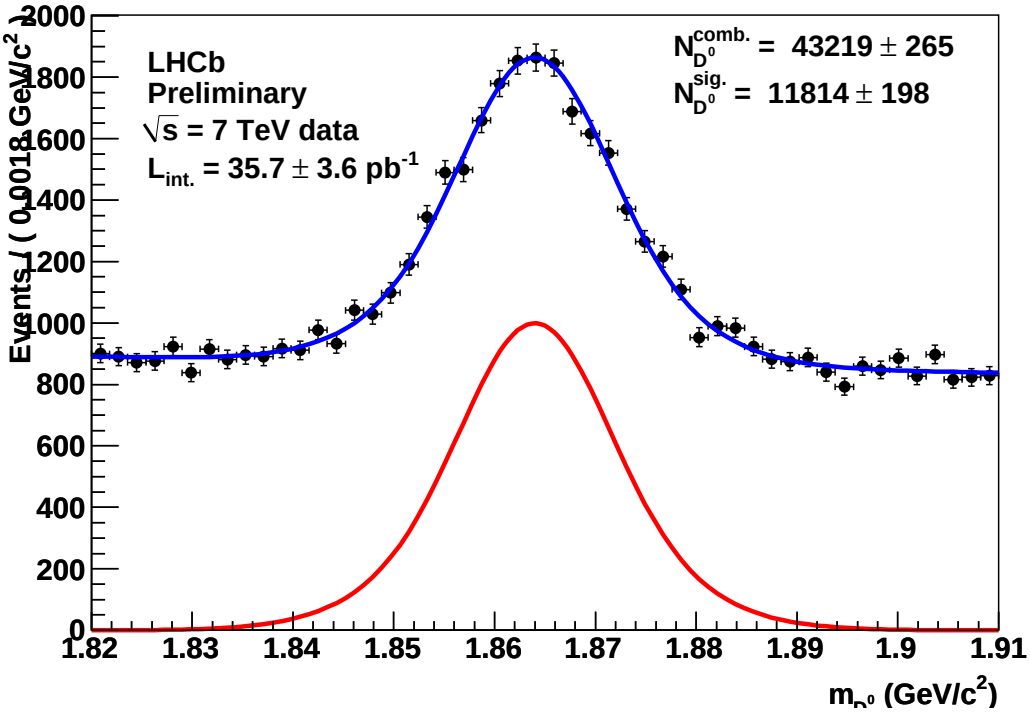

Figure V.16: D^0 mass distribution from the full real data sample after all the selection cuts except the particle identification and the mass window requirements in the $\overline{D}{}^0\rho^0$ selection. Only the $\overline{D}{}^0\rho^0$ distribution is used to compute the PID efficiencies. The signal peak is fitted with a double Gaussian (red curve) and the background is a first order polynomial. The total PDF is plotted in blue. All the shape parameters are fixed to the result of the fit without applying any PID requirement and only the number of events is left free to vary.

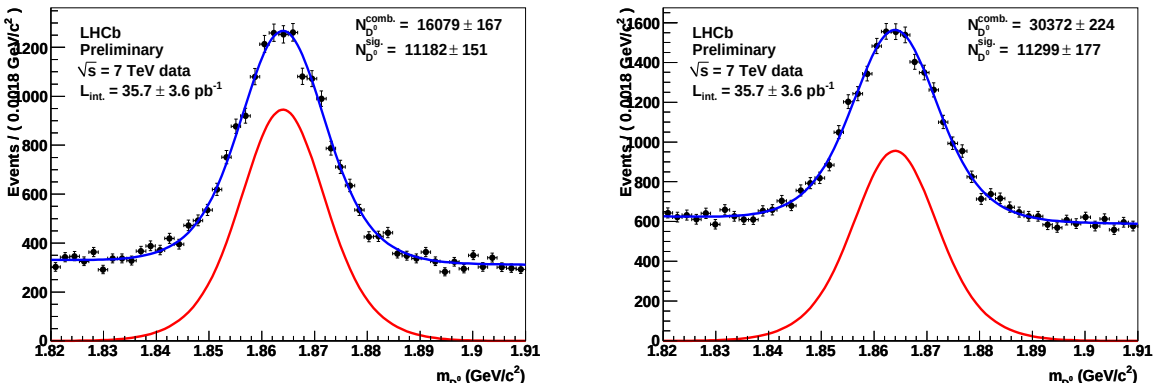

Figure V.17: Same D^0 mass distribution as Fig. V.16 but adding one of the optimal requirements defined in the text. The particle identification on the K or the π from the D^0 only is respectively applied in the left and right plot. These cuts respectively correspond to $\Delta\mathrm{LL}_{K-\pi} > 0$ (left) and $\Delta_{K-\pi} \log \mathcal{L} < 4$ (right). The signal peak is fitted with a double Gaussian (red curve) and the background is a first order polynomial. The total PDF is plotted in blue. All the shape parameters are fixed to the result of the fit without applying any PID requirement and only the number of events is left free to vary.

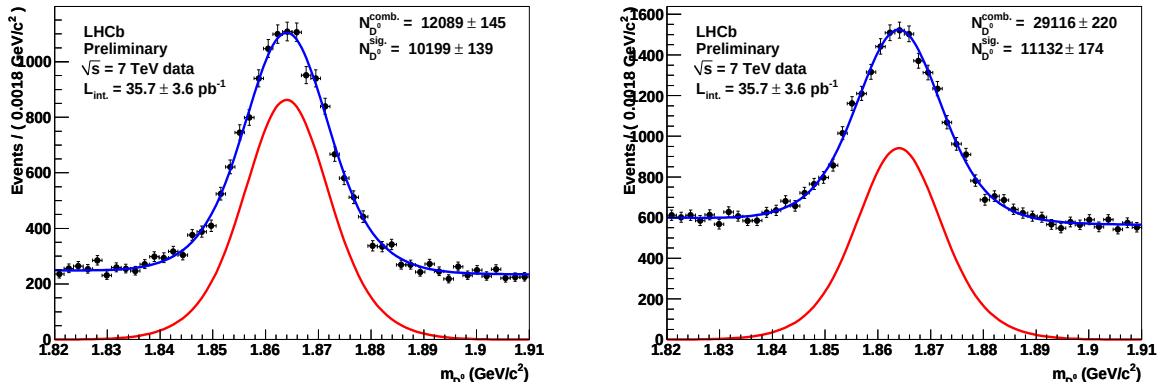

Figure V.18: Same D^0 mass distribution as Fig. V.16 but adding one of the optimal requirements defined in the text. The particle identification on the K or the π from the vector resonance only is respectively applied on the left and right plot. These cuts respectively correspond to $\Delta\mathrm{LL}_{K-\pi} > 3$ (left) and $\Delta\mathrm{LL}_{K-\pi} < 3$ (right). The signal peak is fitted with a double Gaussian (red curve) and the background is a first order polynomial. The total PDF is plotted in blue. All the shape parameters are fixed to the result of the fit without applying any PID requirement and only the number of events is left free to vary.

V.2.3.5 Distributions after the selection

The distributions of the D^0 mass, the vector meson mass, the cosine of the helicity angle and the B mass are given in Figs. V.19-V.24. The deficit of events at high values of $|\cos\theta_{\mathrm{helicity}}|$ in the D^0K^{*0} and the $\overline{D}{}^0\rho^0$ selections are due to the transverse momentum cut on the pions. The signal components of the K^{*0} and ρ^0 invariant mass distributions are described using a Voigtian function (the convolution of a Breit-Wigner with a Gaussian), given in Eq. V.4.

$$\begin{aligned}\mathcal{V}\left(m_V|\mu_V,\sigma_V,\Gamma_V\right) &= \left(\mathcal{G}*\mathcal{BW}\right)\left(m_V|\mu_V,\sigma_V,\Gamma_V\right) &\text{(V.4)}\\ &= \frac{1}{\sqrt{2\pi\sigma^2}}\,\mathrm{Re}\left[\mathrm{ierfc}\left(\frac{2\left(m_V-\mu_V\right)+\imath\Gamma_V}{2\sqrt{2}\sigma}\right)\right] &\text{(V.5)}\end{aligned}$$

with

$$\begin{aligned}\mathcal{G}\left(m_V|\mu_V,\sigma_V\right) &= \frac{1}{\sqrt{2\pi\sigma^2}}\exp\left(-\frac{\left(\mu_V-m_V\right)^2}{2\sigma^2}\right), &\text{(V.6)}\\ \mathcal{BW}\left(m_V|\mu_V,\sigma_V\right) &= \frac{\Gamma_V}{2\pi}\frac{1}{\left(m_V-\mu_V\right)^2+\frac{\Gamma_V^2}{4}} &\text{(V.7)}\end{aligned}$$

and $\mathrm{ierfc}\left(x\right)$ denotes the complex error function defined as

$$\mathrm{ierfc}\left(x\right) = \exp\left(-x^2\right)\left(1-\mathrm{erf}\left(-\imath x\right)\right). \qquad \text{(V.8)}$$

The resolution of the D^0 invariant mass is equal to $(6.17 \pm 0.08)\,\mathrm{MeV}/c^2$ (D^0K^{*0}) or $(6.07 \pm 0.04\,\mathrm{MeV}/c^2$ ($\overline{D}{}^0\rho^0$) in Monte Carlo and $(6.8 \pm 0.6)\,\mathrm{MeV}/c^2$ (D^0K^{*0} selection) or

(7.3 ± 0.3) MeV/c^2 ($\overline{D}^0\rho^0$ selection) in the data (see Tab. V.6). We then choose the D^0 mass to satisfy the requirement $\left|m_{D^0}^{\text{reconstructed}} - m_{D^0}^{\text{PDG}}\right| < 20$ MeV/c^2 as mentioned in Tab. V.5. The B mass (calculated applying a mass constraint on the D^0 meson) is fitted with a double Gaussian[1]. The resolution of the B meson mass is (10.3 ± 0.2) MeV/c^2 in the D^0K^{*0} Monte Carlo while it is (11.1 ± 0.2) MeV/c^2 in the $\overline{D}^0\rho^0$ Monte Carlo. The resolution quoted here is the width of the core Gaussian that contains $f_{\text{core}} = (81 \pm 2)$ % ($\overline{B}^0_s \to D^0K^{*0}$) of the events in the double Gaussian fit (f_{core} represents the ratio of the number of events in the core Gaussian with respect to the total number of events in the core and tail Gaussians). (The width of the second Gaussian is approximately twice as large.) The fraction of events in the core Gaussian and the ratio of widths are compatible for the three Monte Carlo data samples, as shown for the $\overline{B}^0_s \to D^0K^{*0}$ and $\overline{B}^0 \to D^0\rho^0$ Monte Carlo samples in Fig. V.24. These numbers are summarized in the Tab. V.7. It has been checked using the true vector meson daughters information that the small differences are due to the kinematics of the daughters of the vector mesons. Indeed, the momentum distributions are different in the two cases as shown in Fig. V.25.

mass and resolution in MeV/c^2	MC10	data
$m_{K^{*0}}$	897.9 ± 0.5	892 ± 3
m_{ρ^0}	777.2 ± 0.8	767 ± 5
m_{D^0} in D^0K^{*0} analysis	1865.1 ± 0.1	1864.3 ± 0.6
$\sigma_{m_{D^0}}$ in D^0K^{*0} analysis	6.17 ± 0.08	6.8 ± 0.6
m_{D^0} in $\overline{D}^0\rho^0$ analysis	1865.16 ± 0.07	1863.8 ± 0.3
$\sigma_{m_{D^0}}$ in $\overline{D}^0\rho^0$ analysis	6.07 ± 0.04	7.3 ± 0.3

Table V.6: Mass fit results on MC10 and data.

Decay mode	μ	σ	κ_σ	f_{core}
$\overline{B}^0_s \to D^0K^{*0}$	5367.3 ± 0.1 MeV/c^2	10.3 ± 0.2 MeV/c^2	2.10 ± 0.06	0.82 ± 0.02
$\overline{B}^0 \to D^0\rho^0$	5280.1 ± 0.1 MeV/c^2	11.2 ± 0.3 MeV/c^2	2.00 ± 0.08	0.79 ± 0.03

Table V.7: B mass fit results. The PDF used is the sum of two Gaussian sharing the same mean μ, σ is the width of the core Gaussian, the width of the wide Gaussian is $\sigma\times\ \kappa_\sigma$ and f_{core} is the fraction of events in the core Gaussian.

Multiple B candidates are removed by choosing the largest flight distance significance among all the candidates that lie in the restricted mass windows of the D^0 and the vector meson resonance. In the $\overline{B}^0 \to D^0\rho^0$ Monte Carlo data sample we found that (4.46 ± 0.14) % of the events have multiple candidates in agreement with the $\overline{B}^0_s \to D^0K^{*0}$ Monte Carlo (5.23±0.49) %. In the $\overline{D}^0\rho^0$ analysis on real data we found that (4.10 ± 0.12) % of the events have multiple candidates.

[1]The two Gaussian distributions are constrained to have the same mean value.

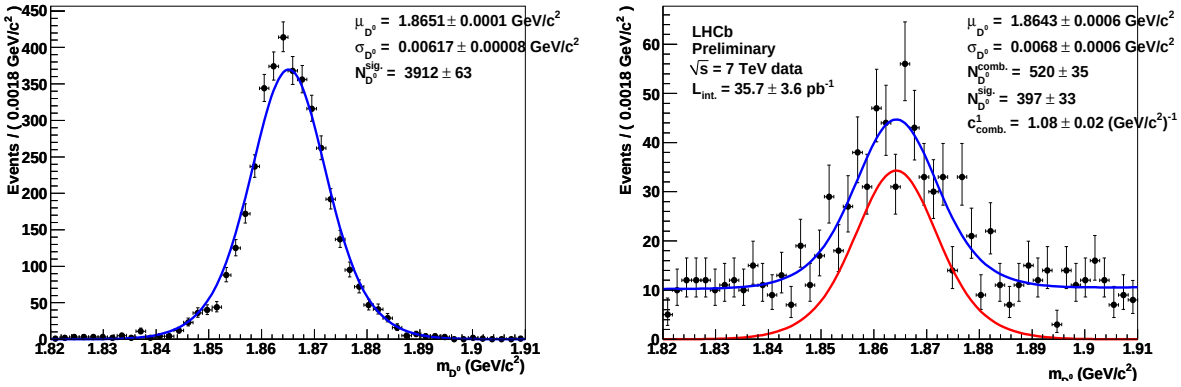

Figure V.19: D^0 mass distributions on Monte Carlo and real data respectively on the left and the right hand sides of the figure, in the $D^0 K^{*0}$ selection. All the selection cuts have been applied except the D^0 and B^0 mass requirements. The Monte Carlo corresponds to the $B^0 \to D^0 K^{*0}$ signal only. The $\overline{B}^0_s \to D^0 K^{*0}$ fit result is in very good agreement and not shown here. The fit consists of a single Gaussian to model the signal shape plus a first order polynomial background in the real data. Data and Monte Carlo resolutions are in reasonable agreement.

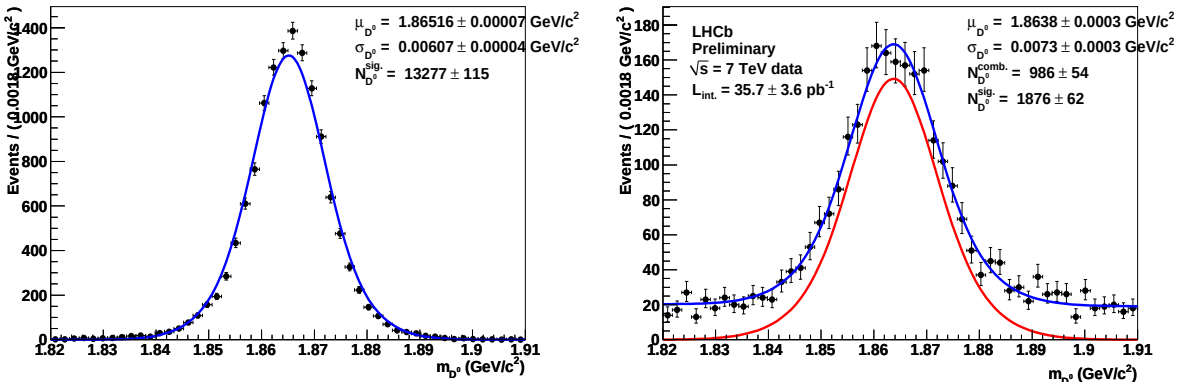

Figure V.20: D^0 mass distributions on Monte Carlo and real data respectively on the left and the right hand sides of the figure, in the $\overline{D}^0 \rho^0$ selection. All the selection cuts have been applied except the D^0 and B^0 mass requirements. The fit consists of a single Gaussian to model the signal shape plus a first order polynomial background in the real data.

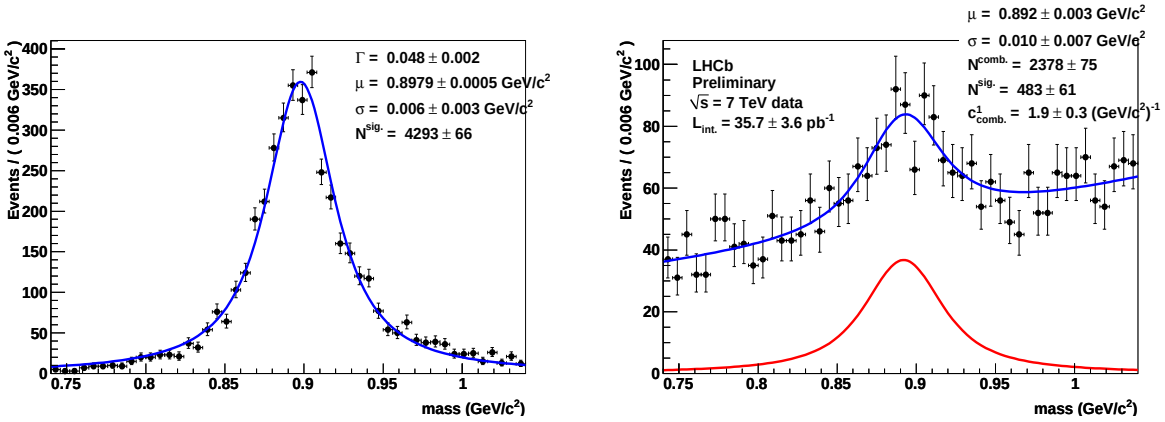

Figure V.21: K^{*0} mass distributions on Monte Carlo and real data respectively on the left and the right hand sides of the figure. All the selection cuts have been applied except the K^{*0} and B^0 mass requirements. The Monte Carlo corresponds to the $B^0 \to D^0 K^{*0}$ signal only. The $\overline{B}^0_s \to D^0 K^{*0}$ fit result is in very good agreement and not shown here. The fit consists of a single Voigtian function given in Eq. V.4 (of which the intrinsic width is fixed to the PDG value) to model the signal shape plus an exponential background in the real data.

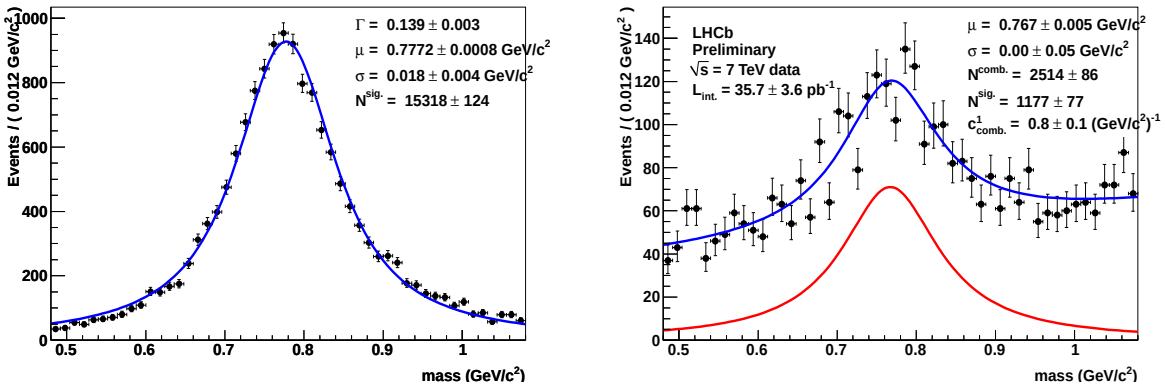

Figure V.22: ρ^0 mass distributions on Monte Carlo and real data respectively on the left and the right hand sides of the figure. All the selection cuts have been applied except the ρ^0 and B^0 mass requirements. The Monte Carlo corresponds to the $\overline{B}^0 \to D^0 \rho^0$ signal only. The fit consists of a single Voigtian function given in Eq. V.4 (of which the intrinsic width is fixed to the PDG value) to model the signal shape plus an exponential background in the real data.

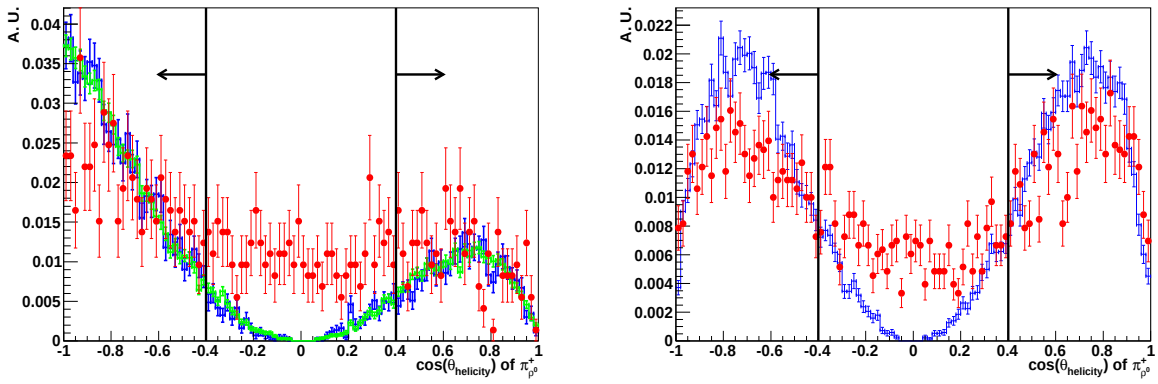

Figure V.23: Helicity angle distributions of the K from the K^{*0} and the π^+ from the ρ^0 respectively on the left and the right hand sides of the figure. All the selection cuts have been applied except the helicity cut and B^0 mass requirement. The red histogram (black in black and white printing printing) corresponds to the real data in both plots. On the left plot, the blue and green points correspond to $B^0 \to D^0 K^{*0}$ and $\overline{B}^0_s \to D^0 K^{*0}$ Monte Carlo respectively. The black vertical lines indicate the final selection cuts.

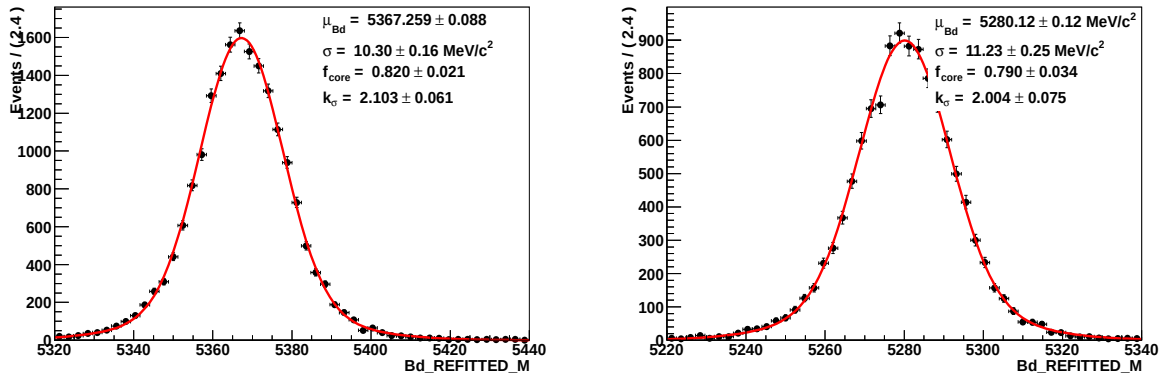

Figure V.24: Mass distribution in the $\overline{B}^0_s \to D^0 K^{*0}$ (left hand side of the figure) Monte Carlo 2010 simulation constraining the D^0 mass to its PDG value. The distribution is fitted with a double Gaussian. On the right hand side of the figure, the mass distribution for the $\overline{B}^0 \to D^0 \rho^0$ Monte Carlo 2010 simulation constraining the D^0 mass to its PDG value is shown. The core Gaussian resolution is higher by 9 ± 3 % while the other fit parameters are fully consistent.

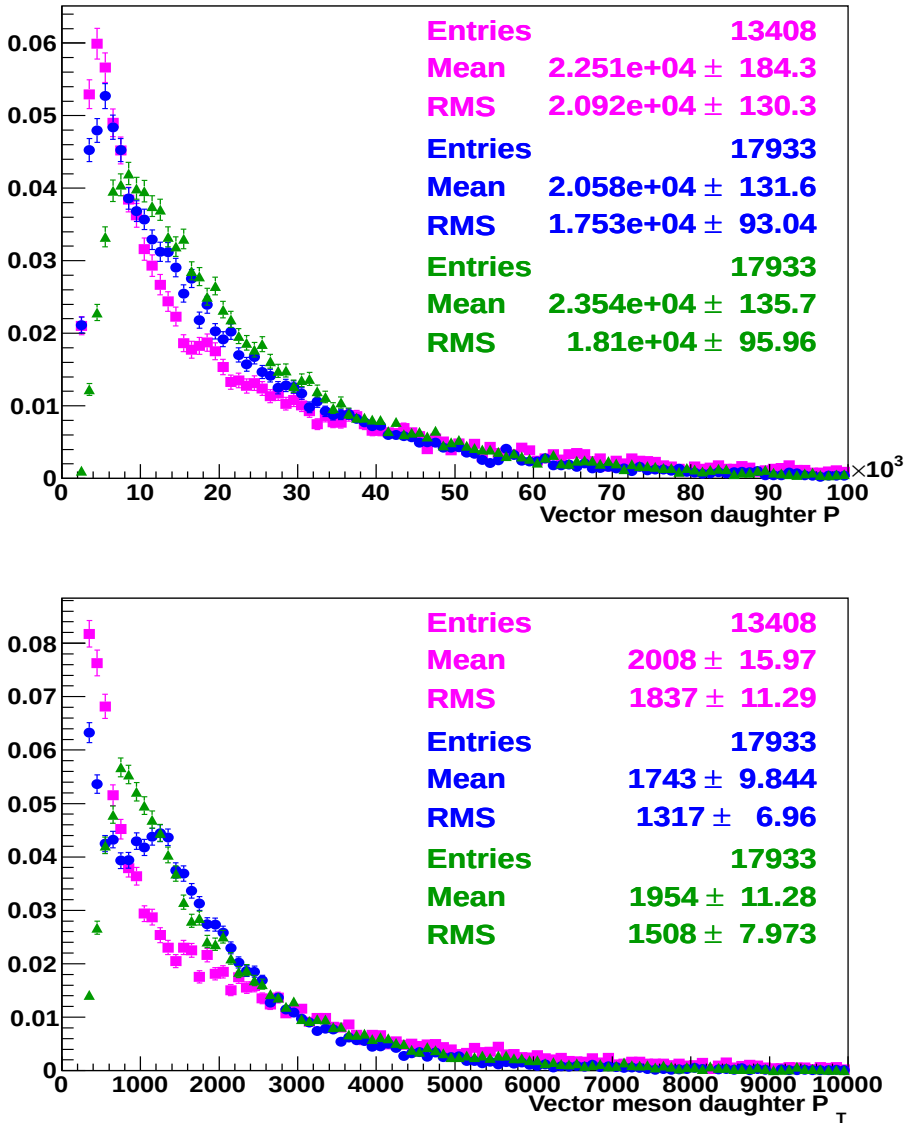

Figure V.25: Momenta (top) and transverse momenta (bottom) of the daughters of the vector mesons. The pink boxes correspond to π from the ρ^0, the blue dots to the π from the K^{*0} and the green triangles to the K from the K^{*0}.

V.2.4 Fit description and results

Short overview The general idea of the fit is to extract simultaneously the number of events in $\overline{D}{}^0\rho^0$ and D^0K^{*0}. The fit contains different categories of events (see next section) and an ad-hoc parametrization for the partially reconstructed background is used. Contributions of signal cross-feeds are also taken into account in the fit.

V.2.4.1 Fitting strategy

Events are assigned to three distinct categories depending on the flavour of the vector resonance (K^{*0} or ρ^0) and, for the K^{*0} category only, depending on the relative charge of the two reconstructed kaons. If the charge of the two kaons (the one from the D^0 and the one from the K^{*0}) are opposite the event is classified as `D0Kstar OppositeSign`. If the two kaons have identical charges, the candidate is classified as `D0Kstar SameSign`. Favoured $B^0 \to D^0K^{*0}$ and suppressed $\overline{B}{}^0_s \to D^0K^{*0}$ decays belong to the `D0Kstar SameSign` category, while suppressed $B^0 \to D^0K^{*0}$ and favoured $\overline{B}{}^0_s \to D^0K^{*0}$ decays populate the `D0Kstar OppositeSign` category. Since the expected yield of the suppressed modes is much smaller than one event with the given statistics, these will be neglected in the following approach and only favoured modes are considered. To summarize, $\overline{B}{}^0_s \to D^0K^{*0}$, $B^0 \to D^0K^{*0}$ and $\overline{B}{}^0 \to D^0\rho^0$ are respectively expected in `D0Kstar OppositeSign`, `D0Kstar SameSign` and `D0Rho0` categories. The `D0Rho0` category is further splitted in two sub-categories in order to directly extract the numbers of fitted signal events in the `L0HadronTOSOnly` and `OtherB` L0 trigger settings.

Mass windows In order to describe the partially reconstructed background, the lower edge of the mass window is restricted to 5.1 GeV in `D0Kstar SameSign` and `D0Rho0` categories where B^0 events are expected. In the `D0Kstar OppositeSign` category, if partially reconstructed background involving D^{*0} resonances is dominant, one expect to have the same background shape, shifted by the mass difference $\delta_\mu = \mu_{B^0_s} - \mu_{B^0}$ between the B^0_s and the B^0, approximately equal to 90 MeV/c^2 [38]. The lower edge of the mass window is then restricted to 5.19 GeV/c^2 in the `D0Kstar OppositeSign` category.

Signal shapes As shown in Fig. V.24, the resolution for $\overline{B}{}^0 \to D^0\rho^0$ and $\overline{B}{}^0_s \to D^0K^{*0}$ are slightly different. In order to take into account this effect in the fit, the value of the ratio of widths $k_\sigma = \frac{\sigma_{D^0K^{*0}}}{\sigma_{\overline{B}{}^0\rho^0}} = (89 \pm 3)$ % is taken from the Monte Carlo and fixed to this value. The ratio of the tail and core Gaussian resolutions $\kappa_\sigma = 2.04 \pm 0.05$ is also fixed to the value obtained from Monte Carlo. Furthermore the mass difference between the means of the B^0 and B^0_s signals is fixed to the PDG value 90 MeV/c^2. Only two parameters (mean and width of the core Gaussian of the B^0 in $\overline{B}{}^0 \to D^0\rho^0$ decays) are thus used to describe the signal shapes given in Eqs. V.9-V.11.

$$\mathcal{G}_{\overline{B}^0 \to D^0\rho^0}\left(m_B|\mu_{B^0}, \sigma_{\overline{D}^0\rho^0}, f_{\rm core}, \kappa_\sigma\right) = \frac{f_{\rm core}}{\sqrt{2\pi\sigma^2_{\overline{D}^0\rho^0}}} e^{-\frac{\left(m_B-\mu_{B0}\right)^2}{2\sigma^2_{\overline{D}^0\rho^0}}} + \frac{1-f_{\rm core}}{\sqrt{2\pi\kappa^2_\sigma\sigma^2_{\overline{D}^0\rho^0}}} e^{-\frac{\left(m_B-\mu_{B0}\right)^2}{2\kappa^2_\sigma\sigma^2_{\overline{D}^0\rho^0}}} \quad \text{(V.9)}$$

$$\mathcal{G}_{B^0 \to D^0 K^{*0}}\left(m_B|\mu_{B^0}, \sigma_{\overline{D}^0\rho^0}, f_{\rm core}, k_\sigma, \kappa_\sigma\right) = \frac{f_{\rm core}}{\sqrt{2\pi k^2_\sigma\sigma^2_{\overline{D}^0\rho^0}}} e^{-\frac{\left(m_B-\mu_{B0}\right)^2}{2k^2_\sigma\sigma^2_{\overline{D}^0\rho^0}}} + \frac{1-f_{\rm core}}{\sqrt{2\pi\kappa^2_\sigma k^2_\sigma\sigma^2_{\overline{D}^0\rho^0}}} e^{-\frac{\left(m_B-\mu_{B0}\right)^2}{2\kappa^2_\sigma k^2_\sigma\sigma^2_{\overline{D}^0\rho^0}}} \quad \text{(V.10)}$$

$$\mathcal{G}_{\overline{B}^0_s \to D^0 K^{*0}}\left(m_B|\mu_{B^0}, \delta_\mu, \sigma_{\overline{D}^0\rho^0}, f_{\rm core}, k_\sigma, \kappa_\sigma\right) = \frac{f_{\rm core}}{\sqrt{2\pi k^2_\sigma\sigma^2_{\overline{D}^0\rho^0}}} e^{-\frac{\left(m_B-\mu_{B0}-\delta_\mu\right)^2}{2k^2_\sigma\sigma^2_{\overline{D}^0\rho^0}}} + \frac{1-f_{\rm core}}{\sqrt{2\pi\kappa^2_\sigma k^2_\sigma\sigma^2_{\overline{D}^0\rho^0}}} e^{-\frac{\left(m_B-\mu_{B0}-\delta_\mu\right)^2}{2\kappa^2_\sigma k^2_\sigma\sigma^2_{\overline{D}^0\rho^0}}} \quad \text{(V.11)}$$

Cross-feed of signal channels Since the expected number of produced $\overline{B}^0 \to D^0\rho^0$ events is six times larger than that of $\overline{B}^0_s \to D^0 K^{*0}$, the contribution from misidentified pions as kaons from real $\overline{B}^0 \to D^0\rho^0$ has to be taken into account. The size of the background from misidentified $\overline{B}^0 \to D^0\pi^+\pi^-$ also depends on the mass and helicity angle requirements on the vector meson. Therefore a dedicated study with $\overline{B}^0 \to D^0\rho^0$ Monte Carlo is required. We found that the ratio of efficiencies to select a signal $\overline{B}^0 \to D^0\rho^0$ candidate in the D^0K^{*0} selection with respect to the efficiency to select it in the $\overline{D}^0\rho^0$ selection is $\frac{\epsilon^{\overline{B}^0 \to D^0\rho^0}_{D^0K^{*0},\ \rm noPID}}{\epsilon^{\overline{B}^0 \to D^0\rho^0}_{\overline{D}^0\rho^0,\ \rm noPID}} = 0.302 \pm 0.013$ (where the subscript denotes the selection applied and the upper script the nature of the Monte Carlo signal). This number do not take into account PID efficiencies that are computed with a dedicated procedure explained in section V.2.5.3. Similarly we found $\frac{\epsilon^{\overline{B}^0_s \to D^0K^{*0}}_{\overline{D}^0\rho^0,\ \rm noPID}}{\epsilon^{\overline{B}^0_s \to D^0K^{*0}}_{D^0K^{*0},\ \rm noPID}} = 0.367 \pm 0.003$. Including the ratio of PID efficiencies from section V.2.5.3, these two numbers become respectively $f_{D^0\rho^0 \to D^0K^{*0}} = \frac{\epsilon^{\overline{B}^0 \to D^0\rho^0}_{D^0K^{*0},\ \rm PID}}{\epsilon^{\overline{B}^0 \to D^0\rho^0}_{\overline{D}^0\rho^0,\ \rm PID}} = 0.0198 \pm 0.0005$ and $f_{D^0K^{*0} \to D^0\rho^0} = \frac{\epsilon^{\overline{B}^0_s \to D^0K^{*0}}_{\overline{D}^0\rho^0,\ \rm PID}}{\epsilon^{\overline{B}^0_s \to D^0K^{*0}}_{D^0K^{*0},\ \rm PID}} = 0.0383 \pm 0.0008$. The cross-feed events of $\overline{B}^0 \to D^0\rho^0$ in D^0K^{*0} are equally splitted in `D0Kstar`

`OppositeSign` and `D0Kstar SameSign`, as well as the cross-feed events of $\overline{B}^0_s \to D^0 K^{*0}$ are equally splitted in `L0HadronTOSOnly` and `OtherB`.

The signal cross-feed in the three categories are fitted by Crystal-Ball functions and the number of cross-feed events are constrained to be equal to the number of corresponding properly identified signals multiplied by the corresponding ratio of efficiencies. Some uncertainty on the ratio of efficiencies is allowed by constraining the ratio of efficiencies with Gaussians centered on the mean values (1.98 % for the $\overline{B}^0 \to D^0\rho^0$ cross-feed in D^0K^{*0} and 3.83 % for the $\overline{B}^0_s \to D^0 K^{*0}$ cross-feed in $\overline{D}^0\rho^0$) with 50 % relative uncertainty on the ratio of PID efficiencies.

The width of the Crystal-Ball is fixed to 1.75 times the signal resolution, following a Monte-Carlo study. Other parameters are taken from a fit to Monte-Carlo events, where $B^0 \to D^0 K^{*0}$ is misidentified as `D0Rho0` or $\overline{B}^0 \to D^0\rho^0$ is misidentified as `D0Kstar0`. It is noticeable that the sign of the α parameter is opposite for the $\overline{B}^0 \to D^0\rho^0$ cross-feed in `D0Kstar0` with respect to the $B^0 \to D^0 K^{*0}$ cross-feed in `D0Rho0`. The distribution of Fig. V.26 shows that a Crystal-Ball function (see Eq. V.12) gives satisfying results in both cases.

$$\mathcal{CB}\left(m_B|\mu,\sigma,n,\alpha\right) = K_{\text{norm.}} \begin{cases} e^{-\frac{(x-\mu)^2}{2\sigma^2}}, & \text{for } \frac{x-\mu}{\sigma} > -\alpha \\ A\cdot(B-\frac{x-\mu}{\sigma})^{-n}, & \text{for } \frac{x-\mu}{\sigma} \leqslant -\alpha \end{cases} \tag{V.12}$$

$$A = \left(\frac{n}{|\alpha|}\right)^n \cdot e^{-\frac{|\alpha|^2}{2}} \tag{V.13}$$

$$B = \frac{n}{|\alpha|} - |\alpha| \tag{V.14}$$

Background shapes In order to minimize bias in the extraction of the yields, it is important to treat carefully the partially reconstructed background both from B^0_s and B^0. It has been found in a previous analysis that a potential important contribution could come from $B_{d,s} \to D^* K^{*0}$ decays and a dedicated effective mass shape description was extracted. Nevertheless, this background is not the only contributor to the partially reconstructed background; moreover the polarization of $B_{d,s} \to D^* K^{*0}$ decays in the simulation was not tuned on real data, so that (due to the correlation between the helicity angle of the missing particle and the partially reconstructed mass) the mass shape description was potentially inappropriate. Thus a more precise description of the partially reconstructed background needs a dedicated simulation to take into account any potentially contributing resonance. Unfortunately, this MC sample (the so-called $B \to DX$ cocktail MC) is not yet ready. The mass shape description at low masses will thus be effective and will use simple formulas, a precise description being postponed to an higher statistics study.

An exponential shape is adopted for the partially reconstructed background in `D0Rho0` to which is added a flat contribution for the combinatorial background. It should be noted that this simple exponential shape should be replaced at high statistics by a more appropriate description,

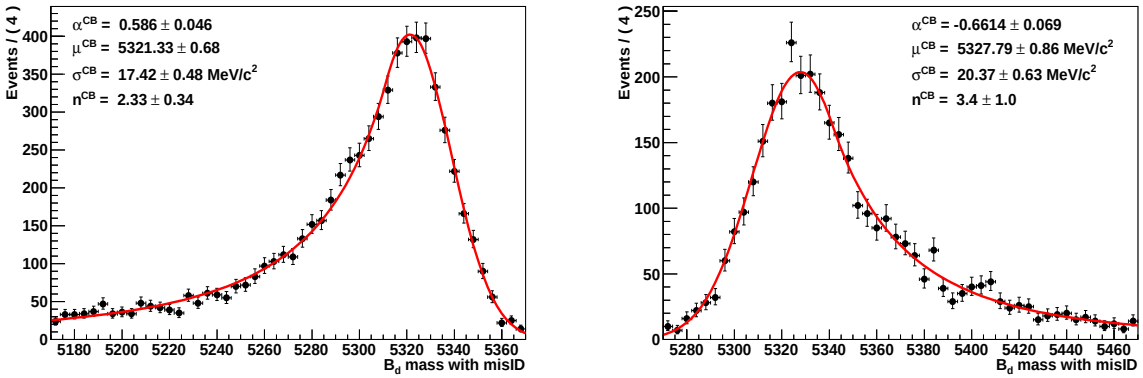

Figure V.26: Fit of the reconstructed $\overline{B}^0_s \to D^0 K^{*0}$ misidentified as $\overline{B}^0 \to D^0 \rho^0$ (Monte Carlo data points) with a Crystal-Ball function on the left of the figure and $\overline{B}^0 \to D^0 \rho^0$ misidentified as $B_{d,s} \to \overline{D}^0 K^{*0}$ on the right of the figure. The fit is in good agreement with the data points, thus validating the shape description by a Crystal-Ball. It is found that the σ^{CB} parameter of the Crystal-Ball is equal to 1.69 ± 0.05 ($\overline{B}^0_s \to D^0 K^{*0}$) or 1.81 ± 0.07 ($\overline{B}^0 \to D^0 \rho^0$) times the value of the resolution (core gaussian) of properly identified signals shown in Fig. V.24. The distribution for $B^0 \to D^0 K^{*0}$ misidentified as $\overline{B}^0 \to D^0 \rho^0$ is consistent with a shift of the mean value of the function by the PDG mass difference between the B^0_s and B^0.

for example tuned on a dedicated Monte Carlo generation. Replacing the flat distribution by a first order polynomial gives a consistent result. The background in `D0Kstar0` categories is also assumed to be the sum of two contributions, one exponential and the other one flat. Nevertheless, the exponential slope in these categories is potentially different (due to the fact that partially reconstructed backgrounds are coming from different decays) to that fitted in `D0Rho0` as shown by the parametrization of the PDFs given in Eqs. V.15-V.16. In these equations $c_{\text{part.},D^0\rho^0}$ and $c_{D^0\ K^{*0}}$ are respectively the slope parameters of the exponential functions. Consequently an additional shape parameter is added to the fit description.

$$\mathcal{E}_{D^0\rho^0}\left(m_B | c_{\text{part.},D^0\rho^0}\right) = \frac{c_{\text{part.},D^0\rho^0}}{e^{c_{\text{part.},D^0\rho^0} m_{B\,\min}} - e^{c_{\text{part.},D^0\rho^0} m_{B\,\max}}} \exp\left(c_{\text{part.},D^0\rho^0} \cdot m_B\right) \qquad \text{(V.15)}$$

$$\mathcal{E}_{D^0K^{*0}}\left(m_B | c_{D^0\ K^{*0}}\right) = \frac{c_{D^0\ K^{*0}}}{e^{c_{D^0\ K^{*0}} m_{B\,\min}} - e^{c_{D^0\ K^{*0}} m_{B\,\max}}} \exp\left(c_{D^0\ K^{*0}} \cdot m_B\right) \qquad \text{(V.16)}$$

Simultaneous fit The strategy is to fit simultaneously the four categories (`D0Rho0` with `L0HadronTOSOnly`, `D0Rho0` with `OtherB`, `D0Kstar OppositeSign` and `D0Kstar SameSign`), using an extended unbinned maximum likelihood fit of the invariant mass distributions to extract the yields and associated uncertainties. Four shape parameters are allowed to vary in the fit, two for signal (mean and width of the core Gaussian of $B^0 \to \overline{D}^0 \rho^0$) and two for exponential backgrounds (one for both of the two `D0Rho0` categories and one for both of the two `D0Kstar0` categories). In addition, twelve event yields are extracted, three (signal, combinatorial and partially reconstructed backgrounds) in each of the four categories. There are also two additional fractions,

for the relative sizes of cross-feed events, that are constrained thanks to the expectation from calibrated PID efficiencies and ratio of Monte Carlo efficiencies for the other selection criteria. All the parameters are summarized in Tab. V.8 and Tab. V.9. The extended fit constrains

parameter	fitted value	comment
μ_{B^0}	5277.2 ± 1.5 MeV/c^2	free
δ_μ	86.8 MeV/c^2	fixed to PDG value
f_{core}	0.81	fixed from Monte Carlo
κ_σ	2.04	fixed from Monte Carlo
$k_\sigma = \sigma_{D^0 K^{*0}}/\sigma_{\overline{D}{}^0\rho^0}$	0.92	fixed from Monte Carlo
$\sigma_{\overline{D}{}^0\rho^0}$	14.7 ± 1.4 MeV/c^2	free
$c_{\text{part.},D^0\rho^0}$	$-24.8 \pm 4.5 \left(\text{GeV}/c^2\right)^{-1}$	free
$c_{D^0\ K^{*0}}$	$-18.6 \pm 8.6 \left(\text{GeV}/c^2\right)^{-1}$	free
$\mu^{\text{CB}}_{B^0\to\overline{D}{}^0\rho^0}$	5327.8 MeV/c^2	fixed from Monte Carlo
$\sigma^{\text{CB}}_{B^0\to\overline{D}{}^0\rho^0}/\sigma_{\overline{D}{}^0\rho^0}$	1.75	fixed from Monte Carlo
$\alpha^{\text{CB}}_{B^0\to\overline{D}{}^0\rho^0}$	-0.66	fixed from Monte Carlo
$n^{\text{CB}}_{B^0\to\overline{D}{}^0\rho^0}$	3.4	fixed from Monte Carlo
$\mu^{\text{CB}}_{\overline{B}{}^0_s\to D^0K^{*0}}$	5321.3 MeV/c^2	fixed from Monte Carlo
$\sigma^{\text{CB}}_{\overline{B}{}^0_s\to D^0K^{*0}}/\sigma_{D^0K^{*0}}$	1.75	fixed from Monte Carlo
$\alpha^{\text{CB}}_{\overline{B}{}^0_s\to D^0K^{*0}}$	0.59	fixed from Monte Carlo
$n^{\text{CB}}_{\overline{B}{}^0_s\to D^0K^{*0}}$	2.3	fixed from Monte Carlo

Table V.8: Summary of the fixed and fitted parameters with the result of the fit on real data.

the sum of event yields of background and signal to be consistent with the number of observed events in the fitting range within Poisson uncertainties. Each component PDF, described in Eqs. V.17-V.20, corresponds to a given category, the Gaussian PDFs $\mathcal{G}$ are described in Eqs. V.9-V.11, $\mathcal{CB}$ stands for the misidentified signal modelled by a Crystal-Ball function, $\mathcal{E}$ for an exponential function and $\mathcal{F}$ for the flat background. The likelihood used for the minimisation is given in Eq. V.21.

$$
\begin{aligned}
f_{D^0\rho^0\ \texttt{L0HadronTOSOnly}} \;=\;& N^{\text{sig.},\ \texttt{L0HadronTOSOnly}}_{B^0\to\overline{D}{}^0\rho^0}\mathcal{G}_{B^0} \\
+\;& \frac{f_{D^0K^{*0}\to D^0\rho^0}}{2} N^{\text{sig.}}_{B^0\to D^0K^{*0}}\mathcal{CB}_{B^0\to D^0K^{*0}} \\
+\;& \frac{f_{D^0K^{*0}\to D^0\rho^0}}{2} N^{\text{sig.}}_{\overline{B}{}^0_s\to D^0K^{*0}}\mathcal{CB}_{\overline{B}{}^0_s\to D^0K^{*0}} \\
+\;& N^{\text{part.},\ \texttt{L0HadronTOSOnly}}_{\overline{D}{}^0\rho^0}\mathcal{E}_{\overline{D}{}^0\rho^0} + N^{\text{comb.},\ \texttt{L0HadronTOSOnly}}_{\overline{D}{}^0\rho^0}\mathcal{F}
\end{aligned}
\tag{V.17}
$$

parameter	fitted value	comment
$N^{\text{comb.}}_{D^0K^{*0}}$	29.8 ± 8.4	free
$N^{\text{comb.}}_{\overline{D}^0K^{*0}}$	56.6 ± 9.3	free
$N^{\text{comb., LOHadronTOSOnly}}_{\overline{D}^0\rho^0}$	95.5 ± 13.1	free
$N^{\text{comb., OtherB}}_{\overline{D}^0\rho^0}$	176.0 ± 17.5	free
$N^{\text{part.}}_{D^0K^{*0}}$	17.5 ± 11.4	free
$N^{\text{part.}}_{\overline{D}^0K^{*0}}$	5.8 ± 4.9	free
$N^{\text{part., LOHadronTOSOnly}}_{\overline{D}^0\rho^0}$	55.4 ± 10.1	free
$N^{\text{part., OtherB}}_{\overline{D}^0\rho^0}$	85.6 ± 12.9	free
$f_{D^0\rho^0\to D^0K^{*0}}$	0.0187 ± 0.0098	Gaussian constraint
$f_{D^0K^{*0}\to D^0\rho^0}$	0.0399 ± 0.0184	Gaussian constraint
$N^{\text{sig.}}_{\overline{B}^0_s\to D^0K^{*0}}$	34.4 ± 6.8	free
$N^{\text{sig.}}_{B^0\to \overline{D}^0K^{*0}}$	11.3 ± 4.5	free
$N^{\text{sig., LOHadronTOSOnly}}_{B^0\to \overline{D}^0\rho^0}$	77.0 ± 10.1	free
$N^{\text{sig., OtherB}}_{B^0\to \overline{D}^0\rho^0}$	77.1 ± 11.2	free

Table V.9: Summary of the fitted yield and cross-feed fraction parameters with the result of the fit on real data.

$$
\begin{aligned}
f_{D^0\rho^0\ \texttt{OtherB}} &= N^{\text{sig., OtherB}}_{B^0\to\,\overline{D}^0\rho^0}\mathcal{G}_{B^0} \\
&+ \frac{f_{D^0K^{*0}\to D^0\rho^0}}{2} N^{\text{sig.}}_{B^0\to\,D^0K^{*0}}\mathcal{CB}_{B^0\to\,D^0K^{*0}} \\
&+ \frac{f_{D^0K^{*0}\to D^0\rho^0}}{2} N^{\text{sig.}}_{\overline{B}^0_s\to D^0K^{*0}}\mathcal{CB}_{\overline{B}^0_s\to\,D^0K^{*0}} \\
&+ N^{\text{part., OtherB}}_{\overline{D}^0\rho^0}\mathcal{E}_{\overline{D}^0\rho^0} + N^{\text{comb., OtherB}}_{\overline{D}^0\rho^0}\mathcal{F}
\end{aligned}
\tag{V.18}
$$

$$
\begin{aligned}
f_{D^0K^{*0}\text{SS}} &= N^{\text{sig.}}_{B^0\to\,D^0K^{*0}}\mathcal{G}_{B^0} + N^{\text{part.}}_{\overline{D}^0K^{*0}}\mathcal{E}_{D^0K^{*0}} + N^{\text{comb.}}_{\overline{D}^0K^{*0}}\mathcal{F} \\
&+ \frac{f_{D^0\rho^0\to D^0K^{*0}}}{2} N^{\text{sig., LOHadronTOSOnly}}_{B^0\to\,\overline{D}^0\rho^0}\mathcal{CB}_{B^0\to\,\overline{D}^0\rho^0}
\end{aligned}
\tag{V.19}
$$

$$
\begin{aligned}
f_{D^0K^{*0}\text{OS}} &= N^{\text{sig.}}_{\overline{B}^0_s\to D^0K^{*0}}\mathcal{G}_{B^0_s} + N^{\text{part.}}_{D^0K^{*0}}\mathcal{E}_{D^0K^{*0}} + N^{\text{comb.}}_{D^0K^{*0}}\mathcal{F} \\
&+ \frac{f_{D^0\rho^0\to D^0K^{*0}}}{2} N^{\text{sig., LOHadronTOSOnly}}_{B^0\to\,\overline{D}^0\rho^0}\mathcal{CB}_{B^0\to\overline{D}^0\rho^0}
\end{aligned}
\tag{V.20}
$$

$$\mathcal{L}_{\text{total}} = c_{\text{cross-feed}} \times \prod_{i \in categories} \left(\frac{e^{-\sum_{k \in component} N_{i,k}}}{N_i^{\text{observed}}} f_i \right) \tag{V.21}$$

$$c_{\text{cross-feed}} = \frac{1}{\sqrt{2\pi\sigma_{f_{D^0\rho^0 \to D^0 K^{*0}}}}} \exp\left(- \frac{\left(f_{D^0\rho^0 \to D^0 K^{*0}} - \mu_{f_{D^0\rho^0 \to D^0 K^{*0}}} \right)^2}{2\sigma^2_{f_{D^0\rho^0 \to D^0 K^{*0}}}} \right) \times \frac{1}{\sqrt{2\pi\sigma_{f_{D^0 K^{*0} \to D^0\rho^0}}}} \exp\left(- \frac{\left(f_{D^0 K^{*0} \to D^0\rho^0} - \mu_{f_{D^0 K^{*0} \to D^0\rho^0}} \right)^2}{2\sigma^2_{f_{D^0 K^{*0} \to D^0\rho^0}}} \right) \tag{V.22}$$

V.2.4.2 Validation of the fit procedure : toy Monte Carlo studies

In order to test the fitting procedure we have generated toy Monte Carlo samples. The values used for the `D0Rho0` categories are those obtained from the fit on data given in section V.2.4.3, for the `D0Kstar OppositeSign` and `D0Kstar SameSign` categories, the background parameters are also taken from the data fit, while the number of signal events for the B_s decay is assumed to be equal to the number of $D^0\rho^0$ signal events divided by 0.8 to take into account for the overall ratio of efficiencies (calculated in section V.2.5) but also divided by six and three[2] for the B_d Cabibbo allowed decay, the values are thus respectively 35 events and 17 events. In order to check the quality of the fits, for each toy Monte-Carlo sample and each fitted variable, the pull distribution P_x of a given parameter x is plotted:

$$P_x = \frac{x_{\text{Fit}} - x_{\text{Gen}}}{\sigma_x} \tag{V.23}$$

For well behaving fits, one expects Gaussian distributions, centred on zero with unit width, for the P_x values. The pulls for the nine events yields are shown in Figs. V.27-V.28 and the pulls of the four shapes parameters are shown in Fig. V.29. In most of the cases, the pulls are indeed following a Gaussian distribution centred at 0 and with a width of 1. The only exception is due to the combinatorial and partially reconstructed background for the `D0Kstar OppositeSign` and `D0Kstar SameSign` categories where, due to the low statistics, the two types of background events cannot be easily separated (though the pulls of the signal yields remain satisfactory). In these cases, the fitted coefficient of the exponential describing the partially reconstructed background is too close to 0, some combinatorial background events are thus assigned to the partially reconstructed background component of the fit. We have checked that if the slopes of the partially reconstructed background components of the `D0Kstar OppositeSign` and `D0Kstar SameSign` categories are fixed, all the pulls behave perfectly. The corresponding pulls are shown in appendix A.1.1.

[2] These numbers are computed assuming $f_d/f_s = 4$, $\mathcal{B}(\overline{B}^0_s \to D^0 K^{*0}) = 2/3\mathcal{B}(B^0 \to \overline{D}^0\rho^0)$ and the PDG value for $\mathcal{B}(B^0 \to D^0 K^{*0})$.

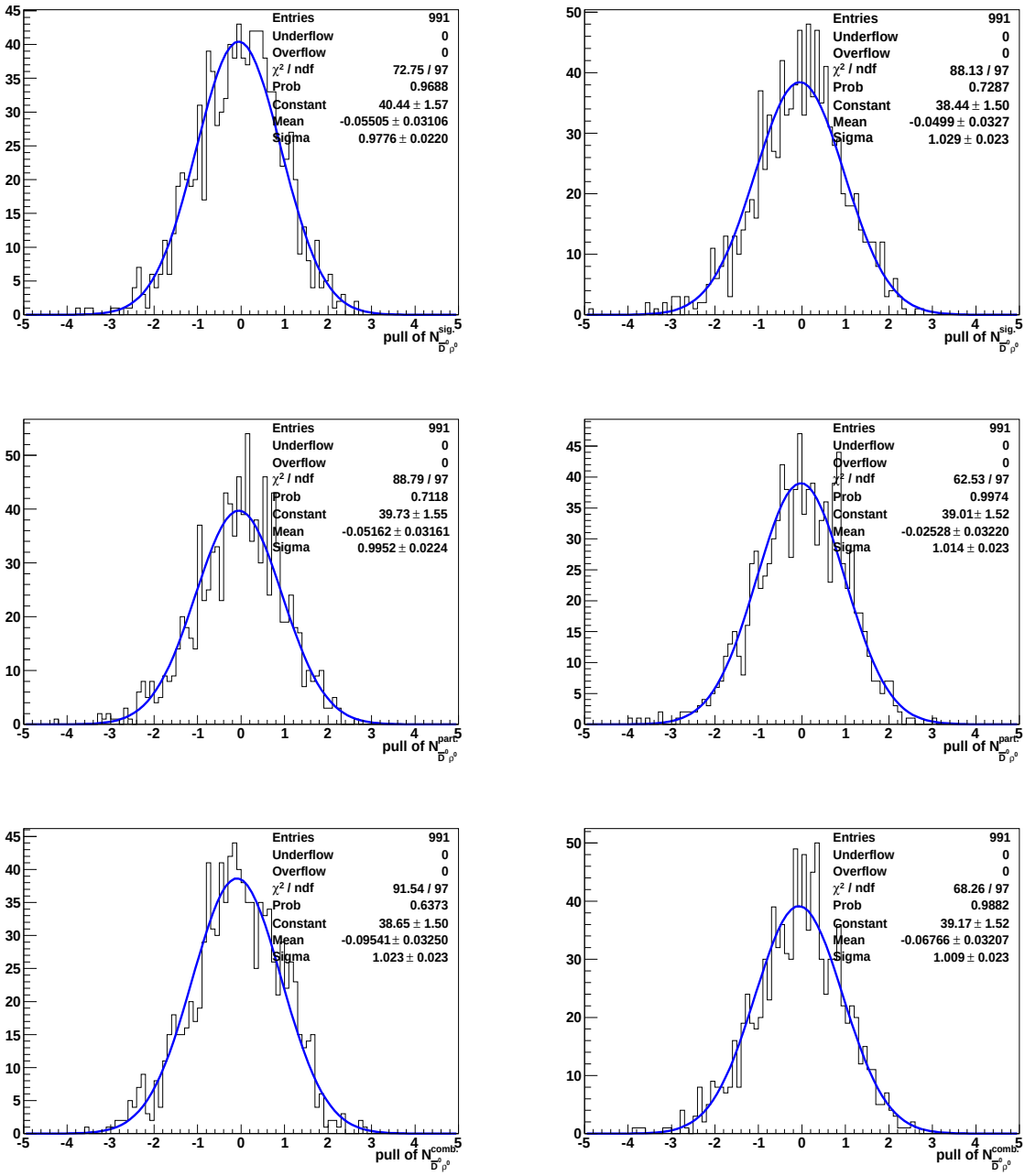

Figure V.27: Pulls of the yields for signal (top), partially reconstructed background (middle) and combinatorial background (bottom) for the two categories in the $\overline{D}{}^0\rho^0$ selection (`L0HadronTOSOnly` on the left and `OtherB` on the right).

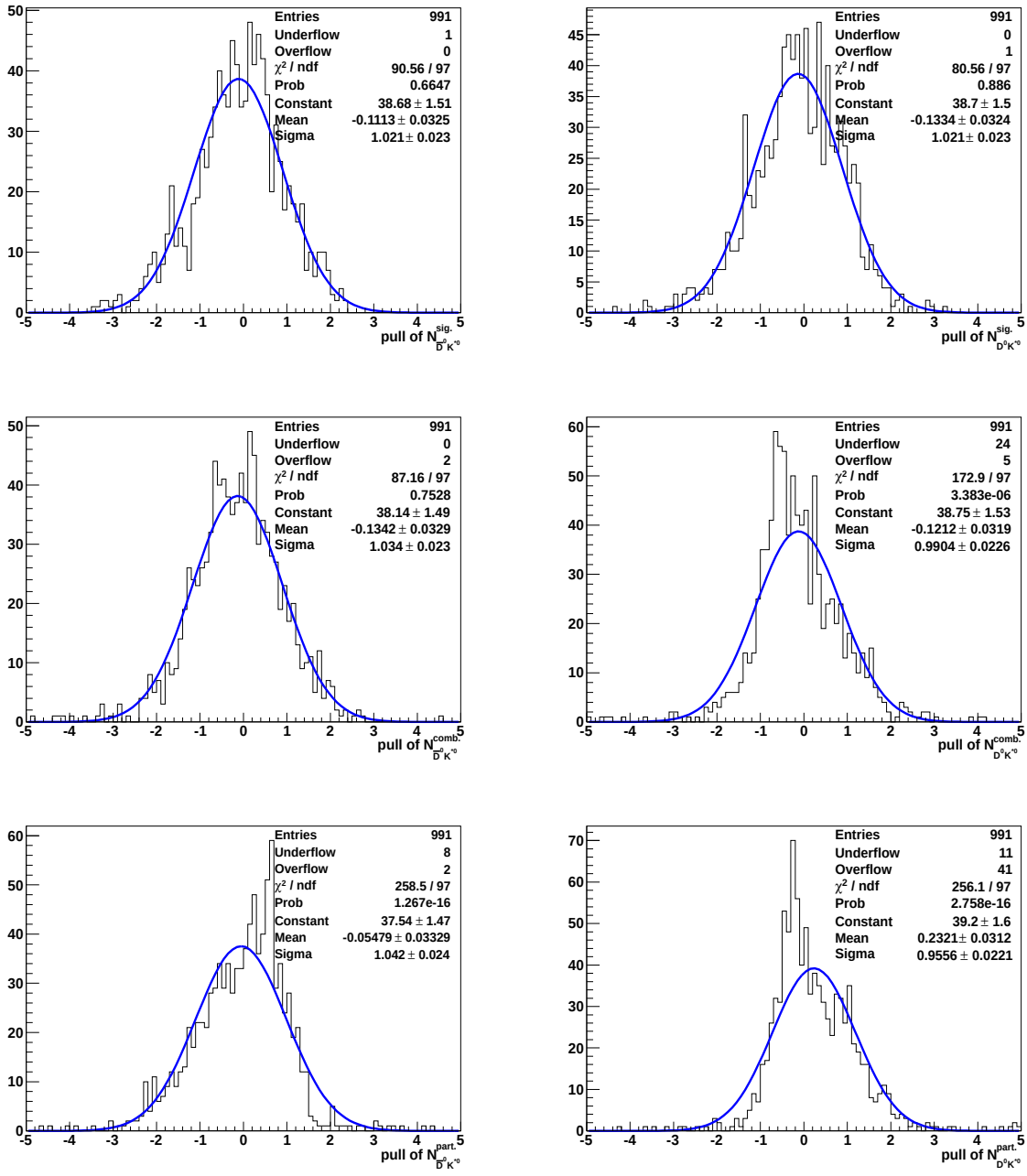

Figure V.28: Pulls of the yields (signal on the top, combinatorial background on the middle and partially reconstructed on the bottom) of the `D0Kstar0` categories (`D0Kstar SameSign` on the left, `D0Kstar OppositeSign` on the right) in the fitting range.

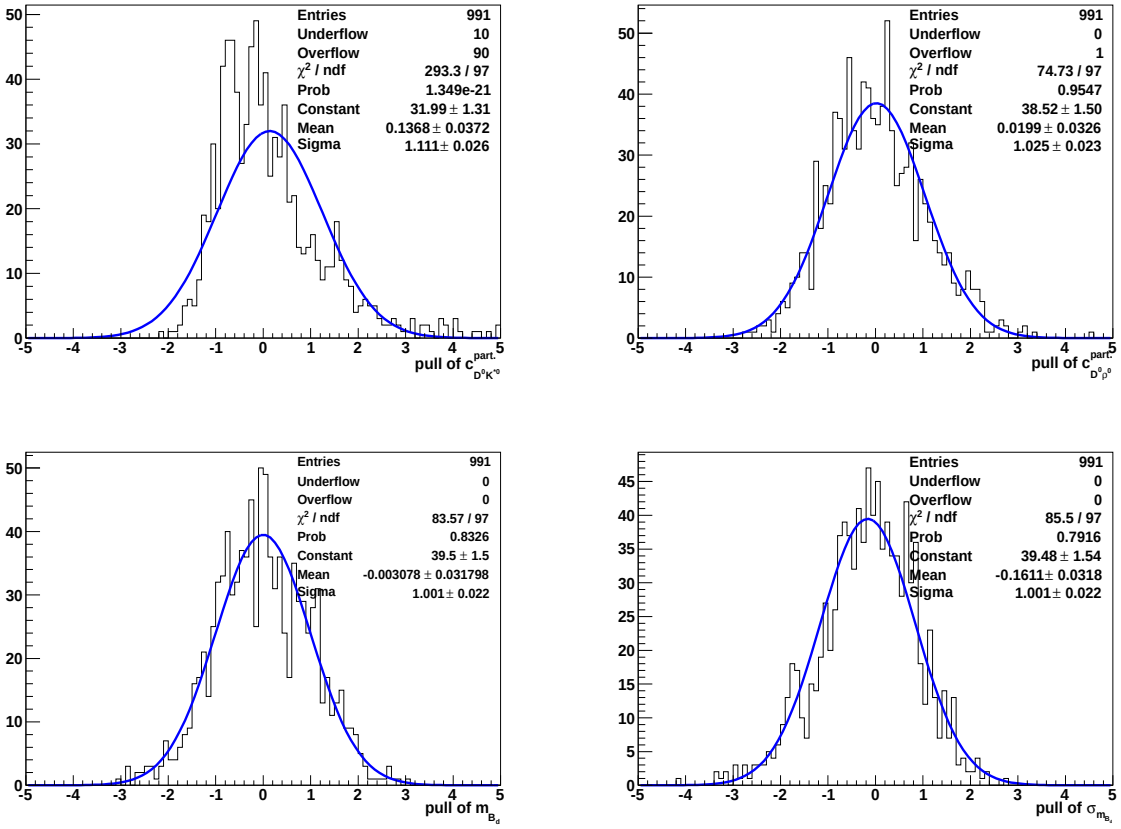

Figure V.29: Pulls of the shape parameters. The slope of the partially reconstructed background in `D0Kstar0` (left) and `D0Rho0` (right) is shown on the top of the figure. Signal $B^0 \to \overline{D}^0 \rho^0$ mass (left) and resolution (right) is shown on the bottom plots.

It is also noticeable that for some parameters the pulls are biased, but looking at the difference between fitted and generated values for each parameter (see appendix A.1.1) there is no evidence for an actual bias on the fitted value, due to a misestimation of the errors with small numbers of events.

V.2.4.3 Fit results

The result of the fit for the $\overline{D}{}^0\rho^0$ is given in Fig. V.30. The signal $B^0 \to \overline{D}{}^0\rho^0$ is clearly visible in both of the two trigger categories, with a yield of 77 ± 10 and 77 ± 11 signal events and a S/B ratio of 4.0 ± 0.7 and 2.1 ± 0.4 in the B signal box of ± 50 MeV/c^2, respectively in `L0HadronTOSOnly` and `OtherB` categories. The resolution of the $B^0 \to \overline{D}{}^0\rho^0$ mass is (15 ± 2) MeV/c^2 which is slightly larger than the fit on Monte Carlo. The numbers are summarized in the Tab. V.8 which contains all the (free and fixed) parameters of the fit.

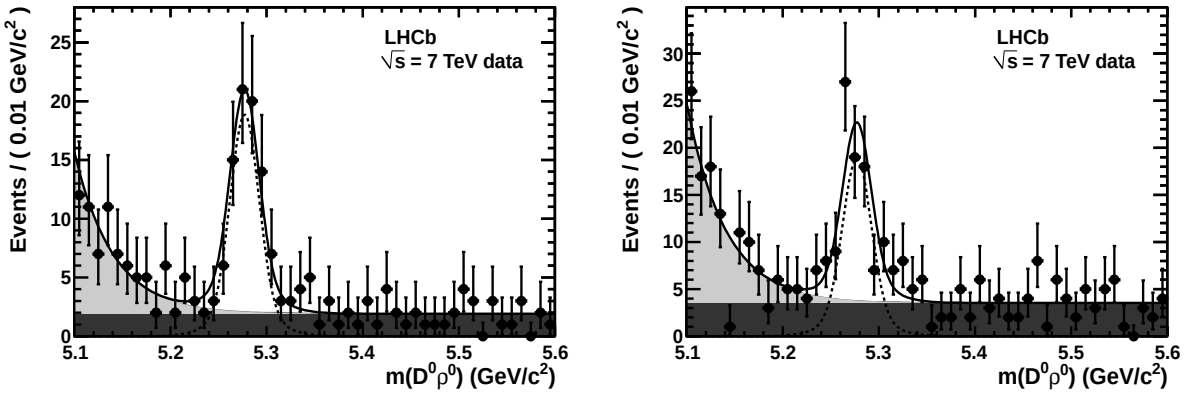

Figure V.30: Invariant mass distribution for the $B^0 \to \overline{D}{}^0\rho^0$ decay mode for the `TOSOnly` (left) and `OtherB` (right) trigger categories with the fit superimposed. The black points correspond to the data and the fit result is represented as a solid line. The signal is fitted with a double Gaussian (dashed line), the partially reconstructed with an exponential function (light grey area) and the combinatorial background with a flat distribution (**dark** grey area) as explained in the text. The contributions from cross-feed are too small to be visible.

The result is shown in Fig. V.31 for the D^0K^{*0} categories. The signal $\overline{B}{}^0_s \to D^0K^{*0}$ is statistically significant with a yield of 35 ± 7 signal events and a S/B ratio of 5 ± 1 B^0_s signal box of ± 50 MeV/c^2.

V.2.4.4 Charmless background

In order to check the possible contribution of charmless B-decays in the analysis, the B^0 mass distribution in the sidebands of the D^0 is given for the three categories in Figs. V.32-V.33. The sideband of the D^0 has been chosen to be in the range

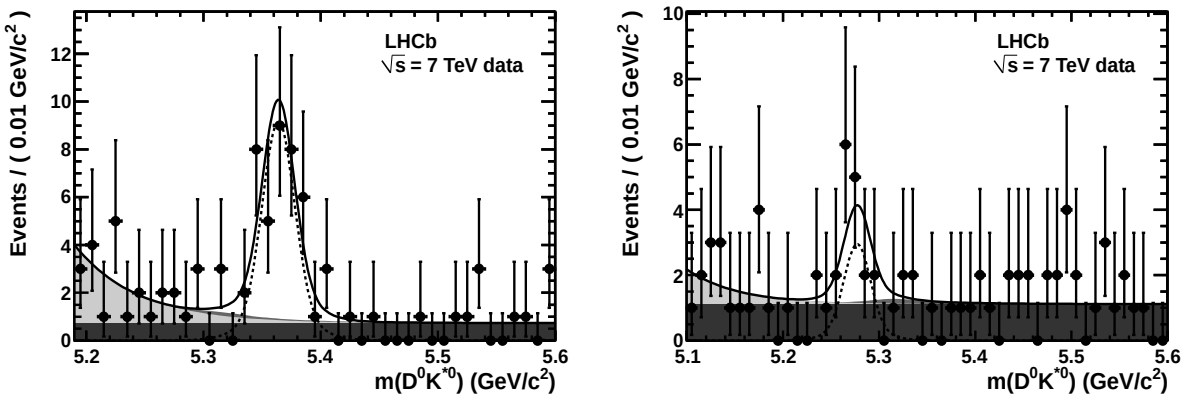

Figure V.31: Invariant mass distribution for the $\overline{B}{}^0_s \to D^0 K^{*0}$ decay mode (`D0Kstar OppositeSign`, left) and $B^0 \to D^0 K^{*0}$ (`D0Kstar SameSign`, right) with the fit superimposed. The black points correspond to the data and the fit result is represented as a solid line. The signal is fitted with a double Gaussian (dashed line), the partially reconstructed with an exponential function (light grey area), the combinatorial background with a flat distribution (dark grey area) and the cross-feed from $B^0 \to \overline{D}{}^0 \rho^0$ (intermediate grey area) as explained in the text.

$$\left[m_{D^0} - 95\ \text{MeV}/c^2, m_{D^0} - 60\ \text{MeV}/c^2\right] \cup \left[m_{D^0} + 60\ \text{MeV}/c^2, m_{D^0} + 95\ \text{MeV}/c^2\right]. \quad \text{(V.24)}$$

A similar fit is performed except that in the three categories a potential signal for both B^0 and B^0_s is allowed. However the masses and widths of the Gaussian PDFs are fixed to the previously fitted values, summarised in the Tab. V.8. All yields are compatible with zero. The charmless background is thus negligible.

V.2.4.5 Data and Monte Carlo momentum distributions

In order to check that the Monte Carlo describes well the kinematics of the B candidates of the real data, sPlots [108] have been built for the `D0Rho0` category. The distributions for the B^0 momentum, transverse momentum and pseudo-rapidity are shown in Fig. V.34 that can be compared to the prediction from the Monte Carlo that is superimposed in blue. There is a reasonable agreement (within the limited statistics) between data and Monte Carlo, except that the number of tracks is significantly underestimated in the Monte Carlo.

V.2.5 Extraction of the ratio of branching ratios

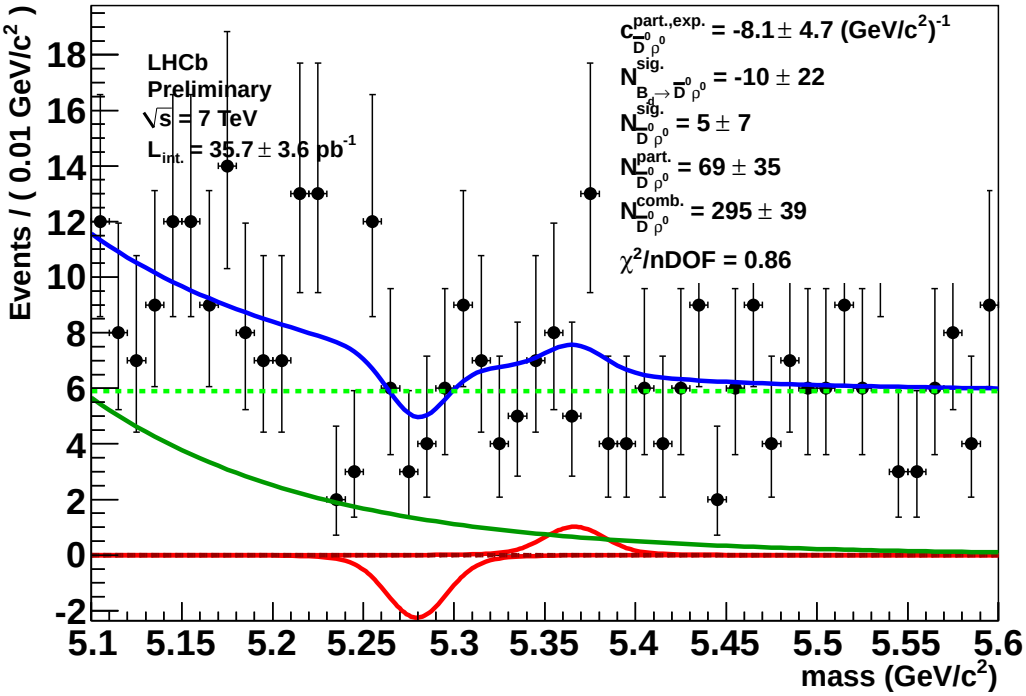

Figure V.32: B^0 mass distribution in the sidebands of the D^0 for the $\overline{D}^0\rho^0$ analysis. No significant peak is observed indicating that charmless B^0 decays do not seem to contribute. The charmless background is fitted with a double Gaussian for which all the shape parameters have been fixed to the value obtained for the signal in section V.2.4.3.

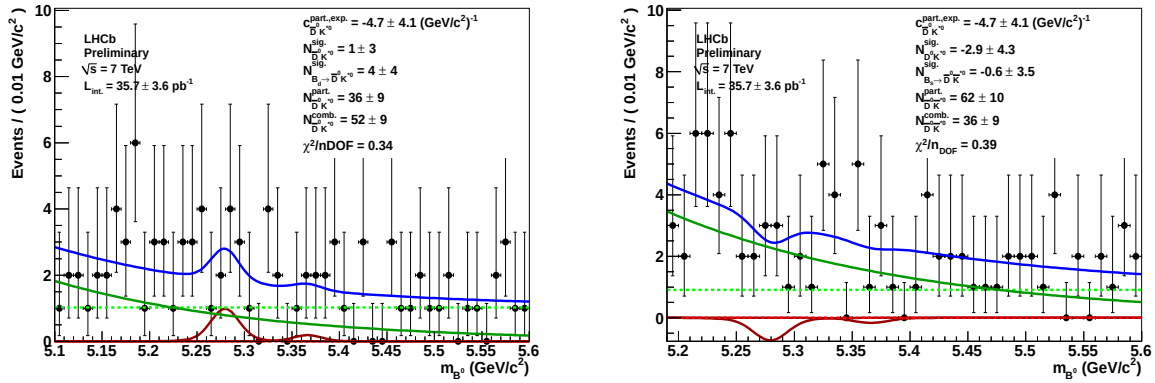

Figure V.33: B^0 mass distribution in the sidebands of the D^0 for the D^0K^{*0} analysis. The distribution in the `D0Kstar SameSign` category is given on the left hand side while the distribution in the `D0Kstar OppositeSign` category is given on the right hand side. The charmless background is fitted with a double Gaussian for which all the shape parameters have been fixed to the value obtained for the signal in section V.2.4.3.

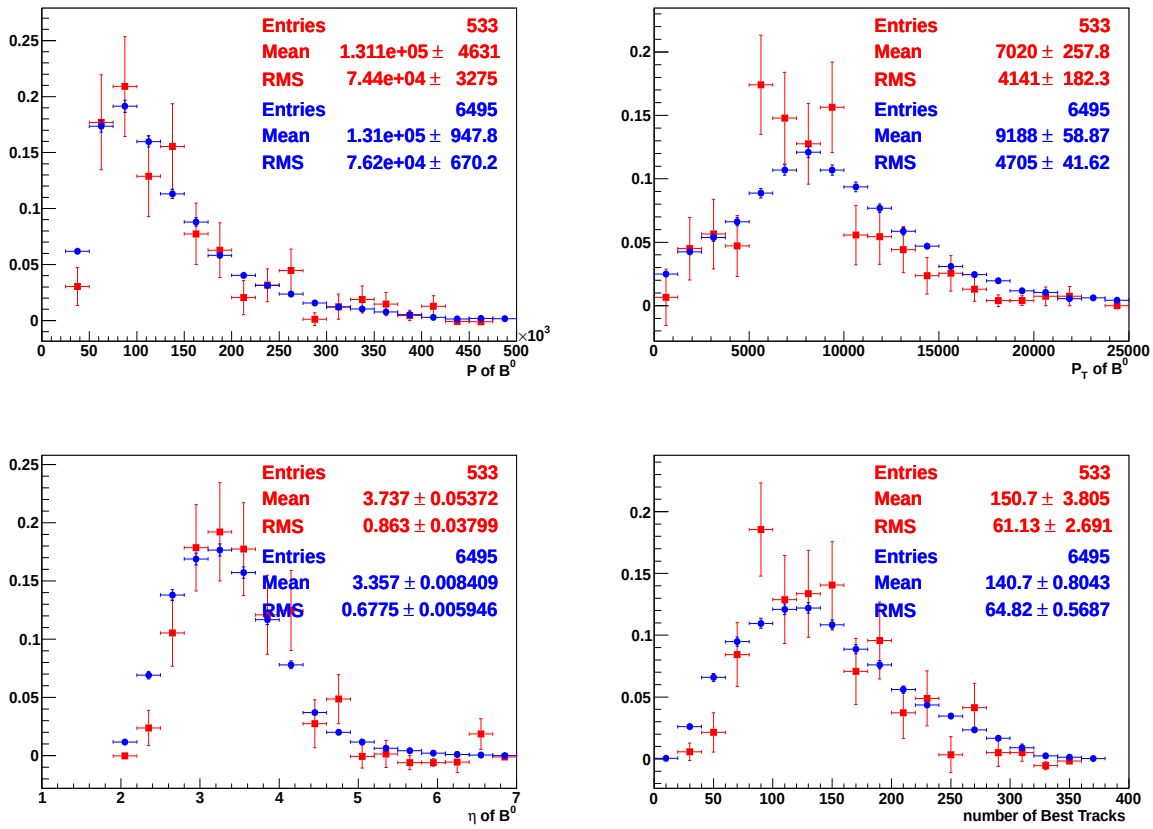

Figure V.34: sPlots in the D0Rho0 category (red points) and Monte Carlo prediction superimposed (blue points). The momentum and the transverse momentum of the B^0 are respectively given in the top left and right plots. The η distribution and the number of *best tracks* are given in the bottom distributions on the left and right of the figure respectively. While there is in general a good agreement between data and Monte Carlo, the momentum spectra seem a bit harder in the real data plots. The number of tracks is slightly underestimated in the Monte Carlo.

V.2.5.1 Calculation of the ratio

The ratio of branching fractions is calculated from the number of fitted events as shown in Eq. V.25, where the ϵ parameters represent the total efficiencies, including acceptance, trigger, reconstruction and selection.

$$\frac{\mathcal{B}\left(\overline{B}^0_s \to D^0 K^{*0}\right)}{\mathcal{B}\left(B^0 \to \overline{D}^0 \rho^0\right)} = \frac{N^{sig.}_{\overline{B}^0_s \to D^0 K^{*0}}}{N^{sig.}_{B^0 \to \overline{D}^0 \rho^0}} \frac{\mathcal{B}\left(\rho^0 \to \pi^+\pi^-\right)}{\mathcal{B}\left(K^{*0} \to K^+\pi^-\right)} \frac{f_d \epsilon_{B^0 \to \overline{D}^0 \rho^0}}{f_s \epsilon_{\overline{B}^0_s \to D^0 K^{*0}}} \tag{V.25}$$

The efficiencies of the two channels can be written as in the Eqs. V.26-V.27. Given the fact that the selections are identical for the D^0 in the two channels of interest, the corresponding selection efficiencies cancel as well as the cuts on the topology of the decay emphasised by the $\epsilon_{B \text{ topology}}$ terms in the Eqs. V.26-V.27.

$$\epsilon_{B^0 \to \overline{D}^0 \rho^0} = \epsilon^{B^0 \to \overline{D}^0 \rho^0}_{\text{acceptance}} \epsilon^{B^0 \to \overline{D}^0 \rho^0}_{\text{reconstruction}} \epsilon^{B^0 \to \overline{D}^0 \rho^0}_{\text{trigger}} \epsilon^{B^0 \to \overline{D}^0 \rho^0}_{D^0 \text{ selection}} \epsilon^{B^0 \to \overline{D}^0 \rho^0}_{\rho^0 \text{ selection}} \epsilon^{B^0 \to \overline{D}^0 \rho^0}_{B \text{ topology}} \tag{V.26}$$

$$\begin{aligned} \epsilon_{\overline{B}^0_s \to D^0 K^{*0}} &= \epsilon^{\overline{B}^0_s \to D^0 K^{*0}}_{\text{acceptance}} \epsilon^{\overline{B}^0_s \to D^0 K^{*0}}_{\text{reconstruction}} \epsilon^{\overline{B}^0_s \to D^0 K^{*0}}_{\text{trigger}} \\ &\times \epsilon^{\overline{B}^0_s \to D^0 K^{*0}}_{D^0 \text{ selection}} \epsilon^{\overline{B}^0_s \to D^0 K^{*0}}_{K^{*0} \text{ selection}} \epsilon^{\overline{B}^0_s \to D^0 K^{*0}}_{B \text{ topology}} \end{aligned} \tag{V.27}$$

The reconstruction, B topology and D^0 selection efficiencies are computed together in the term labeled *selection* while the selection on the vector meson is computed apart (in V *selection*) due to the difference in mass and helicity distributions. The selection efficiencies of the vector mesons (either a ρ^0 or a K^{*0}) are different for three reasons.

- The PID requirement is different on one of the tracks.
- The mass cut and the cosine of helicity angle cut have different effects for the two decay modes.
- The p and p_T distributions of the tracks are different.

V.2.5.2 Ratio of trigger efficiencies

We give the trigger (TOS) efficiencies estimated on Monte Carlo for the three channels that we study here in the Tab. V.10. We found that the HLT efficiencies are in good agreement for all the channels, the only difference coming from the L0 trigger. We have checked that this difference is fully compatible with the difference in transverse momentum spectra, applying the corresponding cuts on the P_T of the tracks.

trigger line	$B^0 \to \overline{D}^0 \rho^0$	$B^0 \to D^0 K^{*0}$	$\overline{B}^0_s \to D^0 K^{*0}$
L0Hadron_TOS	37.0 ± 0.4 %	28.0 ± 0.7 %	29.9 ± 0.3 %
Hlt1TrackAllL0_TOS	81.9 ± 0.6 %	79.6 ± 1.2 %	80.5 ± 0.6 %
Hlt2Topo2Body_TOS	76.8 ± 0.5 %	72.9 ± 1.2 %	74.0 ± 0.5 %
Hlt2Topo3Body_TOS	73.4 ± 0.6 %	77.2 ± 1.1 %	77.4 ± 0.5 %
Hlt2Topo4Body_TOS	34.8 ± 0.6 %	44.6 ± 1.3 %	43.9 ± 0.6 %
Hlt2Topo2or3Body_TOS	85.4 ± 0.4 %	85.1 ± 0.9 %	85.8 ± 0.4 %
Hlt2Topo2or3or4Body_TOS	85.5 ± 0.4 %	85.9 ± 0.9 %	86.1 ± 0.4 %

Table V.10: Summary of the trigger efficiencies estimated on Monte Carlo for the 0x2e002a TCK. The summary of the fixed and fitted parameters with the result of the fit. The efficiencies for the HLT1 and HLT2 has to be understood to be efficiencies with respect to L0 or L0 and HLT1 respectively.

Making use of TOS events only would reduce the available statistics by 30 % and thus significantly decrease the statistical significance of the measurement of the ratio of branching fractions. The data sample is divided into two categories : (i) the events which satisfy only the BdL0Hadron_TOS decision and (ii) the events which are triggered by the other B[3]. Events that do not enter these two categories are marginal (approximately 6 %) and vetoed in the analysis. The obtained relative abundances both in data ($\overline{D}^0 \rho^0$) and Monte Carlo are summarized in Tab. V.11. The values for data have been obtained by a fit of the invariant mass for each of the two categories. We observe that data and Monte Carlo relative abundances are not in agreement (given the statistical uncertainties). This is expected since the value of relative abundances depends on the TCK.

trigger line	$\overline{D}^0 \rho^0$ data	$B^0 \to \overline{D}^0 \rho^0$	$\overline{B}^0_s \to D^0 K^{*0}$
L0HadronTOSOnly	47.19 ± 4.43 %	52.34 ± 0.53 %	48.03 ± 0.50 %
OtherB	46.93 ± 4.40 %	44.53 ± 0.52 %	47.86 ± 0.50 %
L0HadronTOSOnly or OtherB	94.48 ± 8.54 %	96.87 ± 0.18 %	95.89 ± 0.19 %

Table V.11: Summary of the relative trigger abundances estimated on data (fit of the different categories) and Monte Carlo for the 0x2e002a TCK.

The corresponding efficiencies for the two categories of interest L0HadronTOSOnly and OtherB are calculated on Monte Carlo for the TCK 0x2e002a. We observe as expected that the probability to trigger on the OtherB is the same for the two channels of interest. The difference in trigger efficiencies still remains for the L0HadronTOSOnly category.

The ratio of trigger efficiencies can be rewritten as in Eq. V.28 to take into account for the three main types of triggers and the corresponding weights in the delivered luminosity. Note that the ratio of trigger efficiencies ($r^{-1}_{\texttt{OtherB}}$ and $r^{-1}_{\texttt{L0HadronTOSOnly}}$) are the weighted averages of the

[3]These events are satisfying the TIS decision on one of the L0 lines and are not satisfying TOS in any line except the BdL0Hadron. We define isTIS $= \bigcup$ BdL0XDecision_TIS where X represents any of the L0 lines (Hadron, Electron, Photon, Muon, DiMuon) and isNotTOS $= \bigcap \overline{\texttt{BdL0YDecision\_TOS}}$ where Y represents any of the L0 lines except the Hadron line. We denote, by convention, the logical OR operator by $\bigcup$, the logical AND operator by $\bigcap$ and the logical negation by an overline. With these notations the OtherB category corresponds to isTIS$\cap$isNotTOS.

TCK	trigger line	$B^0 \to \overline{D}{}^0\rho^0$	$\overline{B}{}^0_s \to D^0 K^{*0}$	ratio
0x2e002a	L0HadronTOSOnly	27.06 ± 0.34 %	22.04 ± 0.28 %	1.22 ± 0.02
0x2e002a	OtherB	22.95 ± 0.32 %	21.98 ± 0.28 %	1.04 ± 0.02
0x1e0030	L0HadronTOSOnly	33.33 ± 0.37 %	29.70 ± 0.33 %	1.12 ± 0.02
0x1e0030	OtherB	39.89 ± 0.38 %	39.62 ± 0.35 %	1.00 ± 0.01
0x19001f	L0HadronTOSOnly	31.06 ± 0.38 %	28.01 ± 0.31 %	1.11 ± 0.02
0x19001f	OtherB	52.28 ± 0.41 %	52.31 ± 0.35 %	1.00 ± 0.01

Table V.12: Trigger efficiencies for the L0HadronTOSOnly and the OtherB categories on Monte Carlo for the different TCKs. The results obtained for any TCK is obtained after an emulation of the trigger by the MOORE software.

ratios for each class of TCK, see Eq. V.29 for the definition in the case of OtherB. We thus obtain $r_{\texttt{OtherB}} = 1.03 \pm 0.03$ and $r_{\texttt{L0HadronTOSOnly}} = 1.20 \pm 0.02$. The errors are here taken equal to the error on the main contributor to the average for simplicity.

$$\begin{aligned}
\frac{N^{sig.}_{\overline{B}{}^0_s \to D^0 K^{*0}}}{N^{sig.}_{B^0 \to \overline{D}{}^0\rho^0}} \frac{\epsilon^{B^0 \to \overline{D}{}^0\rho^0}_{\text{trigger}}}{\epsilon^{\overline{B}{}^0_s \to D^0 K^{*0}}_{\text{trigger}}} &= r_{\texttt{OtherB}}\, r_{\texttt{L0HadronTOSOnly}} \\
&\times \frac{N^{sig.}_{\overline{B}{}^0_s \to D^0 K^{*0}}}{r_{\texttt{OtherB}} N^{\texttt{L0HadronTOSOnly}}_{B^0 \to \overline{D}{}^0\rho^0} + r_{\texttt{L0HadronTOSOnly}} N^{\texttt{OtherB}}_{B^0 \to \overline{D}{}^0\rho^0}} \\
&= \frac{N^{sig.}_{\overline{B}{}^0_s \to D^0 K^{*0}}}{r^{-1}_{\texttt{L0HadronTOSOnly}} N^{\texttt{L0HadronTOSOnly}}_{B^0 \to \overline{D}{}^0\rho^0} + r^{-1}_{\texttt{OtherB}} N^{\texttt{OtherB}}_{B^0 \to \overline{D}{}^0\rho^0}}
\end{aligned} \tag{V.28}$$

$$\begin{aligned}
r^{-1}_{\texttt{OtherB}} &= \frac{1}{w_{\texttt{OtherB}}} \sum_{i \in \text{ TCK}} r^{-1}_{\text{i, OtherB}} w_{\text{i, OtherB}} \\
\text{with } w_{\text{i, OtherB}} &= \frac{\int \mathcal{L}_i}{\int \mathcal{L}_{tot}} \epsilon^{B^0 \to \overline{D}{}^0\rho^0}_{\text{i, OtherB}} \\
\text{and } w_{\texttt{OtherB}} &= \sum_{i \in \text{ TCK}} w_{\text{i, OtherB}}
\end{aligned} \tag{V.29}$$

V.2.5.3 Ratio of PID efficiencies

PID calibration procedure In order to distinguish the $B^0 \to \overline{D}{}^0\rho^0$ and the $\overline{B}{}^0_s \to D^0 K^{*0}$ decay modes the use of PID information is crucial. Furthermore, for a given PID cut, it is vital to know the kaon efficiency and the proportion of pions accepted. This is achieved using a PID calibration technique that is documented in detail elsewhere [109] and adapted to our channels [110].

This technique allows one to extract directly from a data calibration sample the efficiency and misidentification rates. A large statistics calibration sample of prompt $D^* \to \pi D^0$ decays

is selected using only kinematic cuts, and high purity samples of pions and kaons are available. These samples cover a wide range of momenta, pseudo rapidity and number of tracks[4]. However, the tracks used in the $B^0 \to \overline{D}^0 \rho^0$ and the $\overline{B}^0_s \to D^0 K^{*0}$ have different spectra. The calibration technique described in [109] works by reweighting the calibration sample such that its spectra follow those of the signal. If the PID performance is perfectly described by the kinematic variables used in the reweighting, then the PID Delta Log Likelihood ($\Delta\text{LL}_{K-\pi}$) distributions of the reweighted calibration sample should match that of the signal.

The Monte Carlo (MC10) has been used to extract the momentum, pseudo rapidity and numbers of tracks in the event. It was checked using an sPlot-technique [108] that the distributions between the $B^0 \to \overline{D}^0 \rho^0$ signal sample and the MC10 do not differ too much (see section V.2.4.5).

Validation on Monte-Carlo The plots of Figs. V.35-V.37 compare the distributions of the $\Delta\text{LL}_{K-\pi}$ distribution for the kaon/pion tracks from the D^0, ρ^0 and K^{*0} resonances with the kaon/pion tracks from a Monte-Carlo calibration sample before reweighting (top plots). For the reweighting a binning scheme of $32 \times 4 \times 4$ bins in momentum, pseudo rapidity and number of tracks is used. The bottom plots of Figs. V.35-V.37 compare the distributions of the $\Delta\text{LL}_{K-\pi}$ distribution for the kaon/pion tracks from the D^0, ρ^0 and K^{*0} resonances with the kaon/pion tracks from the Monte-Carlo calibration sample after reweighting. There is a good agreement after reweigthing, which indicates that the procedure is working properly.

Efficiencies and mis-identifications rates obtained from data The data calibration sample, reweighted using a binning scheme of $32 \times 4 \times 4$ bins in momentum, pseudo rapidity and number of tracks and following the MC10 distributions is used. The efficiency curves as a function of the $\Delta\text{LL}_{K-\pi}$ cuts can be computed for each of the four tracks present in the $B^0 \to \overline{D}^0 \rho^0$ and the $\overline{B}^0_s \to D^0 K^{*0}$ decay modes. They are shown in Figs. V.38-V.41. From these curves one can summarize the values useful for the analysis, they are given in Tab. V.13.

	$B^0 \to \overline{D}^0 \rho^0$	$\overline{B}^0_s \to D^0 K^{*0}$
K from D^0 ($\Delta\text{LL}_{K-\pi} > 0$)	91.8 ± 0.4 %	92.0 ± 0.4 %
π from D^0 ($\Delta\text{LL}_{K-\pi} < 4$)	95.0 ± 0.4 %	95.0 ± 0.4 %
K from K^{*0} ($\Delta\text{LL}_{K-\pi} > 3$)	n/a	84.9 ± 0.5 %
π from V ($\Delta\text{LL}_{K-\pi} < 3$)	93.1 ± 0.3 %	93.3 ± 0.4 %

Table V.13: Efficiencies for all tracks to be properly identified as a kaon or as a pion. These numbers have been obtained from the data calibration sample reweighted using a binning scheme of $32 \times 4 \times 4$ bins in momentum, pseudo rapidity and number of tracks obtained from signal Monte Carlo.

[4]The PID performances should be mainly sensitive to these three variables.

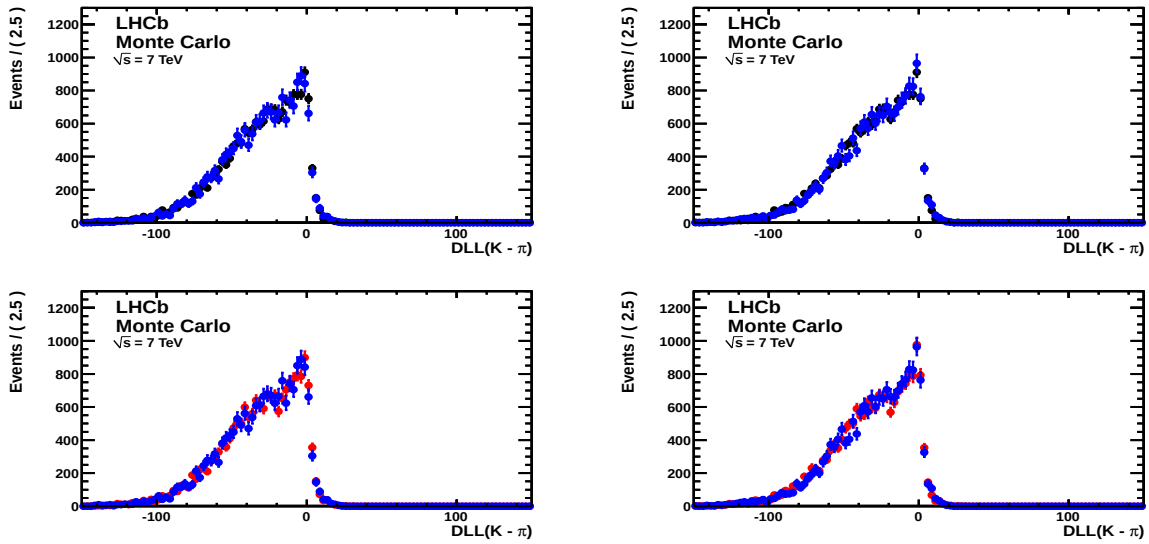

Figure V.35: Comparison of the $\Delta\mathrm{LL}_{K-\pi}$ distributions for the pion tracks from the ρ^0 resonance with the pion tracks from the calibration sample before reweighting (top plots) and after (bottom plots). The blue (grey) distributions correspond to the Monte Carlo signal distributions while the black (in top plots) distributions correspond to the unweighted calibration sample and the red (in bottom plots) distributions correspond to the reweighted calibration sample. The agreement after reweighting is always better than before reweighting.

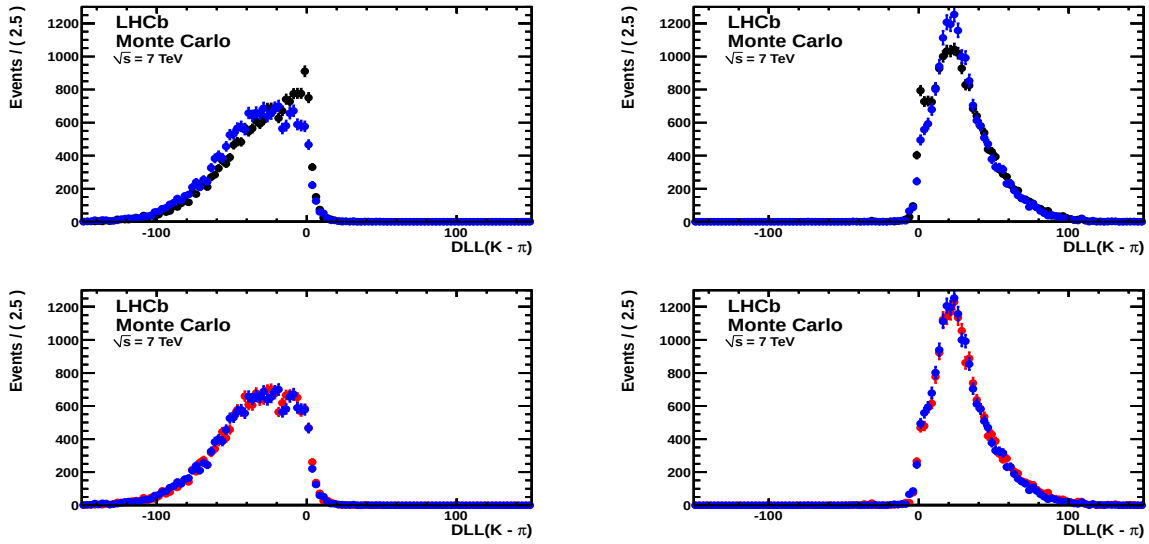

Figure V.36: Comparison of the $\Delta\mathrm{LL}_{K-\pi}$ distributions for the kaon and pion tracks from the K^{*0} resonance with the kaon and pion tracks from the calibration sample before reweighting (top plots) and after (bottom plots). The blue (grey) distributions correspond to the Monte Carlo signal distributions while the black (in top plots) distributions correspond to the unweighted calibration sample and the red (in bottom plots) distributions correspond to the reweighted calibration sample. The agreement after reweighting is always better than before reweighting.

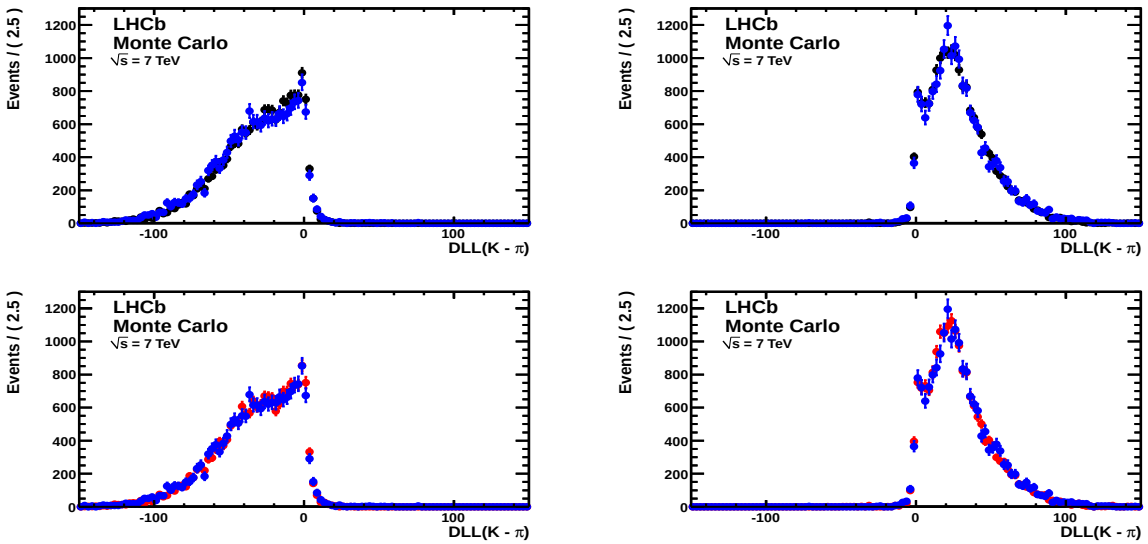

Figure V.37: Comparison of the $\Delta\mathrm{LL}_{K-\pi}$ distributions for the kaon and pion tracks from the D^0 resonance with the kaon and pion tracks from the calibration sample before reweighting (top plots) and after (bottom plots). The blue (grey) distributions correspond to the Monte Carlo signal distributions while the black (in top plots) distributions correspond to the unweighted calibration sample and the red (in bottom plots) distributions correspond to the reweighted calibration sample. The agreement after reweighting is always better than before reweighting.

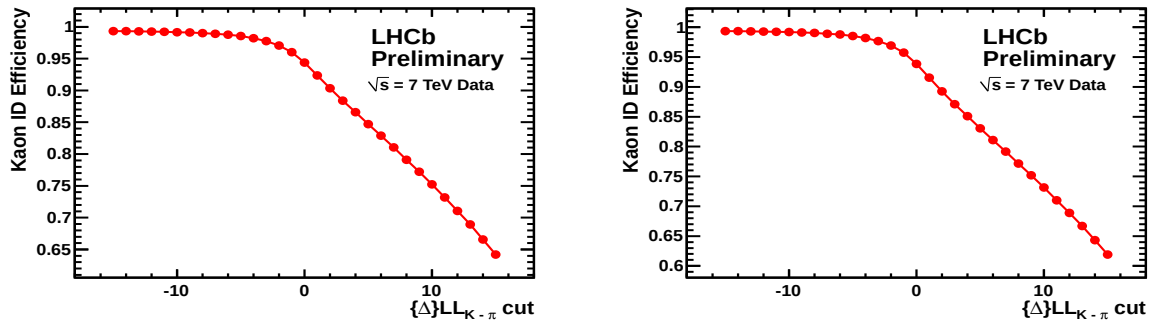

Figure V.38: PID efficiencies as a function of the $\Delta\mathrm{LL}_{K-\pi}$ cut for the K from the D^0 using the reweighting procedure with Monte Carlo kinematics for $\overline{B}{}^0_s \to D^0 K^{*0}$ and the $B^0 \to \overline{D}{}^0 \rho^0$ decay modes on the left and the right plot respectively.

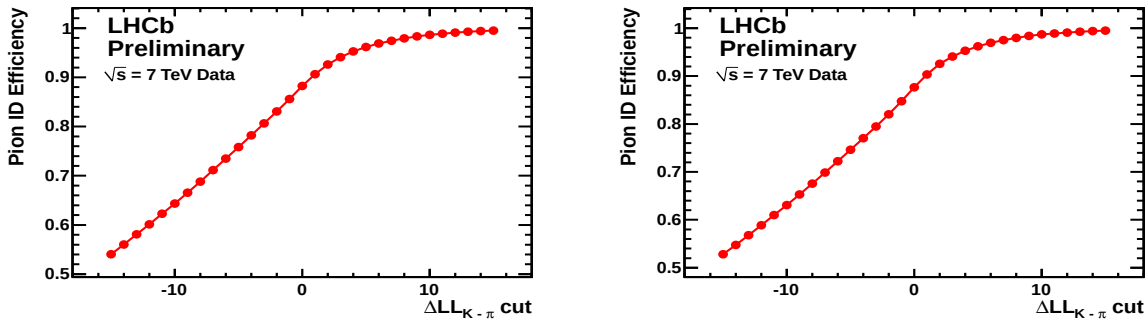

Figure V.39: PID efficiencies as a function of the $\Delta\mathrm{LL}_{K-\pi}$ cut for the π from the D^0 using the reweighting procedure with Monte Carlo kinematics for the $\overline{B}{}^0_s \to D^0 K^{*0}$ and the $B^0 \to \overline{D}{}^0 \rho^0$ decay modes on the left and the right plot respectively.

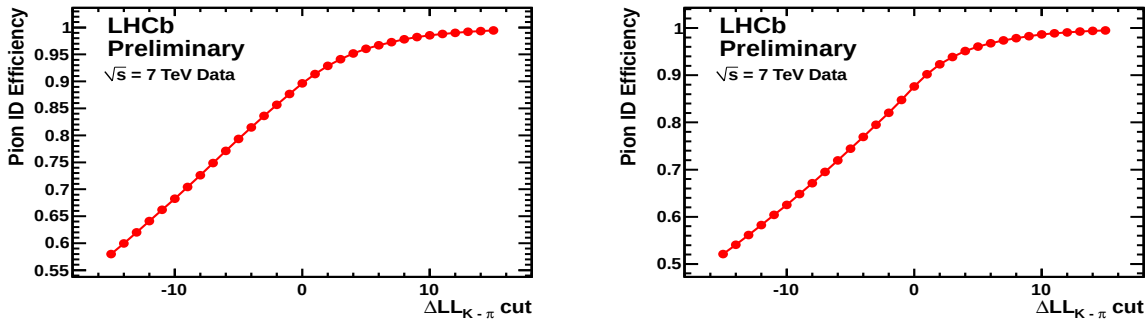

Figure V.40: PID efficiencies as a function of the $\Delta\mathrm{LL}_{K-\pi}$ cut for the π from the vector meson (either a ρ^0 or a K^{*0}) with the reweighting procedure using Monte Carlo kinematics for $\overline{B}{}^0_s \to D^0 K^{*0}$ and the $B^0 \to \overline{D}{}^0 \rho^0$ decay modes on the left and the right plot respectively.

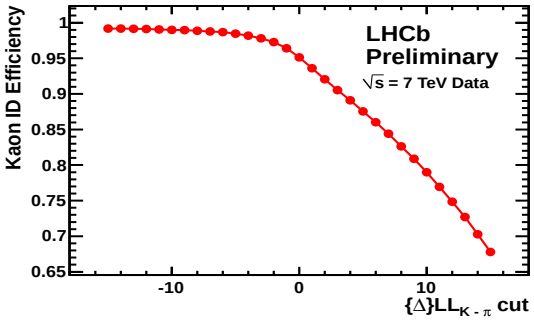

Figure V.41: PID efficiency as a function of the $\Delta\mathrm{LL}_{K-\pi}$ cut for the K from the K^{*0} using the reweighting procedure with Monte Carlo kinematics for $\overline{B}{}^0_s \to D^0 K^{*0}$ decay mode.

Ratio of PID efficiencies From the previous numbers we compute the ratio of PID efficiencies to be $\frac{\epsilon^{B^0 \to \overline{D}^0 \rho^0}_{\text{PID}}}{\epsilon^{\overline{B}^0_s \to D^0 K^{*0}}_{\text{PID}}} = 1.092 \pm 0.014$.

V.2.5.4 Ratio of acceptance efficiencies

At the generator level a cut is applied in order not to generate events for which the final state particles are not in the LHCb acceptance. This gives the acceptance efficiencies before the reconstruction takes place. These efficiencies are computed by GAUSS and listed in [111]. We report in the Tab. V.14 the relevant values for our channels. The ratio of acceptance efficiencies is measured to be $\frac{\epsilon^{B^0 \to \overline{D}^0 \rho^0}_{\text{acceptance}}}{\epsilon^{\overline{B}^0_s \to D^0 K^{*0}}_{\text{acceptance}}} = 0.955 \pm 0.004$.

Monte Carlo data sample	Magnet Up	Magnet Down	Average
$B^0 \to D^0 K^{*0}$	15.76 ± 0.084 %	15.80 ± 0.084 %	15.78 ± 0.06 %
$\overline{B}^0_s \to D^0 K^{*0}$	15.65 ± 0.039 %	15.76 ± 0.039 %	15.70 ± 0.03 %
$B^0 \to \overline{D}^0 \rho^0$	14.98 ± 0.037 %	14.99 ± 0.037 %	14.99 ± 0.03 %

Table V.14: Summary of the acceptance efficiencies as given by GAUSS.

V.2.5.5 Ratio of selection efficiencies

Cumulated efficiencies of the selection The total efficiency of the selection (including reconstruction and stripping) is summarized in the Tab. V.15 for the three Monte Carlo data sample. The PID efficiencies are not included in this table since we are considering the (non calibrated) Monte Carlo. The calibrated efficiencies that have to be used for the calculation of the ratio of branching ratios is detailed in section V.2.5.3. We do not apply here the mass cut and the helicity cut on the vector meson, since these cuts are subject to a special treatment due to the fact that they are not expected to cancel. The ratio of efficiencies is found to be $\frac{\epsilon^{B^0 \to \overline{D}^0 \rho^0}_{\text{selection}}}{\epsilon^{\overline{B}^0_s \to D^0 K^{*0}}_{\text{selection}}} = 0.802 \pm 0.007$. This efficiency difference is only due to the reconstruction and the stripping selection (to which we include the p_T cuts on the tracks, correcting for the difference in stripping selections for the K^{*0} and the ρ^0).

Vector meson cuts The cuts that play an important role in the extraction of the ratio of branching fractions are the mass requirement on the vector meson and the helicity cut. The $m_{K^{*0}} \pm 50$ MeV/c^2 cut efficiency on $\overline{B}^0_s \to D^0 K^{*0}$ Monte Carlo is estimated to be equal to (73.04 ± 0.30) % while the $m_{\rho^0} \pm 150$ MeV/c^2 cut efficiency is (76.75 ± 0.31) % on $B^0 \to \overline{D}^0 \rho^0$. The helicity cut is (91.27 ± 0.18) % on $\overline{B}^0_s \to D^0 K^{*0}$ Monte Carlo and (88.90 ± 0.22) % on

$B^0 \to \overline{D}{}^0\rho^0$. Putting these numbers together to construct the ratio of efficiencies gives us $\frac{\epsilon^{B^0 \to \overline{D}{}^0\rho^0}_{V \text{ selection}}}{\epsilon^{\overline{B}{}^0_s \to D^0 K^{*0}}_{V \text{ selection}}} = 1.023 \pm 0.006$.

V.2.5.6 Ratio of hadronisation fractions

The ratio of fragmentation fractions has been measured at LEP and TEVATRON, but with some discrepancies at the level of 2σ. Thus the combination of the measurements is less precise than the LEP measurement taken alone. The reason of the difference could be due to (i) the difference in transverse momentum spectra of the hadronising b quarks, (ii) the difference in hadronisation processes related to the different environment between electron and hadron machines or (iii) statistical fluctuations. This ratio will be measured at LHCb through different methods [112, 113, 114] with potentially more precise results than the current measurements. The present status is summarized in the Tab. V.16. To perform our measurement we will instead use the value of $\frac{f_d}{f_s} = 3.75 \pm 0.29$ that comes from the combination of the measurements performed at LHCb from hadronic and semileptonic decay modes [115, 116, 117].

V.2.5.7 Correction for non resonant contributions

In order to check the existence of other contributions below the vector mass peaks, an sPlot technique [108] has been used. The resulting plots are shown in Fig. V.34. While the K^{*0} region is extremely clean, the ρ^0 one is much more complicated. An effective "non-ρ^0" contribution has been estimated using a second order polynomial : 30.1 ± 7.9 events contribute in the ρ^0 the mass window (± 150 MeV/c^2). We obtain that the fraction of non-ρ^0 events is 19.5 ± 5.1 %. The measured $B^0 \to \overline{D}{}^0\rho^0$ yield has to be corrected by this amount. The corresponding shapes are shown in Fig. V.42.

V.2.5.8 Summary of the corrections

Putting together all the previous corrections, the ratio of branching fractions is written as in Eq. V.30, where we define the ratio of efficiencies r in the Eqs. V.31-V.36 and the number of events in the two $\overline{D}{}^0\rho^0$ trigger categories are taken from data.

Particle	Cut	$\epsilon^{B^0 \to \overline{D}{}^0 \rho^0}_{\text{selection}}$ [%]	$\epsilon^{B^0 \to D^0 K^{*0}}_{\text{selection}}$ [%]	$\epsilon^{\overline{B}{}^0_s \to D^0 K^{*0}}_{\text{selection}}$ [%]
$\pi^+_{\rho^0}$	$P_T > 300$ MeV/c	6.53 ± 0.03	n/a	n/a
$\pi^-_{\rho^0}$	$P_T > 300$ MeV/c	6.29 ± 0.03	n/a	n/a
K_{D^0}	$P_T > 400$ MeV/c	6.08 ± 0.03	7.45 ± 0.08	7.62 ± 0.04
V	$\min_{\text{PVs}} \chi^2_{\text{IP}} > 25$	5.78 ± 0.03	7.11 ± 0.08	7.24 ± 0.04
D^0	$\min_{\text{PVs}} \chi^2_{\text{IP}} > 4$	5.74 ± 0.03	7.06 ± 0.08	7.19 ± 0.04
D^0	$\left(\chi^2/n_{\text{D.O.F.}}\right)_{\text{vertex}} < 5$	5.43 ± 0.03	6.67 ± 0.07	6.81 ± 0.04
B^0	$\frac{z_{D^0\ \text{vertex}} - z_{V\ \text{vertex}}}{\sqrt{\sigma^2_{z,\ D^0\ \text{vertex}} + \sigma^2_{z,\ V\ \text{vertex}}}} > -2$	5.38 ± 0.03	6.58 ± 0.07	6.72 ± 0.04
B^0	$\min_{\text{PVs}} \chi^2_{\text{IP}} < 9$	5.17 ± 0.03	6.33 ± 0.07	6.48 ± 0.03
B^0	$\left(\chi^2/n_{\text{D.O.F.}}\right)_{\text{vertex}} < 4$	4.94 ± 0.03	6.10 ± 0.07	6.22 ± 0.03
B^0	$\cos$ (Dir. Angle wrt own PV) > 0.99995	4.67 ± 0.03	5.73 ± 0.07	5.82 ± 0.03
D^0	$\left\lvert m^{\text{reconstructed}}_{D^0} - m^{\text{PDG}}_{D^0} \right\rvert < 20$ MeV/c^2	4.50 ± 0.03	5.55 ± 0.07	5.61 ± 0.03

Table V.15: Summary of the cumulative selection efficiencies (number of selected events with respect to the total number of generated events in the acceptance) on Monte Carlo in percent. These numbers include the reconstruction and the stripping efficiencies.

b hadron	fraction at Z^0	combined with $p\overline{p}$
B^+, B^0	40.2 ± 0.9 %	39.9 ± 1.1 %
B^0_s	10.5 ± 0.9 %	11.1 ± 1.2 %
b hadron	9.1 ± 1.5 %	9.2 ± 1.9 %

Table V.16: Fractions of weakly-decaying b hadron species produced in $Z^0 \to b\overline{b}$ decays and in $p\overline{p}$ collisions at $\sqrt{s} = 1.8$ TeV [38]. The ratio of fragmentation fractions $\frac{f_d}{f_s} = 3.71 \pm 0.47$ is taken from [44]. The value $\frac{f_d}{f_s} = 3.75 \pm 0.29$ from LHCb measurements is used in this analysis.

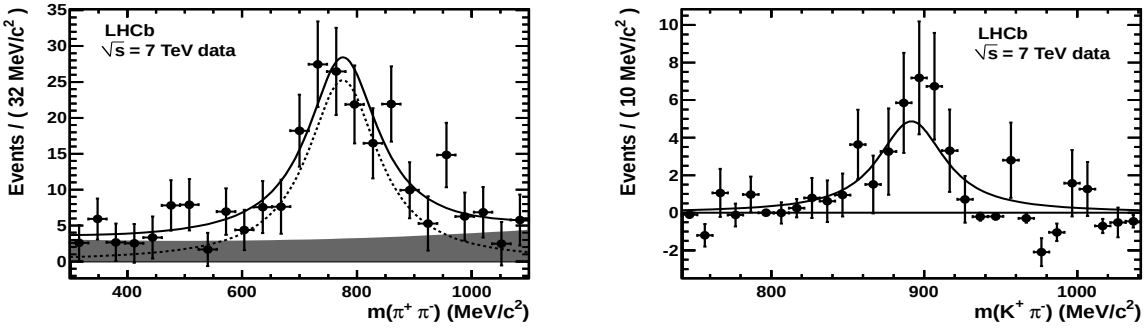

Figure V.42: ρ^0 (on the left) and K^{*0} (on the right) invariant mass distributions obtained on data, using the sPlot technique. The level of non K^{*0} combinations in the $\overline{B}{}^0_s \to D^0 K^{*0}$ peak is clearly extremely low. The $B^0 \to \overline{D}{}^0 \rho^0$ despite being mainly due to D^0 ρ^0 combinations contains a significant contribution of "non-ρ^0" events for which one should correct. The black points correspond to the data and the fit result is represented as a solid line. The resonant component is fitted with a Breit-Wigner convoluted with a Gaussian (dashed line) and the nonresonant part, if present, with a second-order polynomial (grey area).

$$\frac{\mathcal{B}\left(\overline{B}^0_s \to D^0 K^{*0}\right)}{\mathcal{B}\left(B^0 \to \overline{D}^0 \rho^0\right)} = \frac{1}{\mathcal{B}\left(K^{*0} \to K^+\pi^-\right)} \frac{f_d}{f_s} \tag{V.30}$$
$$\times \; r_{\text{acc.}}\, r_{\text{sel}}\, r_V\, r_{\text{PID}}\, r_{\texttt{OtherB}}\, r_{\texttt{LOHadronTOSOnly}}$$
$$\times \; \frac{N^{sig.}_{\overline{B}^0_s \to D^0 K^{*0}}}{r_{\texttt{OtherB}} N^{\texttt{LOHadronTOSOnly}}_{B^0 \to \overline{D}^0 \rho^0} + r_{\texttt{LOHadronTOSOnly}} N^{\texttt{OtherB}}_{B^0 \to \overline{D}^0 \rho^0}}$$

$$\text{where } r_{\text{acc}} = \frac{\epsilon^{B^0 \to \overline{D}^0 \rho^0}_{\text{acceptance}}}{\epsilon^{\overline{B}^0_s \to D^0 K^{*0}}_{\text{acceptance}}} = 0.955 \pm 0.004, \tag{V.31}$$

$$r_{\text{sel}} = \frac{\epsilon^{B^0 \to \overline{D}^0 \rho^0}_{\text{selection}}}{\epsilon^{\overline{B}^0_s \to D^0 K^{*0}}_{\text{selection}}} = 0.802 \pm 0.007, \tag{V.32}$$

$$r_V = \frac{\epsilon^{B^0 \to \overline{D}^0 \rho^0}_{V \text{ selection}}}{\epsilon^{\overline{B}^0_s \to D^0 K^{*0}}_{V \text{ selection}}} = 1.023 \pm 0.006, \tag{V.33}$$

$$r_{\text{PID}} = \frac{\epsilon^{B^0 \to \overline{D}^0 \rho^0}_{\text{PID}}}{\epsilon^{\overline{B}^0_s \to D^0 K^{*0}}_{\text{PID}}} = 1.092 \pm 0.014, \tag{V.34}$$

$$\text{and } r_{\texttt{LOHadronTOSOnly}} = \frac{\epsilon^{B^0 \to \overline{D}^0 \rho^0}_{\texttt{LOHadronTOSOnly}}}{\epsilon^{\overline{B}^0_s \to D^0 K^{*0}}_{\texttt{LOHadronTOSOnly}}} = 1.20 \pm 0.02, \tag{V.35}$$

$$r_{\texttt{OtherB}} = \frac{\epsilon^{B^0 \to \overline{D}^0 \rho^0}_{\texttt{OtherB}}}{\epsilon^{\overline{B}^0_s \to D^0 K^{*0}}_{\texttt{OtherB}}} = 1.03 \pm 0.03. \tag{V.36}$$

V.2.6 Systematic uncertainties

V.2.6.1 Ratio of trigger efficiencies

The relative abundances of `BdLOHadronTOSOnly` and `OtherB` triggered events measured on MC10 signal Monte Carlo are in good agreement with the one measured from data (see Tab. V.11). It gives some confidence in the description of the trigger in the Monte-Carlo. Since these relative abundances are directly measured on data, they do not enter in the systematic uncertainty evaluation. However the differences in trigger efficiency for the $B^0 \to \overline{D}^0 \rho^0$ and the $\overline{B}^0_s \to D^0 K^{*0}$ decay modes is taken from Monte-Carlo. Since we are not interested in the absolute values of these efficiencies, we only need to check if the difference due to the kinematic properties of the decays is well modelled in the Monte-Carlo. Using Monte Carlo events, instead of emulating the trigger with Moore, one requires that the highest transverse momentum of the four tracks exceeds 3.6 GeV/c (the trigger cut), and are able to check if the differences are indeed due to kinematics. The results are given in Tab. V.17 for various p_T cuts. The ratio of trigger efficiencies can be modelled using a simple cut on the highest transverse momentum of the 4 tracks. This allows one to study the effect of the hadronic trigger calibration. It has been shown

[118] that the hadronic trigger calibration is not yet perfectly set, Fig. V.43 is taken from this work. From it, one can conclude that a cut at $p_T > 3.6$ GeV/c at the trigger level corresponds in fact to a "real" cut at 4.2 GeV/c since the ratio of the transverse energy measured at the L0 level by the calorimeters is smaller by 14 % to the value obtained from the tracking system. If one applies this value, the ratio of efficiencies $\frac{\varepsilon_{B^0 \to \overline{D}^0 \rho^0}}{\varepsilon_{\overline{B}^0_s \to D^0 K^{*0}}}$ changes from 1.24 to 1.32 (i.e. 6.4 %). Increasing $r_{\texttt{L0HadronTOSOnly}}$ by 6.4 % changes the ratio of branching ratio by 2.9 % which will be assigned as the systematic uncertainty due to the triggering difference between the two decay modes.

	$\frac{\varepsilon_{B^0 \to \overline{D}^0 \rho^0}}{\varepsilon_{\overline{B}^0_s \to D^0 K^{*0}}}$	$\frac{\varepsilon_{B^0 \to D^0 K^{*0}}}{\varepsilon_{\overline{B}^0_s \to D^0 K^{*0}}}$
TCK 0x002e002a	1.22	0.94
TCK 0x001e0030	1.12	0.95
TCK 0x0019001f	1.11	0.96
$p_T > 4.2$ GeV/c	1.32	0.94
$p_T > 3.6$ GeV/c	1.24	0.94
$p_T > 2.6$ GeV/c	1.15	0.98
$p_T > 2.26$ GeV/c	1.10	0.98

Table V.17: Ratio of "trigger" efficiencies obtained on MC10 Monte Carlo. As expected the difference between the $B^0 \to \overline{D}^0 \rho^0$ and the $\overline{B}^0_s \to D^0 K^{*0}$ decay modes is more pronounced for higher p_T cuts.

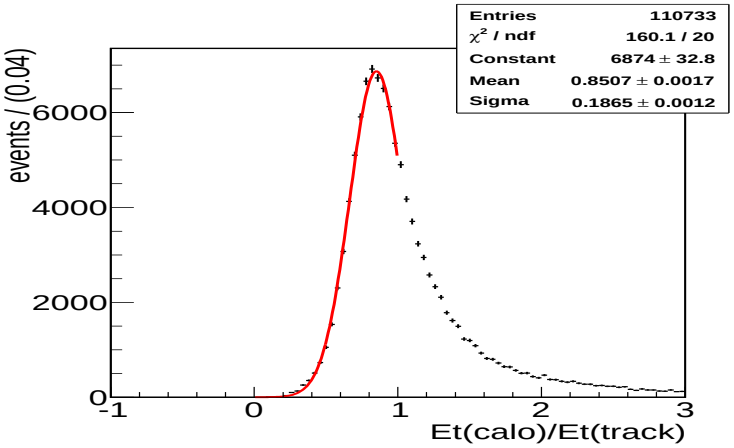

Figure V.43: Ratio of the transverse energy at the `L0Hadron` trigger level to the transverse momentum of the track. The tracks used are the pions from the D^0 decay of a large statistics calibration sample of prompt $D^* \to \pi D^0$ decays data sample.

V.2.6.2 Ratio of PID efficiencies

The data calibration sample has been reweighted using a binning scheme of $32 \times 4 \times 4$ bins in momentum, pseudo rapidity and number of tracks, following the Monte Carlo distributions. The

systematic uncertainty has been assigned using the kinematical distributions directly obtained from the data as well as by varying the binning scheme. Due to the small signal yield in the B^0_s case, this systematic uncertainty suffers from large statistical fluctuations which directly translate into a large systematic uncertainty on the kaon identification.

V.2.6.3 Ratio of selection efficiencies and data/Monte Carlo agreement

The two selections differ by the transverse momentum cut on the vector tracks, the invariant mass cut on the vector particle and the helicity cuts. These two last cuts should be well described by the Monte Carlo however the central value could be a bit different in simulation and real data and we estimate a systematic uncertainty by varying the central value of the cut on the mass window of the vector mesons. Changing 775.49 MeV/c^2 by 767 MeV/c^2 for the ρ^0 (according to Fig. V.22) and 891.66 MeV/c^2 by 898 MeV/c^2 for the K^{*0} (according to Fig. V.21) gives respectively a change of 0.3 % and 0.7 % (we assume these systematic uncertainties fully correlated). In addition there is 0.6 % statistical uncertainty on the ratio of efficiencies. We thus assign 1.2 % efficiency on the ratio of efficiencies for the vector mass and helicity cut.

Moreover the momentum and transverse momentum of the B mesons could be different in data and Monte-Carlo, and this would translate into a small shift in the ratio of efficiencies. We observe on Fig. V.44 that the p_T distribution is shifted by 10 % towards lower values in the data. Thus translating the $p_T > 300$ MeV/c cut on the vector daughters tracks by $p_T > 330$ MeV/c we obtain an estimate of the systematic uncertainty related to data/Monte Carlo discrepancy for the description of transverse momentum. It turns out that the ratio of efficiencies decreases by 2.5 %.

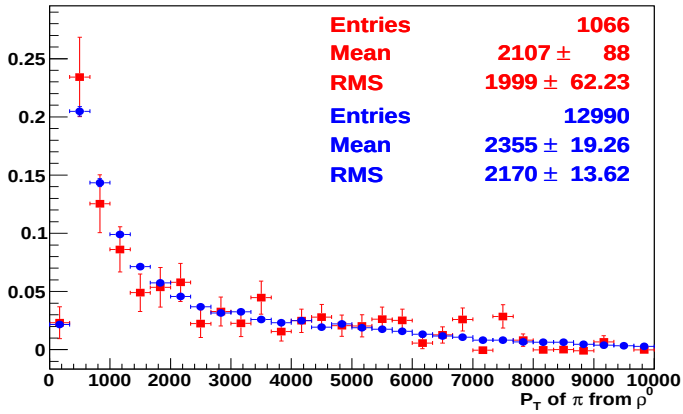

Figure V.44: Transverse momentum distribution for the ρ^0 daughters (π^+ and π^- are added) using the sPlot technique on real data (red distribution) and Monte Carlo (blue distribution).

V.2.6.4 Systematic uncertainties from the fit

The systematic uncertainty associated with the shape used for the background parametrization has been evaluated enlarging the B mass window down to 5000 MeV for the $B^0 \to \overline{D}{}^0\rho^0$ selection and to 5090 MeV for the $\overline{B}{}^0_s \to D^0 K^{*0}$ one, using a single Gaussian to describe the partially reconstructed backgrounds and a linear shape for the description of the combinatorial background (the slope in $D^0 K^{*0}$ is still fixed since the fit founds a result compatible with a flat distribution with big errors), see Figs. V.45-V.46.

The estimation of the systematic uncertainty is then performed by generating 1000 toy Monte Carlo events with this alternative shape and fitting with the *standard* parametrization of the invariant mass used for the fit to extract the yields. The number of generated signal events is respectively 35 and 159 in $\overline{B}{}^0_s \to D^0 K^{*0}$ and $B^0 \to \overline{D}{}^0\rho^0$. The number of fitted signal events follow Gaussian distributions with respectively means and widths of $\mu = 32.67 \pm 0.22$, $\sigma = 6.83 \pm 0.16$ for $\overline{B}{}^0_s \to D^0 K^{*0}$ and $\mu = 147.1 \pm 0.5$, $\sigma = 15.28 \pm 0.35$ for $B^0 \to \overline{D}{}^0\rho^0$, see Fig. V.47. The corresponding relative change in the ratio of events is thus of $+0.95 \pm 0.77$ %, and we assign 1 % of systematic uncertainties due to the parametrisation of the shape.

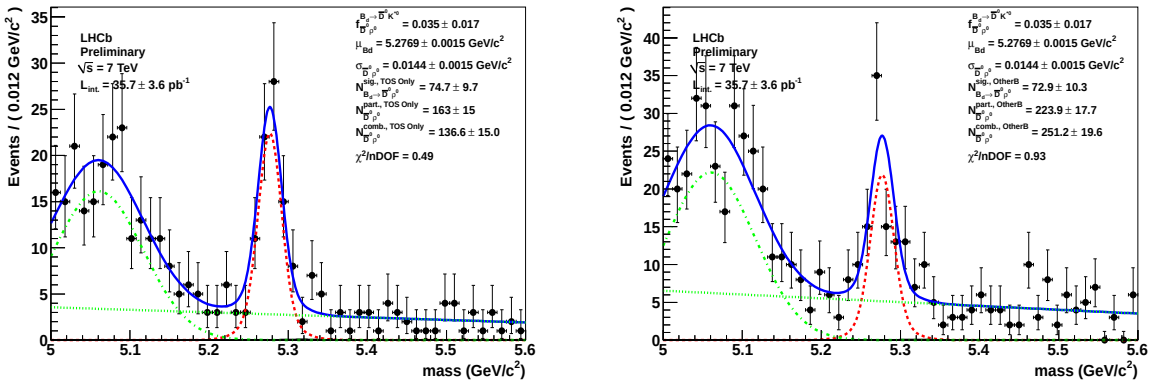

Figure V.45: Result of the fit for the $B^0 \to \overline{D}{}^0\rho^0$ categories. The signal is clearly visible on the two figures corresponding to the two trigger categories (`L0HadronTOSOnly` on the left and `OtherB` on the right). The black points correspond to the data and the fit result is represented as a solid blue line. The signal is fitted with a double Gaussian (dashed red line), the partially reconstructed with a wide Gaussian function (green dash-dotted line) and the combinatorial background with a linear distribution (dashed green line) as explained in the text. Contributions from cross-feed are plotted in thin solid black lines.

V.2.6.5 Systematic on the non-resonant contribution

The statistical uncertainty obtained on the number of *non*-ρ^0 events present in the ρ^0 the mass window (± 150 MeV/c^2) has been propagated in the systematical uncertainty. It gives 6.8 %.

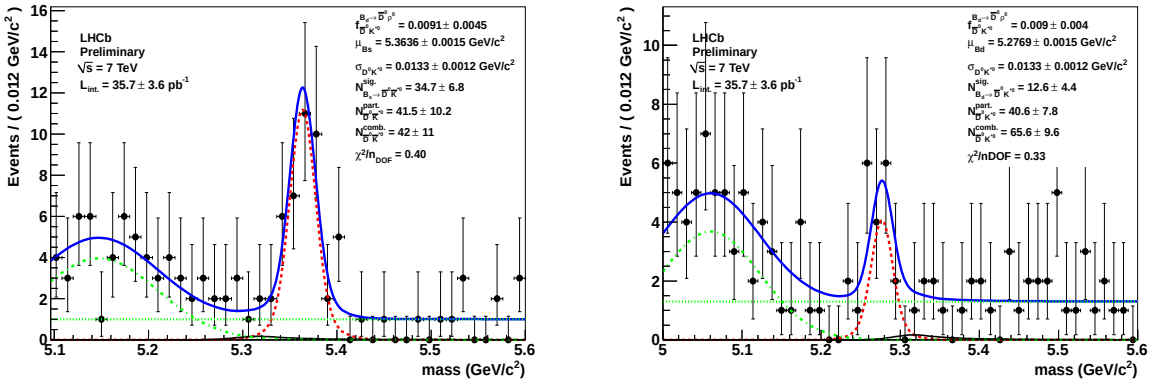

Figure V.46: Result of the fit for the $D^0 K^{*0}$ categories. The signal is clearly visible on the two figures corresponding to the two trigger categories (`D0Kstar OppositeSign` on the left and `D0Kstar SameSign` on the right). The black points correspond to the data and the fit result is represented as a solid blue line. The signal is fitted with a double Gaussian (dashed red line), the partially reconstructed with a wide Gaussian (green dash-dotted line) and the combinatorial background with a flat distribution (dashed green line) as explained in the text. Contributions from cross-feed are plotted in thin solid black lines.

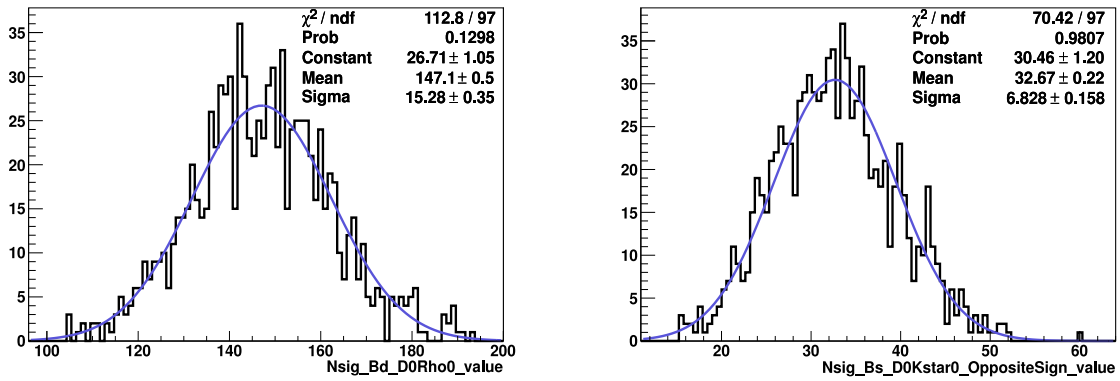

Figure V.47: The distribution of the fitted number of events with the standard parametrization if the events are generated with the alternative parametrization of the invariant mass PDF. 35 and 159 events were respectively generated in $\overline{B}{}^0_s \to D^0 K^{*0}$ and $B^0 \to \overline{D}{}^0 \rho^0$. The change $+0.95 \pm 0.77$ % in the ratio of events is compatible with zero.

V.2.6.6 Systematic uncertainty due to hadronisation

The error on the ratio of fragmentation fractions $\frac{f_d}{f_s} = 3.75 \pm 0.29$ will be used as a systematic uncertainty.

V.2.7 Summary of the systematic uncertainties

The list of the contribution to the systematic uncertainties is given in Tab. V.18, and shows that the dominant contributions are coming from the non-ρ^0 contribution and the estimation of PID efficiencies.

source of the uncertainty	σ_R/R
MC statistics on acceptance ($r_{\text{acceptance}} = 0.955 \pm 0.004$)	0.4 %
MC statistics of overall selection	1.0 %
change in central value of mass window for $r_{\text{V}} = 1.023 \pm 0.010$	1.0 %
p_T distributions of tracks data vs MC $r_{\text{sel.}} = 0.802 \pm 0.020$	2.5 %
Difference between data and MC to compute $r_{\text{PID}} = 1.09 \pm 0.06$	5.8 %
L0 Hadron threshold influence on $r_{\texttt{L0HadronTOSOnly}} = 1.20 \pm 0.08$	3.0 %
`OtherB` trigger efficiency independent of the mode $r_{\texttt{OtherB}} = 1.03 \pm 0.03$	1.6 %
PDF parametrization	1.0 %
statistical uncertainty on the non-ρ^0 component (30.1 ± 7.9)	6.8 %
total uncertainty	10.2 %
$\frac{f_d}{f_s} = 3.75 \pm 0.29$	7.9 %

Table V.18: Summary of the contributions to the systematic uncertainty. σ_R/R stands for the resulting uncertainty on the overall correction applied on the calculation the ratio of branching fractions.

V.2.8 Final result

In 36 pb^{-1} of pp collisions at a centre-of-mass energy $\sqrt{s} = 7$ TeV, we observed for the first time the decay $\overline{B}^0_s \to D^0 K^{*0}$. A clear signal of 34.5 ± 6.9 events is obtained with a statistical significance over 9 standard deviations (according to the change in likelihood when forcing the $\overline{B}^0_s \to D^0 K^{*0}$ to be zero) and we measure its branching ratio relative to the $B^0 \to \overline{D}^0 \rho^0$ branching ratio: $\frac{\mathcal{B}\left(\overline{B}^0_s \to D^0 K^{*0}\right)}{\mathcal{B}\left(B^0 \to \overline{D}^0 \rho^0\right)} = 1.48 \pm 0.34\ (\text{stat}) \pm 0.15\ (\text{syst}) \pm 0.12\,(f_d/f_s)$, where the first uncertainty is statistical, the second systematic and the third is the uncertainty on the ratio of fragmentation fractions f_d/f_s. The number of $B^0 \to \overline{D}^0 K^{*0}$ is 12.1 ± 4.5 which corresponds to a statistical significance of 3.2 standard deviation from the change of likelihood, corresponding to a first evidence for this decay mode. Using the PDG value [38] for the branching fraction of the normalising decay $B^0 \to \overline{D}^0 \rho^0$ $(3.2 \pm 0.5) \times 10^{-4}$, gives a measurement of the $\overline{B}^0_s \to D^0 K^{*0}$ branching fraction: $\mathcal{B}\left(\overline{B}^0_s \to D^0 K^{*0}\right) = (4.72 \pm 1.07 \pm 0.48 \pm 0.37 \pm 0.74) \times 10^{-4}$ where the first uncertainty is statistical, the second systematic, the third due to the hadronisation fraction

(f_d/f_s) and the last is due to the uncertainty of the $B^0 \to \overline{D}^0\rho^0$ branching fraction. This result is in agreement, within large uncertainties, with theoretical and phenomenological predictions [95, 97, 99].

V.3 Conclusion and perspectives for 2011

V.3.1 Data versus Monte Carlo comparison

V.3.1.1 $B^0 \to \overline{D}^0\rho^0$ yield

The number of expected $B^0 \to \overline{D}^0\rho^0$ in the 2010 data sample using the measured $b\overline{b}$ cross-section, the Monte Carlo efficiencies for the trigger and the selection (except for the PID for which we use the calibrated efficiencies) and the PDG values of the branching fractions is $N_{B^0 \to \overline{D}^0\rho^0 \text{expected}} = 186.7 \pm 31.2$ (cross-section) ± 29.3 (branching fractions), where the other uncertainties (selection efficiencies and f_d value are negligible). This expected number is slightly larger than the observed 124.4 ± 14.3 (stat.) $\pm$ 7.9 (non ρ^0 contribution). These two values are compatible within 1.4 standard deviations.

V.3.1.2 Combinatorial background

Given the accumulated statistics and the number of background events in $B_{d,s} \to DK^{*0}$, it is difficult to provide a precise check of the Monte Carlo prediction made in chapter IV for the background level. Using the number of fitted signal B^0 and B^0_s events and interpolating the number of background events in a $\pm 3\sigma_{D^0K^{*0}}$ mass window, we obtain $\frac{S_{B^0 \to \overline{D}^0 K^{*0}}}{B} = 1.0 \pm 0.4$ and $\frac{S_{B^0_s \to \overline{D}^0 \overline{K}^{*0}}}{B} = 5.7 \pm 1.9$. The expected value is $\frac{S}{B}_{B^0 \to \overline{D}^0 K^{*0}} = 3.3 \pm 1.0$, for which the uncertainty is only the statistical uncertainty of the background estimation. The observed value is smaller than the expected value by 2.1σ.

V.3.1.3 Partially reconstructed background

Assuming that all the partially reconstructed background in the `D0Kstar OppositeSign` category is due to partially reconstructed $B^0_s \to \overline{D}^{*0}\overline{K}^{*0}$ background, it is possible, using the parametrization of chapter IV to give an rough estimate of the number of events for each of the $B^0_s \to \overline{D}^{*0}\overline{K}^{*0}$ decays. The fraction of $B^0_s \to \overline{D}^{*0}\overline{K}^{*0}$ with $D^{*0} \to D^0\pi^0$ events in the $[5.19\ \text{GeV}/c^2, 5.60\ \text{GeV}/c^2]$ B invariant mass window is 13 % while the fraction of $D^{*0} \to D^0\gamma$ events in the B invariant mass window is 43 %. We also take into account for the difference in selection efficiencies taken from chapter IV. With the known PDG [38] branching fractions for the two D^{*0} sub-decays, one obtains $N_{B^0_s \to \overline{D}^{*0}\overline{K}^{*0} with D^{*0} \to D^0\pi^0} = 6.95 \pm 4.13$ and $N_{B^0_s \to \overline{D}^{*0}\overline{K}^{*0} with D^{*0} \to D^0\gamma} = 11.85 \pm 7.06$ in the $[5.19\ \text{GeV}/c^2, 5.60\ \text{GeV}/c^2]$ range, where the uncertainty is only accounting for the statistical uncertainty on the number of fitted partially reconstructed background events. This provides a

different estimate of the level of the partially reconstructed $B^0_s \to \overline{D}{}^{*0}\overline{K}{}^{*0}$ background than the upper limits provided in chapter IV, and will be used for the extrapolation for the 2011 running.

V.3.2 Extrapolation for 2011

Assuming similar conditions (trigger and selection efficiencies) for 2010 and 2011 LHC run and a total integrated luminosity of 1 fb^{-1}, the extrapolated number of events is given in table Tab. V.19. The partially reconstructed background in calculated using the efficiencies of the mass window cut estimated in chapter IV. These extrapolated numbers are in fair agreement with those quoted in chapter IV, which gives some confidence that the numbers stated in chapter IV can be seriously taken into account for the toy Monte Carlo study of chapter IV.

decay mode	number of events extrapolated to 1 fb^{-1}
$B^0_s \to \overline{D}{}^0\overline{K}{}^{*0}$	958 ± 192
$B^0 \to \overline{D}{}^0 K^{*0}$	336 ± 125
$B^0_s \to \overline{D}{}^{*0}\overline{K}{}^{*0}$ with $D^{*0} \to D^0\gamma$	203 ± 121
$B^0_s \to \overline{D}{}^{*0}\overline{K}{}^{*0}$ with $D^{*0} \to D^0\pi^0$	1.8 ± 1.1

Table V.19: Extrapolated number of events in the B mass window for 1 fb^{-1}, the errors are only statistical uncertainties from the 36 pb^{-1} measurement. These numbers are compatible with the Monte Carlo prediction of the chapter IV.

V.3.3 Conclusion

The first observation of $B^0_s \to \overline{D}{}^0\overline{K}{}^{*0}$ and an evidence of $B^0 \to \overline{D}{}^0 K^{*0}$ decay modes has been made with the first 36 pb^{-1} of the LHCb data taking. The branching fraction of $B^0_s \to \overline{D}{}^0\overline{K}{}^{*0}$ has been measured relative to the $B^0 \to \overline{D}{}^0\rho^0$ decay mode, and is found to be compatible (within large uncertainties) with theoretical and phenomenological predictions. Extrapolating these numbers for the 2011 running gives numbers in agreement with those expected from the previous Monte Carlo study, detailed in chapter IV. With the 2011 running a measurement of the $B^0_s \to \overline{D}{}^0\overline{K}{}^{*0}$ relatively to the $B^0 \to \overline{D}{}^0 K^{*0}$ decay mode can be performed and will be dominated by the systematic uncertainty from the fragmentation fractions. More interesting, a first competitive measurement of γ can be performed with the 2011 data sample, as shown in chapter IV.

Conclusion

> - Oh oui oui, c'est magnifique, oui, oui... il y a des tâches, c'est tout barré, j'ai tellement raturé que j'ai transpercé le papier... c'est immonde... on dirait que j'ai lavé par terre avec, mais c'est fait...
>
> Jean-Robert Lombart alias *Père Blaise*
> in *Enluminures*, **Kaamelott, Livre I**, Tome 2, Épisode 1,
> écrit par Alexandre Astier.

Two different subjects have been treated in this thesis. First an energy flow technique has been developed and studied in details, both on Monte Carlo and real data collisions recorded in 2010 and 2011. The corresponding calibration constants extracted from data have been applied in the database as a prior for the fine π^0 calibration procedure. The method has also been extended (and the obtained constants applied in the database) to provide further inter-calibration of the cells up to a level of 1.5 %, to which the π^0 calibration was not sensitive, and with systematic biases controlled at the percent level. These results have been widely used by the collaboration to produce physics results with the reprocessing of 2010 data and the 2011 data. The energy flow technique was demonstrated to be an efficient tool for cross-checks of the LED monitoring system and the fine π^0 calibration.

Realistic expectations for the measurement of γ with the LHCb detector in the $B^0 \to D^0 K^{*0}$ channel, with the use of various D decays ($D^0 \to K^\pm\pi^\mp$, $D^0 \to K^\pm\pi^\mp\pi^0$ and $D^0 \to K^\pm\pi^\mp\pi^+\pi^-$) are detailed together with the road to γ. With a pure ADS method the fit is shown to be rather poorly constrained, allowing an approximate 25° precision on γ with 5 fb^{-1} of collisions recorded by the LHCb detector at $\sqrt{s} = 7$ TeV. This result is expected to be improved by adding constraints from GLW decay modes ($D^0 \to K^\pm K^\mp$ and $D^0 \to \pi^\pm\pi^\mp$).

A potential background to the suppressed $B^0 \to D^0 K^{*0}$ decay is expected to come from partially reconstructed $B_s^0 \to \overline{D}^{*0}\overline{K}^{*0}$ decays, which are Cabibbo favoured. However the $B_s^0 \to \overline{D}^0\overline{K}^{*0}$ was never observed before and its measurement is an important step towards a γ determination.

The first observation of this decay was thus performed with the data sample recorded in 2010 by the LHCb detector with the background only hypothesis rejected at more than 9 statistical standard deviations. The branching fraction measurement is performed relatively to the $B^0 \to \overline{D}^0\rho^0$ decay and remains statistically dominated despite of several important systematic

uncertainties on the ratio of hadronisation fractions, the contribution of non-ρ^0 contribution in the $B^0 \to \overline{D}^0\rho^0$ peak and the PID efficiencies (by order of importance). The final result is

$$\frac{\mathcal{B}\left(\overline{B}^0_s \to D^0 K^{*0}\right)}{\mathcal{B}\left(B^0 \to \overline{D}^0\rho^0\right)} = 1.47 \pm 0.34\ (\text{stat}) \pm 0.17\ (\text{syst}) \pm 0.19\,(f_d/f_s)$$

which can be translated in a measurement of

$$\mathcal{B}\left(\overline{B}^0_s \to D^0 K^{*0}\right) = (4.72 \pm 1.07 \pm 0.53 \pm 0.60 \pm 0.74) \times 10^{-4}$$

where the first uncertainty is statistical, the second systematic, the third due to the hadronisation fraction (f_d/f_s) and the last is due to the uncertainty of the $B^0 \to \overline{D}^0\rho^0$ branching fraction. This result is found to be in agreement with theoretical predictions, within large uncertainties.

Appendix A

Appendix

Contents

A.1 Toy Monte Carlo studies

A.1.1 Pulls with fixed slope in D0Kstar0

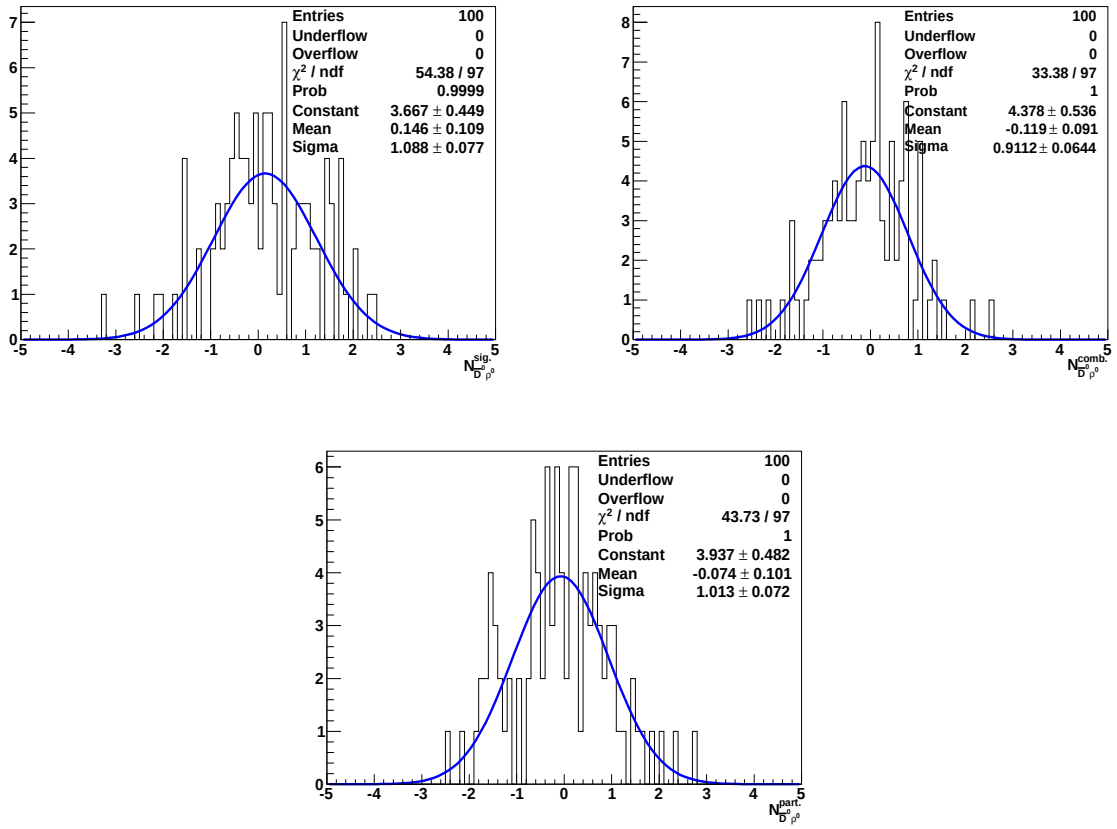

Figure A.1: Pulls of the yields (signal on the top left, combinatorial background on the top right and partially reconstructed background on the bottom) of D0Rho0 categories in the fitting range (with $c^{\text{part.}}_{D^0K^{*0}}$ fixed).

A.1.2 Comparison of pulls and differences

In Figs. A.4-A.9 we compare the pull distributions and the difference between the fitted and the generated value for all free parameters in the fit.

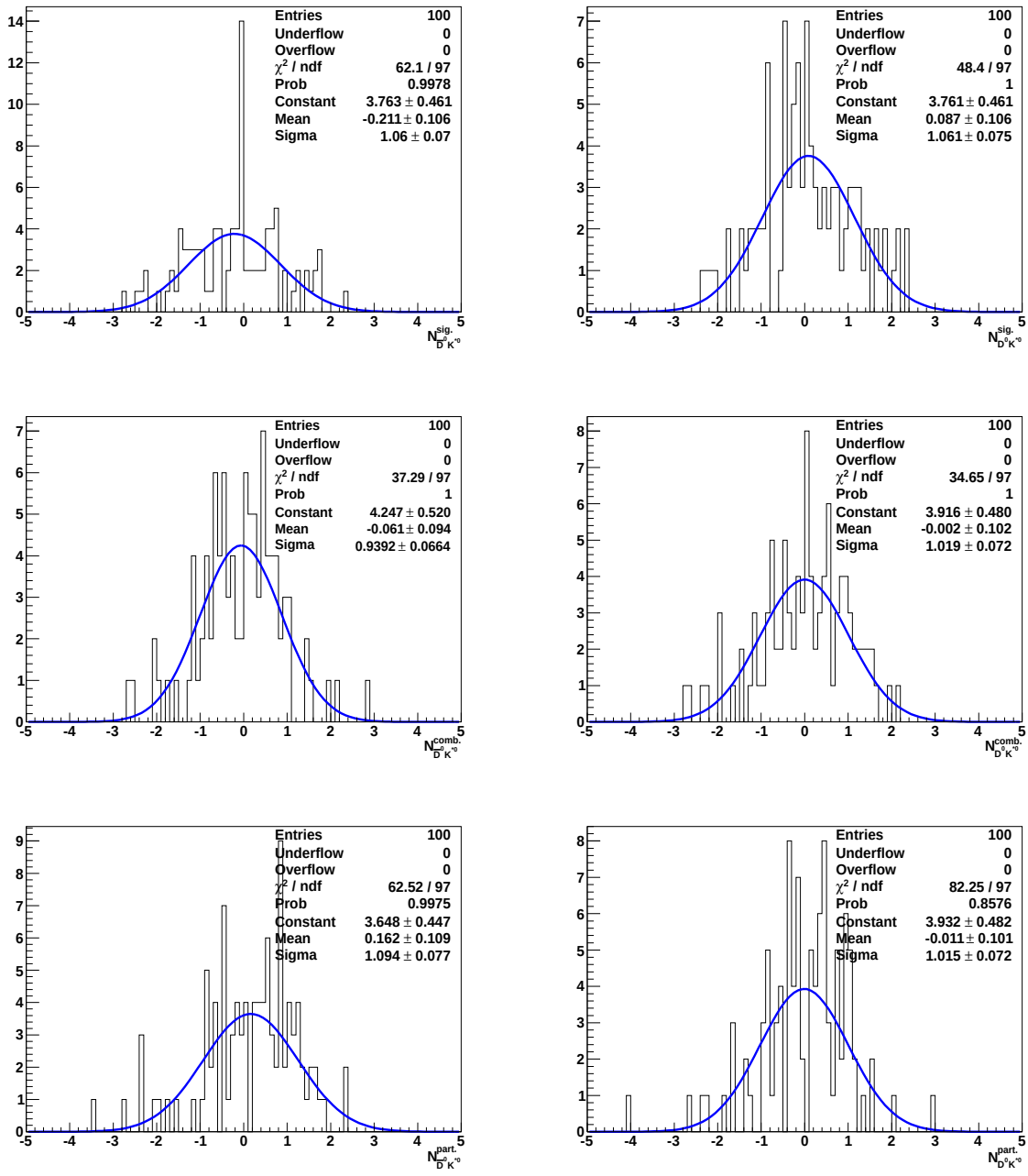

Figure A.2: Pulls of the yields (signal on the top, combinatorial background on the middle and partially reconstructed on the bottom) of the `D0Kstar0` categories (`D0Kstar SameSign` on the left, `D0Kstar OppositeSign` on the right) in the fitting range (with $c^{\text{part.}}_{D^0K^{*0}}$ fixed).

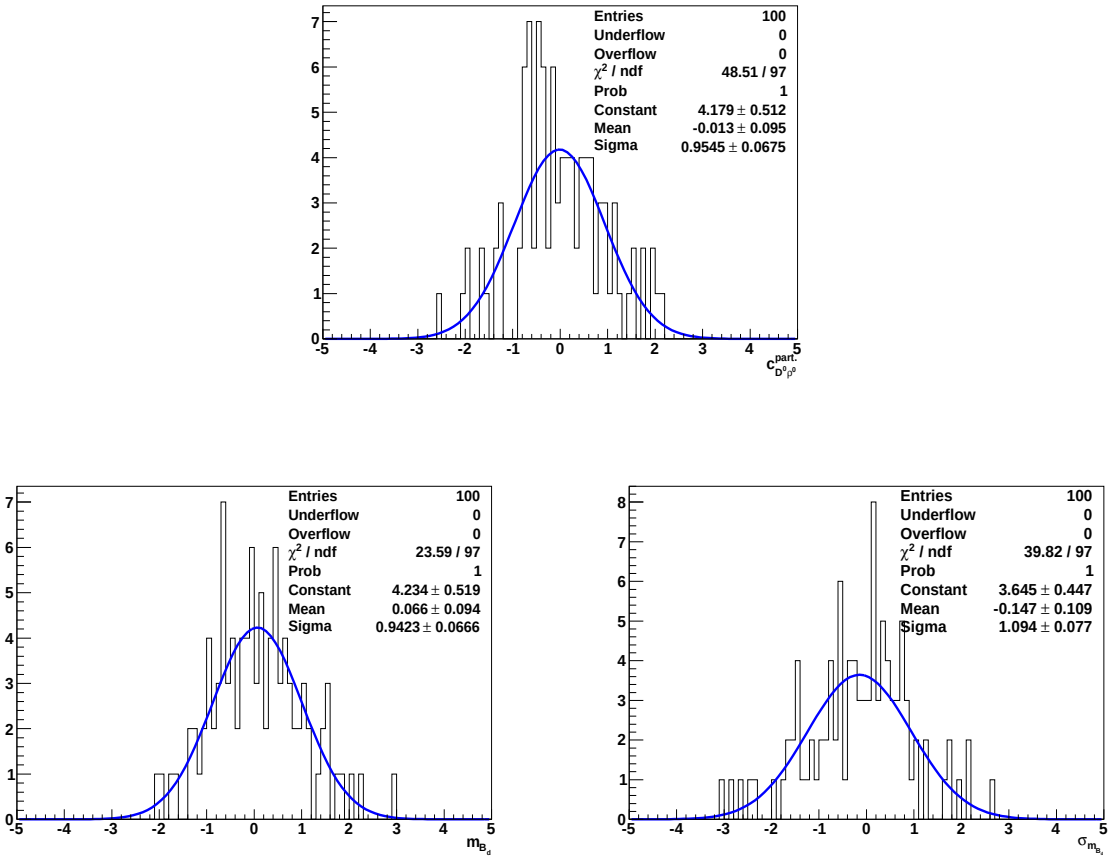

Figure A.3: Pulls of the shape parameters (with $c^{\text{part.}}_{D^0K^{*0}}$ fixed).

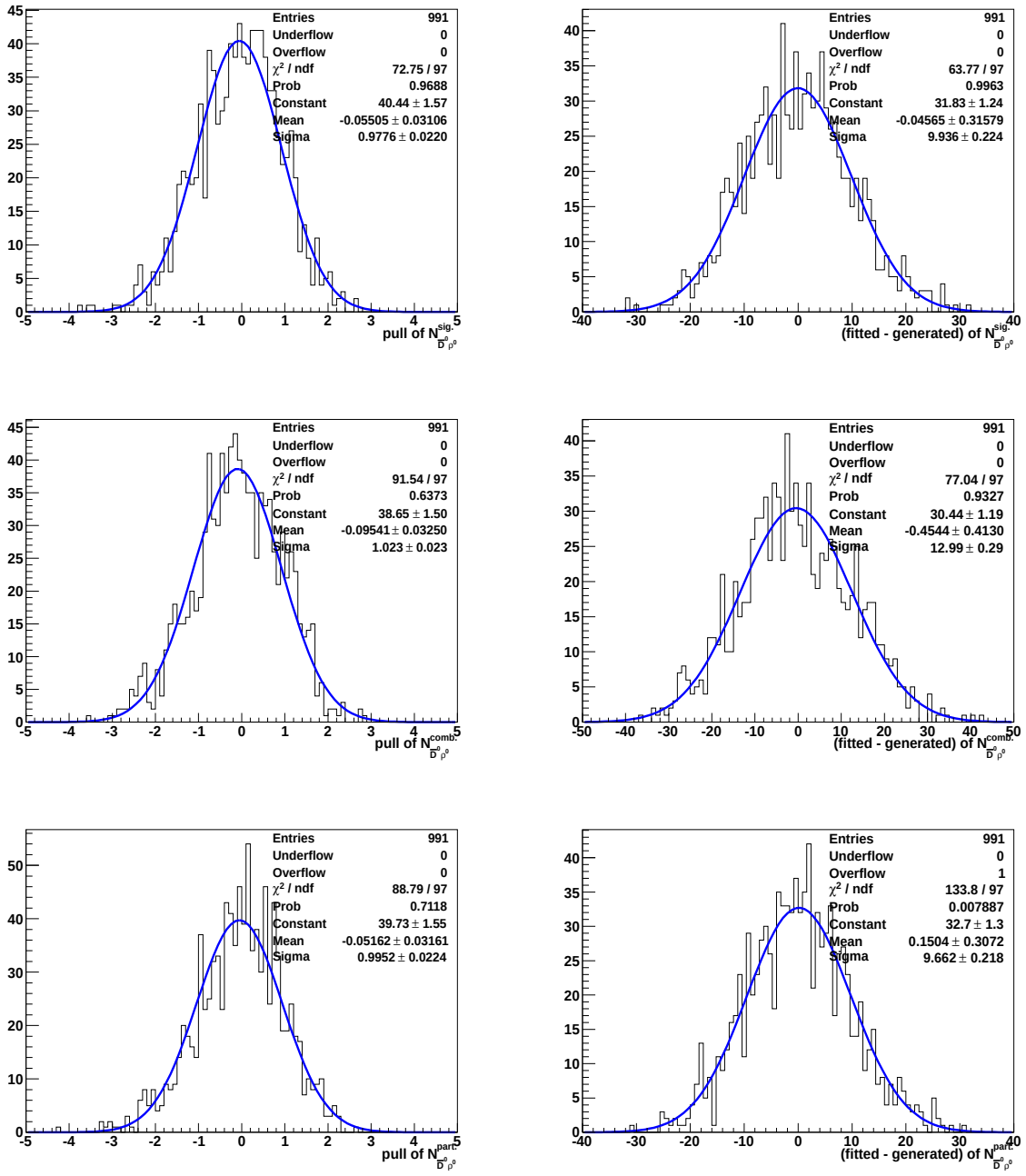

Figure A.4: Pulls (on the left) and difference between fitted and generated values (on the right) of the yields (signal on the top, combinatorial background on the middle and partially reconstructed background on the bottom) in the `D0Rho0 L0HadronTOSOnly` category in the fitting range (with $c^{\text{part.}}_{D^0K^{*0}}$ free).

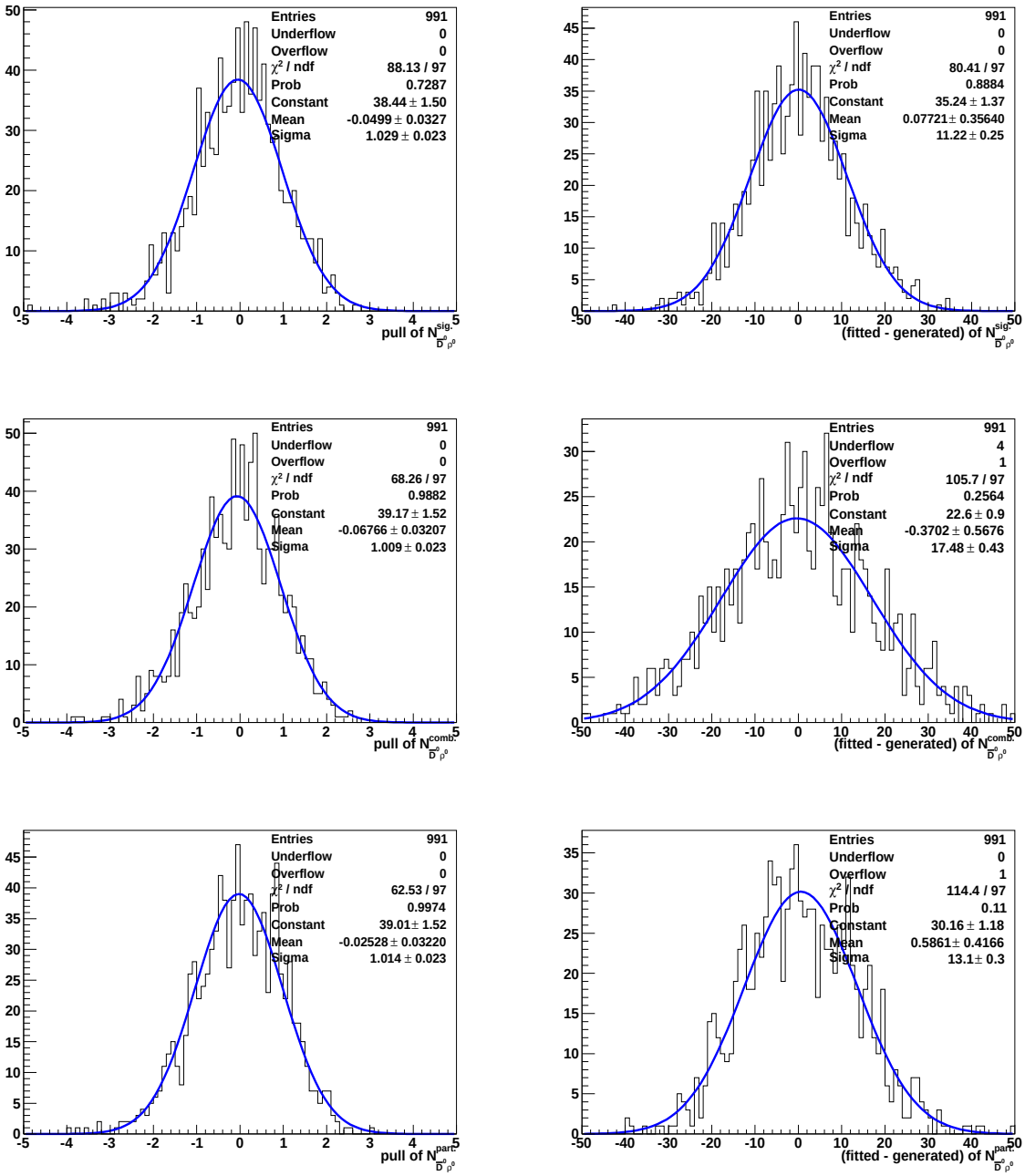

Figure A.5: Pulls (on the left) and difference between fitted and generated values (on the right) of the yields (signal on the top, combinatorial background on the middle and partially reconstructed background on the bottom) in the `D0Rho0 OtherB` category in the fitting range (with $c^{\text{part.}}_{D^0 K^{*0}}$ free).

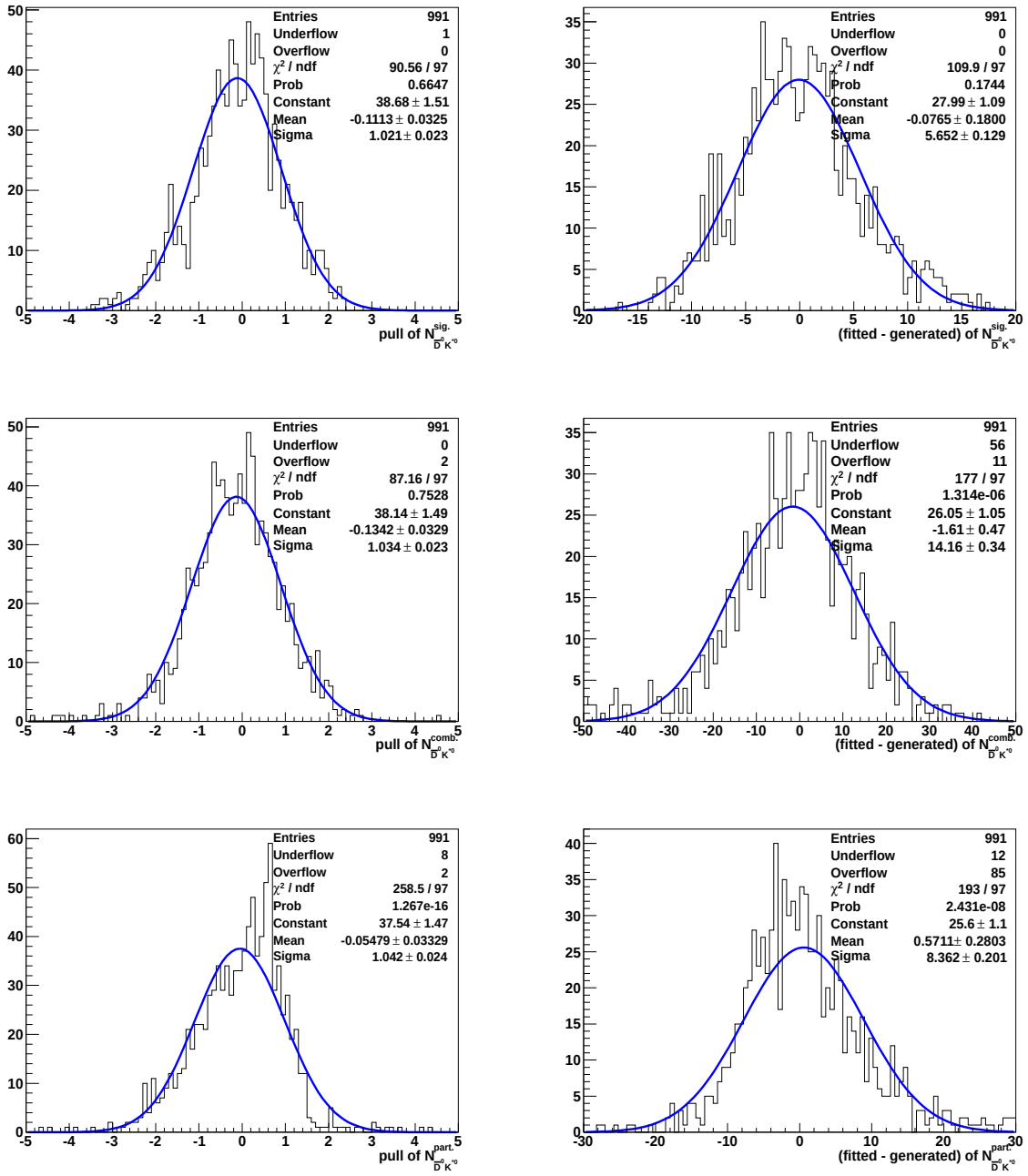

Figure A.6: Pulls (on the left) and difference between fitted and generated values (on the right) of the yields (signal on the top, combinatorial background on the middle and partially reconstructed background on the bottom) in the `D0Kstar SameSign` category in the fitting range (with $c^{\text{part.}}_{D^0K^{*0}}$ free).

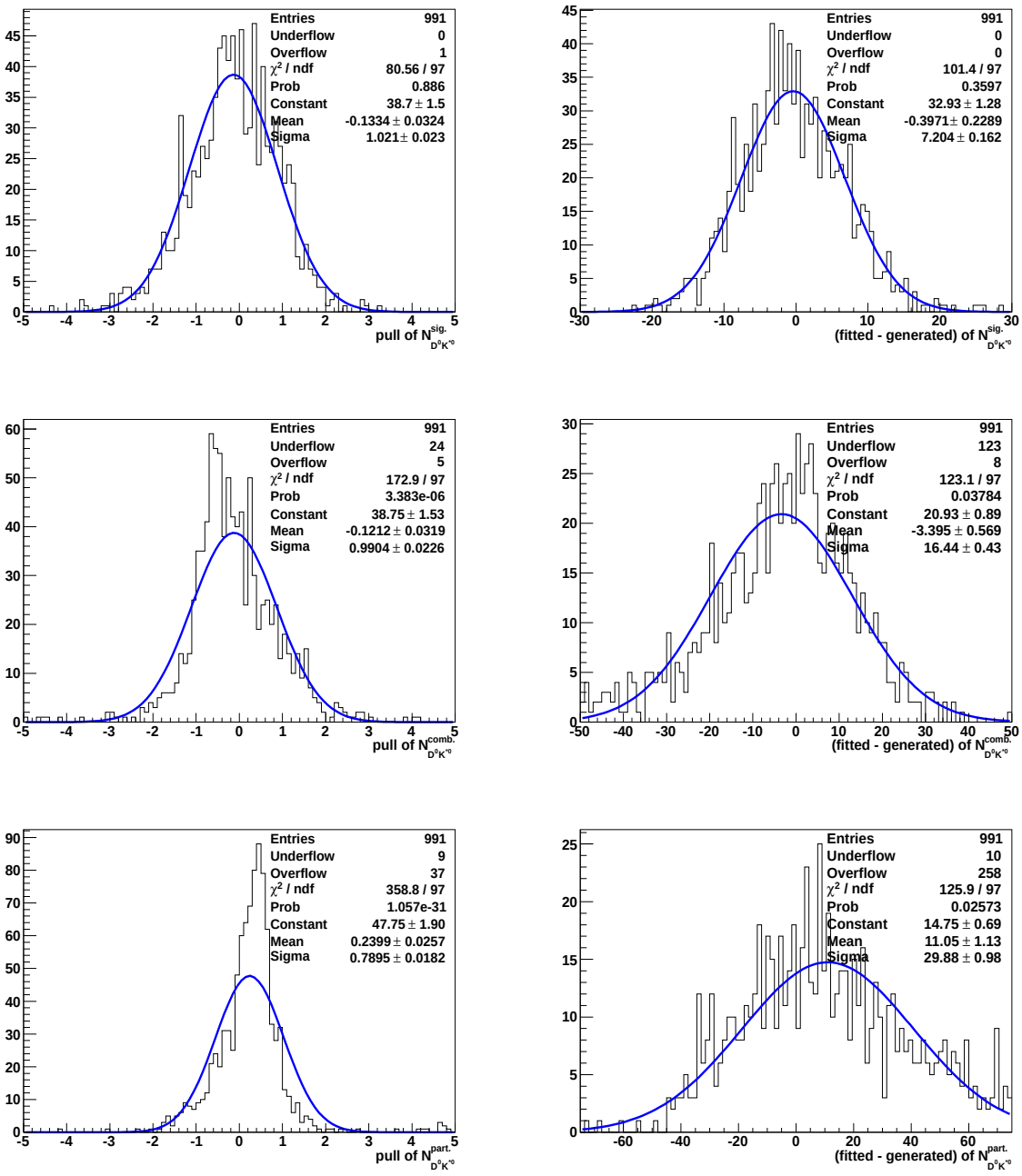

Figure A.7: Pulls (on the left) and difference between fitted and generated values (on the right) of the yields (signal on the top, combinatorial background on the middle and partially reconstructed background on the bottom) in the `D0Kstar OppositeSign` category in the fitting range (with $c^{\mathrm{part.}}_{D^0K^{*0}}$ free).

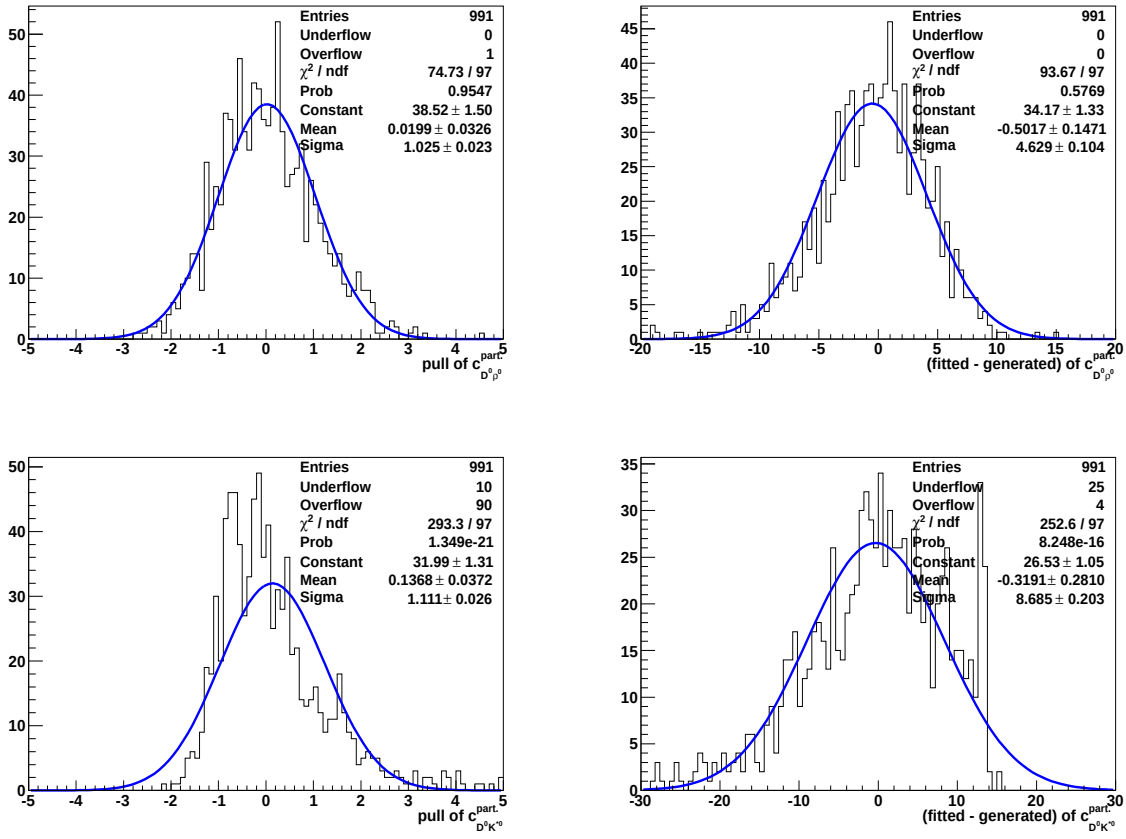

Figure A.8: Pulls (on the left) and difference between fitted and generated values (on the right) of the shape parameters for the partially reconstructed background (`D0Rho0` on the top, `D0Kstar0` on the bottom).

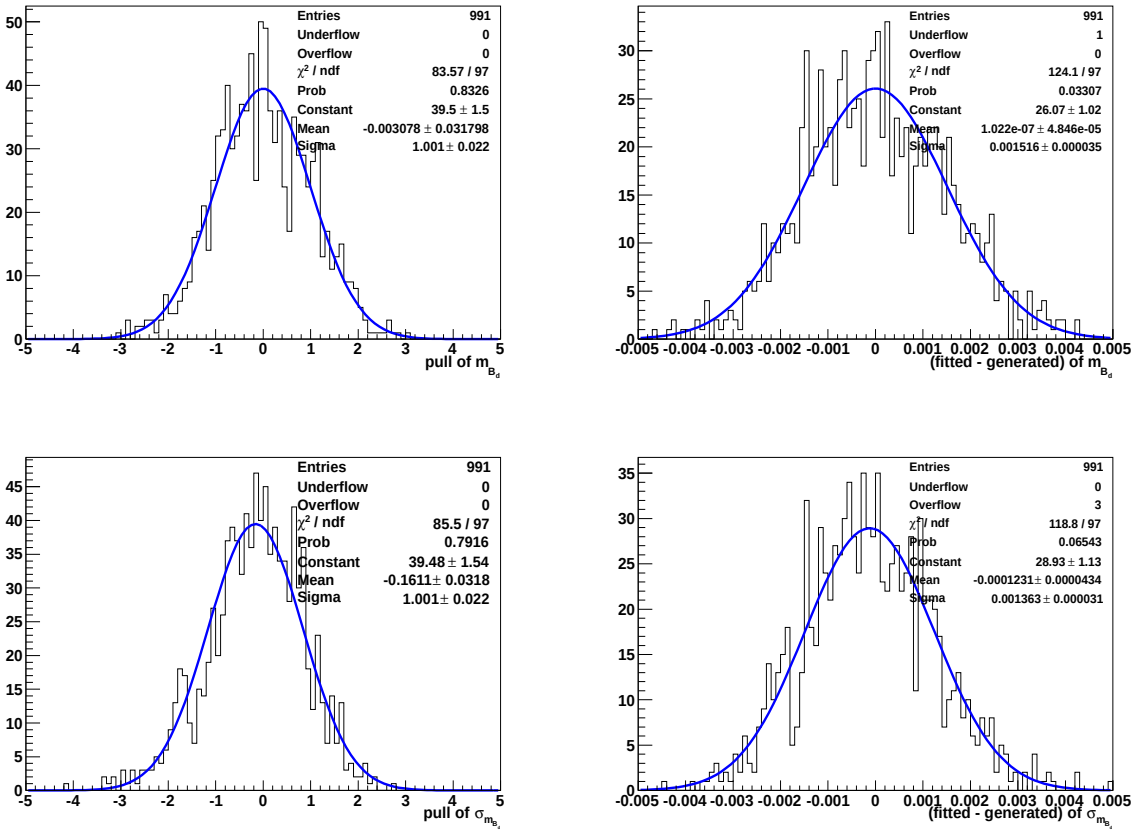

Figure A.9: Pulls (on the left) and difference between fitted and generated values (on the right) of the shape parameters for the signal (mean on the top, sigma on the bottom).

Bibliography

[1] C. M. G. Lattes, H. Muirhead, G. P. S. Occhialini, and C. F. Powell. *Processes involving charged mesons.* Nature **159**, 694–697 (1947).

[2] G. D. Rochester and C. C. Butler. *Evidence for the existence of new unstable elementary particles.* Nature **160**, 855–857 (1947).

[3] A. Pais. *Some Remarks on the V-Particles.* Phys. Rev. **86**, 663–672 (1952).

[4] L. Leprince-Ringuet and M. Lhéritier. *Existence probable d'une particle de masse 900 m_0 dans le rayonnement cosmique.* Comptes Rendus de l'Académie des Sciences **219**(618) (june 1944), Gallica:1944.219.618.

[5] M. Gell-Mann. *Isotopic Spin and New Unstable Particles.* Phys. Rev. **92**, 833–834 (1953).

[6] M. Gell-Mann. *A schematic model of baryons and mesons.* Phys. Lett. **8**(3), 214 – 215 (1964).

[7] G Zweig. *An SU_3 model for strong interaction symmetry and its breaking; Part I.* CERN-TH-401, 24 p (Jan 1964), CERN-TH-401.

[8] G Zweig. *An SU_3 model for strong interaction symmetry and its breaking; Part II.* CERN-TH-412, 80 p (Feb 1964), CERN-TH-412.

[9] T. D. Lee and C. N. Yang. *Question of Parity Conservation in Weak Interactions.* Phys. Rev. **104**(1), 254–258 (Oct 1956).

[10] C. S. Wu, E. Ambler, R. W. Hayward, D. D. Hoppes, and R. P. Hudson. *Experimental test of parity conservation in beta decay.* Phys. Rev. **105**, 1413–1414 (1957).

[11] R. L. Garwin, L. M. Lederman, and Marcel Weinrich. *Observations of the Failure of Conservation of Parity and Charge Conjugation in Meson Decays: The Magnetic Moment of the Free Muon.* Phys. Rev. **105**, 1415–1417 (1957).

[12] M. Goldhaber, L. Grodzins, and A. W. Sunyar. *Helicity of Neutrinos.* Phys. Rev. **109**(3), 1015–1017 (Feb 1958).

[13] J. H. Christenson, J. W. Cronin, V. L. Fitch, and R. Turlay. *Evidence for the 2 pi Decay of the k(2)0 Meson*. Phys. Rev. Lett. **13**, 138–140 (1964).

[14] Nicola Cabibbo. *Unitary Symmetry and Leptonic Decays*. Phys. Rev. Lett. **10**(12), 531–533 (Jun 1963).

[15] S. L. Glashow, J. Iliopoulos, and L. Maiani. *Weak Interactions with Lepton-Hadron Symmetry*. Phys. Rev. D **2**(7), 1285–1292 (Oct 1970).

[16] J. J. Aubert *et al.* *Experimental Observation of a Heavy Particle J*. Phys. Rev. Lett. **33**(23), 1404–1406 (Dec 1974).

[17] J. E. Augustin *et al.* *Discovery of a Narrow Resonance in e^+e^- Annihilation*. Phys. Rev. Lett. **33**(23), 1406–1408 (Dec 1974).

[18] F.J. Hasert *et al.* *Search for elastic muon-neutrino electron scattering*. Phys. Lett. **B46**(1), 121 – 124 (1973).

[19] F.J. Hasert *et al.* *Observation of neutrino-like interactions without muon or electron in the Gargamelle neutrino experiment*. Phys. Lett. **B46**(1), 138 – 140 (1973).

[20] The UA1 collab., G. Arnison *et al.* *Experimental observation of isolated large transverse energy electrons with associated missing energy at $\sqrt{s} = 540$ GeV*. Phys. Lett. **B122**, 103–116 (1983).

[21] M. Banner *et al.* *Observation of single isolated electrons of high transverse momentum in events with missing transverse energy at the CERN pp collider*. Phys. Lett. **B122**(5-6), 476 – 485 (1983).

[22] G. Arnison *et al.* *Experimental observation of lepton pairs of invariant mass around 95 GeV/c^2 at the CERN SPS collider*. Phys. Lett. **B126**(5), 398 – 410 (1983).

[23] P. Bagnaia *et al.* *Evidence for $Z^0 \to e^+e^-$ at the CERN pp collider*. Phys. Lett. **B129**(1-2), 130 – 140 (1983).

[24] M. Kobayashi and T. Maskawa. *CP-Violation in the Renormalizable Theory of Weak Interaction*. Prog. Theor. Phys. **49**(2), 652–657 (1973).

[25] S. W. Herb *et al.* *Observation of a Dimuon Resonance at 9.5 GeV in 400 GeV Proton-Nucleus Collisions*. Phys. Rev. Lett. **39**(5), 252–255 (Aug 1977).

[26] E. Fernandez *et al.* *Lifetime of Particles Containing b Quarks*. Phys. Rev. Lett. **51**(12), 1022–1025 (Sep 1983).

[27] N. S. Lockyer *et al.* *Measurement of the Lifetime of Bottom Hadrons*. Phys. Rev. Lett. **51**(15), 1316–1319 (Oct 1983).

[28] L. Wolfenstein. *Parametrization of the Kobayashi-Maskawa Matrix.* Phys. Rev. Lett. **51**(21), 1945–1947 (Nov 1983).

[29] The D0 collab., S. Abachi *et al.* *Search for High Mass Top Quark Production in $p\overline{p}$ Collisions at $\sqrt{s} = 1.8$ TeV.* Phys. Rev. Lett. **74**(13), 2422–2426 (Mar 1995).

[30] The CDF collab., F. Abe *et al.* *Observation of Top Quark Production in $p\overline{p}$ Collisions with the Collider Detector at Fermilab.* Phys. Rev. Lett. **74**(14), 2626–2631 (Apr 1995).

[31] F. Englert and R. Brout. *Broken Symmetry and the Mass of Gauge Vector Mesons.* Phys. Rev. Lett. **13**(9), 321–323 (Aug 1964).

[32] P. Higgs. *Broken Symmetries and the Masses of Gauge Bosons.* Phys. Rev. Lett. **13**(16), 508–509 (Oct 1964).

[33] E. Noether. *Invariante Variationsprobleme.* Nachr. Akad. Wiss. Gïżœttingen **2**, 235–257 (1918), translation available online.

[34] O. W. Greenberg. *CPT Violation Implies Violation of Lorentz Invariance.* Phys. Rev. Lett. **89**(23), 231602 (Nov 2002), hep-ph/0201258.

[35] M. Lautenbacher A. Buras and G. Ostermaier. *Waiting for the top quark mass, $K^+ \to \pi^+\nu\overline{\nu}$, B_s^0-$\overline{B}_s^0$ mixing, and CP asymmetries in B decays.* Phys. Rev. D **50**(5), 3433–3446 (Sep 1994).

[36] C. Jarlskog. *Commutator of the Quark Mass Matrices in the Standard Electroweak Model and a Measure of Maximal CP Nonconservation.* Phys. Rev. Lett. **55**(10), 1039–1042 (Sep 1985).

[37] M Ciuchini *et al.* *2000 CKM-Triangle Analysis A Critical Review with Updated Experimental Inputs and Theoretical Parameters.* J. High Energy Phys. **07**(LAL-2000-77, RM-3-TH-2000-16, ROMA-1-1307), 013 (Dec 2000), hep-ph/0012308, updated results and plots available online.

[38] Particle Data Group, K. Nakamura *et al.* *Review of particle physics.* J. Phys. **G37**, 075021 (2010), PDG online.

[39] J. C. Hardy and I. S. Towner. *Superallowed $0^+ \to 0^+$ nuclear β decays: A new survey with precision tests of the conserved vector current hypothesis and the standard model.* Phys. Rev. C **79**(5), 055502 (May 2009), arXiv:0812.1202 [nucl-ex].

[40] T. Latham and T. Gershon. *A method of measuring $\cos(2\beta)$ using a time-dependent Dalitz plot analysis of $B^0 \to D^0_{CP}\pi^+\pi^-$.* J. Phys. G **36**(2), 025006 (2009), 0809.0872 [hep-ph].

[41] J Charles *et al.* *CP Violation and the CKM Matrix: Assessing the Impact of the Asymmetric B Factories.* Eur. Phys. J. C **41**(CERN-PH-EP-2004-031. CPT-2004-P-030. LAL-2004-21. LAPP-EXP-2004-01. LPNHE-2004-01), 1–131. (2004), arXiv:0406184 [hep-ph], updated results and plots available online.

[42] R. Fleischer. *New strategies to extract β and γ from $B^0 \to \pi^+\pi^-$ and $B_s^0 \to K^+K^-$.* Phys. Lett. B **459**(1-3), 306 – 320 (1999), hep-ph/9903456.

[43] The LHCb collab., B Adeva *et al.* *Roadmap for selected key measurements of LHCb.* LHCb-PUB-2009-029 (Dec 2009), arXiv:0912.4179v3 [hep-ex].

[44] Heavy Flavour Averaging group, D. Asner *et al.* *Averages of b-hadron, c-hadron, and tau-lepton Properties.* (2010), arXiv:1010.1589 [hep-ex], updates available online.

[45] I. Dunietz R. Aleksan and B. Kayser. *Determining the CP-violating phase γ.* Z. Phys. C **54**, 653–659 (1992).

[46] I. Dunietz and R. G. Sachs. *Asymmetry between inclusive charmed and anticharmed modes in B^0, $\overline{B}^0$ decay as a measure of CP violation.* Phys. Rev. D **37**(11), 3186–3192 (Jun 1988).

[47] I. Dunietz and R. G. Sachs. *Erratum: Asymmetry between inclusive charmed and anticharmed modes in B^0, $\overline{B}^0$ decay as a measure of CP violation.* Phys. Rev. D **39**(11), 3515 (Jun 1989).

[48] I. Dunietz. *Clean CKM information from $B_d \to D^{(*)\mp}\pi^{\pm}$.* Phys. Lett. **B427**(1-2), 179 – 182 (1998), hep-ph/9712401, link.

[49] J. Zupan. *The case for measuring gamma precisely* (Sep 2010), arXiv:1101.0134 [hep-ph].

[50] V. Sordini. *Measurements of $b \to u$ amplitude and CKM weak phase γ using $B^0 \to DK^{*0}$ decays reconstructed with the BABAR detector.* PhD thesis, Université de Paris-Sud 11 Orsay and Università di Roma La Sapienza, Jun 2008, LAL-08-59.

[51] M. Gronau and D. London. *How to determine all the angles of the unitarity triangle from $B_d^0 \to DK_S^0$ and $B_s^0 \to D\phi^0$.* Phys. Lett. **B253**(3-4), 483 – 488 (1991).

[52] M. Gronau and D. Wyler. *On determining a weak phase from charged B decay asymmetries.* Phys. Lett. B **265**(1-2), 172 – 176 (1991).

[53] D. Atwood, I. Dunietz, and A. Soni. *Improved methods for observing CP violation in $B \to DK$ and measuring the CKM phase γ.* Phys. Rev. D **63**(3), 036005 (Jan 2001), hep-ph/0008090.

[54] D. Atwood, I. Dunietz, and A. Soni. *Enhanced CP Violation with $B \to KD^0(\overline{D}^0)$ Modes and Extraction of the Cabibbo-Kobayashi-Maskawa Angle γ.* Phys. Rev. Lett. **78**(17), 3257–3260 (Apr 1997), hep-ph/9612433.

[55] A. Giri, Y. Grossman, A. Soffer, and J. Zupan. *Determining γ using $B \to DK$ with multibody D decays.* Phys. Rev. D **68**(5), 054018 (Sep 2003), hep-ph/0303187.

[56] S. Pruvot. *Mesure de l'angle gamma de la matrice CKM ïžœ l'aide des dïžœsintïžœgrations $B^\pm \to D^0(K^0_S\pi^+\pi^-)K^{*\pm}$ en utilisant le dïžœtecteur BABAR à SLAC.* PhD thesis, Université de Paris-Sud 11 Orsay, July 2007, LAL-07-76.

[57] M. Rama. *Measurement of the CKM angle γ (ϕ_3) using $B \to DK$ decays.* PoS **FPCP2009**, 003 (2009), arXiv:1001.2842 [hep-ex].

[58] K. Akiba *et al.* *Determination of the CKM-angle γ with tree-level processes at LHCb.* LHCb-2008-031 (Jul 2008), CERN-LHCb-2008-031.

[59] T. Gershon and M. Williams. *Prospects for the measurement of the unitarity triangle angle γ from $B \to DK^+\pi^-$ decays.* Phys. Rev. D **80**(9), 092002 (Nov 2009), 0909.1495 [hep-ph].

[60] T. Gershon and A. Poluektov. *Double Dalitz plot analysis of the decay $B \to DK^+\pi^-$, $D \to K^0_S\pi^+\pi^-$.* Phys. Rev. D **81**(1), 014025 (Jan 2010), 0910.5437 [hep-ph].

[61] M. Gronau, Y. Grossman, N. Shuhmaher, A. Soffer, and J. Zupan. *Using untagged $B \to DKS$ to determine γ.* Phys. Rev. D **69**(11), 113003 (Jun 2004), hep-ph/0402055.

[62] S Ricciardi. *Measuring the CKM angle γ at LHCb using untagged $B_s \to D\phi$ decays.* LHCb-PUB-2010-005 (May 2010), CERN-LHCb-PUB-2010-005.

[63] J. Nardulli and S. Ricciardi. *Determination of the CKM angle γ with $B^0 \to D(h^+h^-)K^{*0}$ decays.* LHCb-2008-038 (2008), CERN-LHCb-2008-038.

[64] L. Evans and P. Bryant. *LHC Machine.* J. Instrum. **3**(08), S08001 (2008).

[65] The ALICE collab., K Aamodt *et al.* *The ALICE experiment at the CERN LHC. A Large Ion Collider Experiment.* J. Instrum. **3**, S08002 (2008).

[66] The ATLAS collab., G. Aad *et al.* *The ATLAS Experiment at the CERN Large Hadron Collider.* J. Instrum. **3**, S08003 (2008).

[67] The CMS collab., R. Adolphi *et al.* *The CMS experiment at the CERN LHC. The Compact Muon Solenoid experiment.* J. Instrum. **3**, S08004 (2008).

[68] The LHCb collab., A. Alves *et al.* *The LHCb Detector at the LHC.* J. Intrum. **3**, S08005 (2008).

[69] The Totem collab., G. Anelli *et al.* *The TOTEM Experiment at the CERN Large Hadron Collider*. J. Instrum. **3**(08), S08007 (2008).

[70] The LHCf collab., O. Adriani *et al.* *The LHCf detector at the CERN Large Hadron Collider*. J. Instrum. **3**(08), S08006 (2008).

[71] J. Pinfold *et al.* *Technical Design Report of the MoEDAL Experiment*. MoEDAL-TDR-001 (Jun 2009), CERN-LHCC-2009-006.

[72] T Sjïżœstrand, S Mrenna, and P Z Skands. *PYTHIA 6.4 Physics and Manual*. JHEP **05**(FERMILAB-Pub-2006-052-CD-T, LU-TP-2006-13), 026. 570 p (Mar 2006), hep-ph/0603175.

[73] The LHCb collab., S. Amato *et al.* *LHCb: Technical Proposal*. LHCC-P-4 (1998), CERN-LHCC-98-004.

[74] V. Gligorov. *A single track HLT1 trigger*. LHCb-PUB-2011-003 (2011), CERN-LHCb-PUB-2011-003.

[75] S Amato *et al.* *LHCb calorimeters: Technical Design Report*. LHCb-TDR-2 (2000), CERN-LHCC-2000-036.

[76] Y. Amhis. *Time alignment of the electromagnetic and hadronic calorimeters, reconstruction of the $B \to D^-\rho(770)^+$, $B_s^0 \to D_s^-\rho(770)^+$ and $B_s^0 \to D_s^- K^*(892)^+$ decay channels with the LHCb detector*. PhD thesis, Université de Paris-Sud 11 Orsay, July 2009, LAL-09-93.

[77] I. Korolko, V.F. Obraztsov, S. Popescu, and O. P. Yushchenko. *On the possibility of in situ calibration of LHCb calorimeters*. LHCb-2000-051 (2000), CERN-LHCb-2000-051.

[78] U. Fano. *Ionization Yield of Radiations. II. The Fluctuations of the Number of Ions*. Phys. Rev. **72**(1), 26–29 (Jul 1947).

[79] I. Machikhiliyan. *Pre-calibration of PM gain by photo-statistics*. Calorimeter calibration meeting (july 2009).

[80] K. Voronchev and V. Belyaev. *Energy flow calibration of LHCb ECAL*. LHCb-2006-051 (2006), CERN-LHCb-2006-051.

[81] F. Machefert. *LHCb calorimeter electronics, Photon identification, Calorimeter calibration*. Mémoire d'habilitation à diriger les recherches, Université de Paris-Sud 11 Orsay, Mar 2011.

[82] M. Gronau. *Improving bounds on γ in $B^\pm \to DK^\pm$ and $B^{\pm,0} \to DX_s^{\pm,0}$*. Phys. Lett. B **557**(3-4), 198 – 206 (2003), hep-ph/0211282.

[83] The BELLE collab., U. Bitenc *et al.* *Improved search for D^0 mixing using semileptonic decays at Belle.* Physical Review D **77**, 112003 (2008), arXiv:0802.2952 [hep-ex].

[84] S. Pruvot, M. H. Schune, V. Sordini, and A. Stocchi. *Measuring gamma with $B^0 \to D^0 K^{*0}$ decays at BaBar.* (2007), arXiv:hep-ph/0703292.

[85] The CLEO collab., D. M. Asner *et al.* *Determination of the $D^0 \to K^+\pi^-$ relative strong phase using quantum-correlated measurements in $e^+e^- \to D^0\overline{D^0}$ at CLEO.* Physical Review D **78**(1), 012001 (2008), 0802.2268 [hep-ex].

[86] The CLEO collab., N. Lowrey *et al.* *Determination of the $D^0 \to K^-\pi^+\pi^0$ and $D^0 \to K^-\pi^+\pi^+\pi^-$ coherence factors and average strong-phase differences using quantum-correlated measurements.* Phys. Rev. D **80**(3), 031105 (Aug 2009), 0903.4853 [hep-ex].

[87] M. Williams. *$B \to DK^*$ Coherence Factor.* talk at Dkstar micro group meeting (apr 2010).

[88] B. Aubert *et al.* *Search for $b \to u$ transitions in $B^0 \to D^0 K^{*0}$ decays.* (2009), arXiv:hep-ph/0904.2112.

[89] The Babar collab., B. Aubert *et al.* *Measurement of $\overline{B}^0 \to D^{(*)0}\overline{K}^{(*)0}$ branching fractions.* Phys. Rev. D **74**, 031101 (2006), arXiv:0604016 [hep-ex].

[90] The Belle collab., A. Kuzmin *et al.* *Study of $\overline{B}^0 \to D\pi^+\pi^-$ decays.* Phys. Rev. D **76**, 012006 (2007), arXiv:0611054 [hep-ex].

[91] The Belle collab., P. Krokovny *et al.* *Observation of $\overline{B}^0 \to D^0\overline{K}^0$ and $\overline{B}^0 \to D^0\overline{K}^{*0}$ decays.* Phys. Rev. Lett. **90**, 141802 (2003), arXiv:0212066 [hep-ex].

[92] A. Satpathy *et al.* *Study of $B \to D^*\pi^+\pi^-$ decays.* Phys. Lett. **B553**(3-4), 159 – 166 (2003).

[93] H. Dijkstra, M Gandelman, and B. de Paula. *Trigger optimisation for L0 at 300 or 100 kHz and Hlt1 at 10 or 4 kHz.* LHCb talk at Trigger and Stripping meeting (feb 2010).

[94] M. L. Mangano. *The Saga of bottom production in p anti-p collisions.* AIP Conf. Proc. **753**, 247–260 (2005), arXiv:0411020 [hep-ph].

[95] P. Colangelo and R. Ferrandes. *Model independant analysis of a class os $\bar{B}_s^0$ decay modes.* Phys. Lett. B **627**(1), 77 – 81 (2005), hep-ph/0508033.

[96] M. Gronau, O. F. Hernàndez, D. London, and J. L. Rosner. *Decays of B mesons to two pseudoscalars in broken SU (3) symmetry.* Phys. Rev. D **52**(11), 6356 (Dec 1995), hep-ph/9404283.

[97] C.-W. Chiang and E. Senaha. *Updated analyiss of two-body charmed B meson decays.* Phys. Rev. D **75**(7), 074021 (Apr 2007), hep-ph/0702007.

[98] C.-K. Chua and W.-S. Hou. *Rescattering effects in $\bar{B}_{u,d,s} \to DP, \bar{D}P$ decays.* Phys. Rev. D **77**(11), 116001 (June 2008).

[99] C.-D. Lü R.-H. Li and H. Zou. *$B(B_s) \to D_{(s)}P$, $D_{(s)}V$, $D^*_{(s)}P$, and $D^*_{(s)}V$ decays in the perturbative QCD approach.* Phys. Rev. D **78**(1), 014018 (Jul 2008), arXiv:0803.1073 [hep-ph].

[100] S. Stone *et al. Measurement of $\sigma\left(pp \to b\bar{b}X\right)$ at 7 TeV in the forward region.* LHCb-ANA-2010-003 (2010), CERN-LHCb-ANA-2010-003.

[101] The LHCb collab., R. Aaij *et al. Measurement of $\sigma\left(pp \to b\bar{b}X\right)$ at $\sqrt{(}s) = 7$ TeV in the forward region.* Phys. Lett. B **694**, 209 (2010).

[102] J. Albrecht *et al. Updated measurement of the J/ψ production cross-section in LHCb.* LHCb-ANA-2010-012 (2010), CERN-LHCb-ANA-2010-012.

[103] D. J. Lange. *The EvtGen particle decay simulation package.* Nucl. Inst. Methods **A462**, 152 (2001).

[104] R. Le Gac *et al.*, *List of the trigger settings with accumulated statistics at the LHCb detector in 2010*, http://marwww.in2p3.fr/ legac/LHCb/.

[105] M. Williams *et al. The HLT2 Topological Lines.* LHCb-PUB-2011-002 (2011), CERN-LHCb-PUB-2011-002.

[106] A. Poluektov *et al.*, *Stripping selections for Gamma from Trees working group*, Twiki B2DXStripping.

[107] A. Martens and M.-H. Schune. *Why do we need to measure $\frac{\mathcal{B}\left(B^0_s \to \overline{D}^0 \overline{K}^{*0}\right)}{\mathcal{B}\left(B^0 \to \overline{D}^0 K^{*0}\right)}$?* LHCb-INT-2010-018 (2010), CERN-LHCb-INT-2010-018.

[108] M. Pivk and F.R. Le Diberder. *SPlot: A statistical tool to unfold data distributions.* Nucl. Inst. Methods **A555**, 356 (2005), physics/0402083.

[109] A. Powell. *talk at the LHCb UK Meeting, Imperial College, Thursday 6th January 2011.* LHCb Internal Note in preparation X (2011).

[110] E. Smith and S. Ricciardi, *Estimation of PID efficiencies with a dedicated weighting procedure for the DKstar micro working group*, DKstar twiki page.

[111] The LHCb Collaboration, *MC10 Generator statistics*, MC10 Statistics.

[112] T. Gershon. *Physics Opportunities with Non-leptonic Decays of B_s^0 and B_d^0 Mesons into Identical Final States*. LHCb-INT-2011-008 (2011), CERN-LHCb-INT-2011-008.

[113] S. Stone. *Measuring Absolute B_s^0 Branching Fractions at LHCb*. LHCb-INT-2009-013 (2010), CERN-LHCb-INT-2009-013.

[114] R. Fleischer, N. Serra, and N. Tuning. *New strategy for B_s branching ratio measurements and the search for new physics in $B_s^0 \to \mu^+\mu^-$*. Phys. Rev. D **82**(3), 034038 (Aug 2010), arXiv:1004.3982 [hep-ph].

[115] The LHCb collab., Aaij *et al.* *Determination of f_s/f_d for 7 TeV pp collisions and a measurement of the branching fraction of the decay $B^0 \to D^-K^+$* (Jun 2011), arXiv:1106.4435 [hep-ex], CERN-PH-EP-2011-075, LHCB-PAPER-2011-006.

[116] The LHCb collab., Aaij *et al.* *Measurement of b-hadron production fractions in 7 TeV centre-of-mass energy pp collisions* (Jun 2011), CERN-LHCb-CONF-2011-028.

[117] The LHCb collab., Aaij *et al.* *Average f_s/f_d b-hadron production fraction for for 7 TeV pp collisions* (Jul 2011), CERN-LHCb-CONF-2011-034.

[118] A. Martín Sánchez *et al.*, *Calorimeter meeting February 9th, 2011, Note in preparation*, Presentation.

[119] A. D. Sakharov. *Violation of CP Invariance, c Asymmetry, and Baryon Asymmetry of the Universe*. Pisma Zh. Eksp. Teor. Fiz. **5**, 32–35 (1967).

[120] A. D. Sakharov. *Quark-muonic currents and violation of CP invariance*. JETP Lett. **5**, 27–30 (1967).

[121] A. Stocchi. Current Status of the CKM Matrix and the CP Violation. in *Particle Physics and Cosmology: The Interface*, edited by D. Kazakov and G. Smadja, volume 188 of *NATO Science Series*, pages 31–82. Springer Netherlands, 2005.

[122] I. Dunietz. *CP violation with self-tagging B^0 modes*. Phys. Lett. B **270**(1), 75 – 80 (1991).

[123] The BABAR collab., P. del Amo Sanchez *et al.* *Dalitz-plot Analysis of B0 –¿ D0bar pi+ pi-*. (2010), arXiv:1007.4464 [hep-ex].

[124] The BABAR collab., B. Aubert *et al.* *Measurement of branching fractions and resonance contributions for $B^0 \to \bar{D}^0K^+\pi^-$ and search for $B^0 \to D^0K^+\pi^-$ decays*. Phys. Rev. Lett. **96**, 011803 (2006), arXiv:hep-ex/0509036.

[125] The BABAR collab., B. Aubert *et al.* *Branching fraction measurement of $B^0 \to D^{(*)} + \pi^-$, $B^- \to D^{(*)}0\pi^-$ and isospin analysis of $\bar{B} \to D^{(*)}\pi$ decays*. Phys. Rev. **D75**, 031101 (2007), arXiv:hep-ex/0610027.

[126] The Belle collab., P. Krokovny *et al.* *Observation of $\bar{B}^0 \to D^0\bar{K}^0$ and $\bar{B}^0 \to D^0\bar{K}^{*0}$ Decays.* Phys. Rev. Lett. **90**(14), 141802 (Apr 2003), hep-ex/0212066.

[127] S Amato *et al.* *LHCb magnet: Technical Design Report.* LHCb-TDR-1 (2000), CERN-LHCC-2000-007.

[128] S Amato *et al.* *LHCb RICH: Technical Design Report.* LHCb-TDR-3 (2000), CERN-LHCC-2000-037.

[129] P R Barbosa-Marinho *et al.* *LHCb muon system: Technical Design Report.* LHCb-TDR-4 (2001), CERN-LHCC-2001-010.

[130] P R Barbosa-Marinho *et al.* *LHCb VELO (VErtex LOcator): Technical Design Report.* LHCb-TDR-5 (2001), CERN-LHCC-2001-011.

[131] P R Barbosa-Marinho *et al.* *LHCb outer tracker: Technical Design Report.* LHCb-TDR-6 (2001), CERN-LHCC-2001-024.

[132] P R Barbosa-Marinho *et al.* *LHCb online system, data acquisition and experiment control: Technical Design Report.* LHCb-TDR-6 (2001), CERN-LHCC-2001-024.

[133] P. R. Barbosa-Marinho *et al.* *LHCb inner tracker: Technical Design Report.* LHCb-TDR-7 (2002), CERN-LHCC-2002-029.

[134] R. Antunes-Nobrega *et al.* *LHCb reoptimized detector design and performance: Technical Design Report.* LHCb-TDR-9 (2003), CERN-LHCC-2003-030.

[135] R Antunes-Nobrega *et al.* *LHCb trigger system: Technical Design Report.* LHCb-TDR-10 (2003), CERN-LHCC-2003-031.

[136] R Antunes-Nobrega *et al.* *LHCb computing: Technical Design Report.* LHCb-TDR-11 (2005), CERN-LHCC-2005-019.

[137] I. Dunietz. *CP violation with beautiful baryons.* Zeit. Phys. C **56**(1), 129–143 (1992).

[138] The CLEO collab., N. Lowrey *et al.* *Determination of the $D^0 \to K^-\pi^+\pi^0$ and $D^0 \to K^-\pi^+\pi^+\pi^-$ Coherence Factors and Average Strong-Phase Differences Using Quantum-Correlated Measurements.* (2009), arXiv:0903.4853 [hep-ex].

[139] Particle Data Group, C. Amsler *et al.* *Review of Particle Physics.* Physics Letters B **667**, 1 (2008), PDG online.

[140] A. Contu. *First look at selection of $B \to D\left(K\pi\pi^0\right)K$.* Presented at CP measurements WG: gamma with trees (jan 2009).

[141] P. Hunt. *DC06 selection studies of $B^+ \to D\left(K\pi\pi\pi\right)K^+$.* Presented at CP measurements WG: gamma with trees (dec 2008).

Remerciements

> - Je ne comprends pas comment on peut avoir peur des oiseaux. [...]
> - Ce sont des monstres [...] parce qu'ils n'ont pas de bras. [...] C'est affreux j'ai toujours l'impression qu'ils vont culbuter vers l'avant, ça n'a aucun sens.
>
> Alexandre Astier alias *Arthur* et Anne Girouard alias *Guenièvre*
> in *Guenièvre et les oiseaux*, **Kaamelott, Livre I**, Tome 2, Épisode 5,
> écrit par Alexandre Astier.

Je souhaite remercier Guy Wormser et Achille Stocchi de m'avoir permis de faire ma thèse au sein du laboratoire. Mes remerciements vont aussi aux personnels administratif, du service *missions* et du service informatique du laboratoire pour l'aide qu'ils ont su m'apporter. Je réserve un remerciement un peu plus particulier aux secrétaires du bâtiment 208, Jocelyne et Laurence, pour leur soutien occasionnel mais efficace.

Thank you to my referees for having accepted the heavy and long task of reading this thesis in detail and allowing the defence. Thank you again for your questions and comments that are always rewarding. Thank you also to Sébastien Descotes-Genon, Roger Forty, Timothy Gershon and Achille Stocchi, for having accepted to be part of the committee. Specific acknowledgements are devoted to Tim for his reading and understanding of the analysis before and during the internal review by the collaboration. Désolé Achille, mais j'étais obligé de mettre une figure de CKM Fitter en face de celle de UT Fit. Sébastien, désolé d'avoir fait court pour la partie d'introduction théorique, et merci d'avoir répondu à mes questions en Ukraine.

Merci Frédéric et Marie-Hélène de m'avoir permis de découvrir un peu le monde de la recherche et celui de la physique des particules du point de vue du calorimètre, en 2006, alors que je m'adonnais à des études sur un sujet bien différent. Merci aussi à Jean-Pierre Maillet sans qui je n'aurais peut-être jamais atteri au LAL et à Fabian Zomer sans qui je n'aurais peut-être jamais frappé à la porte du groupe LHCb. Si je remonte dans l'histoire je dois aussi remercier Cécile Durieu et Sylvie Galdin-Retailleau, qui se sont laissées convaincre de me laisser étudier en Master 2 un domaine bien différent de celui dans lequel je baignais, et de m'avoir même aidé à chercher un nouveau domaine d'études. Merci enfin à Corinne Augier de m'avoir accueilli dans ses cours de cumulatifs de physique des particules du master 1 de physique fondamentale et appliquée d'Orsay et surtout de m'avoir encouragé à continuer dans cette voie.

Merci à mes deux encadrants, Frédéric et Marie-Hélène, d'avoir bien voulu me supporter ces trois dernières années, je sais que cela n'a pas toujours été très facile, et ce pour diverses raisons. Merci en particulier de m'avoir permis d'aborder les deux thèmes qui sont présentés aujourd'hui dans ma thèse et pour votre complémentarité. Cela a été un plaisir de travailler avec vous et j'ose espérer que nos routes se recroiseront dans un avenir relativement proche. Merci pour toute l'expertise technique et votre maîtrise de la physique que vous avez su me transmettre. Merci aussi pour les fous-rire, les anecdotes, la compassion parfois nécessaire et votre aide pour surmonter les épreuves, notamment celle du 19 septembre 2008.

Merci à tous les membres du groupe LHCb du LAL que j'ai cotoyé pendant tout ou partie de ces trois années. Yasmine, merci de m'avoir lancé dans le bain de LHCb, merci pour ton aide, tes conseils et ta bonne humeur constante. Merci aussi pour toutes ces bières suisses et ton soutien à distance ! Thanks Jibo for your help with the grid and the LHCb software, it was quite reassuring to have you in the office next door to ask you silly questions, I owe you so much ! Thanks also to you Wenbin, for your nice *Chinese jokes*, it takes time to understand the Chinese humour but it is good afterwards. Viktor, thank you for the meal in your flat at Kiev, it was nice to see you there also, mais souviens toi qu'ici, on parle français ! Michelle, I'm sorry I miserably failed in getting your weird, but cute, but weird, but cute, Scottish accent. Thanks for sharing the office, The Fight Against The Fly, and other stories. Alexandra, merci pour ta bonne humeur espagnole et ton soutien moral, c'est maintenant à toi de jouer ! Merci Patrick pour ton humour que j'apprécie toujours autant, merci aussi de m'avoir laissé gagner le gros poisson en chocolat noir. N'oublie pas de finir de rédiger ton HDR avant la soutenance d'Alexandra, entre deux blagues sur le PS et le temps de trouver des citations pour tes débuts de chapîtres (si, il s'agit bien là d'un défi). Serguey, thanks for your coffees, thanks for coming early at the lab, so that I am not alone at 8 :30 a.m. at the second floor of the building 208 (enfin excepté le préfabriqué, Nicolas). Benoît, merci pour ton humour, tes histoires de thèse, ton imagination débordante, et enfin de m'avoir accompagné à Kiev pour entendre des présentations en russe. Ioana, merci pour les quelques instants que nous avons passé dans le même bureau, cela a été pour moi un plaisir sincère. Bernard J.-M., merci pour tes énigmes du midi, tes explications sur le fonctionnement des PMTs que tu m'as gentillement proposées en 2006, et surtout tes noix-presque-AOC. Enfin, Jacques, merci pour avoir toujours été prêt à répondre à n'importe quelle question à n'importe quel moment, en particulier sur le calorimètre, merci pour tes questionnements permanents sur des sujets qui ne sont pas forcément de physique des particules, et de nous les faire partager lors des repas. Merci, merci à tous.

Je me dois aussi d'étendre mes remerciements au-delà du groupe LHCb du LAL. Merci à Laurent S. d'avoir accepté d'être mon *tuteur* (cela existe-t-il encore au labo ?), et par conséquent pour les quelques repas passés ensembles. Merci aussi à Laurent S. (pas le même) et à Elias pour m'avoir supporté tout ou partie de ces trois années de monitorat, merci de m'avoir laissé un peu de champ libre, ce fut un plaisir d'enseigner dans vos équipes pédagogiques. Merci Nicolas de

crier SEMINAIRE tous les mardis matin où j'étais en meeting EVO. Au delà du LAL, merci à la team de Clermont, Olivier, Stéphane et Régis pour les pas assez nombreux moments passés ensemble. Merci Stéphane pour ta guitare à l'aube du jour ukrainien. Merci Justine pour les quelques moments passés ensemble.

La liste serait très incomplète si je ne citais pas la Guilde des Thésards en Physique des Saveurs du 208, par ordre chronologique approximatif. Joao, merci pour ton humour et ton amitié, merci pour le voyage à Lisbonne que tu (avec Séverine) m'as permis de faire, avec Véro. Denis, merci de m'avoir accueilli dans ton bureau pour des discussions toujours animées qui finissaient parfois dans le RER, la troisième année sans toi m'a fait bizarre (je sais que tu parles de mieux en mieux français, ceci est un entrainement supplémentaire). Andrey et Leonid, un chaleureux merci pour ces quatres années passées ensemble, merci pour les taquineries. Leonid, il est temps que tu te mettes au français pour lire des remerciements écrits en français (Andrey tu lui traduiras et s'il t'ennuies je t'autorise à lui dire, en russe et si il n'y a pas d'âme sensible autour, ce que tu m'as appris...). Thanks Leonia, for the time spent in Ukraine, don't be ashamed of the time we spent in Kiev. I hope we all meet again and continue to spent a lot of time together. Merci aussi aux thésards de la force sombre du 208, celle qui n'a pas choisi la savoureuse physique de la beauté.

Mes remerciements vont aussi à plusieurs groupes que je ne peux pas me permettre de détailler nominativement (ce serait trop long et j'en oublierais). Aux anciens de NPAC, merci pour le temps passé, des devoirs *en temps libre* de TQC aux bars jusqu'à pas d'heure. A ceux que j'ai croisé à TESHEP 2008, merci à tous pour les bons moments passés ensemble, je ne les oublierai pas (merci en particulier aux Mathieu's pour les vodkas). Merci aussi à ceux que j'ai croisés aux JRJC 2009, merci pour les bons moments passés ensemble dans le pays du canard et de la prune d'Ente. Thanks to the young people I've met at NPAE 2010, we spent some good time together and I hope connections won't disappear with time. Enfin, merci à l'équipe de D2I2, merci pour les repas et les verres échangés, merci pour ce qu'on a pu réaliser ensemble, même si je suis un râleur et un insatisfait continuel. Cette histoire n'est pas finie et j'espère que *la sauce prendra* de manière durable.

Merci aussi à l'ensemble de mes amis qui m'ont supporté pendant ces trois années, merci aussi d'avoir compris mon indisponibilité lorsque c'était le cas. Merci particulièrement aux doctorants d'un autre milieu que celui de la physique des particules de m'avoir fait comprendre la chance que j'ai eue *d'avoir été considéré en tant que tel*[1].

Merci à mon chirurgien de m'avoir rafistolé lorsque ce fut nécessaire. Sans lui, je ne sais si cette thèse aurait pû se terminer sur deux jambes.

Merci à l'ensemble de ma famille mais surtout à Jean-Claude et Marthe pour votre soutien distant mais néanmoins présent. Papa, Maman, je n'ai pas de mots pour vous remercier...sans

[1] Franck Pitiot alias *Perceval* in *Tel un Chevalier*, **Kaamelott, Livre I**, Tome 2, Épisode 39, écrit par Alexandre Astier.

vous je ne serais pas ce que je suis aujourd'hui, en particulier cette thèse ne serait pas. Merci pour l'éducation que vous m'avez insuflée, merci pour votre soutien et votre curiosité sur ce que je fais même si je n'arrive pas toujours à vous l'expliquer comme je le devrais.

Enfin, merci à toi Véro qui m'a supporté pendant toutes ces années d'études et de thèse. Merci de m'avoir soutenu ces trois dernières années, de m'avoir apporté le réconfort dont j'avais besoin lorsque nécessaire, de m'avoir remonté à bloc lorsque ce n'était pas la forme. Merci aussi de m'avoir rappelé que si tout n'est pas rose ce n'est pas si sombre, ainsi que les raisons qui me font aimer ce que je fais lorque j'ai eu tendance à les oublier. Sans toi, cette thèse n'aurait pas été possible, en tout cas pas comme ça. La vie nous réserve encore beaucoup d'aventures à vivre à deux...

Si j'ai oublié ne serait-ce que une personne je m'en voudrais énormément et ce serait involontaire, merci de ne pas m'en tenir rigueur.